Liquid uptake by fibrous absorbent materials

Mark Landeryou

Supervisors: *Dr. Alan Cottenden (UCL)*
Dr. John Gilby (Sira)

PhD. Instrumentation

University College London

This research was undertaken within the Postgraduate Training Partnership established between Sira Ltd and University College London. Postgraduate Training Partnerships are a joint initiative of the Department of Trade and Industry and the Engineering and Physical Sciences Research Council. They are aimed at providing research training relevant to a career in industry, and fostering closer links between the science base, industrial research, and industry.

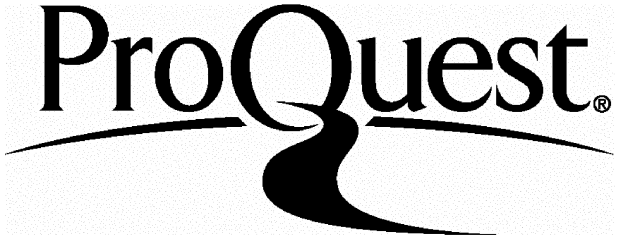

Abstract

The thesis elucidates the mechanisms for fluid-material interactions within incontinence pads and helps to address the lack of understanding in this area. By providing a better understanding of liquid uptake by fibrous materials, the work will contribute to the design of better products for incontinence sufferers.

A review of flow in porous media is presented covering the methods used to measure and model fluid transport, particularly relating to flow in textiles and other fibrous materials.

The majority of the work described in the thesis focuses on the wicking properties of needle-felt fabrics. Such felts are used in reusable (washable) incontinence pads and also provide a simplified model for the more complex materials used in disposable products. An apparatus was designed, built, and used to measure wicking in textile materials. The simplified case of one-dimensional semi-infinite liquid uptake from an infinite reservoir was studied in detail for a range of felts. Mass uptake and wetted area were measured using a digital balance and camera. In particular, the impact on wicking of liquid temperature, sample orientation (horizontal, vertical and angles between), and felt compression were investigated.

Wicking into textile materials is commonly understood using a simple capillary tube model for flow. To evaluate the application of capillary models the felt microstructure was examined. Encapsulated cross-sections of felt samples were prepared, and software written to identify fibres penetrating the plane of an examined section.

While some aspects of liquid wicking, were found to be as expected from a simple capillary tube model, wicking appeared to be reduced in very open structured fibrous materials. It is suggested that this was due to the existence of unsaturated flow where only saturated flow was assumed. Considerable variation in liquid saturation was found in the samples during wicking.

Preface

Liquid uptake by absorbent materials was studied with the primary objective being to investigate the mechanisms of liquid-material interactions in incontinence pads. At present, a lack of understanding in this area hampers the design of better products.

Incontinence is a costly problem in both financial and human terms. Absorbent pads account for about two thirds of expenditure on incontinence products. There is great demand from both users and carers for more effective and cheaper products. Nevertheless, the best products for heavy incontinence still leak about one third of the time.

It is known that the leakage performance of pads is principally determined by the volume of the capillary spaces in the core material. Other factors, such as the speed and extent to which liquid is distributed are also important in deciding the overall performance of a product. The design of current incontinence products is largely based on the intuition and experience of the designer. This research explores the relationship between simple absorbent structures, similar to those used in incontinence products, and measurements of their ability to wick liquid. The problem of urinary incontinence is introduced in the first chapter, together with a description of current absorbent products and materials.

Liquid uptake by, and flow within porous structures is applicable to many areas, from the development of sports clothing to the movement of groundwater in earth and sand structures. Such capillary driven flows have been studied since the beginning of the century, but detailed understanding of the process still remains incomplete. The second chapter presents a review of flow in porous materials covering the methods used to measure and model fluid transport, particularly relating to flow in textiles and other fibrous materials such as paper.

The majority of the work in the thesis focuses on the wicking properties of needle-felt fabrics. Such felts are used in reusable (washable) incontinence pads and also provide a simplified model for the more complex materials used in disposable products. In the third chapter the design and use of an apparatus to measure wicking in textiles is presented. The simplified case of one-dimensional semi-inflnite liquid uptake from an infinite reservoir was studied in detail for a range of felts. Mass uptake was measured by means of a digital balance beneath the reservoir. The wetted area was recorded with a camera, images being captured and stored using a computer. Image processing was used to automatically extract measurements of wetted area from sequences of recorded images. In particular, the impact on wicking of liquid temperature, sample orientation (horizontal, vertical and angles between), and felt compression were investigated.

Wicking into textile materials is commonly understood using a simple capillary tube model for flow. In order to evaluate the application of such capillary models to the felt microstructure, direct examination of the felt samples was carried out using optical microscopy. The encapsulation of felt samples and preparation of cross-sections is also de-

scribed in this chapter. Cross-sections through needle-felt fabrics were analysed with the help of software written to identify fibres penetrating the plane of an examined section.

In the fourth chapter results from the experimental measurements of one-dimensional wicking are presented. A program of experiments was undertaken to investigate the major factors defined by simple capillary models to determine wicking performance.

The experimental apparatus and results obtained are discussed in the fifth chapter. Although some aspects of liquid wicking, were found to be as expected from simple capillary models, wicking appeared to be reduced in the more open structured fibrous materials. It is suggested that this was due to the existence of unsaturated flow where only saturated flow was assumed. Considerable variation in liquid saturation was found in the samples during wicking.

The sixth chapter summarises the conclusions drawn from the experimental work, and suggests how the aims of the research might be pursued in future work.

The final chapter is concerned with a related piece of work using nuclear magnetic resonance (NMR) to investigate absorption in the principal constituents of disposable incontinence pads. The absorbent layer in disposable pads consists principally of super-absorbent polymer (SAP) grains scattered in cellulose based fluffed wood-pulp. NMR images of liquid in a disposable product were obtained. The initial absorption process is extremely rapid, and the majority of the liquid appeared to be taken up by the SAP grains. The nature of the absorbed liquid, particularly within the SAP, was further investigated using spectroscopic NMR. The unique absorbent properties of SAP are not characterised by tight water bonding. In contrast, in the fluffed wood-pulp, MTC data indicated that a considerable proportion of the water becomes cross-relaxed by contact with the cellulose molecules.

Acknowledgements

I would like to express my thanks to some of the many people who made this project possible; and, more importantly for me, made it an enjoyable and enlightening experience.

My supervisors, both at UCL and Sira Ltd, Alan Cottenden, John Gilby, and Tony Allnutt have provided invaluable advice and support throughout the project.

This work was conducted in collaboration with an industrial sponsor, Acordis Ltd whose support and active involvement is gratefully acknowledged. In particular, Roger Ibbett, Warren Lineton, and Nigel Briggs gave generously of their time and expertise.

The nonwoven felt used in the wicking experiments was supplied by Ledatec Ltd; and I would like to thank Stephen Kershaw and Bob Worthington for their assistance in recommending and supplying a considerable quantity of this material.

Bespoke nonwoven fabrics were made using a prototyping facility at Texon UK Ltd, who I would like to thank for their help in producing these felts. I am particularly grateful

to Roger Chapman, and Susan Johnson for their assistance in discussions related to these felts and general problems in wicking work.

The opportunity to explore nuclear magnetic resonance (NMR) would not have arisen without a great deal of help and support from Roger Ordidge. I would also like to thank Gaby Pell who was responsible for the technical elements of the NMR work, and above all made this area a pleasure to pursue. I am indebted to the Royal College of Surgeons Unit of Biophysics at the Institute of Child Health, University College London, where the majority of this work was carried out.

Paul Hartmann AG supplied the raw materials for NMR investigation, and their support is gratefully acknowledged. As is the assistance of Stockhausen GmBH, in particular Edgar Hermann for his advice regarding the properties and use of the superabsorbent polymer.

Contents

List of Figures

List of Tables

Chapter 1

Incontinence and incontinence products

This study focuses on the uptake of liquid by fibrous porous materials. The primary motivation for this work is to elucidate the mechanisms of liquid absorption by incontinence pads. The management of incontinence using absorbent products is important in both financial and human terms. Many current products perform poorly and often fail by leaking, despite having ample absorbent capacity.

All absorbent incontinence products share the same basic design of an absorbent core contained within a liquid permeable coverstock, with a sheet of waterproof plastic as backing. Incontinence pads can be grouped into four major categories – underpads, and bodyworn products available in both disposable (single use) and reusable (washable) forms. The most immediately recognised products are disposable bodyworns, which are similar to baby diapers. Adults, however, have more individual requirements leading to a much more diverse and specialised range of products.

Reusable incontinence products are becoming increasingly popular for reasons of cost, and because they are perceived to be more environmentally friendly. The absorbent core of reusable products is usually made from a nonwoven felt. Nonwoven fabrics are distinguishable from woven fabrics in that they are produced directly from fibres, without forming a yarn. Manufacturers are able to make use of many kinds of fibre. The wide selection of raw fibres, and simple processing techniques means nonwovens can be found in an extremely diverse range of products, particularly those where cost is an important factor. In the automotive industry alone, nonwovens can make up to 26 kg per vehicle; being found in tyre reinforcements, carpet backing, silencer wraps, moulded fuel tanks, carburetter filters, and door trim linings.

The variety of available fabrics, and the extent to which fabric properties can be affected by the choice of fibres and consolidating technique makes nonwoven materials particularly suitable for experimental investigation.

Having reliable methods for evaluating incontinence products and their constituent materials is important to both consumers and manufacturers. Incontinence products can be tested in a number of different ways; with different tests suitable for different purposes. In user trials products are given to a large number of incontinent people for assessment. The advantage of this type of trial is that the product is tested under realistic conditions and can be graded according to criteria that the users feel are important.

In an attempt to reproduce some of the realism of user trials, together with the control possible in measurements made under laboratory conditions, imitative testing has been developed. The most recognisable imitative tests measure leakage using a posable mannequin fitted with a bodyworn product.

Many standard tests are available to measure a single property of absorbent materials. Standard tests are most valuable for grading properties of absorbent materials and are commonly used in quality control. Although many laboratory methods exist to test absorbent products, none are universally agreed to provide a reliable indication of overall product performance or function.

This chapter introduces the key designs and materials used in absorbent incontinence pads. Nonwoven materials were used as the primary experimental model for a fibrous porous medium, and the properties and manufacturing of nonwovens are discussed in some detail. Current methods for testing incontinence products are outlined and the lessons for product function discussed.

1.1 The problem of incontinence

It is estimated that throughout the world 200 million people have some form of incontinence [1]. For each of these people the availability of effective methods for curing or managing incontinence is important in determining their overall quality of life.

1.2 The prevalence of urinary incontinence

Urinary incontinence, as defined by the International Continence society, is the 'involuntary loss of urine which is objectively demonstrable and a social or hygienic problem.' [6]. This definition is not well suited to use in epidemiological investigations. The requirement for objective demonstration cannot be easily established outside a clinical environment, making it difficult to gather data from incontinent people in the community. A subjective element is introduced into the definition by only including cases where the condition is a 'social or hygienic problem'. For both these reasons it is preferable to use definitions derived from frequency, or quantity, of urine loss in epidemiological studies; for example any uncontrolled urine loss in the past month [1].

The problem of defining urinary incontinence is further complicated by the nature of

Group	Age-band	Prevalence
Women living at home	15-44	5-7%
	45-64	8-25%
	65+	10-20%
Men living at home	15-64	3%
	65+	7-10%
Both sexes living in institutions		
Residential homes		25%
Nursing homes		40%
Hospital		50-70%

Table 1.1: Percentage of the population who have urinary incontinence based on averaged data from various studies. (this table from the Royal college of physicians working party on incontinence, 1995 [33])

the condition. Urinary incontinence is a symptom of a wide range of disorders, and can affect individuals very differently. Being a chronic condition, incontinence may change in character over time. As time passes, people are inclined to become accustomed to their incontinence and regard it as less severe. Together with the usual drawbacks associated with survey and epidemiological research, these factors lead to wide variations in prevalence estimates for urinary incontinence [1].

Table 1.1 summarises the prevalence of urinary incontinence, based on average data from several studies [33]. Similar results have been reported more recently [52], in this study between between five and nine percent of the adult population were found to suffer from incontinence. If slight incontinence is included the prevalence rises to between 20 and 30 percent.

Older men and women are more likely to develop urinary incontinence and experience, on average, more serious forms of incontinence. The incidence of urinary incontinence for elderly residents in institutions has been found to be twice that for elderly people living in their own homes, affecting an average of 40 percent of institutionalised elderly [52]. Indeed, incontinence is thought to be a common deciding factor in elderly people having to move into residential accommodation [1].

The emergence of an aging population in developed countries means that the portion of the population suffering from incontinence is likely to continue to increase in the future.

1.3 The management of urinary incontinence

For many sufferers incontinence can be cured, or alleviated, through the use of drugs, surgery, or physiotherapy. There are, however, likely to always remain people who expe-

rience some degree of incontinence. For these people the best method for managing their problem will frequently be the use of an absorbent product.

1.4 Absorbent products

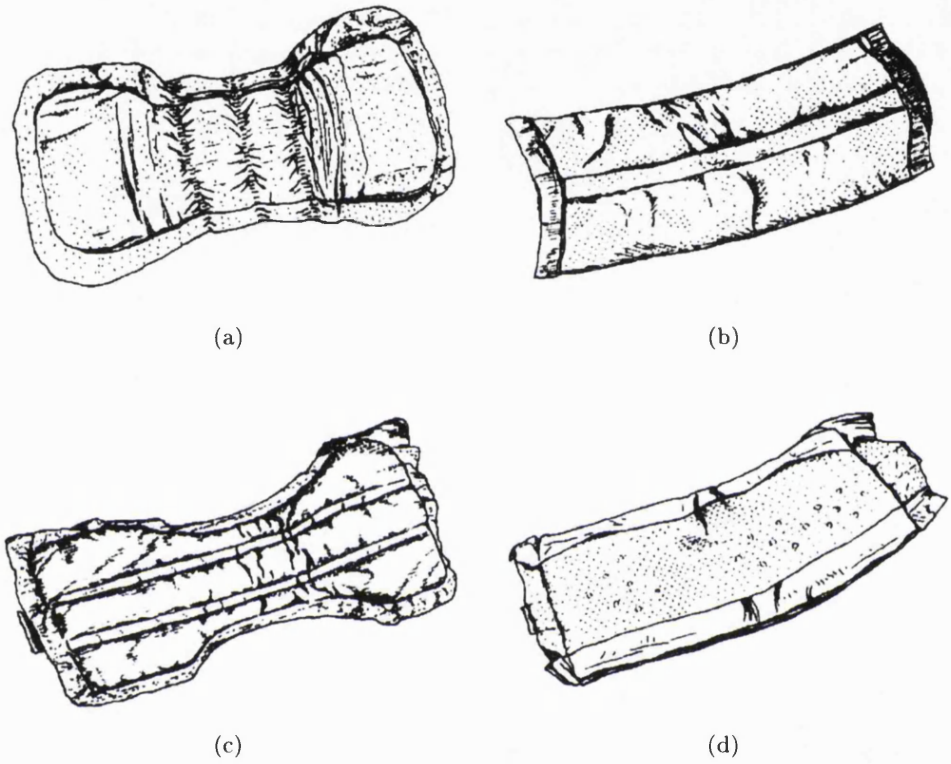

Figure 1.1: Example types of absorbent incontinence pads

The absorbent pad is the most widely used aid for incontinence. Absorbent pads can be divided into two design categories: underpads and bodyworn pads.

Figure 1.1 shows a small sample of the many designs for bodyworn pads. They are available in different styles and sizes to accommodate various volumes of urine and types of use. As well as pads similar to all-in-one disposable baby diapers there are pads designed to be held in place by a separate outer pant. Pads are often shaped and include features such as elastication to improve the fit to an individual's body shape.

Underpads are large (about a metre square) absorbent sheets, intended to be placed between an incontinent person and their bed or chair. They may be used in conjunction with a bodyworn product, and are most effective for people with light urinary incontinence.

Both underpads and bodyworn pads are available in reusable and disposable form. Disposable pads are designed for single use, whereas reusable pads are intended to be laundered and reused; a standard bedpad can withstand at least 100 washes [196].

Reusables avoid some of the problems associated with regular purchasing and storage of disposable products. Disposables, on the other hand, can be easier to handle and do not incur the inconvenience of laundering.

An overview of absorbent incontinence products, from the perspective of textiles technology can be found in Cusick *et al.* [44]. The practical and theoretical aspects of absorbency, related to textile materials, are discussed in the text edited by Chatterjee [28].

1.5 Functional aspects of absorbent products

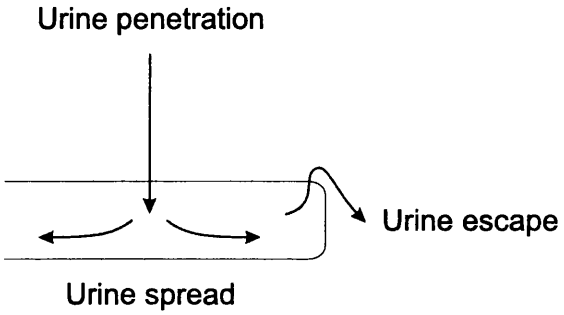

Figure 1.2: Functions and failure for an incontinence pad

The overall absorbent efficacy of an absorbent product will depend largely on its ability to deal with three distinct situations. These are illustrated in figure 1.2 [38];

Penetration: rapid entry of urine should be permitted through the top sheet into the absorbent core.

Dispersal: liquid entering the absorbent core should be encouraged to disperse quickly. This ensures efficient use of the available absorbent material. It is also desirable to move fluid quickly away from the initial point of entry so as not to inhibit further liquid inflow, and to prevent liquid remaining close to the skin.

Containment: once urine has been captured within the absorbent core it should not be allowed to leak out. Liquid should not be able to escape through or around the edges of the waterproof layer. Reverse flow of liquid back through the coverstock material should be prevented. It is also important to retain liquid under more demanding conditions, such as increased pressure or during deformation of the pad.

When selecting an incontinence pad every user has individual requirements, the four most important of which are likely to be [38]:

- Freedom from leakage.

- Comfort and the prevention of skin damage.
- Ease of putting on and taking off.
- Good aesthetics.

1.6 The components of absorbent products

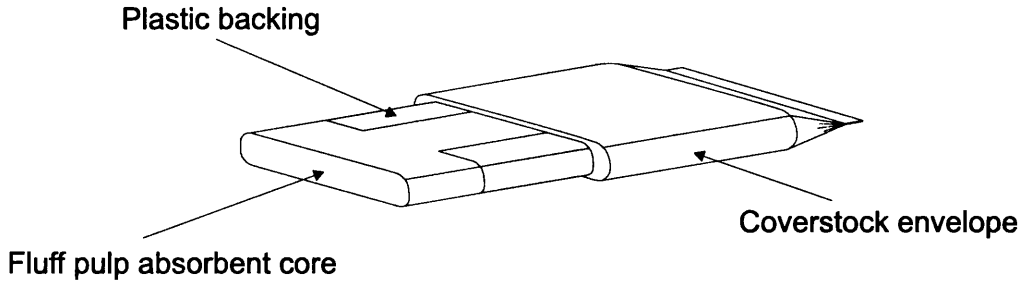

Figure 1.3: Generic incontinence pad construction

Figure 1.3 shows the generic construction of an absorbent pad [38]. The most important feature of the pad is a central core of absorbent material. Enclosing the core on the underside is a water proof backing, to prevent the escape of captured urine. Lying next to the skin is a permeable material, called a coverstock, that acts to retain the absorbent core.

1.6.1 The coverstock

The coverstock will come into direct contact with the skin, and so should be soft, and compliant. The coverstock must be able to contain the absorbent core and so should maintain good mechanical integrity when the pad is both dry and wet. Rapid transmission of fluid across the coverstock should be encouraged during the inflow of liquid. An ideal coverstock would present no resistance to the movement of fluid into the pad, but would subsequently block the movement of absorbed liquid back out of the pad, and onto the skin. Claims have been made for coverstocks that act as one-way membranes, but these are unproven. The coverstock should aim to not only prevent the reverse flow of fluid, but also to keep absorbed liquid away from the user's skin. Over the last ten years there has been a trend towards the use of hydrophobic coverstocks which act as a barrier to liquid flow. Although hydrophobic coverstocks resist the movement of absorbed liquid back towards the skin, penetration into the product is also more difficult.

Modern disposable products mostly have a hydrophobic coverstock made from polypropylene. Current reusable products have top-sheets made from knitted polyester, or cotton.

1.6.2 The absorbent core

Many types of material are used to form the absorbent core in disposable incontinence products. Disposable underpads often contain layers of cellulose wadding, made from recycled paper. The most common core material used in modern absorbent products is fluffed wood pulp. Fluff pulp manufacture is similar to the paper manufacturing process. After the drying stage the wood pulp board is mechanically separated to form a fluffed pulp. Fluff pulp is not a compacted or bonded material, and breaks apart very easily. The absorbency of fluff pulp is related to the properties of the wood from which it is made, and to the processes used in manufacturing [28, 44].

The high void fraction, and low strength, of fluff pulp leads to a marked loss of thickness when the material absorbs liquid. This occurrence is termed wet collapse, and can contribute to leakage from a product. To help resist wet collapse, rigid synthetic fibres are often added to the fluff pulp [28].

1.6.3 Hydrogel polymers

It would be hard to complete a modern account of absorbent material without mentioning hydrogel polymers. Hydrogel polymers are water soluble cross linked macromolecular polymers. Introduced in the 1970s hydrogels, also called superabsorbers, have quickly transformed the design and efficiency of absorbent pads. Today, personal hygiene products account for most of the consumption of superabsorbers [19].

The term hydrogel is used to describe a material that can absorb liquid and hold it in a swollen gel. Many hydrogels can absorb up to 100 times their own weight of liquid. A distinguishing feature of swollen hydrogel particles, in the gel state, is that they remain insoluble in the absorbing liquid. Liquid enters hydrogels driven by an osmotic potential gradient, and swelling occurs as the polymer chains move apart. Water is held in the swollen hydrogel by ion-dipole interactions between water molecules and ions within the polymer.

Hydrogels are produced in many forms, for most incontinence applications grains or powders are used. Although, increasing interest is being shown in the use of fibres containing hydrogels, since they are easier to process than powders. At present these newer hydrogel fibres are prohibitively expensive for disposable applications.

Particle size and shape are important from the point of view of handling and product quality. The size and shape of a hydrogel particle is also a determining factor for the absorption rate of the material.

Superabsorbent technology is an extensive topic, and detailed discussion can be found in the text by Buchholz *et al.* [19].

The use of hydrogel polymers in absorbent products

Hydrogels are almost always used in conjunction with other materials in absorbent applications. Hydrogels do not transport liquid well, and another component is often needed to encourage liquid distribution. Swelling of a hydrogel occurs mainly through diffusion and is slow, with swelling times typically of the order of minutes. When liquid starts to enter a hydrogel particle a surface coating of gel forms, which greatly inhibits further liquid uptake. This is called *gel blocking* and is another reason why hydrogel particles benefit from being kept apart in an accompanying porous medium. The slow absorption rate of hydrogels also means that some form of temporary reservoir may be needed in absorbent products that are required to cope with rapid liquid entry [44].

1.6.4 The backing sheet

The backing sheet serves to contain the absorbed volume of urine. A thin polyethylene backing sheet is commonly used in disposable diapers.

The backing sheets for reusable products are largely made from polyurethane or butyl rubber.

1.7 Disposable versus reusable products

Reusable products are beginning to receive more attention as the increasing size of the incontinent population has led to greater expenditure on disposable bodyworn pads. In addition, health providers have become more aware of the local cost implications of managing incontinence. Together, these factors have led many people to take a fresh look at reusable products, which are often claimed to be cheaper.

At the same time, disposable products have come to be viewed with disapproval as the public becomes more aware of environmental issues. In contrast reusables are perceived to be more environmentally friendly. [39].

A number of studies have been conducted to evaluate the relative effectiveness of reusable and disposable products. A three week trial comparing reusables with disposables in an intermediate care facility is described by Haeker [82]. Reusable products were preferred because the disposables in the study were associated with an increased incidence of skin problems.

In another investigation Dolman [57] reported on the use of disposables and reusables for a group of 11 incontinent people in residential accommodation. This study found a number of points in favour of disposable products; including ease of use, maintenence of skin health, and a reduced level of urine odour in the home. The disposable products, although more expensive, were felt to be better for both residents and their carers.

A review of reusable and disposable product evaluations has been conducted by Cot-

tenden [39, 1], who concludes that neither type of product can claim to be superior. Instead, the most suitable choice of product will depend upon individual circumstances and priorities.

Cottenden has also evaluated studies comparing the environmental impact of disposable and reusable products; considering all aspects of the product: raw materials, manufacture, distribution, washing and drying, and disposal. There is no standard method for making such an environmental impact analysis; and conclusions can be very dependent on underlying assumptions, such as the expected useful lifetime of a reusable product. Overall, these comparisons have been unable to show that either category of product is less environmentally damaging [39, 1].

1.8 The importance of nonwoven materials

Liquid distribution and retention in incontinence products is achieved using a porous structure formed from individual fibres. In disposable products this absorbent core is commonly made of fluffed wood pulp into which grains of superabsorbent polymer are scattered. In reusable products the absorbent function is fulfilled by a felted fabric called a nonwoven.

Strictly the fluffed wood pulp that forms the absorbent core in a disposable product is not usually classified as a nonwoven; it is, though, similar to an air form pulp, except that no bonding agent is present [28].

Being a natural product, formed from cellulose fibres, the porous structure of a fluffed wood pulp is extremely complex and variable. This complexity and variability of fluff pulp makes controlled study of its performance, and understanding of its structure difficult.

Nonwoven materials on the other hand, although they have a complex porous structure, can be simplified and controlled to an extent that is not possible with fluffed wood pulp. The complexity of a nonwoven can be increased, for example by adding cellulosic fibres, until it begins to resemble a fluffed pulp. The similarity between nonwovens and fluff pulp, together with much greater variety and control make nonwovens a more suitable experimental model. In addition, nonwovens are extensively used in reusable products as well as in many other absorbent applications, such as industrial spillage mats.

1.9 Definition of a nonwoven fabric

Nonwoven materials are used in a wide range of applications, such as absorbent hygiene products, inter-linings, furnishings, and building construction. Despite their common usage few people are aware of nonwovens as a separate class of textiles.

Defining exactly what is meant by the term 'nonwoven material' can be problematic. The ISO have proposed that 'A nonwoven is a manufactured sheet of directionally or ran-

domly orientated fibres, bonded by friction, and/or cohesion, and/or adhesion, *excluding* paper and products which are woven, knitted, tufted, stitch-bonded, incorporating binding yarns or filaments or felted by wet-milling whether additionally needled or not. The fibres may be of natural or man-made origin. They may be staple or continuous filaments or be formed in situ.'.

A key feature of nonwoven felts is that they can be produced directly from fibres, without the need to form a yarn. This can greatly simplify the manufacturing process, making nonwovens particularly suitable for applications where low cost is a deciding factor. This is the reason why nonwovens are so often found in disposable products, such as absorbents, operating theatre gowns, and household wipes [203].

Nonwovens are not a new type of textile; felts are nonwoven, and must be one of the earliest fabrics man has made [135]. For many applications, such as clothing, woven fabrics can provide better quality products, making nonwoven felts less well-known. An increasing demand for inexpensive textiles means that, for many applications, nonwovens are preferable to wovens or knits, in cost-performance terms [203].

1.10 Manufacturing of nonwoven fabrics

The manufacturing processes for nonwoven fabrics are extremely varied, much more so than those used to produce woven and knitted fabrics. Nevertheless, each nonwoven manufacturing process will comprise the following common stages [203]:

- Fibre selection.
- Web formation and laying.
- Web consolidation.
- Finishing.

The exact details of the process and materials used at each stage will eventually determine the properties of the nonwoven fabric produced. The manufacture of nonwoven materials is a large and evolving field, and more detailed introductions can be found in textbooks such as those by Lunenschloss and Albrecht, Krčma, and Turbak [135, 120, 203].

1.10.1 Fibres

Like all textile materials, nonwovens are produced from individual fibres. Almost any fibre type can be used in nonwovens manufacturing, with speciality fibres and fibre blends often employed to tailor the performance of a final product.

The fibres may be short, perhaps only a few millimetres long, or they can be extruded directly to form the web in a single, uninterrupted process. If the fibres are cut the average fibre length is often refered to as the *staple* length of the fibres.

The thickness of a fibre is commonly expressed as linear density, that is *tex* or *decitex* (*dtex*); where one tex = $1\,\mathrm{g}\,1000\,\mathrm{m}^{-1}$.

The properties of a fibre are greatly dependent upon the raw material from which it is made, but size, shape, additional processing, and chemical treatment can all alter the fibre's characteristics.

It is convenient to divide fibres into two groups; those that are naturally occuring and those that are man-made. Naturally occuring fibres can come from either animal, vegetable or mineral sources. Similarly, artificial fibres can be organised into three categories depending on whether the fibres are based on: naturally occuring polymers, synthetic polymers, or inorganic materials [28].

1.10.2 Manufacturing of fibres

Many methods are used to manufacture fibres, but most can be categorised as either solution or melt processing [212].

Melt spinning

In the melt spinning process, polymer pellets are fed into an extruder. As the polymer pellets are heated and pass along the extruder they melt. The molten polymer can then be extruded through a spinneret, having thousands of holes, each forming a single fibre.

Solution spinning

Solution spinning techniques involve polymer being dissolved at high concentration in a solvent. The liquid polymer is extruded under pressure through a spinneret. As the fibre hardens, the fibre skin is the first region to form, the interior of the fibre is still swollen with solvent. When the inner polymer solidifies it shrinks, leading to a fibre that does not have a round cross-section, often instead being bi or trilobal.

For man-made fibres the fibre cross-section results from the shape of the holes in the spinneret through which the fibre is drawn. Fibres can have almost any cross-sectional shape. Some examples of polyester fibre cross sections are shown in figure 1.4. Man-made fibres are extruded in an endless process; staple fibres are a result of cutting the fibre. In addition, unlike many natural fibres, man made fibres generally have no texture. For this reason, artificial fibres are often 'textured', that is altered from a straight, rod like, configuration into a crimped or helical structure [212].

1.10.3 Promoting the absorption properties of man made fibres

All natural fibres derived from animal and vegetable sources have chemical groups on their molecules which attract water. Most synthetic fibres, on the other hand, contain few if

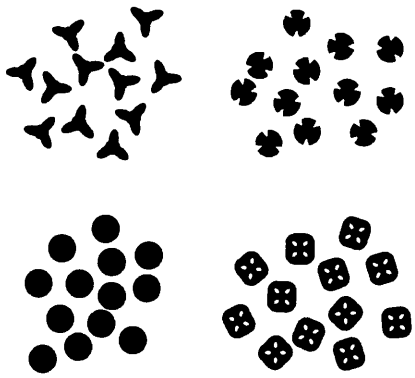

Figure 1.4: Example polyester fibre cross-sections

any water attracting groups. To address this shortcoming a number of techniques have been developed to enhance the absorbent properties of man made fibres:

- Artificial fibres have been produced with novel cross sectional shapes. For instance, the *Galaxy I* fibre is characterised by a well defined and essentially uniform trilobal cross-section. It is this cross-sectional shape that enhances the absorbent capacity and rate of liquid uptake in materials that use the *Galaxy I* fibre [217].
- A surfactant may be applied to the surface of a fibre to enhance wetting by a given fluid. Such surfactants, used to impart hydrophilicity to fibres, are called rewetting agents, and produce a low value for the solid-liquid interfacial tension.

1.11 Manufacturing processes for nonwoven materials

As has been indicated, nonwoven fabrics can be made from a variety of different fibres. A number of methods are available to produce nonwoven fabrics from fibres, in most cases the fibres are assembled into a fibre web as a preparatory step before consolidation.

1.11.1 The fibre web

The term 'fibre web' refers to a textile that is loosely held together by inter fibre friction. The web is usually little more than a sparse collection of fibres having an open structure and not much strength.

The arrangement of fibres making up the web plays an important role in determining the properties of the nonwoven material. An important consideration for the fibre web is whether the constituent fibres have a dominant orientation direction. The pore size distribution, and pore morphology of a nonwoven fabric are influenced by the orientation of the fibres. Ultimately, the ability of a material to act as an absorbent is related to the construction of the fibre web [28].

The fibre web can be produced in many ways, the most common of which is the carding process.

Carding process

The purpose of the carding process is to open out the fibre flock, pulling apart fibre clumps, and forming a web of particular area density. The principal operations of a carding machine are to separate and distribute the fibres, ready for fabric production.

To produce a carded web, a carding machine passes the fibres through a series of rollers covered with a fine metallic wire toothed clothing. The carding machine comprises one, or more, main cylinders surrounded by a number of smaller rollers. The carding action takes place between pairs of rollers, and consists of the fibres being combed by the opposing teeth of the rollers. The fibres are held by one surface and combed with the other; this leads to some alignment of the fibres, and breaks up fibre clumps.

Fibres are picked up by the combing rollers, and need to be put back onto the main roller. The transfer of fibres between rollers in the carding machine is achieved by stripping rollers. The fibres are carded again, repeatedly processing the fibre mass. Over time, a workable web with an even fibre distribution forms on the main cylinder, when ready, the finished web can be drawn off the machine [203].

Carding, also called the dry form process, tends to form a web with the fibres predominantly parallel and orientated in the longitudinal, or machine direction. Other web formation processes can produce webs with different physical properties. In the air lay process, fibres are suspended in an air stream before being collected on a screen to form the web. Fibres in air formed webs have a random orientation, often resulting in larger void spaces.

1.11.2 Web laying

To reach the desired mass and mechanical properties the fibre web is usually doubled: several webs are combined by laying one top of another. Achieving an even fibre density in the doubled web is important, as is obtaining the required weight and orientation of the fibres, in order to produce a specified product.

The dominant orientation of the fibres in the web is a key feature in the final nonwoven. The resulting orientation may be broadly classified into the following types: longitudinal, transverse, longitudinal and transverse, and non-oriented (random), see figure 1.5.

Depending on the end use for the nonwoven, the laying process can be altered to achieve a more appropriate orientation of the fibres.

Parallel laying is the simplest web laying method for producing a higher mass of fibre per unit area in the resultant material. Orientated webs can be doubled directly from the carding process and delivered on to a conveyer belt from cards arranged one behind the

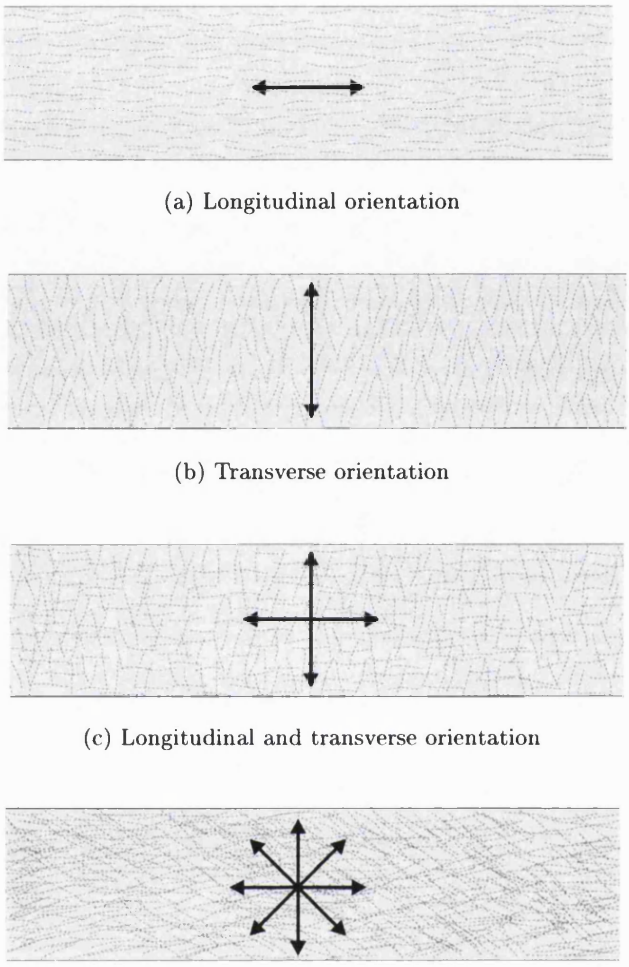

(a) Longitudinal orientation

(b) Transverse orientation

(c) Longitudinal and transverse orientation

(d) Random orientation

Figure 1.5: Fibre orientation in the web [203]

other, see figure 1.6.

For many applications it is important that the nonwoven fabric does not have a preferred fibre orientation. In order to obtain a more even distribution of fibre orientations webs may be 'cross-laid'. The web is delivered at alternating 45° angles to a conveyer belt, see figure 1.7.

A number of webs having differently orientated fibres, or even made from entirely different fibres altogether, can be layered to form a composite web. With this technique, layers can be introduced to reinforce, or otherwise alter the properties of the web, before it is worked into a finished product.

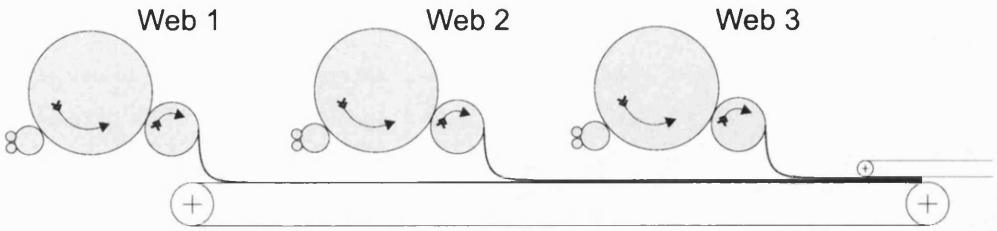

Figure 1.6: Continuous laying of the fibre web, cards or combs are arranged one behind the other [203]

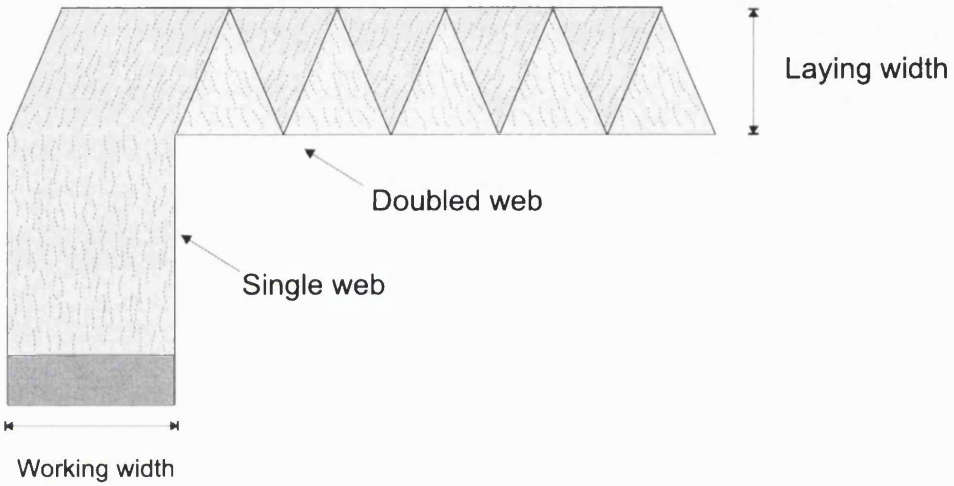

Figure 1.7: Manufacture of a cross-laid web [203]

1.11.3 Bonding

Finally, a number of different methods are used to bond the web. The simple fact that fibres can be entangled is often the sole basis of bonding techniques. Alternatively, fibres can be bonded thermally, or using a chemical binder.

Mechanical bonding

Mechanical bonding is taken to mean the entangling of fibres, bonding the web either by felting using needles, or jets of water.

Needle punching is perhaps the simplest method of nonwoven production. In needle punching the fibres are entangled by use of barbed needles, see figure 1.8. These barbed needles are set into an oscillating board penetrating the web and then withdrawing again, see figure 1.9. When the web is punched through by the needles, small bundles of fibres are caught on the barbs and driven into the fabric, forming a local tangle of fibres. The fibres are released from the barbs as the needle board is lifted away from the fabric, allowing the web to be moved forward. The regions of highly entangled fibres left by the action of

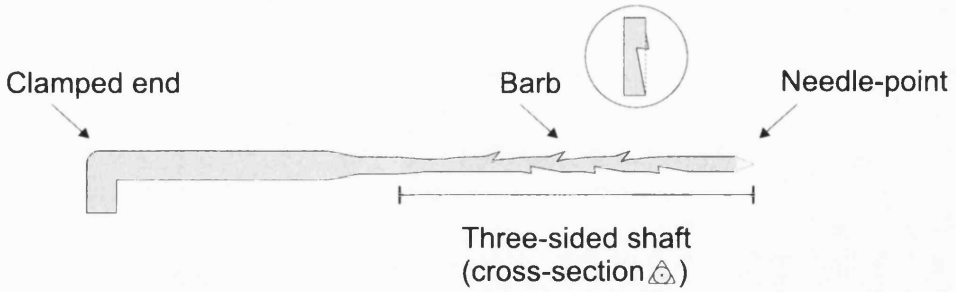

Figure 1.8: Barbed needle used in the needle-punch process [135]

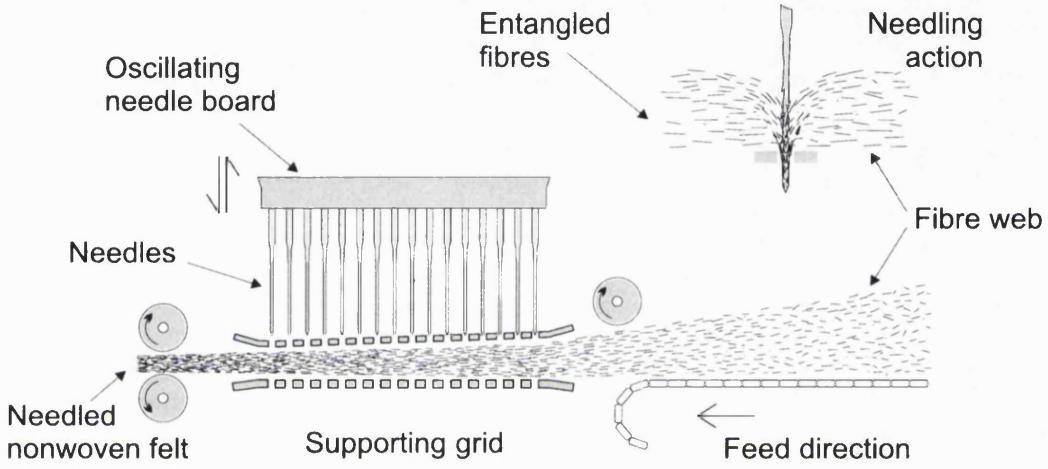

Figure 1.9: Needle-punch process [135]

a single needle are known as *z-pegs*, because the fibres become predominantly orientated perpendicular to the plane of the fabric (the z-direction).

The degree of entanglement can be changed by altering the layout of the needles, penetration depth, needle barb shape, or web advance rate.

The function of the needles in the needling process can be achieved using jets of water. Hydro-entangling uses fine jets of water at high pressures to bond the web. The water jets hit the fabric and deflect the fibres, whirling the fibres around, and so interlocking the web. At higher impact energies for hydro entanglement, the fibre surface structure can be modified causing fibrillation [187].

Chemical bonding

A chemical binding agent can be added to the fibrous web, and then cured to achieve a bonded fabric.

Thermal bonding

Thermal bonding is achieved by fusing adjoining thermoplastic fibres in the web, by applying heat and pressure. Thermal bonding is often used to produce nonwoven coverstocks.

1.12 Finishing of nonwoven fabrics

For many applications nonwoven fabrics are used without any additional treatment following the bonding stage. Nevertheless, finishing treatments are often applied to improve the aesthetics or functional performance of a fabric.

Mechanical finishing methods can impart a particular surface texture to the nonwoven. Often the nonwoven is passed through a series of heated rollers to improve its softness and give it a glossy surface. Many other mechanical techniques are also used: for example, brushing raises surface fibres giving a fur-like feel to the material.

The most common chemical finishing technique is, of course, dyeing. Other less visible finishes are frequently applied to fabrics: such as anti-microbials to prevent the growth of bacteria or microorganisms [203].

1.13 Testing of absorbent products

Strong competition between manufacturers has led to the development of many product variants, and rapidly changing product lines. Although the variety of products available is huge, it is very difficult for individuals to identify the product which will best meet their needs. Only a few specialists are familiar with even a small fraction of the available products, making it hard to find reliable advice about choosing a suitable product; especially when most products are purchased by institutions or health trusts [39]. To address some of these problems a variety of tests and testing strategies have been developed in order to evaluate incontinence products and their components.

For manufacturers of absorbent products testing is important, not only in as much as it influences users choice of products. Product testing is also fundamental to good product design. In order to design, and develop new products it is necessary to have proper understanding of how current products work, and why they often fall below users expectations. Although many laboratory methods exist to test absorbent products, none are universally agreed to provide a reliable indication of overall product performance or function. Similarly, there are many tests that define and measure the properties of component absorbent materials, but again it is not well understood how these properties translate into product performance. The current design process is hampered by a lack of fundamental understanding of how the physical makeup of products leads to their absorbent properties, and then how whole absorbent products function in practice. As a consequence, the majority of product design is led by intuition only allowing for progress by small incremental

changes.

As will be discussed, there are a large number of laboratory tests for absorbent products and their components. However, mostly these are used for quality assurance, looking for consistency and ensuring that a product meets a quantifiable specification.

1.13.1 User trials

In user trials products are given to a large number of incontinent people, who assess their performance. This may mean making subjective comments relating to issues such as comfort, ability to prevent leakage, and ease of use. Objective measurements, such as the weight of absorbed urine in the pad, may also be recorded.

User trials offer some clear advantages over other methods of evaluation; the product is tested under realistic conditions, subject to criteria that gauge user perceived performance. User trial testing is invaluable for grading products, making such data particularly useful to purchasers.

On the other hand, user trials covering a representative range of products using statistically robust methods are enormously expensive, and time consuming to carry out. This means that comprehensive, reliable data from user trials incurs a high price, both financially, and in terms of the relevance of the results. This limitation is made worse by the rapid rate at which manufacturers modify their product ranges, meaning trial data quickly becomes out of date often soon after, or even before, appearing in print.

A number of comparative user evaluations of disposable bodyworn pads have been published, and these have been reviewed by Cottenden [39, 1]. Fader *et al.* have published a trial, using many test centres, of all the disposable pads for heavy incontinence available in the UK in 1996 [66]. Despite improvements the best products were still found to leak about a quarter of the time. Furthermore, the cost of the pads was not found to be a good indicator of performance. In some cases cheaper pads performed better, but using cheaper pads is not guaranteed to be more economical, as they may need to be changed more frequently.

There are few published evaluations of reusable bodyworn products, and none are very comprehensive. However, Phillip *et al.* have reported an informal study of reusable bodyworn products on the UK market in 1990 [170]. Reusable products were found to be most popular with lightly incontinent women.

Only a very few clinical trials of disposable bedpads have been published [87, 202]. No definite conclusions were drawn in these investigations.

User trials of reusable bedpads have been reviewed by Cottenden [39]. The bedpads examined in these trials were shown to leak a lot. Few general conclusions could be drawn, though users often expressed concerns for factors other than leakage, such as personal preferences for design features.

1.13.2 Imitative tests

Imitative testing aims to reproduce life-like situations while measuring product performance under laboratory conditions.

The clearest example of a group of imitative tests are those that involve a mannequin. The mannequin test for leakage uses a mannequin that can be adjusted to simulate different body positions. An absorbent product is placed onto the mannequin and a known volume of test fluid applied at a known flow rate, the quantity of leaked urine is measured.

A number of specialist companies supply mannequins and mannequin testing services. Courtray Consulting Labservice [43] use a range of mannequins created from mouldings of people. The mannequins are available in a variety of types and postures, for example: new born, junior, adult man or women – standing, sitting, and lying. In addition dynamic testing can be performed using mannequins that reproduce walking motions, or simulate the pressures of sitting.

By using transparent mannequins and video capture, as in the Courtray 'Panda', it is possible to record the movement of liquid within a product in order to identify the possible origin of leakage.

Between mannequin tests and user trials, Yerworth has developed apparatus to monitor urine absorption in an incontinence pad when being used by an incontinent person [222]. In this research resistive and optical sensors were used map the spread of urine within a bodyworn product. Results from experiments with users were compared to laboratory measurements of the spread of liquid using a fixed geometry, with liquid being introduced at well defined flow rates.

Other imitative tests are much simpler, but still try to capture some aspect of the product in clinical use. For example, an absorbency test to measure the extent of liquid spreading might be carried out with the absorbent sample in a curved configuration.

It is difficult to judge to what extent imitative testing can be used to evaluate and design incontinence products. In many circumstances it is desirable to monitor product performance under controlled yet realistic conditions. Unfortunately, there is very little published data relating results from imitative testing to other measurements, such as user trials.

1.13.3 Comparative testing

Many tests measure a single property of an absorbent pad or pad component. The SCAN[1] [191] test measures the absorption time of a 50 mm diameter, three gramme cylinder of fluffed wood pulp. Tests such as this are simple to perform and the results easy to interpret. This makes them ideal for comparing different incontinence pad materials and also in testing to ensure good quality control.

[1]Scandinavian pulp, paper, and board committee

There are likely to be a number of different test methods available to evaluate any given property of an absorbent material; with many companies favouring methods developed in-house. The choice of test method will depend on, both the objectives of the test, and the researcher's individual judgement. Cary and Sproles [22] have compared five different test methods for measuring the absorbency of Terry towels. The test methods examined each led to different conclusions regarding relative absorbency, with only one method giving the same ranking of the hand towels as a user evaluation.

Comparative tests are not intended to mimic realistic situations, but because they measure particular attributes of a pad component some relation should be expected between test results and clinical performance. Comparative test results are often taken into account when selecting components for specific purposes in an absorbent pad design.

1.13.4 Tests for physical properties

Fundamental physical properties of the component materials in an incontinence pad can be important in determining the overall function of a material. A low contact angle is essential if a material is to transport liquid readily (see section 2.3.3).

1.14 Laboratory tests and clinical performance

As described above (section 1.13.1) clinical trials are the most reliable method for assessing product effectiveness, but are costly and time consuming to perform. It would, therefore, be very beneficial to be able to infer some aspects of product performance, as measured by clinical trials, from laboratory test results.

Cottenden [38, 41] has sought to relate clinical performance of absorbent pads to their design and the properties of their constituent materials. Thirty four subjects each used ten products for a week and recorded whether leakage was a problem. Absorption time and capacity of the absorbent core was then measured for pads with fluffed wood pulp. The time for fluid to penetrate the coverstock, the strike through time, under standard conditions was also measured using an EDANA[2] test [55]. The leakage properties of a pad were found to be largely determined by the absorption capacity of the material near its centre. For light wetters, pads using coverstocks that allow fluid to penetrate rapidly leaked less. The comfort of wet pads was found to be reduced by using coverstocks with slow strike-through times.

More recently, Cottenden *et al.* studied the leakage performance of large bodyworn incontinence pads for heavily incontinent users [42]. One hundred incontinent people in thirteen user test centres evaluated each of six different products. Each used pad was weighed and the severity of leakage recorded. Correlation was then sought between this

[2]European Disposables and Nonwovens Association

clinical trial data and the results from fifty tests run by sixteen technical test centres. The majority of the technical tests measured either absorption capacity or absorption time.

At low urine weights the most important indicator of pad leakage performance was shaping, with shaped pads leaking less. At higher urine weights both absorption capacity and absorption time became increasingly important until, at 350 g, these two parameters and shaping were equally important.

Taking all urine weights together absorption capacity alone was found to be a good predictor of overall pad leakage performance.

A similar study was carried out using smaller pads for lightly incontinent women [40]. As a result of these studies, international standards have been published [100, 101] defining methods for predicting leakage performance from laboratory tests.

1.15 Current trends in absorbent products

1.15.1 Thin absorbent products

Feminine hygiene products have steadily progressed towards the use of much thinner absorbent cores. This trend continues today, where the current average pad thickness is within the range 2-5 mm, reduced from 15-20 mm common in the mid 1980s [26].

The main reason for the introduction of very thin baby diapers has been distribution costs rather than to meet user demand [26]. Lower transport and packaging costs, together with reduced shelf space requirements all reduce overall product costs. New materials continue to be developed offering even thinner products, without adversely affecting the absorbent performance.

1.15.2 Composite materials

It is difficult to find a single material that allows rapid liquid penetration with good distribution properties, that can also prevent subsequent leakage.

Composite materials, made from multilayered structures, are being used to address this problem, and produce a single absorbent component that meets a number of functional requirements. One such proposal [65] has a top sheet consisting of a blend of fibres to present an open, resilient and wettable material enabling fast acquisition. The middle layer is more dense to achieve good liquid distribution. Finally, the main function of the third layer is to take liquid from the distribution layer and deliver it for storage in the underlying absorbent core.

As well as composite units, materials are being developed in order to fulfil very specific roles within composite products, for example surge management [37].

1.15.3 Developments in superabsorbents

One of the most important recent developments in absorbent products has been the addition of superabsorbent polymers. When first introduced into baby diapers, the polymer made up about twelve percent by mass of the absorbent core. More recent designs contain up to sixty percent polymer, producing much thinner absorbent cores [19]. Superabsorbents were originally placed into pads, within cost constraints for the product, simply to maximise the absorbent capacity for urine. In newer designs the polymer is seen as a part of a larger composite structure, and must function in close association with the other components of the product.

Superabsorbent polymer research has made it possible to better understand, and modify, many aspects of polymer function, such as swelling time and retention under pressure. Modern superabsorbents are being developed with properties that are tailored to meet the demands of the intended application [19].

Superabsorbent fibres have been developed which can be easily blended with other fibres, either in fibre form or into a fabric structure. One possible advantage of using fibres over particles is that they have much less tendency to move from their original location, particularly in diapers [36].

Much of this innovation has been applied to baby diapers, with less work being done to optimise superabsorbent application in adult incontinence products. In many respects adult products have the potential to gain greater benefit from advances in superabsorbents [19]. Adults are more likely to require thin products, and products that can offer some form of odour control. Elderly adults, in particular, have a greater need for products that can help promote good skin health.

1.16 Summary

Urinary incontinence is a distressing and increasingly common problem, with many suffers using absorbent pads.

Absorbent products are available in many different geometries and often use sophisticated materials, but leakage remains very common. The design of pads is, in general, not based on a good fundamental understanding of liquid transport and distribution within the structures being used. Most design is reactive, adding features or elements such as layered structures in response to perceived, or known, shortcomings in existing products. Although products have improved immensely, some of the central problems such as moving the required volumes of liquid against gravity, or choosing raw materials with appropriate properties, have not been fully addressed. This means that a rational design process for the development of incontinence products remains incomplete.

The next chapter will look at some of the mechanisms that affect liquid absorption, as well as attempts to describe and measure liquid transport by porous materials.

Chapter 2

Porous media

The fibrous materials of interest to this study fall into the much larger category of porous materials. Porous materials are used and seen continually in daily life, and have been the subject of detailed studies in physics, biology, and engineering.

The pore structure of a porous medium can be extremely complicated, and it is often helpful to describe average macroscopic parameters for the medium. The more important macroscopic parameters are defined in this chapter, and some methods for determining them discussed.

The fundamentals of liquid movement in porous materials will be described as they relate to the simple capillary models applied to textiles. For most cases, the resistance to single phase flow of a liquid in a porous medium can be expressed by analogy to electrical conduction. Measurement of such saturated flows, although in principal straightforward, can present subtle practical problems. A number of measurement techniques have been developed, some specifically for fibrous materials.

Clearly the conductance of a material is related to its physical microstructure but the correlation is unlikely to be simple. The main approaches taken to modelling liquid conductivity by porous media will be discussed.

Saturated flows are somewhat artificial, and in most cases two or more fluids will flow simultaneously in a porous medium. In this situation the flow becomes much more complicated. Methods for measuring and modelling unsaturated flows in porous media will be outlined.

The spontaneous uptake of liquid by textile materials is referred to as wicking. Wicking in textiles has been the subject of many experimental investigations. In the case of longitudinal wicking from an infinite reservoir the distance covered by the liquid is usually measured and described using a simple capillary model. A review of methods for measuring wicking in fabrics will be presented.

The theme of this chapter is general mechanisms of, and models used to describe, flow in porous media. Particular attention is to be paid to fibrous materials, and flow in paper

which has received more research attention. This chapter aims to introduce the underlying mechanisms of porous flow, and show that the term porous flow describes a wide variety of processes. In all but the most contrived situations, both the geometry of the porous material and the mechanisms of flow will be extremely complicated. Undeterred by the microstructural details, simple models are in regular use and serve to capture many of the essential features of porous flow.

Comprehensive reviews of porous media and porous flow can be found in the excellent monographs by Bear, Dullien, and Scheidegger [10, 61, 192]. Many of the fundamental aspects of absorbency, particularly those associated with textile materials have been reviewed by Chatterjee *et al.* [28].

2.1 Porous media

The absorbent properties of a material are determined by its ability to receive, transport, and retain liquid. In most materials liquid is absorbed by passing through a connected network of void spaces. Such a material, having spaces distributed throughout its volume, can be classed as a porous medium.

There is a huge variety of porous media, from textiles, and columns packed with regularly size spheres; to macromolecules such as hydrogels, and rocks such as granite. Clearly the voids within porous materials are very different, ranging from materials that are mostly formed of void space, to media in which the pore space needs to be considered on a molecular scale.

Pores cannot really be separated from the porous medium as individual objects and only exist as part of the continuous connected pore space. Frequently, to aid description, the void space is imagined to be broken into regions consisting of pores and throats. Within the void space there are likely to be identifiable constrictions (throats), and these may be used to locate pores. Pores can then be visualised as regions of space bounded both by solid material, and by the nearest constrictions; see figure 2.1. The pore size may now be defined using any definition of size suitable for an irregular volume [61, pages 28-29].

As the preceding description shows, it is possible to intuitively describe a pore size, but such a definition is not rigorous and the term pore size is often geometrically meaningless. The problems of defining a pore size are discussed in detail by Scheidegger [192, pages 5–8].

2.2 Pore space parameters

The pore space within many porous materials will much too complex to be adequately described by almost any macroscopic model. Keeping this limitation in mind, it is useful, nevertheless, to define a number of parameters to characterise the pore space.

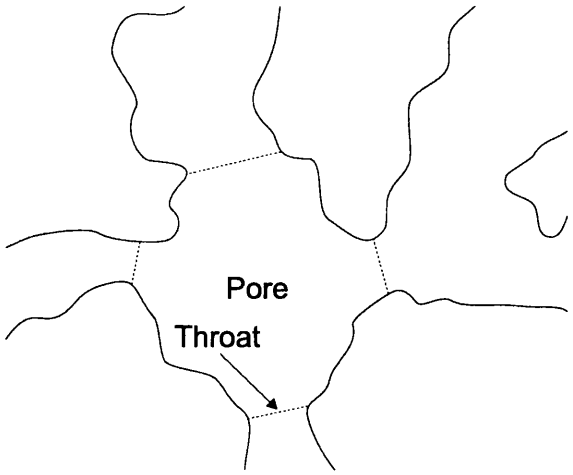

Figure 2.1: Representation of a porous material, to show pores and pore-throats [61].

2.2.1 Porosity

The porosity of a porous material is the ratio of void volume to total volume.

$$f = \frac{V_f}{V_t} \tag{2.1}$$

where, V_f = volume of pores, and V_t = total volume of porous material

Various experimental methods have been suggested to determine porosities. Detailed reviews of these methods can be found in monographs by Scheidegger [192, pages 10-14], and Dullien [61, pages 6-8]. Broadly these methods have been grouped into the following categories:

Direct methods: the bulk volume of the porous sample is measured and then the medium is reduced until only the solid portion remains, the volume of which can now be measured.

Optical methods: provided the pore structure is random enough, the porosity can be determined by examining cross-sections of the sample under a microscope. It may be necessary to encapsulate the porous sample before sections can be obtained. A dye is often used to make the void space more visible.

Rebollo *et al.*, have taken a different approach and propose a correlation between surface roughness and porosity [177]. The speckle produced by scattered laser light incident on a porous rock was used to determine the surface roughness. A linear relationship was found between the porosity and the roughness.

Imbibition methods: the porous sample can be immersed in a perfectly wetting fluid, filling the pore space with fluid. The sample is weighed before and after saturation

with the fluid in order to determine the pore volume. Imbibition methods give the best estimates of pore volume available for liquid flow.

Density methods: Since the mass of a porous medium is almost entirely made up by the solid material, porosity can be calculated by measuring the bulk density of a sample, and comparing this to the density of the solid alone.

Any porosity measurement describes a complex network of pores using only a single number. Porosity is an average macroscopic property of the material, and two porous media with exactly the same porosity can have very different microstructures.

2.2.2 Specific surface

The specific surface of a porous material is the ratio of the surface area of the void space to either the bulk volume, or bulk mass of the porous material. The common methods for measuring specific surface are:

Optical methods: as for porosity measurement, photo micrographs of cross-sections of the porous medium are prepared. The specific surface can then be determined using quantitative stereological methods. Stereology deals with the development of methods to infer properties of three dimensional objects, from the examination of two dimensional sections; see for example the introductory text by Reed and Howard [179]. In this case, the ratio of the perimeters of the pores to the total area of the section, gives the specific surface of the porous material.

Berryman and Blair have used an optical method to examine thin sections of sandstone [11]. A scanning electron microscope was used to capture images of pore structure from polished cross-sections. The images were digitised and processed, applying a number of image processing techniques. A binary image was obtained using a simple thresholding technique, with all pixels above the threshold value being assigned to the pore space. The porosity and specific surface was then estimated directly using spatial correlation functions.

Adsorption: the surface area of the solid portion of the porous material can be estimated by measuring the mass of a vapour adsorbed.

Fluid flow: a number of formulas have been developed relating the rate of fluid flow through a porous material to its specific surface, (see section 2.5.2).

The experimental methods used for determining specific surface are described fully in Scheidegger [192, pages 14-15], and Dullien [61, pages 14-16].

2.2.3 Pore size distribution

In the vast majority of porous media the pore space will not be adequately described by reference to a single pore size. A better approach, described by Scheidegger [192, pages 7-8], is to consider some form of pore diameter for each point within the pore space. The pore size distribution can then be defined by the fraction of the total pore space having a pore diameter between δ and $\delta + d\delta$. Standard statistical distributions curves are then fitted to describe actual pore size distributions.

Pore size distribution can be measured by many different methods, but they do not all share the same definition of pore size. Measured properties of the medium are related to pore size using an assumed model for the void space. It is therefore, important to use pore distribution results only as appropriate given the underlying pore model.

The most popular method for measuring pore size distributions is mercury intrusion porosimetry, introduced by Ritter and Drake [182].

Porosimetry is based on the fact that external pressures applied to one of the phases can be used to control the movement of liquid into a porous medium. If liquid is introduced into a porous sample under changing pressure, controlled filling or emptying of pores will occur. The largest pores will be affected at lower pressures, with increasing pressure needed to reach the smallest pore size. By monitoring the displacement of liquid and the pressure applied, an estimate of the pore volume distribution can be made.

The model underpinning the calculation of pore size distributions from liquid intrusion porosimetry measurements is one of a bundle of circular capillary tubes. Dullien *et al.* [62] have determined the pore size distribution of sandstone samples using porosimetry. These were then compared with the pore size distribution obtained by optical methods. From this work it has been apparent that mercury porosimetry is insensitive to the existence of larger pores, wrongly assigning their volume to the controlling pore throats through which they can be reached. Using only optical methods, though, it is difficult to find the size of the much smaller pore throats [61, page 169].

The information contained in pore size distributions obtained using mercury porosimetry while it may not accurately represent the pore structure, is often valuable for understanding flow. The resistance to liquid flow can be largely attributed to the constrictions of the pore throats, which are easily found from porosimetry curves [61, page 169].

Mercury is generally used as the imbibing liquid because it has a high surface tension and will not penetrate any pores without the application of external pressure. This can, however, be a problem for easily deformed materials that are likely to be compressed as liquid is forced into the pore space. As a result, the apparent pore distribution is not the same as that present in an undistorted sample. To overcome this problem, liquid porosimetry has been developed using more easily displaced liquids, often in extrusion mode; that is, with liquid being driven out of the initially saturated porous material. An automated method suitable for use with fabrics has been developed by the Textile Research

Institute (TRI) in the USA [151, 152]. As well as avoiding the problems of distorting the sample, Miller [151] has suggested another advantage to having a choice of liquids. Using hexadecane as a reference liquid (having no contact angle with most fabrics), and an aqueous surfactant solution as the test liquid, Miller has used a porosimetry technique to find advancing contact angles (see section 2.3.3) within nonwoven fabrics.

Pore size characterisation equipment suitable for nonwoven materials is available from a number of commercial suppliers, for example Porous Materials Inc (PMI) [97]. The use of porosimetry and other techniques for pore measurements in nonwovens has been reviewed by Dixon (senior applications engineer at PMI) [56].

Another method that considers a fabric to be made of a bundle of continuous capillaries of various radii has been proposed by Steele [198]. The water concentration gradient in a vertical fabric was assumed to result from the distribution of channel radii. Water concentration gradients in suspended wet fabrics were determined by cutting the sample into sections which were weighed, dried and re-weighed. The curves obtained were then used to determine the distribution of capillary sizes within the fabric. A similar approach, assuming a capillary model for the pore structure but using a centrifugal method for liquid removal, has been described for pore size estimation in fabrics [139].

A number of optical methods have been used to measure pore size distributions. As for porosity and specific surface, measurements can be made from prepared sections of the porous sample.

Several researchers have used quantitative stereological methods to make pore size distribution measurements, these are reviewed by Dullien [61, pages 35-46]. Defining a pore within the irregular pore space remains the principal problem. Often the special case of spherical particles is assumed. A method for non-spherical objects, of similar shape, has been described by Chang and Dullien [25].

Dullien and Mehta have compared methods to determine pore size distribution for a porous network made from a packed bed of salt [64]. Woods metal was used to fill the void space, and the salt dissolved. The particle size distribution of the salt was known from a standard sieve test, giving a good estimate of the pore size distribution formed in the medium. The pore size distribution from quantitative stereological analysis of polished sections of the material was similar to that obtained from the sieve fractions. Mercury intrusion porosimetry was performed on this material. The pore volume distribution measured using mercury porosimetry was heavily shifted towards the smaller pores, in comparison with that from the cross-sectional analysis.

In the case of nonwoven materials scanning electron microscopy has been used for structural examination, for example Das *et al.* [47]. This work has revealed a lot about the structures in needle punched fabrics and the relationship between fibre arrangement and needling methods. Unfortunately, reconstructing pore space models, or extracting microscopic parameters using any of these direct methods can be problematic (see section

2.5.4).

Six methods, including optical and porosimetry techniques, for measuring pore size distributions in woven and nonwoven geotextiles have been compared by Bhatia *et al.* [12]. Geotextiles are fabrics used in civil engineering at soil boundaries to improve the soil's hydraulic properties, or stablise structures. The measured pore size distribution for each sample fabric was found to be dependant on the test method used.

Huang *et al.* [94] have obtained pore characterisations using image analysis of micrographs of thin nonwoven webs, ranging in thickness from 0.3 mm to 0.43 mm. Optical micrographs were obtained of the webs, and image processing used to obtain binary images in which individual pores can be identified. The number, orientation, sizes (areas and equivalent circle diameters), shapes (aspect ratios), and total area for the pores in the images were calculated. Results from image analysis were compared to pore size results from porometer measurements. Agreement was found to be good between the two measurements for the smaller range of the porometer data.

Recently, liquid extrusion and optical microscopy of cross-sections have been compared to asses pore size distributions in carpet pile [225]. Cross-sections were recorded at six or seven levels through the pile of carpet samples embedded in resin. Pores were outlined and their cross-sectional areas measured. The pore size distribution curve from image analysis gave a higher percentage of smaller pores than was found using liquid extrusion. In addition, larger pores were badly under counted using image analysis, compared with liquid extrusion. The authors attributed these differences to edge effects in the image analysis, arising from the use of a relatively small field of view. The results were then rescaled to give good agreement between the two methods.

2.2.4 Tortuosity and interconnection within a porous medium

The movement of fluid into, and within, the maze of pores that define a porous material depends both on the geometry of the individual pores, and also on the way in which they are connected.

The void space within a porous material often forms an irregular, three-dimensional network. The complexity of this branching network means that the flow of fluid from one region of the medium to another takes place through many tortuous paths. This tortuosity is characteristic of the medium and is defined as the average ratio between the actual path taken by fluid and the straight line route.

An important consideration for porous networks is the degree to which the void space is connected. Within an irregular pore structure, the connectivity may be characterised from a series of closely spaced parallel sections. Macdonald *et al.* have described such a technique, using a computer to analyse digitised micrographs of the sections [136, 137]. Corresponding features were identified by finding features in a section, and then examining the same region in the section below. If an overlapping feature was found the two

features were connected. Networks representing the pore space were then constructed. This technique requires particular care in dealing with edge effects.

2.3 Fundamentals of capillary flow

Capillary absorption refers to the spontaneous imbibition of liquid by a porous solid resulting from capillary pressure. The forces that lead to the liquid motion result from the free energies of the interfaces.

2.3.1 Surface tension and the liquid-gas interface

Cohesion between molecules in liquids results from many different forces. Unlike solids, liquid molecules are not constrained to motions about a fixed point, and can act to minimise the liquid surface.

A molecule within the interior of the liquid, far from any liquid surface, will on average experience the same force in all directions. A liquid molecule close to the liquid-gas interface has fewer neighbouring liquid molecules towards the gas phase, and will be subject to a net inward force. Figure 2.2 illustrates this: molecule A inside the liquid is attracted equally in all directions by cohesive forces, but molecule B, at the surface, experiences an attraction into the liquid phase.

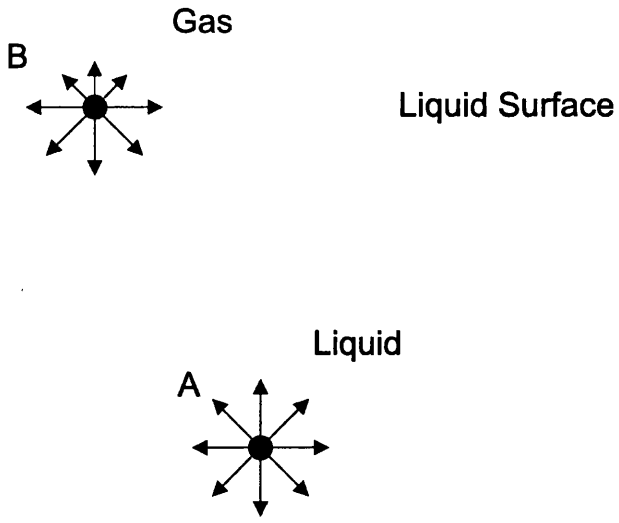

Figure 2.2: Cohesive forces acting on a molecule inside a liquid and at the surface

2.3.2 Surface tension and surface free energy

Surface tension is often referred to as a free energy per unit area, but it is equally well described as a force per unit length.

Consider a liquid film stretched over a wire frame, one end of which can be moved, as shown in figure 2.3.

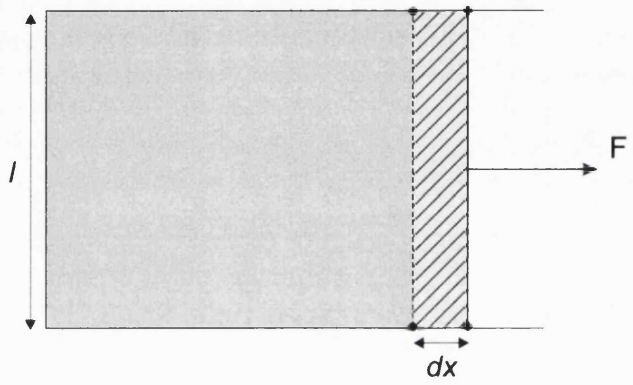

Figure 2.3: A liquid film stretched across a wire frame with a single movable side

If the wire is moved so as to increase the surface area of the film the work needed is dependent upon the length of the wire.

$$\text{Work} = 2\gamma\, dA \tag{2.2}$$

γ is the energy per unit area, and dA is the change in area.

The value of the surface tension is usually expressed in units of *force/length*, and for textile-liquid interactions as *dynes/cm*

2.3.3 Contact angle

When contact is established between the three phases, a three phase boundary line is formed. This situation is best demonstrated by the simple case where a drop of liquid has been placed on a smooth, horizontal, solid surface, as illustrated in figure 2.4.

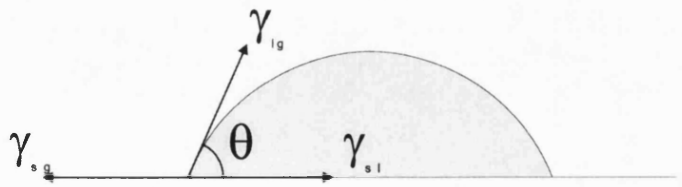

Figure 2.4: Contact angle shown by a liquid drop on a solid substrate

At equilibrium the liquid might stay as a single drop, having a finite angle, θ, between the liquid-gas and solid-liquid interfaces. The contact angle formed is the angle – measured

through the liquid – between the tangent to the liquid-gas interface and the tangent to the solid-liquid interface (determined on the three phase boundary line). Equating the force components parallel to the supporting surface the following equation can be written,

$$\gamma_{lg} \cos\theta = \gamma_{sg} A_{sg} - \gamma_{sl} A_{sl} \tag{2.3}$$

where, γ is the surface tension and the subscripts lg, sg, sl refer to the liquid-gas, solid-gas, and solid-liquid interfaces, and θ is the contact angle.

This equation (2.3) was first postulated by Thomas Young [223] and is often called Young's equation. The contact angle, θ, can be between 0° and 180°. A liquid for which $0^\circ \leq \theta < 90^\circ$ is usually termed the preferentially wetting fluid, with the surrounding fluid being called the non-wetting fluid [61, pages 122-124].

In many systems no equilibrium position for the line of contact exists. One fluid will spread over the surface of the solid, excluding the competing fluid. The spread layer forms *no contact angle* with the solid surface, since no equilibrium line of contact can be maintained [73]. The circumstances of no contact angle are particularly important in the study of absorbency, because this is the most desirable situation for good absorption.

The Young equation (equation 2.3) is often too great a simplification to be applicable to dynamic wetting. In nearly all cases considerable difference can be observed experimentally between the angle measured when the interface is about to advance over the solid surface (advancing angle θ_A) and that measured when it is about to recede (receding angle θ_R). This difference is the contact angle hysteresis.

The existence of contact angle hysteresis can be seen in the case of a stationary drop on an inclined surface, figure 2.5. The drop is distorted by gravity resulting in the contact angle on the upward side being smaller than the contact angle on the downward side. In the absence of contact angle hysteresis the drop would move down the slope as soon as it was inclined at even a slight angle [193].

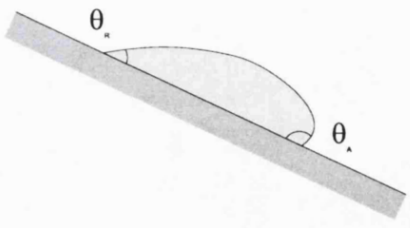

Figure 2.5: Droplet on a slope, demonstrating contact angle hysteresis

According to Adamson [4] there are three classes of phenomena that cause contact angle hysteresis. The first is due to contamination of either the liquid, or the contacting surface. The second cause of hysteresis is due to roughness of the solid surface. In this case the angle between the liquid-gas interface and the solid surface varies with the position of

the interface. The third cause of contact angle hysteresis appears to be surface immobility on a macromolecular sheet.

If a liquid is forced to move over a solid surface sufficiently rapidly, the angle observed during the motion may be greater than the advancing contact angle observed when the liquid is static. This angle is referred to as the dynamic advancing contact angle. The difference between the *dynamic* advancing contact angle, and the advancing contact angle, increases with the speed at which the interface moves, but can be significant even at low speeds [193].

2.3.4 Measurement of surface tension

The most widely used methods for measuring surface tension are those where measurement is made of the force exerted on a body as it is withdrawn from, or extends an interface [28]. This calculation forms the basis of the duNuoy [165] and Wilhelmy plate techniques [218].

The duNuoy tensiometer measures the maximum force needed to pull a platinum ring away from a liquid surface. Platinum is used because it is unreactive and can be cleaned by flaming. Freud and Freud [70] established a theoretical basis for the duNuoy ring method, and the accuracy of measurements was enhanced by Harking and Jordan [84]

Another common instrument uses the Wilhelmy method. A solid that is partly immersed in a wetting liquid will experience an attractive force due to the surface tension. Figure 2.6 shows the forces acting on a partly immersed cylindrical solid.

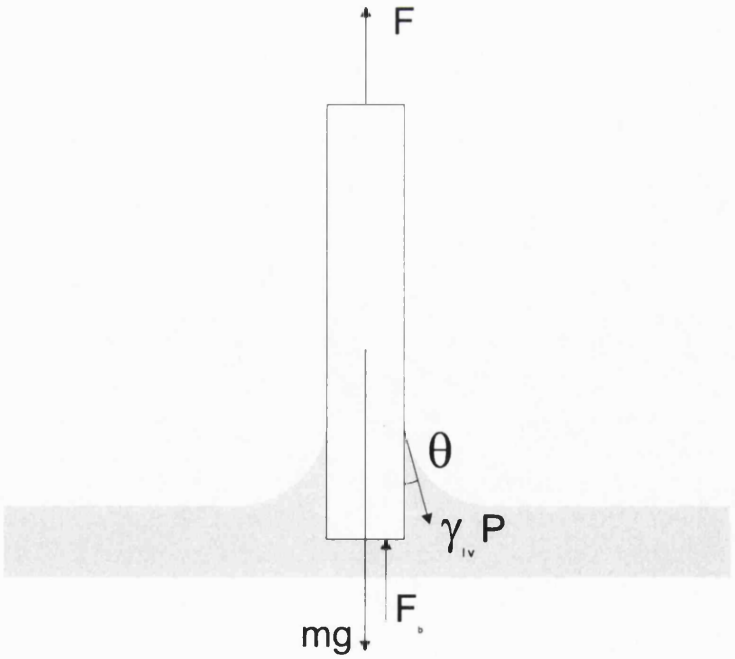

Figure 2.6: Forces experienced by a partly submerged solid, suspended from a balance.

The weight of the solid, and the buoyancy forces are usually removed in the anal-

ysis of experimental measurements, leaving the usual equation for the Wilhelmy force, equation 2.4.

$$F_w = \gamma_{lv} P \cos\theta \tag{2.4}$$

where, F_w is the measured Wilhelmy force, γ_{lv} the surface tension of the liquid, P the perimeter of the solid, and θ the equilibrium contact angle.

Strictly, the Wilhelmy relationship is not a rigorously derived formula, and some researchers do not accept its validity except in cases where there is no contact angle.

There are many applications of this technique, for example Boucher [15] discusses determining the interfacial tension of a liquid by measuring the vertical component of the attractive force, experienced by a solid rod when partly immersed. An accurate balance may then be used to measure the force pulling the rod down into the liquid [32].

It has been suggested that the value of the surface tension measured using the Wilhelmy plate method requires correction for the ends of the plate and the lowering of the liquid level in the reservoir by the meniscus formed when the liquid touches the plate [106].

2.3.5 Contact angle measurement

Contact angle measurements can be made directly by placing a liquid drop on a horizontal surface and recording the drop profile. The measured angle might, however, not be the equilibrium contact angle. The angle formed may be susceptible to local physical or chemical characteristics in the area where the drop is placed [28]. This method can be accurate if sufficient care is taken. Clearly, direct contact angle measurement cannot be made within a porous medium. Instead, it is often possible to make measurements using a flat, solid sheet formed from the same material as the solid in the porous medium.

When studying fibrous materials it is desirable to know the contact angle for the liquid against the fibres. It is possible to make direct observation of the physical contact angle of drops placed on individual fibres [154]. The fibre was supported horizontally on a frame and viewed under a microscope. Using a micromanipulator and micro-syringe a single droplet of the wetting liquid was placed on the fibre. When the droplet had reached equilibrium the contact angle was measured directly. This was done either by projecting and measuring the silhouette of the droplet and fibre, or by photographing the droplet.

In the case of liquid drops on fibres the meniscus close to the thin cylindrical fibre has high principle curvatures of opposite sign. It has been suggested that this high curvature jeopardises methods involving direct visual measurements of contact angle [21], because it becomes impossible to draw a tangent to the three phase contact line with confidence. To overcome this problem Carroll has derived analytical expressions [21] relating the length, surface area, volume, and Laplace excess pressure of a drop on a cylindrical fibre to the drop's dimensions and contact angle. Using these calculations a more accurate method for

measuring contact angles from drop shapes on fibre samples has been established.

The Wilhelmy wetting force technique is particularly suitable for making contact angle measurements on fibres [34, 154, 153]. Following Wilhelmy's relationship (equation 2.4) if the perimeter of the fibre, and the surface tension of the liquid are known, the contact angle of the liquid on the fibre can be found. This can be done by weighing the wetted fibre and making corrections for the buoyancy of the submerged portion.

The Wilhelmy technique remains popular for determining contact angles in a wide variety of industrially important fibre-liquid systems. Morra *et al.* have used a Wilhelmy method to measure contact angle on carbon fibres of a kind used in manufacturing composites [158]. In this experiment plasma treated fibres were shown to have improved wettability compared with untreated fibres.

Contact angles on nylon fibres have been measured by a Wilhelmy method [166]. Contact angle measurements were made in order to understand the wetting behaviours in dyeing and finishing of textile fibres. In this experiment contact angle was shown to increase as the nylon surface became hydrophobic because of the absorbance of surfactant.

In studies of paper fibres, Shen *et al.* have found good correlation between fibre-water contact angles found using the Wilhelmy method and surface energy determined by inverse gas chromatography for pulp fibres [197]. The water absorption rates of the pulps were also measured and found to correlate closely to the contact angles.

Immersing short lengths of fibres can be impractical for some flexible textile fibres, only allowing examination of a few centimetres of the fibre length. A technique for scanning the length of a suspended fibre has been devised [105]. Here a small volume of liquid is held in a ring that surrounds the fibre. The liquid membrane is moved up and down the fibre while the wetting force is recorded using a microbalance. This allows the wetting force over lengths of about 20 cm of fibre to be measured. This technique is typically used to discover the degree of heterogeneity for the chemical finishes that are often used to alter the wetting characteristics of fibres. Wessen *et al.*, using a computer model of this scanning-wetting balance, have been able to reproduce the effective wetting hysteresis caused by microscale heterogeneities [216].

Hsieh *et al.* have used the Wilhelmy principal to measure contact angles on samples of woven fabrics [93]. A totally wetting liquid was used to estimate the contacting perimeter between the liquid and fabric samples. In addition, a correction was made for the water taken up into the pore structures of the fabrics. The wetting properties for single cotton fibres were found to be the same as those for whole woven fabric samples.

2.4 Wetting and capillarity

The process by which a solid-gas interface is replaced by a solid-liquid interface is called wetting. It is this wetting process that allows porous materials to imbibe liquid sponta-

neously. The simplest structure that demonstrates this phenomenon is a capillary tube.

2.4.1 The rate of liquid rise in a capillary tube

Capillary flow results from pressure differences across regions of liquid. A curved liquid interface is subject to forces normal to its surface. Liquid will flow until an equilibrium configuration is reached, with no resultant pressure difference across the interface.

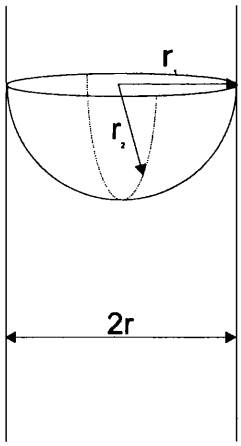

Figure 2.7: Approximation of the meniscus as a hemisphere for small circular cross-section capillary (the two principal radii, r_1 and r_2 for the meniscus are assumed to be equal to the radius of the capillary tube)

The pressure difference P_c across the curved liquid-gas interface attributable to capillary forces is given by the Laplace equation [4]

$$P_c = \gamma \left(\frac{1}{r_1} + \frac{1}{r_2} \right) \tag{2.5}$$

where, P_c is the capillary pressure across the interface. r_1, and r_2 are the principal radii of curvature of the meniscus. γ the surface tension of the liquid,

If the liquid wets the material of the capillary tube the liquid interface will have a concave shape. For a circular cross-section tube of small radius, the meniscus will be *approximately* hemispherical[1]. In solid-liquid systems that are not perfectly wetting, the liquid will form a contact angle where it meets the side of the capillary, equation 2.5 reduces to:

$$P_c = \frac{2\gamma \cos\theta}{r} \tag{2.6}$$

where, P_c is the capillary pressure across the interface. r is the radius of the capillary. γ the surface tension of the liquid, θ the equilibrium contact angle.

[1] In a circular cross-section capillary the shape of the air-water boundary is only assumed to be representable by part of a sphere. In general this will only be a simplifying approximation to the true geometry of the meniscus within a capillary tube.

If h is the height of the meniscus in a vertical capillary, above the liquid surface in the supplying reservoir, then the pressure, ΔP, driving penetration will be the capillary pressure less the hydrostatic pressure drop for the liquid column in the capillary.

$$\Delta P = P_c - \Delta\rho g h \tag{2.7}$$

where, P_c is the capillary pressure across the interface. $\Delta\rho$ is the difference in density between the liquid and gas phase, g is the acceleration due to gravity, and h is the height of the meniscus.

Combining equations 2.6 and 2.7, and neglecting the density of air, the maximum equilibrium height reached by liquid in the capillary can be found when there is no net driving pressure

$$h_{eq} = \frac{2\gamma\cos\theta}{\rho g r} \tag{2.8}$$

Liquid movement in a capillary tube can be found using Poiseuille's law for laminar flow through a pipe. In the case of liquid displacing air from the tube, the resistance to air movement can be ignored. The volume rate of flow for liquid in the tube is then given as:

$$q(r) = \frac{\Delta P \pi r^4}{8\eta l} \tag{2.9}$$

where, q is the volumetric flow rate (dV/dt), ΔP is the pressure drop across the column of liquid, r is the radius of the tube through which the liquid is flowing, η is the viscosity of the flowing liquid, and l is the length of tube through which flow is occuring.

Equations 2.7 and 2.9 result in the following differential equation:

$$\frac{dh}{dt} = \frac{r^2}{8\eta}\left(\frac{\Delta P}{h} - \rho g\right) \tag{2.10}$$

The expression for the encroachment distance of liquid into a capillary was derived by Washburn [213], and for vertical rise is often given in the form:

$$\frac{r^2\rho g}{8\eta h_{eq}} t = \ln\left(1 - \frac{h}{h_{eq}}\right)^{-1} - \frac{h}{h_{eq}} \tag{2.11}$$

where, h is the height of liquid rise, h_{eq} is the equilibrium height rise, r is the radius of the capillary tube, and t is the elapsed time for the height rise.

For short times, when h is much smaller than h_{eq}, or for movement in a horizontal capillary, equation 2.11 can be reduced to the following expression, known as the Washburn equation (where the length of penetration is described by a $t^{1/2}$ relationship) [28]:

$$h = \sqrt{\frac{r\gamma\cos\theta}{2\eta}} t^{\frac{1}{2}} \tag{2.12}$$

The Washburn equation may be taken to be rigorous for capillary driven flow into a circular capillary tube [61, page 387]. Washburn verified this relationship for horizontal

penetration into capillaries, using a number of different liquids. Fisher and Lark have shown that the Washburn equation is obeyed for infiltration into hollow horizontal capillary tubes in the range of capillary radii from 3 to 400 μm [67]. For water in capillaries of radius less than 0.3 μm bubbles were seen to appear in the flowing liquid and decrease the flow rate. Szekely *et al.* [200] saw the need to amend the Washburn equation, because the wetted length tends to zero for small times, but the rate of liquid rise tends to infinity. The failure of the Washburn equation for short times is due to the fact that the Poiseuille law (equation 2.9) is not appropriate for situations where the rate of liquid flow is rapidly changing. A more complete treatment presented by Szekely is based on energy balance for liquid entering the capillary. This rigorous description differs from the Washburn equation only during the very initial stages of capillary penetration. In most practical systems, the Washburn and Szekely equations predict identical behaviour, after one or two seconds following the start of capillary action

In very small diameter capillaries the viscous term may be of the same order of magnitude as the surface tension and gravity terms after a relatively short time. For larger capillaries, however, inertia cannot be neglected and the error in assuming Poiseuille's flow becomes significant. Jeje [103] has recorded liquid motion in five capillary tubes with internal diameters ranging from 266 to 1191 μm, which were held horizontally or vertically over a reservoir into which water could be introduced. The meniscus movement into the capillaries was recorded using a high speed camera, and later analysed frame by frame. Deviations from theoretical predictions assuming Poiseuille flow were found to be significant.

Joos *et al.* [104] have shown that in some cases, where the advancing contact angle is velocity dependent, the Washburn theory is not followed for an advancing meniscus. The capillary rise of high viscosity silicone liquids was recorded in a capillary of radius 250 μm. Good agreement between experiment and theory was observed when the dynamic contact angle was modelled as dependent on the speed of the advancing meniscus.

Peiris and Tennakone have demonstrated a simple method using the rate of height rise of the meniscus in a capillary tube to measure the viscosity and surface tension of a liquid [169]. The height of capillary rise is plotted as a function of time and the value of dh/dt determined from this graph. Combining this with the expression for the equilibrium height rise gives the desired values for the viscosity and surface tension. Case [23] has shown the explicit solution for h and hence dh/dt to be:

$$h(t) = h_0 - h_0 \sum_{n=1}^{\infty} \frac{e^{-nt/t_0} n^{n-1} e^{-n}}{n!} \tag{2.13}$$

where $h_0 = 2\gamma\cos(\theta)/\rho g r$ and $t_0 = 16\eta\gamma\cos(\theta)/\rho^2 r^3 g^2$

Liquid rise in triangular and square cross section capillary tubes has been examined by Mason and Morrow [145](triangular), and Dong and Chatzis [59](square). Liquid infiltration in these systems is altered by the liquid behaviour in the corners, and begins to

show some of the characteristics of uptake by porous media.

2.4.2 Thermodynamics of capillary action

As described previously (section 2.4.1) the classical approach to capillary problems proceeds by finding the pressure difference across a curved meniscus. Princen [173, 174] has taken such an approach for capillary rise within an idealised textile yarn, assuming the fibres to be perfectly cylindrical rods. As Princen notes, real systems will involve extra complications, and an approach based on calculating the curvature of the liquid interface becomes impractical. Often the situation can be simplified by examining the changes in energy that lead to capillary action.

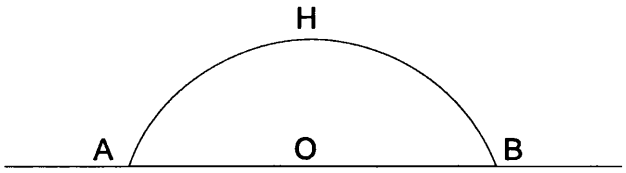

Figure 2.8: Droplet on a plane solid surface

The system in figure 2.8 shows a profile of a flat solid plate of total surface area S, upon which a drop of liquid has been placed. The free energy of the system is

$$F = \text{Area}_{LV}\gamma_{LV} + \text{Area}_{SL}\gamma_{SL} + \text{Area}_{SV}\gamma_{SV} \tag{2.14}$$

where, LV refers to the liquid-vapour, SL to the solid-liquid, and SV to the solid-vapour interfacial areas.

Considering the geometry of the system equation 2.14 becomes:

$$F = \text{Area}_{LV}\gamma_{LV} + \text{Area}_{SL}(\gamma_{SL} - \gamma_{SA}) + K \tag{2.15}$$

Equation 2.15 can be used as the defining equation for the forces that drive liquid motion into capillary systems.

This example is from Schwartz and Minor [194, 195], who also provide practical thermodynamic examples for capillary tubes, Wilhelmy plate, and equilibrium contact angles. As Schwartz and Minor go on to point out, this treatment is particularly suited to liquid-textile systems, where there are many liquid fronts fed from the same reservoir.

A rigorous review of the thermodynamics of capillary action applied in particular to porous media has been presented by Morrow [159].

A thermodynamic approach has been used to produce computer simulations of droplets. The shape that lowers the surface tension is optimised using an Ising model [99]. Manna *et al.* [142] used an Ising model in a stochastic simulation to determine the shape of a droplet on a wall. The spreading of microscopic liquid droplets has been simulated using

a 3D Ising model by Coninck *et al.* [50], and compared to experimental observations. In the textiles area, spreading of liquid droplets on fibres has been modelled by Lukáš [133] using an Ising model. Ising models provide simple simulations of complex processes, and the results are in good qualitative agreement with the behaviour of real systems.

2.5 Single phase flow in a saturated porous medium

The simplest situation of flow through a porous medium involves a single fluid filling the entire void space, with flow caused by a persistent pressure gradient. French engineer Henry Darcy proposed a description of this kind of flow in 1856 [46], from his investigations of the passage of water through vertical columns packed with sand. Darcy's law defines a permeability for a porous material, this is a measure of the resistance of a medium during the saturated flow of a fluid,

$$q = \frac{kA\Delta P}{l\eta} \tag{2.16}$$

where, q is the volumetric flow rate, k is the permeability, A is the normal cross-sectional area of the sample, l is the length of the sample in the macroscopic flow direction, ΔP is the hydrostatic pressure drop causing the flow, and η is the viscosity of the flowing fluid.

In using Darcy's law the complex microscopic details of flow within the pore space is described as an average macroscopic flow. The precise microscale pattern of flow is ignored and the porous material treated as a uniform medium. For Darcy's law to be valid flow must be slow; more precisely the Reynold's number must be small enough that viscous forces dominate inertial forces. Estimates of the largest possible Reynolds number for Darcy flow vary, but a value of between one and ten has been suggested [10, page 126].

2.5.1 Measurement of permeability

Laboratory measurement of permeability is made by means of a permeameter.

Figure 2.9 shows a sample of porous material, through which a constant flow of water is driven by a fixed pressure difference across the sample. Here, the pressure difference is obtained by keeping the water in the supplying reservoirs at a constant pressure head. The hydraulic head drop driving liquid flow can then be found from the difference in head between these two reservoirs. The rate of liquid flow can be measured from the volume of water that flows out of the lower reservoir in a known time interval [144].

As described the experimental method for measuring permeability is very simple, but a number of difficulties can arise in practice. It is important to take precautions to ensure accurate measurements. Unwanted pressure drops within the apparatus should be avoided. Care is needed not to disturb the pore space in the material when obtaining the experimental sample. The sample must be fixed in the apparatus so that fluid cannot bypass the pore space. The liquid used for making flow measurements should be degassed

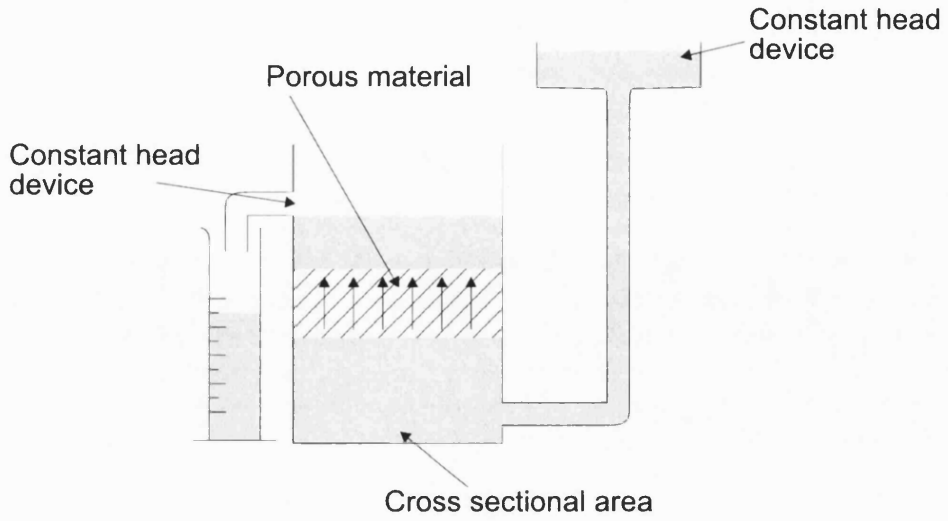

Figure 2.9: Schematic of a permeameter for measuring saturated flow through a porous sample, to determine permeability

to avoid gaseous entrapment, as any gas pockets within the sample will further restrict the flow leading to inaccurate measurements [144].

The measurement of permeability is often subject to considerable error. Also, Darcy's law might not be valid at very low and high flow rates. For these reasons experiments are generally performed over a range of low flow rates.

A number of different permeameter designs exist, often specialised for use with a particular kind of porous material [10]. Permeability is an important parameter used in soil physics, as a consequence permeameters have been developed for use with geotextiles. Test methods for the measurement of water permeability in geotextiles have been reviewed by Koerner *et al.* [115].

Liquid flow through combinations of soils and geotextile fabrics has been investigated, looking in detail at the effect of clogging and cyclic compressions on the permeability [215].

Flow in the plane of a fabric is of particular interest here because this is the kind of flow associated with liquid spread in an absorbent product. Standard test methods, such those from the ASTM [8, 9], have been devised for making permeability measurements in geotextiles. ASTM D4716-87 describes a test method for determining the constant head hydraulic transmissivity within the manufactured plane of a geotextile, see figure 2.10.

The change in in-plane permeability caused by varying needle-punching parameters and compression in nonwoven geotextiles has recently been investigated [95]. A series of 14 needle-punched nonwoven geotextiles of varying needle density, depth of needle penetration, and mass density were produced from polyester staple fibres. The in plane hydraulic transmissivity was measured, using a method based on ASTM D4716-87. The transmissivity parameter was found to decrease with increasing depth of needle penetration,

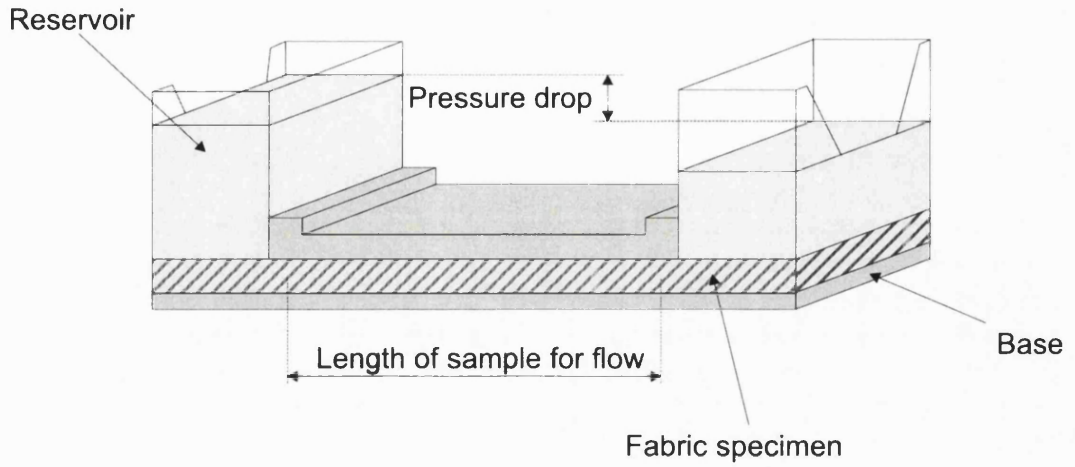

Figure 2.10: Permeameter for measuring saturated flow in the plane of a porous sample, ASTM D47167-87

needling density, and mass per unit area. Also as normal stress was increasingly applied to the sample the transmissivity was shown to decrease, approaching a constant value.

Filtration apparatus for measuring the gas permeability of needled fabrics has been described by Igwe [96]. Within most of the measured region, Darcy's law was found to be followed. At higher flow rates Darcy's law did not appear to hold in the needle felts, but the increased resistance of the sample was thought to be due to compression of the fabric sample. Overall, fabric thickness, weight, and density were important parameters in determining the permeability of a sample, but the internal structure of the needle felts had little effect on air permeability.

Steady state liquid flow through the plane of fabrics has been studied particularly in the area of filtration. In a method devised by Miller and Clarke, liquid is moved by a piston, at a constant rate, through the plane of a fabric while the resulting changes in pressure are measured [148]. Using this approach both the resistance to liquid flow in the steady state, and the wetting response on initial contact can be measured.

Darcy's law has been applied to determine the permeability of woven cotton and polyester cloth (for example, Terry towel) [206]. Here a textile column was constructed from fabric samples stacked into a 50 mm diameter Perspex^{TM} tube. Water was pumped upwards through the fabrics and the pressure drop determined using manometers at measuring points above and below the fabric. Permeability coefficients were determined for various fabric package heights. Good straight line fits were found (correlation coefficients above 0.99) with small intercepts.

If the flow rate is dependent on the direction in which pressure is applied, or in which fluid flow occurs, the permeability is anisotropic. Anisotropy results from inhomogeneities in the structure, orientation, or distribution of pores that make up a porous medium.

Measurements of anisotropic permeability can be made by measuring both the flow rate and the pressure drop for flow in specific directions within the material. This usually means making measurements at different angles across the material.

Measurement of anisotropic permeability in consolidated media can be made simply by sectioning the sample, and finding the flow rate for an applied pressure drop in a given direction. Methods of measurement and results from experiments to measure anisotropic permeabilities, particularly in geological materials have been reviewed by Rice *et al.* [180].

Adams and Rebenfeld [3] have studied anisotropic permeability for liquid spread in fabrics. A radial in-plane flow cell is formed between two plates. The lower glass plate allows observation of the spreading fluid front, as viscous liquid is injected through an inlet hole in the centre of the cell. Circular isotropic, and elliptical anisotropic fronts were observed. The shape and evolution of the wetted region was used to define directional permeabilities in the fabric. Montgomery *et al.* [157] have used the same approach to map the spatial distribution of local permeabilities in fabrics. A range of values for the local permeabilities in nonwoven geotextile samples was found, the standard deviation was approximately 20% of the average permeability in many cases.

A permeability technique has been used to investigate the porous structure of paper. Air permeability was measured in thin sheets of paper and thick mats of wood pulp (basis weight approximately 2300 gm^{-2}) [13]. In the thick mats of wood pulp the Kozney-Carmen equation was found to apply. In thinner handsheets, a modified Kozney-Carmen equation incorporating the pore size distribution was needed. Lindsey and Brady have developed and used an apparatus to measure both in-plane and transverse permeability in hard and soft wood pulps [131]. In-plane permeability was found to be greater than transverse permeability by a factor of 5 to 10.

2.5.2 Models of permeability in porous media

The permeability of a porous material will clearly be related to its microscopic structure, as well as the properties of the flowing fluid. There been many attempts to correlate properties of a porous material with its permeability. Most approaches represent the porous medium using an assumed model of the pore space, flow is then predicted and compared to the observed permeability behaviour.

A comprehensive review of attempts to model permeability using various theoretical models has been given by Scheidegger [192, pages 126-134], and Dullien [61, pages 254-266].

Hydraulic radius theories

The most widely used models for permeability from geometric properties of a porous medium follow an approach based on the Kozeny-Carmen equation.

The Kozeny theory represents the porous medium as a collection of conduits having

different cross-sections, but fixed length. The Navier-Stokes equations are solved simultaneously for fluid paths passing through a cross section perpendicular to the flow [119]:

$$k = \frac{C\phi^3}{S^2} \tag{2.17}$$

where, k is the permeability, C is the Kozeny constant, ϕ is the porosity (fraction of the bulk volume of the sample occupied by pore space), S is the specific surface of the channels.

The Kozeny constant, C, is a shape parameter the value of which depends on the cross-sectional shape of the channel (C=0.5 for a circular tube). Equations similar to equation 2.17, where the permeability is proportional to $1/S^2$, are often refered to as Kozeny equations.

In a real medium the pores are not straight and a tortuosity τ is often included as a modification to the Kozeny equation:

$$k = \frac{C\phi^3}{\tau S^2} \tag{2.18}$$

Carmen has proposed an empirical refinement to the Kozeny model, to include the effects of tortuosity as well as pore shape. The Kozeny-Carmen equation has been widely used and tested in a variety of media, but its application is still challenged, for example by Reed [178]. In addition, the tortuosity factor is introduced to compensate for the shortcomings of the one-dimensional model. As such, tortuosity has been criticised for simply being an arbitrary correction factor [61, page 257].

The Kozeny-Carmen approach is classified by some authors as a hydraulic radius theory. This classification stems from dimensional considerations, as it may be argued that the permeability should be described with dimensions of length. This length is called the *hydraulic radius* of the material. By analogy with flow in open channels the hydraulic radius may be defined as the ratio of the cross-sectional area available for flow to the wetted perimeter [10, page 165] [192, page 137]. In this case Dullien argues that the Kozeny-Carmen approach is closer to a capillaric model because certain assumptions are made about the underlying pore structure [61, page 254].

Bundle of parallel capillary tubes

The simplest capillary model considers a porous medium to be made up of identical straight parallel cylindrical tubes of specified size. The total permeability can then be predicted by considering Poiseuille's law (equation 2.9) for a single capillary. In an actual porous medium the capillary diameter can be thought of as representing an average pore diameter. [192, page 128].

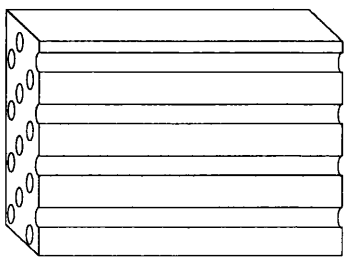

Models of this kind allow for liquid to flow only in the direction of the capillaries. A pseudo three-dimensional model can be made by assuming that a third of the capillaries lie

in each of the three spatial dimensions. This introduces a further factor of $\frac{1}{3}$, not unlike the tortuosity factor [61, pages 260-261].

Bundle of capillaries of different diameters in parallel

The previous model can be improved by assuming a bundle of straight parallel capillaries, but allowing the diameters of the capillaries to be different from one another.

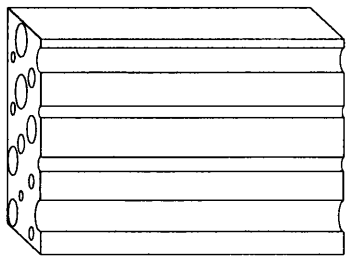

The pore size distribution of such a model can be obtained from measurements of the actual porous medium. Except that, if the pore size distribution is estimated using mercury intrusion porosimetry, then the model radii will be physically unlike the pore sizes in the porous material (see section 2.2.3).

Parallel capillary models of distributed radii have little more to offer than single-capillary type models, although the meaning of the average pore radius is more precisely defined [192, page 130].

Bundles of periodically constricted capillary tubes

In general moving through a porous medium liquid will encounter locally more constricted pore regions, and more open pore cavities. To be a better physical model the permeability model must include not only flow paths of different size, but changes in diameter in the direction of flow through those paths. This can be addressed by introducing changes in diameter along the length of the capillaries that make up the model material. This will more accurately represent the kind of spatial variations experienced by fluid as it passes through the pores and pore throats of a porous medium. This kind of model was introduced by Dullien [60]. Obtaining accurate information for the pore size distributions to use in these types of models is difficult.

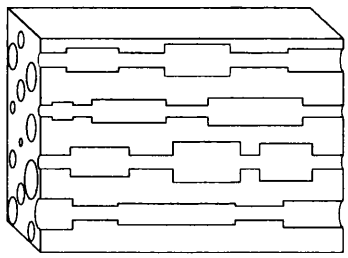

Networks of capillaries

Models of three-dimensional, intersecting, capillary networks, with a distribution of sizes, come closest to mimicking the pore space in real porous media [61, pages 276].

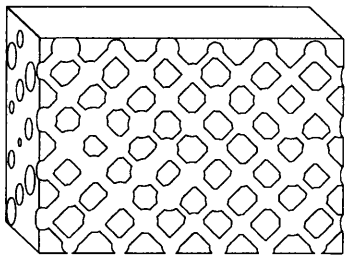

Koplik has modelled flow in two-dimensional networks made up of straight capillaries (throats) having circular junctions (pores) where they meet [116]. By observing that there is a linear relationship between pressure difference and fluid flux, the problem can be treated as an electrical resistor problem. The flow problem can then be reduced to a linear-network problem and solved numerically.

Drag theory of permeability

As an alternative to flow through an interconnected pore space, fluid flow in a porous medium can be described as flow around a matrix of solid obstacles. The drag of the fluid around the solid phase can be calculated from the Navier-Stokes equations, allowing the permeability for the medium to be estimated. [192, page 145].

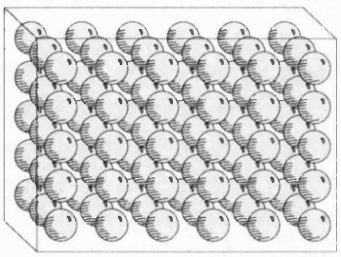

Drag theories are most appropriate for highly porous media; where the pore microstructure is better viewed as a solid phase interrupting void space, rather than a network of connected pore volumes meeting at constrictions.

2.5.3 The permeability of fibrous porous materials

Porous media constructed from fibres deserve special consideration. This is because fibrous materials can be formed at extremely low solid volume fractions, and can have porosities not achievable by granular material.

The Kozeny-Carmen equation has been used with some success, to predict permeability in fibrous porous media. Fowler and Hertel [68] studied the air permeability properties of fibrous plugs at various porosities. The plugs were compressed using a movable plunger to vary the distance between fibre surfaces. The Kozeny-Carmen equation was found to be in agreement with experimental results within the porosity range investigated. Ingmanson *et al.* have since suggested that empirical modification of the Kozeny equation is needed at higher porosities [98]. The internal pressure drops were measured for water flow through thick fibrous mats up to a porosity of 0.96.

The effect of fibre cross-sectional shape on the water permeability of fibrous mats has been studied by Labrecque [123]. In these experiments, the hydrodynamic properties of fibre mats were well described using Kozeny factors. The cross-sections of fibres were examined using micrographs of embedded sections. An increase in fibre aspect ratio had only a small impact on permeability for liquid flow through fibres below a ratio of 3:1. A nonlinear relationship for the Kozeny factor was found at higher aspect ratios.

In general, attempts to model the permeability of fibrous materials represent the problem as one of flow around an assemblage of cylinders. In much theoretical work the cylinders are assumed to be arranged on a regular lattice. This allows a repeating unit cell to be defined, within which Stokes equation can be solved. The development of experimental and theoretical models for flow in fibrous materials is reviewed in detail by Jackson and James [102]. This review forms the basis of the following discussion.

Some of the earliest applications of this technique were by Happle [83]. In the case of flow around cylindrical rods the Navier-Stokes equations were solved for a unit cell consisting of: an inner cylinder representing the obstacle, and an outer cylinder representing the free surface of the fluid envelope. For flow parallel to an array of cylinders the following

relationship was derived:

$$\frac{k}{a^2} = \frac{1}{4\phi}\left(-\ln\phi - \frac{3}{2} + 2\phi + \frac{\phi^2}{2}\right) \tag{2.19}$$

where, k is the permeability, ϕ is the volume fraction of solid material, and a is the radius of the cylinders.

and for flow normal to the array:

$$\frac{k}{a^2} = \frac{1}{8\phi}\left(-\ln\phi + \frac{\phi^2 - 1}{\phi^2 + 1}\right) \tag{2.20}$$

These theories are for uniform media, Yu and Soong [224] have shown that inhomogeneity can increase the permeability by as much as a half.

Using more recent estimates for the resistance to flow than Happel's, Jackson and James have presented a revised prediction for the permeability of a three dimensional array of rods:

$$\frac{k}{a^2} = \frac{3}{20}\left(-\ln\phi - 0.931 + O(\ln\phi)^{-1}\right) \tag{2.21}$$

Experimental data collected from the literature for many different fibrous media was found to be well approximated by this equation (equation 2.21) [102].

In investigating fibrous dust filters Davies [48] has gathered experimental data for air flow through a wide range of fibrous materials and packing densities. From dimensional analysis of Darcy's law, together with these permeability measurements, two empirical relationships were proposed:

$$\frac{k}{a^2} = \frac{2}{64\phi^{\frac{3}{2}}(1 + 56\phi^3)} \tag{2.22}$$

and,

$$\frac{k}{a^2} = \frac{2}{70\phi^{\frac{3}{2}}(1 + 52\phi^3)} \tag{2.23}$$

applicable when $\phi > 0.98$

In the previously mentioned study by Ingmason *et al.* [98] the permeability was found to be related to the porosity by a function with the same form as those due to Davies.

Kyan *et al.* [121] have observed that fibrous beds give rise to an unexpectedly high pressure drop, in spite of the high porosity of the fibrous bed. They propose that the pressure drop is larger than expected both because a portion of the free space in the bed does not contribute to the permeability (but instead contains stagnant fluid); and because there is an additional energy loss caused by deflection of the fibres.

The permeability of paper has been modelled by reference to flow around fibres [162]. The permeabilities for arrays of circular and band shaped cylinders were calculated using

a fluid dynamics package. Measured flow through hand sheets and pulp were found to be in reasonable agreement with modelled data, assuming the cellulose fibres to be randomly arranged band shaped rectangular cross-section obstacles.

2.5.4 Permeability of irregular microscopic geometries

As Rothman has observed [184], the frequent failure of theoretical models to predict measured permeability must have as its root cause: poor flow models, or incomplete descriptions of porous structure. Most porous materials have very irregular pore geometries that are not well described by simple models. An approach to this problem has been to model flow within a more accurate representation of the pore space, obtained from direct observation of the porous microstructure.

Lin and Cohen [130] have described techniques for making measurements from serial rock sections. High resolution scanning electron microscope images were used to obtain microscopic data.

Using a similar method, Berryman and Blair [11] estimated the porosity and specific surface which were then used to estimate permeability from a Kozeny type equation. For glass beads and sandstone samples at low permeabilities the permeability estimates agreed to within ±10-30%.

Koplik *et al.* [117] collected detailed images of cross-sections through sandstone samples. The micrographs were analysed by tracing them into a computer, and reconstructing connected cross-sections. The resulting flow paths were then simplified into twisting cylinders having elliptical cross-sections. Permeability estimates were found by solving Stokes equation for the pore space. The permeability obtained using this model was about 10 times greater than the measured value. This error was attributed to local anisotropy, or inadequate representation of the pore distribution, due to the small size of the sample used.

A method for three dimensional simulation of a porous medium, using measurements from thin sections of the material has been suggested by Quiblier [175]. The simulated medium is recreated by measuring the probability density function, and auto correlation function for a representative two-dimensional cross-section.

The relationship between fibrous structure and permeability in geotextiles has been investigated by Masounave *et al.* [146]. Polished cross-sections through encapsulated nonwoven samples were prepared, from which pore diameter estimates could be made. A relationship between the water permeability and fibre density was noted.

Accurate reconstruction of the pore space from serial sections is difficult to achieve. Care must be taken to sample the material over a large enough area, and frequently enough to capture good pore statistics. In fact, in order to achieve correct identification of the pore necks a multi-orientation scanning technique is necessary [138].

2.5.5 Cellular automation fluids

An interesting, and increasingly popular, development is the use of cellular automata to model fluid motion. Cellular automata are arrays of locations that can have discrete states. If made sufficiently large the behaviour of systems such as fluids can be reproduced [220].

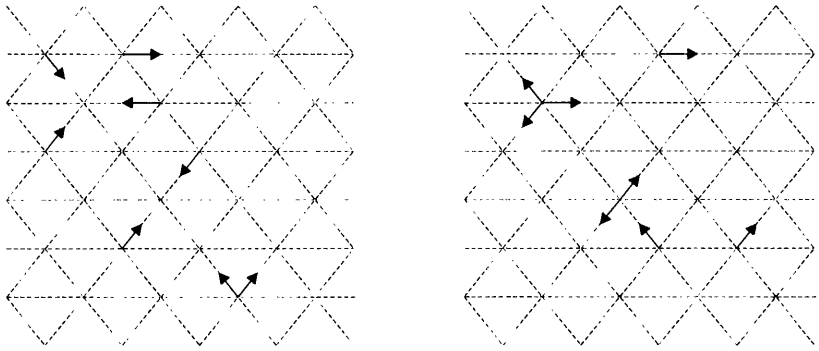

Figure 2.11: The cellular automaton gas, Frisch *et al.* [71]. Particles are represented during evolution of the gas during one time step.

The lattice gas model was introduced in 1986 by Frisch, Hasslacher and Pomeau [71]. This model essentially consists of fluid particles that populate a hexagonal grid, as shown in figure 2.11. To simulate a fluid, particles initially occupy the lattice at random locations. Each particle has a unit mass and moves with unit speed in one of the six possible directions corresponding to the links on the lattice. Evolution of the fluid is modelled by advancing each particle and applying local interaction rules in a simulated time step. All the particles at each lattice site are allowed to collide in such a way that the total momentum and number of particles at the site are conserved. Particles then move off in new directions at the beginning of the next time step.

Cellular automaton fluids have been applied to flow within two dimensional models of porous solids. The method is based on knowledge of the microscopic geometry of the porous material. Here the standard lattice model, such as that employed by Frisch *et al.* [71] is augmented by an extra piece of information to show whether the site is part of the void space or the solid fraction of the porous material. For locations that are part of the solid material, interaction rules are used that mean any fluid particle arriving is returned with the negative of its inbound velocity. Flow in the highly irregular geometry of a 2-D porous medium can be simulated in a representative portion of the material, leading to numerical estimation of permeability [184, 5]. If cellular automaton models can be shown to predict laboratory measurements of permeability they may offer some interesting clues about the underlying characteristics of flow. In the model described by Rothman [184], a large contribution to the flow came from a small number of winding paths, with many pore space regions containing fluid that was relatively stagnant.

Three-dimensional lattice gas automata are difficult to implement because issues remain about the collision rules to apply, as well as there being a huge increase in the computational work needed.

2.6 The flow of immiscible fluids in porous media

The situation where two or more fluids or fluid phases flow simultaneously in a porous medium is significantly more complicated than for a single phase; whether the flow results from forces external to the system or wetting forces.

For steady state flow the macroscopic saturation of the porous medium remains the same for all flowing fluids. Unsteady state flow, where an invading fluid displaces an existing fluid is more obviously a case of immiscible flow.

2.6.1 Relative permeability

When two fluids flow through a porous medium there are a number of different ways in which flow may occur at the pore level. This can best be illustrated by using a few examples. Figure 2.12(a) shows two fluids flowing through the same porous medium, but by means of entirely separate pore networks. In the second example, figure 2.12(b), the two fluids share the same pores when flowing through the medium. Finally figure 2.12(c) shows two fluids flowing through the same pore network, but with one fluid dispersed in the other [61, pages 334-336].

Darcy's law is applicable to each fluid, and can be written for flow involving multiple fluids for conditions of fixed saturation as

$$Q_i = \frac{k_i A \Delta P_i}{L \eta_i} \tag{2.24}$$

where, Q_i is the volumetric flow rate of fluid i, k_i is the effective permeability of the porous medium to fluid i, A is the normal cross-sectional area of the sample, L is the length of the sample in the macroscopic flow direction, ΔP_i is the hydrostatic pressure drop causing the flow of fluid i, η_i is the viscosity of fluid i [61, pages 338-339].

The effective permeability will be strongly dependent on saturation of the fluid within the medium. Measurement of effective permeability is similar to that for saturated flow, except that both fluids are introduced together into the medium at known flow rates or pressure. Saturation can be determined by gravimetric means, x-ray absorption, nuclear magnetic resonance, or x-ray computed tomography techniques. Details of techniques for measurement, together with attempts to model effective permeabilities are reviewed by Dullien [61, pages 367-380], and Bear [10, pages 473-474].

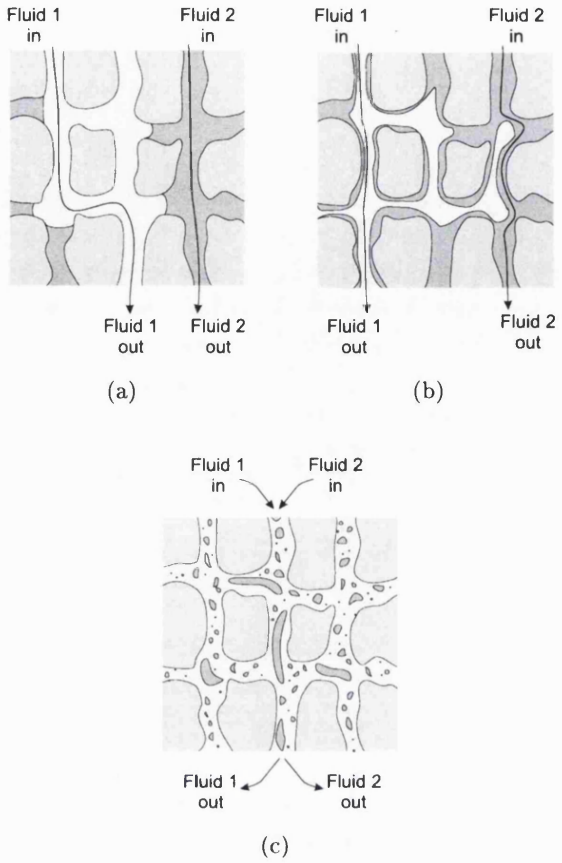

Figure 2.12: Example types of flow of two fluids within a porous medium [61].

2.6.2 Unsteady state flow, displacement imbibition

In the case of liquid flow in the unsteady state, saturation within the medium changes over time. This is usually because one fluid is infiltrating into the porous material, displacing another fluid. This may result from the liquid being forced into the material or, of more interest from the point of view of absorption, the liquid may be driven by capillary forces. This kind of flow is referred to as unsaturated flow, meaning simply that the fluid flowing through the medium does not saturated the available space. Imbibition into porous media is described in detail by Scheidegger [192, page 247-289] and Dullien [61, pages 380-478].

The displacement mechanisms in a three-dimensional random network of pores can be extremely irregular. To provide some idea of the details of microscopic displacement Lenormand *et al.*'s experiment using a simplified network will be briefly described.

Lenormand *et al.* [127] have examined displacement in artificial two-dimensional regular networks of intersecting ducts. Ducts with a rectangular cross-section of depth 1 mm and variable width (greater than 0.1 mm) were etched into a resin. A network was formed from these ducts meeting at 90° and small networks of around 135 nodes were created.

Quasi static motion was obtained by slowly increasing the pressure of the wetting fluid to obtain imbibition, or increasing the pressure of the non-wetting fluid to obtain drainage. The network is horizontal, and gravity forces are insignificant. Two types of displacement of the meniscus were identified in a single duct,

Piston type motion the non-wetting fluid enters the duct filled with wetting fluid only if the capillary pressure is equal to or greater than a given value. The interface is convex and its motion is reversible.

Snap-off when the capillary pressure is greater than the applied pressure the non-wetting fluid will infiltrate the duct. However, the wetting fluid is observed to move initially only along the edges of the duct. This motion can lead to a portion of the non-wetting fluid becoming trapped behind the advancing front, forming a dislocation, or 'snap-off'.

At the intersection of four ducts the imbibition behaviour depends on the number and spacing of those ducts filled with non-wetting fluid. The observed behaviour was divided into different types by Lenormand *et al.* [127].

In the later stages of imbibition, non-wetting fluid remained trapped in the network of capillary ducts. Snap-off events were observed to disconnect and trap these portions of non-wetting fluid.

Vizika and Payatakes [209] have described two types of infiltration front. The primary of these two fronts consists of the invading fluid filling the pore space. The secondary front moves ahead of the primary by unsaturated flow, as a surface film moving along pore walls close to the solid of the medium.

Air entrapment causes a serious problem in the manufacturing of fibre composites. A method for characterising pockets of trapped air within glass fibre networks has been described by Mahale *et al.* [141]. Liquid motion was recorded, using a video camera, during forced radial flow into nonwoven fabrics. In common with other observations, the entrapment of voids was found to be more pronounced at low capillary numbers [2] and low contact angles.

Results from experiments such as those conducted by Lenormand show that liquid imbibition into even simplified porous media is a complex process. Liquid is unlikely to move in a porous medium with piston like flow, where fluid fills the entire void space behind a distinct advancing wetting front.

2.6.3 Distribution of fluid phases at the pore level

It is apparent that even in simplified two dimensional networks the form of the interface between wetting and non-wetting phases can become highly irregular. In order to get some

[2] *Capillary number* is the ratio of viscous to capillary forces

idea of the nature of liquid imbibition in actual porous networks resin impregnation has been used to freeze the interface.

A suitable pair of immiscible fluids are chosen for displacement experiments in a sample of the porous material. At equilibrium one of the liquid resins is hardened, this fixes the microscopic distribution of the liquid in the pores. Photomicrographs of polished sections can then be obtained, in which the three phases (wetting, non-wetting fluid, and solid matrix) can be identified. Coloured resin is often used to distinguish the phases. The relative fractions occupied by each phase can then be determined.

Such a technique has been used by Payne [168] to investigate drainage from random packings of spherical beads. These results indicate that for a material composed of spheres the work during liquid invasion is equal to the increase in surface free energy of the system. Morrow [159] notes that Payne makes an assumption that all of the liquid had been drained from the bead pack, whereas it cannot be reduced to below its residual saturation, leaving some of the wetting phase trapped. Morrow also used a solidified liquid technique to examine imbibition and drainage in columns of packed beads. Morrow found that the efficiency for initial drainage was 79%, and for imbibition was 92.5%.

Classical mean field descriptions such as the Washburn equation fail to explain the often irregular motion of wetting interfaces in porous media. The Washburn description breaks down where the random forces are significant compared with the uniform driving forces. Buldyrev *et al.* [20] have reported a simple experiment examining the equilibrium interface formed by a suspension wicked vertically into a paper towel. The observed rough interface is modelled by growth in which cells are randomly blocked, past which the interface cannot propagate vertically. This leads to an equilibrium interface pinned by a directed path of blocked cells spanning the sample width, perpendicular to the wicking direction.

The irregular motion of liquids in porous media can be mostly attributed to the complex nature of the pore space. This geometric complexity can be represented using a lattice of locations. A property controlling movement through the system can then be distributed at random to these lattice locations. The system now has a property describing the situation under which wetting can occur for each lattice site. Discrete representations such as this can be used for percolation based models of liquid transport.

Infiltration into porous media can be modelled using invasion percolation [45]. In invasion percolation the wetting front advances step wise at the point of least resistance. Chandler *et al.* [24] have examined a fluid displacement process using a percolation approach. Features such as a rough wetting interface with trapped regions of non-wetting fluid, can be seen in the results of percolation modelling.

Simulations of wicking into fibre networks have been undertaken by Lukáš using an Ising model [132]. Lukáš divided the co-ordinate system into cells with spin variables indicating the presence, or not, of water. To incorporate the fibre network into the system the cells were marked with a further variable to indicate whether the cell was occupied

by a fibre. The Ising model was used to model the wetting behaviour of the liquid. The method is simple to apply, and gives rise to simulations of wetting behaviour that appear realistic. Lukáš found the behaviours observed in his simulations to be similar to those seen in real fabrics [134]. Parameters such as the exchange energies used by Lukáš are chosen empirically, however. The dynamic interpretation of the model is complicated, and further research comparing Ising model dynamics with real liquid-solid systems is needed.

2.6.4 Absorption of liquid by porous materials

The spontaneous movement of liquid into a porous medium driven by capillary forces is often called wicking, particularly in the case of textile materials. For wicking to take place there must be a positive change in free energy when new liquid-solid interface is formed. Liquid must wet the walls of the absorbing material.

The role of wetting and wicking in absorption by textile systems has been reviewed by Kissa [113]. Although a lot is known about the factors governing the rate and nature of flow during wicking, as Kissa states, understanding remains incomplete.

The motion of liquid through a porous medium can itself introduce changes in the pore space. This is particularly likely when the medium is made up of loosely bound fibres. Liquid bridges form between fibres, pulling the fibres together. In addition the fibres can swell on contact with water. Natural fibres, such as pulp, and cotton swell on contact with water, which in part makes them attractive for use in absorbent products. Most of this swelling occurs across the cross-section of the fibre rather than along its length [28].

2.7 Modelling of liquid imbibition

The preceding section gives some indication of the complexity of the processes underlying liquid absorption by a porous medium. Many approaches to modelling liquid imbibition have been tried. A brief overview will be given followed by discussion of methods relevant to measuring and modelling wicking in nonwovens.

In broad terms approaches to modelling unsaturated flow can be categorised in a similar way to those for saturated flow.

2.7.1 Capillary-driven flows into porous media

In the case of capillary-driven flows the porous material is considered to be equivalent to a capillary tube or bundle of capillary tubes and the simplest equation used to model the rate of capillary penetration is that due to Washburn (see section 2.4.1).

Dullien *et al.* [63] used the Washburn equation to model visually measured rates of rise in various sandstones. A theoretical expression was derived for the rate of rise in cylindrical capillaries of arbitrary orientation, but with step changes in their diameter.

The diameter of the capillaries ranged from a minimum found using mercury intrusion porosimetry to a maximum obtained from photomicrographs. These were then used to find the effective capillary radius, which was generally in good agreement with the values calculated from the rates of rise using Washburn's equation. In addition, the permeability of the sandstone samples were found to be proportional to the measured effective capillary radius.

Van Brakel and Heertjes [204] observed capillary rise in cylindrical beds with a diameter of 23 mm and heights ranging from 10 to 25 mm. Porous media were constructed using glass beads or sand. The infiltrating liquid was either water or toluene. Each packed column was submerged 2 mm below the liquid surface, with care being taken to ensure a controlled temperature and constant liquid level at the free surface. The capillary uptake was observed visually, at the wall of the sample, yielding height rise as a function of time. In some experiments the capillary rise was also measured using x-ray absorption, yielding the saturation of the porous medium as a function of time in 1 mm sections. Two features of capillary rise were observed, (i) presence or absence of a saturation gradient, and (ii) rapid or slow capillary rise. These observations were combined to give four patterns of imbibition[3]:

Class Ia Imbibition began with rapid capillary rise of a sharp liquid front, for which dh/dt versus $1/h$ was linear, that is the rise obeyed the form of the Washburn equation (equation 2.12). After some time a saturation gradient started to develop, equilibrium was reached in 1-3 days.

Class Ib A sharp liquid front was observed initially. Over several days this developed into a gradual saturation gradient. Equilibrium was reached after several months.

Class IIa Equilibrium was reached in a few minutes. No saturation gradient was seen to develop. The capillary rise followed the form of the Washburn equation.

Class IIb The capillary rise did not follow the Washburn equation, except during the initial part of the rise. Several weeks elapsed until equilibrium was reached. No saturation gradient could be observed.

Van Brakel and Heertjes [205] concluded that the contact angle played an important role in determining the observed behaviour. The development of a wide saturation gradient at equilibrium (class IIa, IIb) was associated with a contact angle approximately equal to zero. A sharp wetting front, with no saturation gradient (class IIa, IIb), was seen for contact angles greater than a critical value. Capillary rise did not follow the predictions of classical theory in some cases (class Ib, IIb).

Van Brakel and Heertjes [207] have offered a possible explanation to account for the relationship between the width of the saturation gradient at equilibrium and the contact

[3]All times are for the capillary rise of water in a 350 μm glass bead sample.

angle at the interface. They have suggested that many models of porous imbibition fail because they assume that the pores within the porous medium contain a large number of isolated menisci. In reality the menisci within individual pores are connected and form part of the same liquid front, making up a single meniscus.

2.7.2 Darcy's Law and unsaturated flow, the diffusion analogy

A different method for modelling flow in porous materials is to take a continuum approach to find the equations governing flow. In this case the microscopic details of pore structure and pore level fluid flow are not taken into account explicitly.

In most examples of liquid infiltration into porous media the degree of wetting phase saturation will change along the direction of flow. This saturation gradient will continue to change during subsequent liquid uptake and has an important impact on the characteristics of fluid flow .

Darcy's law (equation 2.16) can be generalised into a three dimensional macroscopic differential equation for unsaturated porous media. For multi-fluid immiscible flow of fluids in an isotropic medium Darcy's law can be written:

$$\boldsymbol{Q_i} = \frac{k_i S_i}{\eta_i} \nabla \Phi_i \tag{2.25}$$

where, Q_i is the volumetric flow rate of fluid i, k_i is the effective permeability of the porous medium to fluid i, k_i is the saturation of fluid i, Φ is the total hydraulic potential (being the total of pressure, and gravitational potentials).

The law of conservation of mass may be combined with Darcy's equation, to give the governing equation for flow within the medium. Making the assumption that resistance to the movement of air in the medium can be ignored; Richards [181] proposed the following equation [61, page 395]:

$$\frac{\partial \theta}{\partial t} = \nabla \cdot (K \nabla \Phi) \tag{2.26}$$

where, θ is the volumetric moisture content, K is the hydraulic conductivity of the material, Φ is the total potential.

This equation is similar to heat conduction and diffusion equations leading to the analogy between liquid infiltration into porous media and a diffusion process; however, flow does not occur through the same mechanisms as diffusion. The diffusivity is strongly dependent on moisture content, resulting in a non-linear diffusion equation. Using a model of permeability at a given moisture content, Childs and Gardner [29, 75] have shown that the movement of water down a gradient of moisture can be predicted. The diffusion theory has been experimentally verified for soil water systems [110, for example]. The Richards equation is widely applied to the movement of water in soil, and there are many texts devoted to this subject, for example [111, 144]. Solving the nonlinear diffusion equation

(equation 2.26) usually requires numerical methods [211, 7], and a number of software packages are available to do this, for example SUTRA [210].

2.7.3 One-dimensional diffusion model

Taking the simplified case of one-dimensional flow in a horizontal semi-infinite medium. Subject to the boundary conditions that one end of the initially dry sample is in contact with a wetting fluid and maintained at 100 percent saturation. It can be shown that the rate of liquid penetration by the wetting front is inversely proportional to time, regardless of the dependence of diffusivity on the degree of saturation. Just behind the wetting front, the distance travelled, for a given degree of saturation, will be proportional to the square root of time [74]. From this it follows that the distance travelled by the visually observed wetting front will be proportional to the square root of time, and this is in agreement with the Washburn equation.

Kirkham used soil samples and washed quartz sand, packed into glass cylinders, to look at horizontal motion of moisture into a dry sample from a large reservoir. The volume of water absorbed and distance of the wetting front were found to be strictly proportional to the square root of time. Kirkham points out that in itself this does not prove the diffusion theory because the same behaviour is predicted by the capillary tube hypothesis. After water had penetrated the soil a certain distance, the glass tube was rapidly broken into sections. The moisture distribution could then be determined by weighing. It was, however, not possible to verify the diffusion theory from these measurements [110].

The distribution of water in horizontal samples of glass beads, and sand was measured using a gravimetric procedure, by Bruce and Klute [16]. In all cases a decrease of moisture content with distance was observed. The decrease started rapidly, then slowed, and ended with a very steep decrease in moisture content at the wetting front. From the moisture distribution curves the diffusivity-moisture curves were determined. This method, however, is not advocated by the authors for calculating diffusivity curves.

Gardner and Mayhugh [74] measure the one-dimensional flow of water into soils and sands packed into aluminium channels. A reservoir was formed at one end of the channel, at the end of the experiment the reservoir was emptied and the sample immediately cut into 1 or 2 cm sections to determine the moisture distribution. In most cases plots of the total quantity of water entering the soil plotted against the square root of time was a straight line, although not always passing through the origin. The moisture content distribution within the sample was in good agreement with predictions based on an exponential diffusivity relationship for the soils.

2.7.4 Measuring wicking in fabrics

A number of laboratory tests routinely used to measure wicking in fabrics are reviewed and compared by Harnett and Mehta [85]. Briefly, the three main methods are described by Harnett and Mehta as follows:

Longitudinal wicking strip test A preconditioned strip of the test fabric (20° centigrade 65% relative humidity) is suspended vertically, with its lower end dipped in a reservoir of distilled water. A dye may be added to the liquid to aid visualisation of the wetted region providing the dye is known not to affect wicking performance. At a fixed time following the start of wicking the liquid height rise is recorded. Two published standards are listed for this test [17, 54]

Turbak [203] describes a method for nonwoven fabrics as follows: The fabric strip to be tested is marked at 1 cm intervals and vertically suspended above the surface level of water in a container. The strip is brightly illuminated and a stopwatch is used to record the encroachment distance for liquid in the sample. The liquid container is raised to initiate wicking, and the stopwatch is started. As the advancing wetting front passes the markings on the test strip the time is noted, recording the wetted length as a function of time.

Transverse wicking plate test A horizontal sintered glass plate is supplied from below with water. A sample of test fabric is placed on the plate and contact maintained under a controlled pressure. Mass transfer into the fabric is recorded by measuring the liquid lost from the source reservoir.

A sophisticated automatic instrument to perform this test, known as the gravimetric absorbency testing system (GATS) is commercially available. In this device the liquid source rests on top of an electronic balance, supported on a coiled spring. The supporting spring has a spring constant such that the liquid level is compensated for loss or gain of liquid, and maintained at a constant height [28]. The GATS apparatus is able to record extremely small changes in liquid absorption while being able to remove and return large volumes of liquid to the sample.

Areal wicking spot test The method is based on a modified version of BS 3554 [18]. A light is used to produce a bright reflection from the surface of a liquid on a fabric sample. A drop of liquid is delivered from a height of approximately 6 mm onto a horizontal test fabric (preconditioned at 20° centigrade. 65% relative humidity). The time taken for the reflection from the liquid surface to be no longer visible, following contact between the drop and fabric, is recorded.

In a variation on this method the drop is replaced by continuous supply of liquid at minimum pressure head. The change in the diameter of the area of liquid spread is then measured.

2.7.5 Results of experiments to measure wicking in fabrics

The Washburn equation (equation 2.11) is the model most frequently used to explain wicking into textiles [28, 203].

An interesting investigation of wicking into textiles was conducted by Hollies *et al.* [90] In the first part of this work, the vertical wicking behaviour of several fabrics was examined. It was evident that most of the wicking action took place within the yarns rather than between them. Using a dyed liquid the wicking front in the yarns could be followed under a microscope. The square of the distance travelled was found to be linear with time, and this was taken to support the view that water transport occurs by capillary action. Using simulated yarns the capillary sizes in the yarns were altered by changing the degree of yarn twist. High twist yarns were found to have low wicking rates. As the yarn twist was decreased wicking performance was improved, as would be expected if larger capillaries produce higher wicking rates. Towards the lowest yarn twists, however, a decrease in the rate was noted in all three fibre types studied, with performance being on a par with that in the highest twist fabrics. Hollies *et al.* attributed this to a reduction in the number and continuity of inter-fibre capillaries, in some cases causing wicking to cease along the yarn.

In the second part of this work, Hollies *et al.* [91], looked at the speed of liquid travel in fabrics. The rate of water uptake along a horizontal fabric strip 1 inch wide and $3\frac{1}{2}$ inches long was measured. The volume of water wicked into the sample was measured using a manometer attached to the reservoir. By placing electrical contact pins along the sample the distance water travelled could be determined – the contacts sounded a buzzer when water was present. Results of horizontal wicking show that the square of the distance travelled was linear with time. Not all curves passed through the origin, suggesting a time constant was needed for each fabric. This was interpreted as an initiation period before the start of the main capillary process. The mass uptake rates were found to be closely related to the rates at which the front advanced by the water holding capacity of the fabric samples.

Minor and Schwartz [155] have also demonstrated that the distance travelled by the liquid front wicking into yarn or fabrics is proportional to the square root of time. On the basis of the Washburn equation Minor and Schwartz have attempted to predict the rate of liquid movement into prepared yarn samples. The hydraulic radius was taken to be proportional to the square root of the open cross-sectional area in the yarn. The open area in a cross-section through the yarn was estimated by assuming circular fibres and taking measurements of yarn and fibre diameter. Nylon and viscose were used for the experiments and re-twisted to a known number of turns per centimetre, in order to make loose and tight yarns. Vertical wicking was observed using a dyed liquid, well below the equilibrium wicking height (about 2 m in these yarns). The ratio of equivalent radii in the tight to loose yarns was found to be in good agreement with the experimentally measured ratio of wicking rates in the yarns. An anomalously high ratio was observed in yarns made

from viscose fibres. The viscose fibres have a crenulated cross-section, and when twisted can pack closely together. The wicking in the highly twisted viscose yarns was thought to be reduced for this reason.

In the same study, Minor and Schwartz looked at wicking into a yarn for a single droplet placed on its surface. Before the droplet disappeared the front was found to advance as the square root of time, this was called *unlimited reservoir wicking.* After the drop had sunk fully into the yarn, the front was seen to slow and then cease moving, called *limited reservoir wicking.* The final wetted length was found to be dependent on the contact angle hysteresis. Once the period of unlimited reservoir wicking had finished, further liquid movement occurred under capillary forces from larger spaces into smaller ones; that is, into spaces having greater liquid-solid interfacial area per unit liquid volume. Liquid moving into the smaller spaces took on the advancing contact angle, and as it left the larger spaces it did so with the receding contact angle. If there was contact angle hysteresis the advancing contact angle would be greater than the receding contact angle and this would inhibit the motion and hence wicking [156].

Miller and Jansen [150] have tested the Washburn equation for one-dimensional wicking in nonwovens. A 35 mm wide strip of fabric was mounted on a support which could be quickly lowered to a fixed position. The fabric passed over a first Teflon^{TM} roller and across to another, the height of which was adjustable. The relative height of the rollers determined whether liquid wicked upwards, horizontally, or downwards. A reservoir of wicking liquid rested on a balance, to record mass loss as wicking occurred. When the fabric was lowered into the reservoir there was an abrupt change in the reading due to buoyancy and wetting effects, and this was used to locate the start of wicking. The arrangement was enclosed and any losses attributable to evaporation were found to be small, and ignored. A plot of the rate of mass uptake against the reciprocal of the mass uptake was found to be linear for the nonwoven fabric tested, as predicted by Washburn's equation.

The case where wicking specifically occurs in a downward direction has been investigated by Miller *et al.* [149]. The sample was mounted so that it left a reservoir of liquid at an angle, with a large portion hanging vertically downward over a roller. The rate of liquid uptake was recorded by measuring the mass loss from the reservoir using a microbalance. The results are interpreted in terms of the Poiseuille equation. Wicking was measured for hexadecane moving along a paper towel. Both theory and experiment show that downward wicking can produce an essentially constant uptake rate over a very long period of time. In the case of downward wicking it appeared that the entire pore volume was not filled with liquid, as liquid uptake continued after the wetting front had reached the end of the sample.

A study of capillary absorption into vertically suspended samples of cotton and felt has been carried out by Laughlin and Davies [124]. In these experiments the wicking liquid was a light grade of lubricating oil. A radioisotope method was used to follow the

moving wetting front. In some of these experiments quite good straight line fits could be performed for the Washburn form of the height *vs.* time curve, but in general it was found that this relationship did not hold. Instead, the following modification to the law was made:

$$h = Ct^k \tag{2.27}$$

where, h is the wicked height, C is a constant, t is the elapsed time, k is a constant.

This power law (equation 2.27) was found to be valid for moderate time values. After between 30 minutes and 5 hours it again became necessary to correct for the curvature. The exponent, k, varied from 0.50 down to 0.41 with the degree of deviation from 0.5 being taken as an indication of the deviation from pure capillary action.

Similarly, the mass of liquid absorbed as a function of time was found to be given by:

$$m = Bt^\kappa \tag{2.28}$$

where, m is the wicked mass, B is a constant, t is the elapsed time, κ is a constant.

κ was always smaller than k. It was visually observed that there was considerably more liquid at the bottom of the wick, near the reservoir, than at the top.

It is also interesting to note that Laughlin and Davies have commented on the reproducibility of their results. To determine the variation in height against time in similar samples four separate 50 cm strips were tested simultaneously. Good agreement was found in the exponent and coefficient, the coefficient having a deviation of about 1%. The same wicking test performed a week prior gave a difference of about 4% compared with the mean coefficient for the four simultaneous samples. The authors conclude that data taken on different days might vary due to environmental changes

Rates of wicking in highly porous samples, such as mats formed from fibres and wood pulp, have been investigated more recently by Nederveen [161]. These experiments are particularly interesting because the role of permeability and wetting tension is considered in the Washburn equation.

Permeability was measured through the length of the mats. The mat was clamped between two plates, and liquid introduced with a small head at one of the open sides. As liquid emerged from the other side it was collected in a reservoir on a balance. Readings were taken every minute during one hour, and the Darcy permeability calculated.

Vertical rise in the samples was measured using a holder which effectively allowed simultaneous measurement over a range of mat densities. Two thick Perspex™ plates were hinged along one side to form a wedge. The mat was placed between these two plates, forming a vertical wedge of the product. A sample was now produced with a density that varied across its width. Transfer of liquid across the width of the sample was verified to be negligible. The lower edge of the wedge was placed into a reservoir of the test fluid, and vertical wicking was recorded by observing the front at regular time intervals.

The permeability data was modelled using the empirical equation due to Davies [48], and a similar equation due to Ingmanson [98]. For mats of polyester fibres (r = 15.5 μm) the permeability calculated using the Davies equation gave the better fit, but was about 25% too low compared with the measured value.

Vertical wicking in the polyester mats was measured using the wedge shaped former. In order to predict the maximum height rise for a given density the wetting tension had to de determined. To determine the suction pressure in a cross-section, Nederveen considers two approaches. The first follows a method proposed by Gupta [79]. The cross-section was assumed to made up of a number of circular channels. Taking the number of channels to be twice the number of fibres, the capillary pressure was derived. In the second approach the wetted length was calculated assuming a homogenous structure of parallel fibres [31]. The contact angle was not known, but a surfactant was used giving no contact angle between the fibres and the wicked water. The maximum height rise for various mat densities was predicted using these models. The second model gave a much better prediction of the height than the first, which predicted values that were much too high. Experiments were also performed using viscose and wood-pulp. In the viscose, for all densities, the rise appeared to be much slower than theory would indicate, but wicking continued after the maximum theoretical height had been reached. This was partially explained by swelling of the fibres.

Pillai *et al.* [171] have measured vertical wicking across a regular array of aligned fibres, formed between a pair of plates. The height and volume of liquid wicked was very small, constrained by the size of the medium (3.18 mm in height and 12.7 mm $\times$ 3.18 mm in cross section). A microbalance was used to record the wicking for volume fractions of fibre ranging between 0.4 to 0.8 using a number of viscous liquids (for example, silicon oil, and corn syrup). The results were modelled using several different models for both the permeability of the test material, and the suction pressure. Washburn's equation was found to be good at predicting wicking, whereas an energy balance model for the suction pressure mostly predicted wicking performance in excess of the experimental observations.

Gupta [80, 79] has used the gravimetric absorbency testing system (GATS), additionally measuring web thickness during liquid uptake, to characterise absorbency in nonwovens. A predictive model for the rate of liquid uptake was developed using the Washburn equation. The hydraulic radius was obtained assuming that a capillary is bounded by three fibres. The predicted rates of liquid uptake were found to show good correlation with the measured rates, though it was necessary to introduce a web constant, ranging between 4 and 9 into the model[4]. The needled webs were found to have superior absorbency properties compared with the hydro-entangled webs.

[4]This is lower than the range usually found by Gupta for needled webs, which can be up to 30

2.7.6 One-dimensional distribution of liquid in paper

Wicking phenomena in paper have received quite a lot of research interest, particular in paper chromatography. For example, Rudd [185] presents a mathematical analysis that demonstrates the movement of the solvent front and separation of the solute bands.

Early studies assumed that the distribution of liquid ascending in a filter paper was always uniform. Experiments by Takashi, and subsequent analysis by Fujita [72] have demonstrated that this is not the case. Fujita uses the equation of motion for capillary flow together with a diffusion analogy, to reproduce Takashi's experimentally observed saturation gradients.

Gillespie also notes that there appears to be a characteristic distribution of liquid ascending a filter paper, but criticises some aspects of the analysis presented by Fujita. Gillespie models the rate and distribution of a liquid by assuming that liquid has a tendency to move into the smaller pores. Wicking experiments were performed, with the distribution of liquid being measured by weighing sections of the wetted paper. Good agreement was found between results from these experiments and the predicted liquid distributions. Further, when gravity can be neglected the height rise was found to be proportional to the square root of time [77].

Ruoff *et al.* [186] have also studied concentration profiles formed during one-dimensional flow of water into filter paper. They, too, predict and find that the distance (representing a point of constant saturation) develops as the square root time. Further, the saturation profiles for different times are identical, except for differences in the distance scale. The experimental results were modelled by reference to the diffusion analogy. The diffusion coefficient as a function of concentration was determined from the measured concentration profile and the flow rate coefficient. In these cases the following relationship was proposed as an approximation to the diffusion coefficient:

$$D = \frac{D_0}{1 + \alpha s + \beta s^2} \tag{2.29}$$

where, D is the diffusion coefficient, D_0 is a constant, s is saturation (grammes of solvent per gramme of paper), α is a constant, β is a constant.

Using this relationship for the diffusion coefficient, predictions of liquid saturation, in sections of the paper, during radial flow were made using a numerical method. These gave good agreement with experimental results, confirming the existence of diffusion like flow.

In a later paper Ruoff *et al.* [185] have tried to estimate the diffusion coefficient using an interconnected capillary pore model. An expression for the diffusion coefficient is derived, based on knowing the liquid properties and the pore size distribution in the paper. This expression was found to have the correct form for the diffusion coefficient but the calculated values were larger than those found experimentally.

2.7.7 Two-dimensional spreading in textiles and paper

The two-dimensional spreading of liquid drops has been the subject of a number of studies. The last few years has seen a resurgence of interest in droplet spreading in paper, due the advent of ink jet printers.

An important early investigation was conducted by Gillespie [76]. Using an optical method, droplet spreading on various types of filter paper was assessed. Strips of paper were mounted on large microscope slides, and placed on the stage of a microscope. Drops of undyed liquid were released from a syringe mounted with the needle tip 1 cm above the paper sample.

In the first part of the experiment, the diameter of the spread liquid area was measured using a microscope and a graticule, with the sample illumination from below. In the second part, the local saturation of liquid in the wetted sample was estimated from the attenuation of a beam of light 1.5 mm in diameter. A photo-multiplier tube determined the light intensity, which in a separate experiment was found to be directly proportional to the degree of liquid saturation. By moving the slide under the eyepiece the droplet could be scanned to record its saturation profile.

The spreading process may be split into two phases. In the first, part of the liquid droplet remains on the surface of the paper. In the second stage, all the liquid is contained within the paper. The first stage was completed in a short time and was regarded as less important than the second phase. At the beginning of the second stage the centre of the wetted area is saturated. The liquid then spreads, as the result of capillary forces.

Spreading was modelled by reference to the diffusion analogy. An assumed relationship was used for the permeability, but this was not derived quantitatively. Experimental and theoretical liquid distribution curves for the drops were in good agreement, as were predictions of the spreading rate.

In a similar experiment, Kissa [112] investigated droplet spreading in fabrics and paper, using a number of liquids. The wetted area and time were recorded by photographing the wetted substrate and a stopwatch simultaneously. The area of the spread liquid was determined by cutting out the wetted region from the photograph and weighing it. The equation developed by Gillespie is slightly modified to be in accordance with Kissa's experimental results. Finally, a generalised equation is presented for droplet spreading in fabrics:

$$A = K\left(\frac{\gamma}{\eta}\right)^{u} V^{m} t^{n} \tag{2.30}$$

where, A is the area covered by the spreading liquid, K is a capillary sorption coefficient, γ is the surface tension, η is the liquid viscosity, V is the volume of the liquid droplet, t is the elapsed spreading time, and u, m, n are constants.

The spreading of liquid drops in fabric has been examined in detail, using a similar

technique to Gillespie's. In these experiments Kawase *et al.* [108, 109] studied the spreading of water, water-ethanol, and n-decane droplets. In these experiments the area covered by the spreading liquid was found to follow Kissa's exponential relationship.

Kawase *et al.* [107] describe an improved experimental technique, using an image analyser system to capture digital images of the spreading stain on videotape. Images of 256 × 256 pixels, and sixteen grey levels were later obtained from the videotaped sequences. These images could then be thresholded and the wet pixels counted to determine the wetted area.

2.8 Summary

A variety of descriptions of, and techniques to measure, liquid flow within porous media have been reported. Observations of infiltration into simplified porous media have been reviewed to show that liquid transport at the pore level can be a complex process, often involving the development of saturation gradients.

Sophisticated models for liquid behaviour in porous media have been briefly described to demonstrate some of the possible refinements needed to simple models. The multiplicity of approaches to what is, after all, a complex process should not be surprising. More remarkable is that liquid flow, and imbibition, in textile materials is overwhelmingly understood using a simple capillary-tube model.

On balance, capillary models although they might not represent the details of flow in a complex geometry, do retain the most important liquid and structural features. For this reason, and their popularity, simple models were chosen for use in the first instance to understand liquid uptake by nonwovens. Simple models can be tested and built on by comparison with experimental measurements, strengthening them where results indicate the models to be inadequate.

The next chapter describes the development of an apparatus to measure simplified liquid uptake. A method for characterising the microstructure of a fibrous material is also presented.

Chapter 3

Experimental materials and methods

As described in the previous chapter a porous material can retain liquid within its pore space and transport liquid under the action of wetting forces. It is clearly important that absorbent products have an adequate capacity, indeed there is some evidence to suggest that incontinence products with larger absorbent capacities have better clinical performance (see section 1.14). The majority of absorbent products, however, have huge absorbent capacities in comparison with the volumes of liquid that are typically encountered in normal use. Yet, despite having relatively large absorbent capacities current products are remarkably leaky. A typical reusable bedpad can hold two litres of liquid, but eighty percent of used bedpads contain less than 200 ml of urine [164, 163]. In use one third of bedpads containing 200 ml of urine will leak a little, and one third will leak a lot [164, 163].

Such relatively large absorbent capacities suggest that absorbent incontinence products do not leak because they have insufficient absorbent capacity. Rather, it is more likely that the absorbed liquid is being contained in a small region of the absorbent product, or is being forced out by external pressure. In practice, the total void volume of the porous material might not be available for the absorption of liquid. Where liquid has to be transported against gravity it is less likely to reach the full void volume of a product. As a consequence many absorbent incontinence products leak at their lowest points. Diapers tend to leak around the legs, and bedpads often leak towards the user's head – a region whose slope is steep to the sides and feet, but gentle towards the head for a user on a mattress in bed.

If incontinence pads have a larger absorbent capacity than will ever be used, much of the material is being wasted. There are many good reasons for designing incontinence products using as little absorbent material as possible. The raw material cost is reduced, which is particularly important for single use disposable products. Also, producing a less bulky product reduces transport and disposal costs, as well as supplying a more discreet

product to the incontinent user. In the case of reusable products, although the initial purchase cost is less important, the ongoing laundry cost is increased for larger volumes of absorbent material. During washing, a reusable product will absorb a large volume of water, all of which must be removed when the product is dried.

In order to improve the current design of incontinence pads, the absorbent material should be placed into the product in such a way that it is used as efficiently as possible to absorb liquid. An ideal product would rapidly wick liquid away from its entry point, and the user. Liquid would then be stored away from the user's skin, distributed throughout the available void volume.

In order to better understand the transport of liquid within an absorbent structure this research concentrates on looking in detail at the wicking process. Through a better understanding of how the properties of a material determine its wicking behaviour, it is hoped that products can be designed which leak less and offer improved user comfort.

3.1 Experimental approach

The process by which urine comes to be distributed within an absorbent product can be extremely complicated. A simplified description follows the following phases:

- Liquid enters the product under the action of an external pressure. The liquid initially distributes itself largely as a result of being forced into the void volume.
- Liquid may then redistributed under the actions of capillary forces.

This is similar to the two phase distribution, described by Gillespie, of a liquid droplet placed on absorbent paper (see section 2.7.7).

Many modern incontinence products are designed to deal with these different phases of absorption by using layered structures (see section 1.15.2). In the early phase an acquisition layer presents a structure with little resistance to liquid flow, serving to receive incoming liquid, and separate the user from liquid once it is absorbed in the core of the product. A distribution layer may also be used to move liquid out of the acquisition layer, and encourage it to spread throughout the product. Often an overflow layer may be present to act as temporary storage for liquid that can not be immediately accommodated by the distribution layer.

The redistribution process is of primary interest due to its importance in the absorbent function of the pad. To reduce the complexity of redistribution the special case of one-dimensional wicking into an initially dry, semi-infinite, porous sample, from a reservoir of liquid with no external pressure was considered. The experimental situation described is greatly simplified compared to the actual absorption process that occurs in an incontinence pad. Taking this approach meant that wicking phenomena could be simplified

for experimental investigation. In using an idealised one-dimensional experiment it was hoped that some insight could be gained into how the properties of the absorbent material affect the wicking process. Extension to more realistic wicking experiments can proceed, building gradually from an understanding of this simple case.

The experimental approach taken concentrated on examining and understanding the wicking process in absorbent structures. A reliable and accurate method for measuring the rate of wicking was designed. The resulting measurements of wicking rate were interpreted in light of the simple models previously discussed (see section 2.4). Additional experiments were performed to examine cases where the wicking model refers to effects such as the angle of wicking, the properties of the wicking liquid, or the properties of the absorbent material. Broadly, the following wicking experiments were conducted:

- Wicking was carefully measured in a simple nonwoven fabric, where the microstructure can be expressed in the simple terms of a wicking model such as the Washburn equation (equation 2.11).
- A range of nonwovens were selected to examine wicking in materials having different underlying fibrous structure.
- Angled wicking experiments were performed to look at the effect of gravity on the rate of wicking at angles between the horizontal and vertical.
- Solutions of different viscosities and surface tensions were produced, and used to examine the impact these factors had on the wicking rate.
- A fabric was taken and compressed to various degrees between Perspex™ sheets producing controlled changes in the fibre microstructure. Wicking in these samples was measured to see if compression had a predictable effect on the observed wicking performance.

In order to apply capillary models of wicking some characteristic measurements of the fibrous microstructure are needed. It is possible to estimate many microstructural parameters from bulk measurements of a porous material; in cases where expected wicking rates do not match determined rates, however, it becomes difficult to know whether the flow model is in error, or the model used to represent microstructure is inaccurate. Direct measurements were used to provide the required microstructural parameters for evaluating simple models of wicking. Using direct measurements has the further advantage that it offers a better insight into the actual physical microstructure of the material. In the case of the fibrous felts studied, the size of the average distance between neighbouring fibres is notable.

Direct measurements were made using optical microscopy of polished cross-sections through felt samples. Fibres with a circular cross-section intersecting the plane of the

examined section can be identified as ellipses. To make characterisation of the cross sectional micrographs easier software was written to automatically identify and record the ellipses in these images.

In this chapter, the fabrics chosen for experimental work are described. The design and operation of apparatus used to measure liquid wicking is outlined. This apparatus was validated, to check both for accurate measurement, and the extent to which external conditions, such as liquid temperature, influence wicking performance. A description of the method used to analyse the microstructure of a felt is provided. To examine wicking in materials having different microstructure, bespoke felts were produced. These bespoke fabrics were made using small scale prototyping equipment. When manufacturing a range of bespoke fabrics it can be difficult to modify a single property of the material in isolation. To explore the effect changes in fibre volume fraction had on wicking, a cell was constructed in which a felt sample could be compressed to a controlled degree.

3.2 Choosing test absorbent materials

A simple porous medium was needed to act as a model absorbent material for experimental work. Most of the materials in both disposable and reusable products, are fibrous. Fibrous materials represent a rather special kind of porous structure, due mainly to the high void fractions that can be achieved (see section 2.5.3). For this reason, it was decided that any experimental material should be made from fibres from the outset.

Having chosen to study wicking in a fibrous material the type of constituent fibre can be considered. Here, again it is desirable to try to begin with simple fibres, that will not introduce a large number of complications when interpreting experimental results. Ideally, the fibre should have a circular cross-section, not swell or change shape on contact with water, and the surface should be homogenous.

The absorbent material made from the fibres should also be as homogenous and simple as is practical. The material should be made from identical fibres.

In many respects the criteria described for the experimental fabric can be met by using a nonwoven material. Using a nonwoven material also means that the model absorbent will be similar to the absorbent core of a reusable bedpad.

It would be possible to use a small scale prototyping machine to make up an experimental nonwoven to specification directly from fibres. Although this offers advantages in being able to control the makeup and manufacture of the material, it suffers from a lack of consistency due to the small-scale, operator-intensive nature of the process. A typical prototyping carding machine requires the fibres to be laid out by hand. One metre wide webs are formed which are then be needled into nonwoven samples a few metres in length. Both the initial hand laying of fibres and the short working width of the fabric can lead to local variation in the properties of the material. In addition, each sample is only a few

metres square and variation between samples can be considerable. For these reasons it is preferable, if possible, to choose a commercially produced material. Commercial manufacturing machines produce samples several metres wide and many metres in length. This means, not only is the sample likely to have much less local variation in its properties, but also a single material batch can be used for all the experimental work.

A number of manufacturers were contacted to find a suitable commercial nonwoven to use as a model absorbent. The material finally chosen which most closely met the described criteria was supplied by Ledatec [126]. It is a needle-felt made from round cross-section polyester fibres, and coded NP450P. Polyester swells little on contact with water, having a moisture absorption of between 0.2% and 0.5% [118].

3.3 Wicking measurements

The most common method for measuring wicking is to record the visually determined distance travelled by the wetting front over time. Other methods measure the volume or mass of liquid lost from a reservoir as liquid wicks into a sample.

An apparatus was designed to measure both mass uptake and wicked distance simultaneously. Measurement of mass lost from a reservoir was achieved using a computer-controlled microbalance. During the experiment readings from the balance were recorded every tenth of a second and stored for later analysis. The balance was set to its most sensitive mode of measurement, minimising any averaging of measurements. The balance could be read to 0.001 grammes and the response time was measured to be approximately a quarter of a second.

Measurements of wetted distance are usually made by noting the times at which the wetting front reaches predetermined distances as liquid wicks into a sample. A dye is often added to the wicking liquid to aid visualisation of the wetted area. Even though this approach is widely accepted for determining wicking rates it has some limitations. When the front is moving quickly it is difficult to note down sufficient readings to record the motion accurately. Equally, when the wetting front is moving slowly it can be difficult to perceive small changes in the wetted area. An intrinsic problem with this method is that it involves making a judgement as to when the wetting front has reached a prescribed distance. In some cases the front can be easily distinguished. In most cases, however, the wetting front is not well defined; not only does the front frequently have an irregular shape, but it also represents a region of varying saturation. At the wetting front the degree of liquid saturation might fall off gradually, rather than being sharply wet behind the front and dry ahead of it. Where a dye has been introduced the change in saturation leads to a decrease in the intensity of the wetted region towards the wetting front.

Using a camera to record the motion of the wetting front makes it possible to study fast and slow wicking rates with accuracy. Much of the image capture can be automated

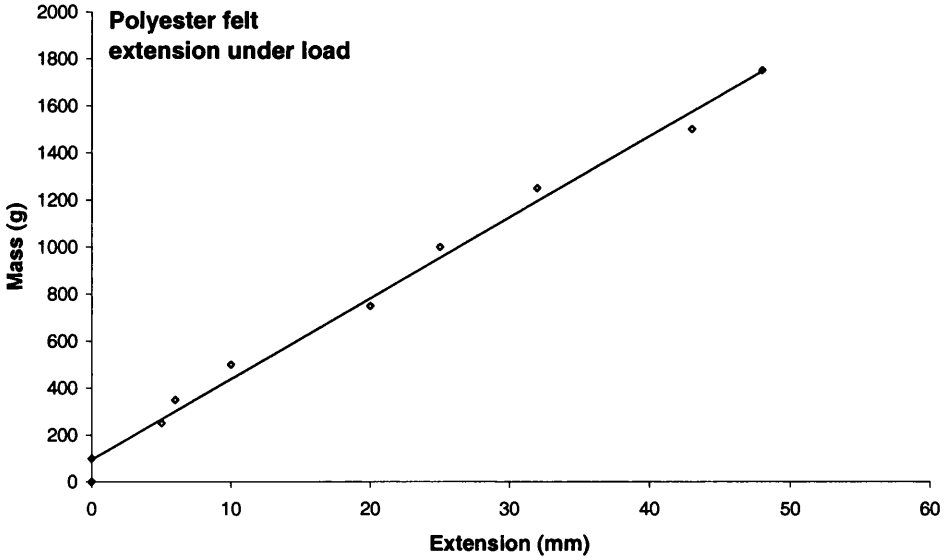

Figure 3.1: Extension measurement for polyester needlefelt, to verify fabric sample is not significantly distorted by mass used in tensioning (5 cm wide sample, initial length 40 cm)

making measurements less prone to operator error and, because images are recorded, less detail of the wicking process is lost. By applying image processing to the sequence, measurements of wetted distances can be automated and made with reference to fixed criteria.

3.4 Apparatus to measure wicking

The apparatus was designed to enable accurate measurements of one-dimensional semi-infinite wicking based on the strip test (see section 2.7.4). Wicking could be measured for a sample supported horizontally, vertically, as well as inclined at an angle. A sample width of 50 mm was chosen as this width is recommended in the British standard wicking test (BS:3424 [17]). A sample length of 300 mm was used to allow several minutes of horizontal wicking to be examined in most materials, before the process might be affected by the sample end.

A support was designed to hold the fabric securely at the required angles. The sample rests on a series of nylon lines, diameter 0.24 mm, at 10 mm intervals perpendicular to the wicking direction. By supporting the fabric on nylon line any effects that might be introduced between the sample and the supporting surface can be minimised. Provision

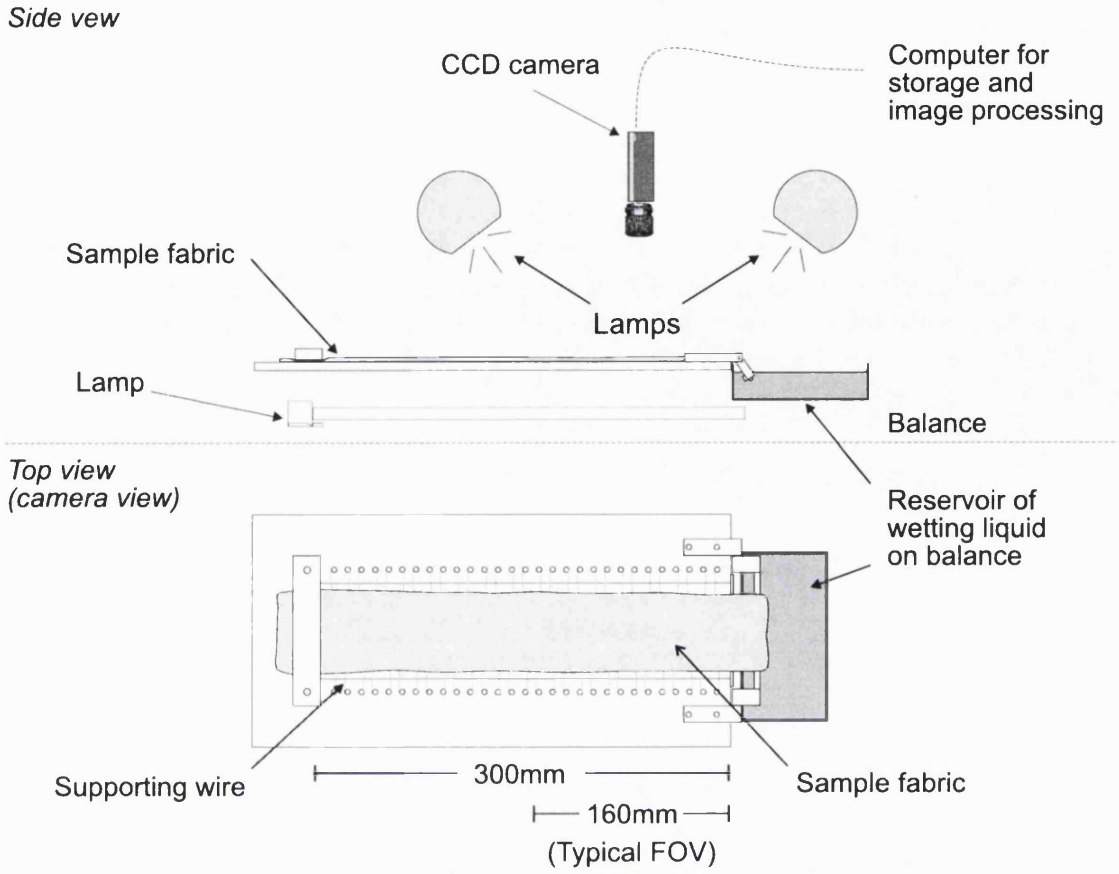

Figure 3.2: Diagram of apparatus to support a fabric sample while recording mass lost from a reservoir and wetted distance using a camera.

is made for illuminating the sample from below by including a central translucent section, directly underneath the fabric sample. This acts as a diffuser to give even illumination of the sample. Fabric samples need to be lightly tensioned to ensure they lie flat on the support. Tension is applied to the samples by hanging a 200 gramme mass from one end, while the opposite end of the sample is pinned to the holder. A mass of 200 grammes is large enough to cause the sample to lie flat without significantly distorting the fabric structure. The extension was measured to be linear up to at least 1750 grammes for a 5 cm wide strip of the sample fabric, with 200 grammes representing less than 2% strain (see figure 3.1) The sample is clamped securely to the sample holder before liquid is introduced. It is important to secure the sample to minimise motion and changes in the fabric's size during wetting. Figure 3.2 shows a diagram of a sample fabric supported with one end in a reservoir ready to image the wicking process.

Liquid is introduced into the fabric sample by placing one end of the sample into a reservoir of wicking liquid. In the case of horizontal wicking, liquid should wick through the sample at the same level as the free surface in the reservoir. There should not be

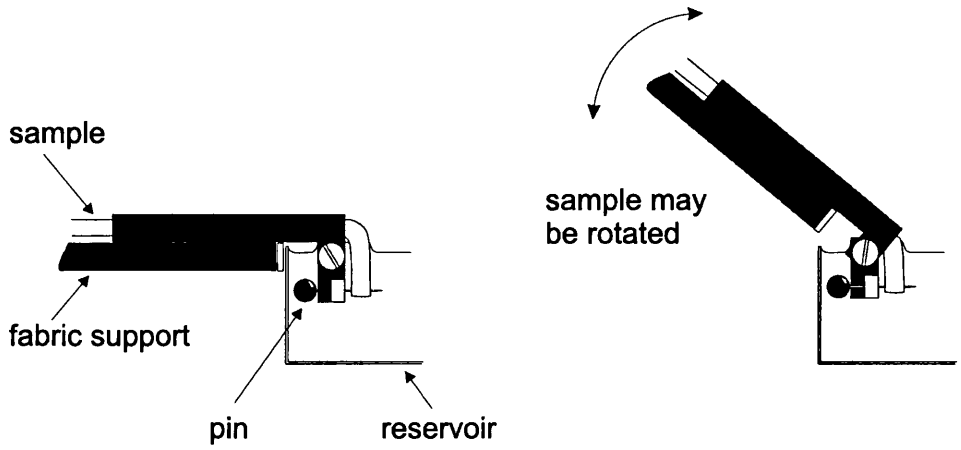

Figure 3.3: Side view showing the front portion of the fabric support. The fabric sample is held below the level of the liquid in the reservoir by pinning one end. Liquid introduction is kept consistent for varying angles of wicking by rotating the front section of the sample support.

any additional pressure drop caused by the liquid having to wick against gravity before it is able to wick horizontally. To achieve this, as far as is possible, the liquid in the reservoir is brought level with the bottom of a horizontal sample. Good contact between the sample and the liquid in the reservoir is sustained by placing a 10 mm portion of the fabric below the level of the liquid. Figure 3.3 shows a side elevation of the front portion of the fabric support. The fabric sample is held using pins rather than a clamp because this leaves the cut end of the sample relatively undisturbed. Liquid is able to enter easily and variations that might result from clamping the sample and inhibiting flow through the cut end are minimised. The fabric sample is passed over a cylindrical roller and pinned to a hinged support. Also, the hinge mechanism, and supporting roller, allow samples to be held at various orientations while keeping similar configurations for the submerged portion of fabric.

Detailed drawings for the fabric support are included in the appendix, see figure D.1.

Finally, the fabric support is held in a framework that allows the sample to be held at a chosen angle. This framework is designed not to obstruct the lighting or field of view of the camera, but particular care was taken to ensure the support did not interfere with the measurements of mass in the reservoir. The framework includes adjustable legs so that the sample can be levelled accurately before beginning a wicking experiment. Figure 3.4 shows a photograph of the sample holder and supporting framework. Detailed drawings of the framework are included in the appendix, figures D.2, and D.3.

Figure 3.4: Photograph of apparatus to support a fabric sample horizontally, vertically, or at an intermediate angle (shown).

3.4.1 Liquid introduction

It is important that liquid is introduced evenly and reproducibly to begin wicking into a fabric sample. At first, a labjack was used to raise both the balance and liquid reservoir, submerging one end of the fabric sample. A locknut placed on the lab jack ensured that the reservoir was always raised to the same height. Measurements without a sample showed that raising the reservoir by hand was not reproducible when submerging the end portion of the sample holder. Alternative methods were tried, for example liquid was kept on the balance, but the level lowered below the sample by evacuating an upturned vessel. By then opening the vessel to air the liquid refilled the reservoir and submerged the fabric end. Although this method was reproducible, and had the advantage that the volume of liquid remained on the balance; it was rejected because, without designing a purpose built reservoir, the act of releasing the liquid, and the additional components placed on the reservoir disrupted the experimental measurements during wicking. Instead, a measured volume of liquid was allowed to flow into the reservoir from a second reservoir by releasing a solenoid valve. A labjack was still used to raise the reservoir to the correct height, but liquid was introduced into the reservoir after it has been positioned. Experimental readings were taken from the instant that the solenoid valve was released, filling the wicking reservoir. Figure 3.5 shows the solenoid valve and reservoir used to fill the wicking reservoir.

Figure 3.6 shows a graph of the mass recorded as the reservoir is filled a number of times with no sample on the sample support. From this graph it can be seen that running liquid into the reservoir results in a reproducible rate of liquid introduction, though the exact time at which filling starts is not well controlled.

3.4.2 Image capture apparatus

Images of wicking into a fabric sample are captured using an S-VHS quality CCD array camera (759 $\times$ 574 pixel resolution). The rates of capture required are sufficiently low that images can be acquired and stored directly via a frame grabber onto hard disk storage using a personal computer.

A mounting was designed so that the camera could be easily and accurately positioned to view the fabric sample during wicking. The camera mounting was secured to an optical carriage running on a piece of optical rail. This rail was attached to a backing board and pivoted so that the camera could accommodate wicking experiments at any angle between horizontal and vertical. Detailed drawings for the camera mounting rail and support can be found in the appendix, figures D.4, D.5, D.6, D.7, D.8, and D.9

The camera acquired monochrome images at 256 intensity levels. To enhance the contrast between wet and dry sample regions, a green filter was placed on the camera lens, and a red dye (0.02 grammes/litre Terasil red) was introduced into the liquid. The sample

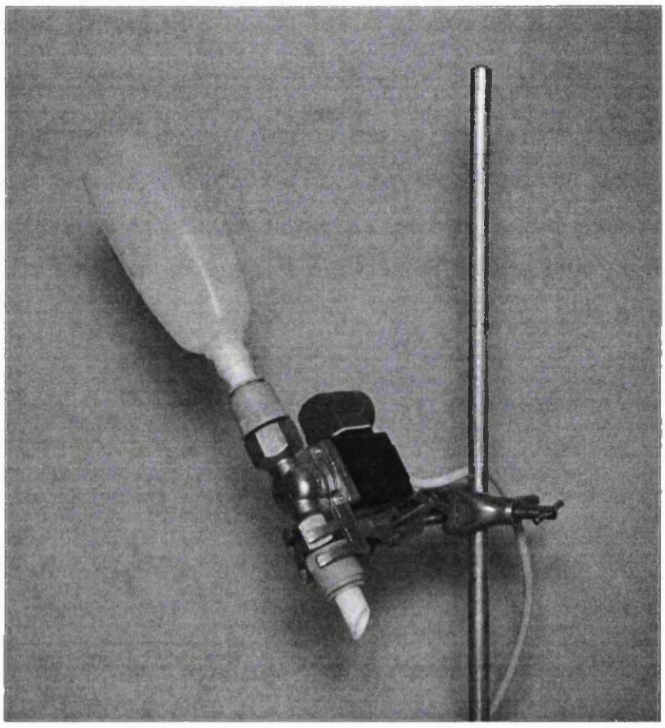

Figure 3.5: Photograph of the solenoid and reservoir used to introduce liquid into the wicking reservoir.

was illuminated using high frequency (40kHz) fluorescent lamps, to avoid interference that might result from standard mains frequency lighting. The sample could be illuminated from above or below, allowing thin samples to be illuminated through the fabric. When lit from above a pair of fluorescent lamps were used, and it was important that the lamps could be positioned so that the imaged area was evenly illuminated, whatever the angle of the sample. To provide flexible positioning of the lighting, the fluorescent lamps were mounted on chains and hung from rails above the sample support. This allowed the height above the sample and position of each lamp to be easily changed. A wooden cabinet was constructed allowing the experiment to be completely enclosed, excluding any external changes in the lighting level, and minimising disturbance of the balance due to air movements.

A diagram of the entire wicking apparatus is shown in figure 3.7. Photographs of the apparatus used are shown in figures 3.8 (horizontal wicking), and 3.9 (vertical wicking).

Technical details for the wicking apparatus are included in the appendix (see section C.1).

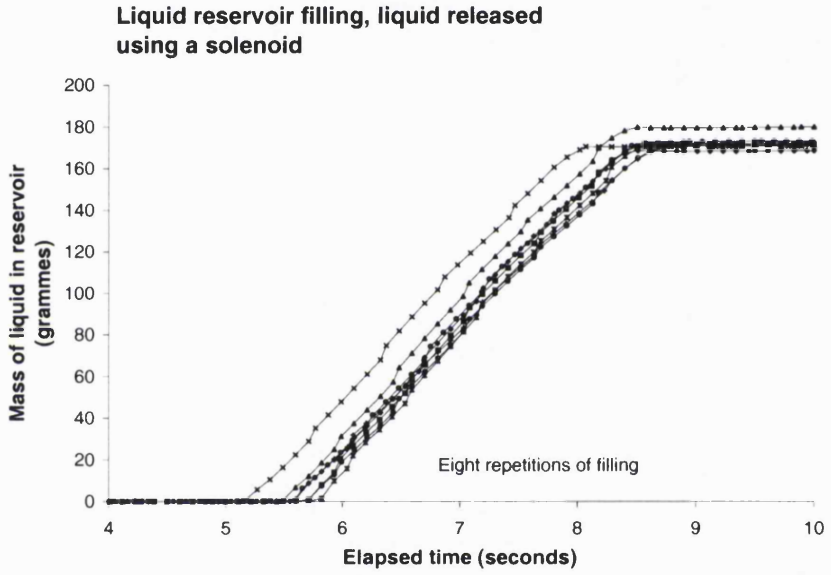

Figure 3.6: Chart showing mass of liquid in the reservoir, including the sample holder but no fabric sample. Eight repeats are shown for comparison.

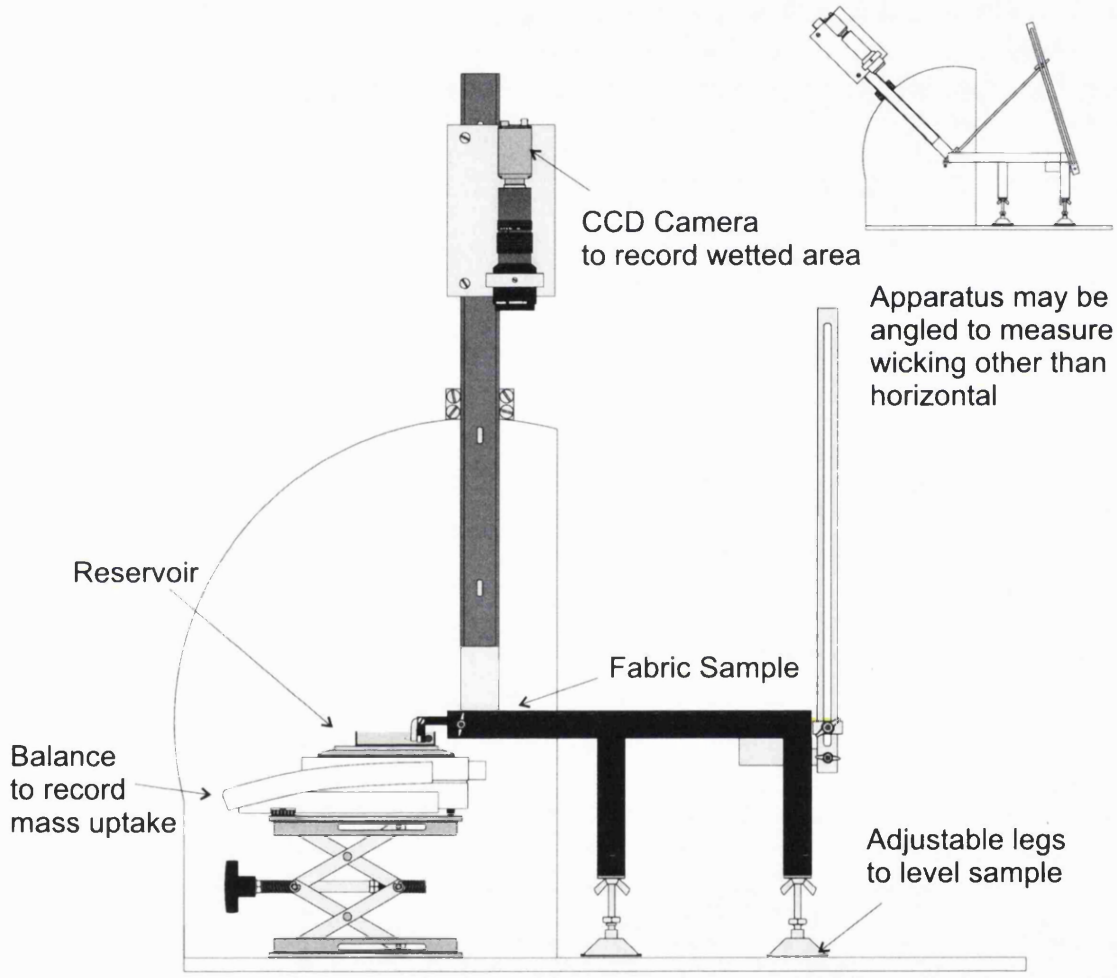

Figure 3.7: Diagram of the apparatus to measure angled wicking using a CCD array camera and balance

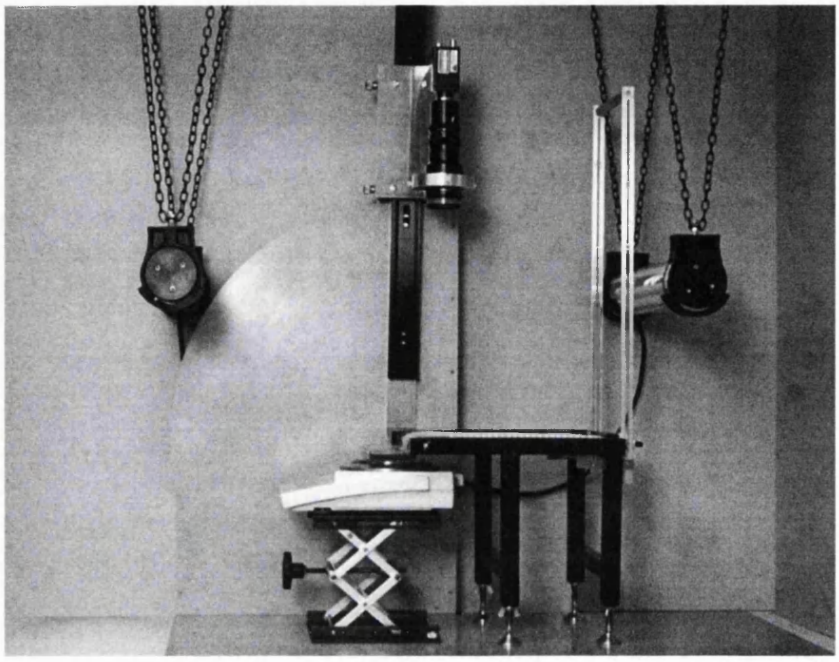

Figure 3.8: Photograph of wicking apparatus being used to record images and mass uptake during horizontal wicking

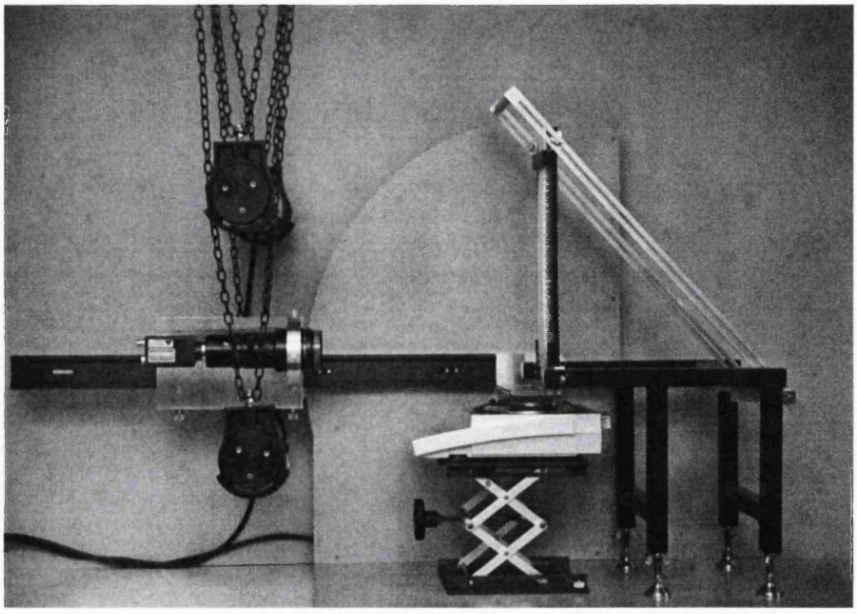

Figure 3.9: Photograph of wicking apparatus being used to record images and mass uptake during vertical wicking

3.5 Image capture and processing

To obtain an image sequence of liquid wicking into a fabric sample a piece of software was written. The software integrates the recording of experimental details with control of image acquisition, and synchronisation between image capture and mass readings from the microbalance.

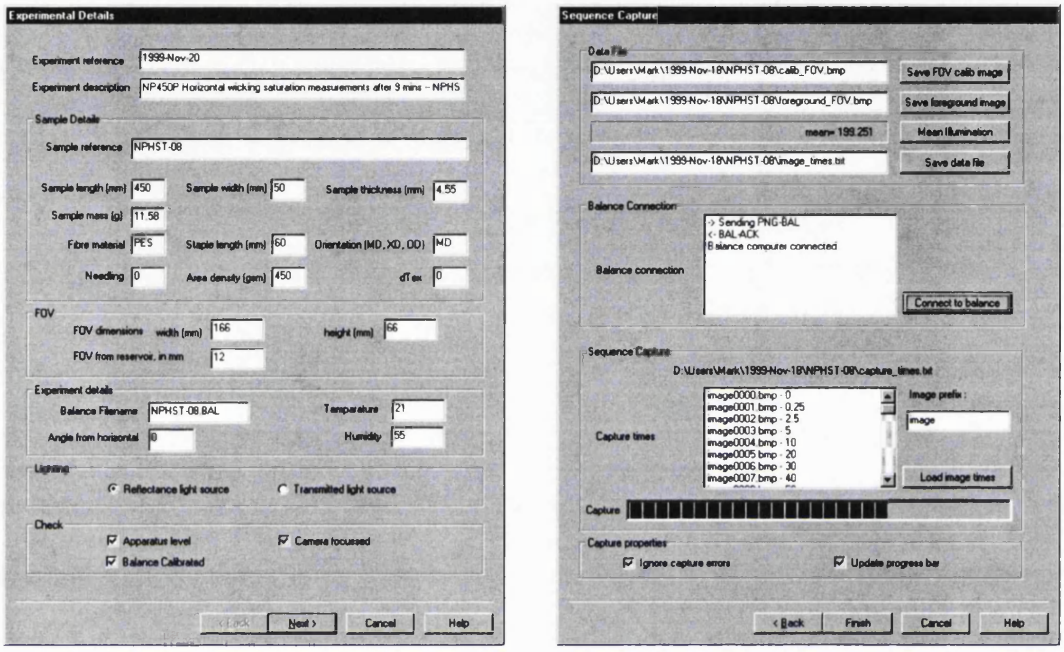

(a) (b)

Figure 3.10: User interfaces from software used to record details of a wicking experiment. (a) captures details of the experimental conditions and sample. (b) captures images to aid processing; establishes a connection to the balance; loads the times at which image capture should take place; and shows the progress of image capture during the experiment.

The main interface has two elements. The first interface, figure 3.10(a), simply records information about the experiment; for example experiment date, details of the fabric sample, and size of the field of view used. Information needed to capture the wicking sequence is entered into the second interface, figure 3.10(b).

Calibration images were obtained for every field of view by placing a piece of graph paper, a ruler, or both on top of the sample and recording an image that could later be used to verify the conversion from pixels to wicked distances for the experiment.

The same level of illumination was maintained between experiments by calculating a mean intensity for the entire field of view. By filling the field of view with a uniform surface, for example a piece of white card, the mean intensity was adjusted to a consistent

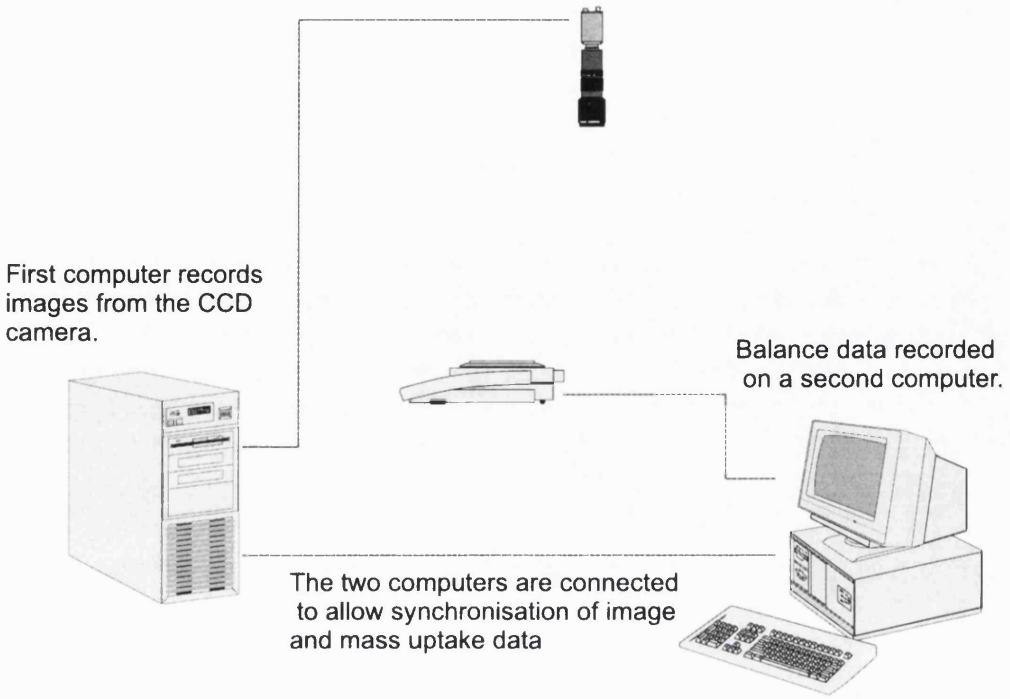

Figure 3.11: Connections between computers used to record mass uptake and images during wicking. The computers are themselves connected to synchronise mass and image data.

level for all experiments.

The elapsed times at which images should be acquired were read from a text file. This gives good control over the image capture times that make up a sequence. In general rapid image acquisition was used at the beginning of the sequence, and the rate of capture was then reduced as wicking progressed. If an image cannot be captured at the designated time, owing to limiting factors such as disk access speeds, it is queued and acquired as soon as possible. The actual start and end times of each image acquisition are stored. The actual start times for each acquisition were then used when analysing the wicking sequence.

In order to synchronise the image acquisition with the recording of mass uptake the computer responsible for recording mass uptake is linked to the computer that acquires images. Communication is achieved between the two computers using a serial link (see [53]). Figure 3.11 shows the connections between the devices.

Information provided about the experiment is written into a text file and placed into the same location as the image sequence and calibration images. An example output file is included in the appendix F.1.1. This file can be read to identify the experiment that relates to a sequence of image files. These text files are used when processing image sequences to find the times for each image acquisition and convert image measurements to distances.

3.6 Image processing

Once an image sequence has been captured the images in the sequence may be processed to extract results for the wicking process. In order to measure the wetted area in an image the change in intensity for each pixel is found. Intensity changes are measured with respect to the intensity of a pixel when it is known to be dry, at the beginning of the sequence. It is easy to find the change for every pixel in an image by taking the difference between a reference image (before any wicking occurred) and the image of interest. The difference image is then thresholded to determine those pixels whose intensity has changed sufficiently that they can be deemed wet.

Figure 3.12 shows the difference process:

- figure 3.12(a) is an example of an image captured during wicking. The wetted area can be clearly seen as the darker portion of the fabric.
- figure 3.12(b) is a difference image taken between the previous image and an image taken when the sample was completely dry (before wicking occurred).
- finally, figure 3.12(c) shows the previous difference image after it has been thresholded to a predetermined level.

The wetted area image is in fact improved slightly by ensuring the illumination is even and removing some of the noise from the images. The fact that the sample is illuminated using a pair of fluorescent lamps leads to some variation in the illumination level across the imaged area, in the wicking direction. To compensate for this, a correction is found using an image of the dry sample, and then applied to each image in the sequence. Before taking the image difference, a median filter is applied to each image. Still, often a few pixels remain that have been inaccurately marked as wet. In this case, the fact that the liquid is known to wick from one end of the field of view, and progress to the other, is used to improve identification of the wet region. Thresholded pixels are only kept if they are in contact with the edge of the image nearest the reservoir.

This processing results in an image that contains pixels marked wherever the fabric was deemed to be wet for this instance in the wicking sequence. The progress of the wetting front for a sequence of images can be summarised by using a spatio-temporal slice. Taking a single row of pixels from every image in the sequence a composite image can be formed showing how the pixels in the chosen row change over time. Figure 3.13(b) shows such an image, where the row of pixels indicated in 3.13(a) have been collected from a sequence of images, showing the progress of the wetting front. The same process can be used to show the pixels that have been classified as wet in the sequence, this is shown for the example sequence in figure 3.13(c). Images such as those shown are useful in providing a summary of the wetting sequence, and a quick check of the processing and threshold values used to

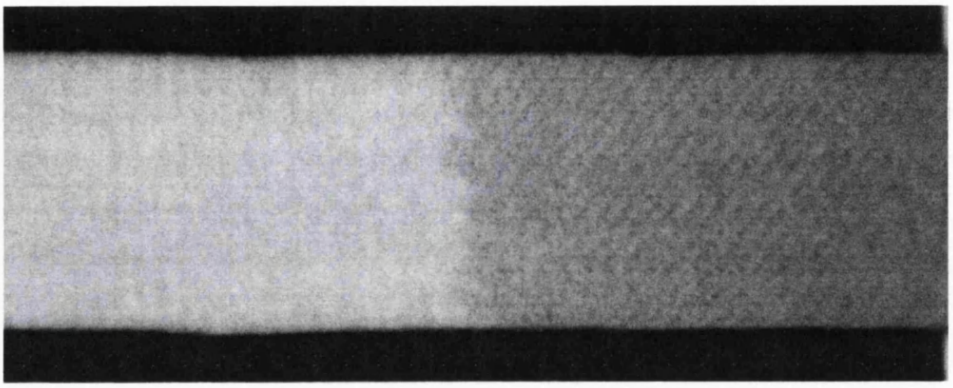

(a)

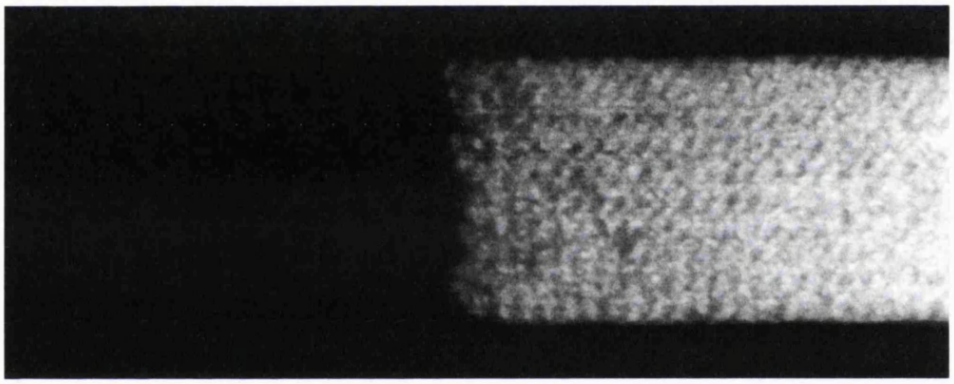

(b)

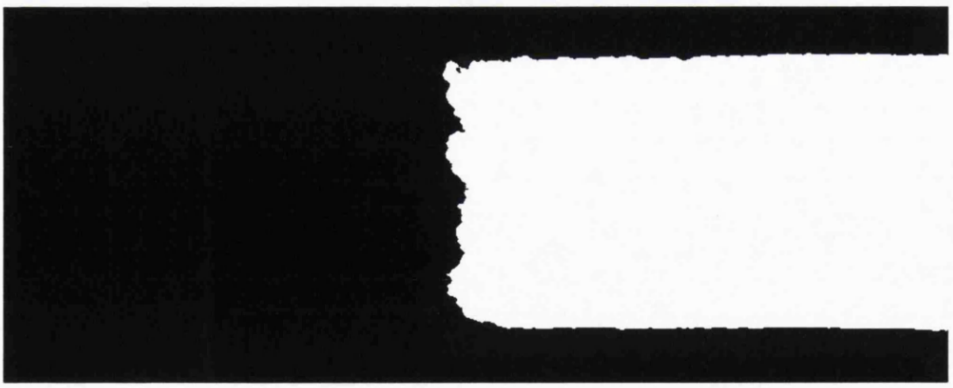

(c)

Figure 3.12: Steps used in image processing of wicking images. (a) captured image, wetted region appears darker, (b) difference image is found between each image in the wicking sequence and an image of the fabric prior to wetting. (c) the difference image is thresholded to find the wet pixels in the image.

identify wet pixels. The processing method developed generates these summary images and stores them together with the wicking results. Images representing the captured sequence are more difficult to interpret if the images are not obtained at fixed time intervals.

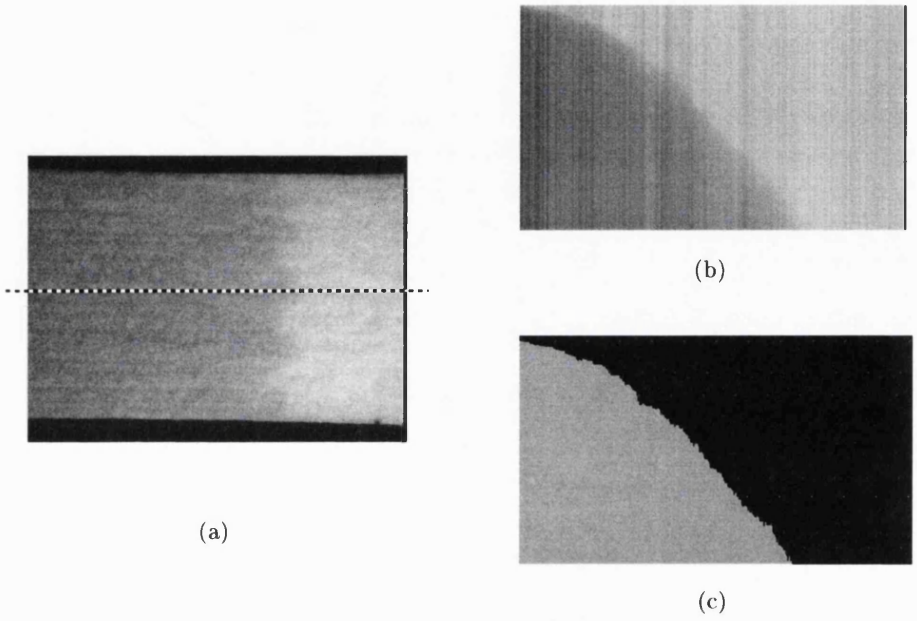

Figure 3.13: Example image from a sample during wicking. The wicking sequence is illustrated using a composite image (b) made up of a single row of pixels from each image in the wicking sequence (a), forming a spatio-temporal slice. The wetted pixels in the sequence, resulting from a thresholding operation, are also shown (c).

The wetted area can be calculated from the total area of the pixels in the thresholded image. The area was estimated from the total number of *on* pixels in the image. Accuracy was improved by also considering the two-by-two neighbourhood of pixels when calculating the area of a given pixel [172].

The wetted distance is determined from the wetted area by dividing by the mean width of the sample. The mean width of the sample is found using a thresholded image of the dry sample, and finding the mean sum across the sample width.

An alternative procedure for measuring the wetted distance is to extract the wetting front from the image of the wetted area. Firstly, the perimeter pixels of the wetted area image were obtained. The perimeter image contains the wetting front, but also the sides of the fabric. The fabric sides were removed by masking the perimeter image with an inverse mask of the fabric area. The fabric mask was obtained from the thresholded image of the dry fabric. This leaves only the wetting front as shown in figure 3.14. This wetting front image clearly shows that assigning a single value for the wetted distance can hide some of the detail of the wicking process.

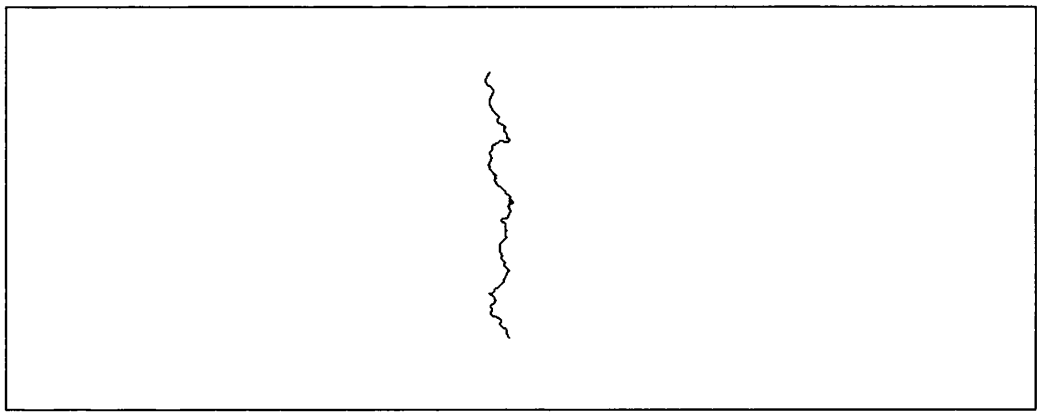

Figure 3.14: Wetting front extracted from captured images of wetted area.

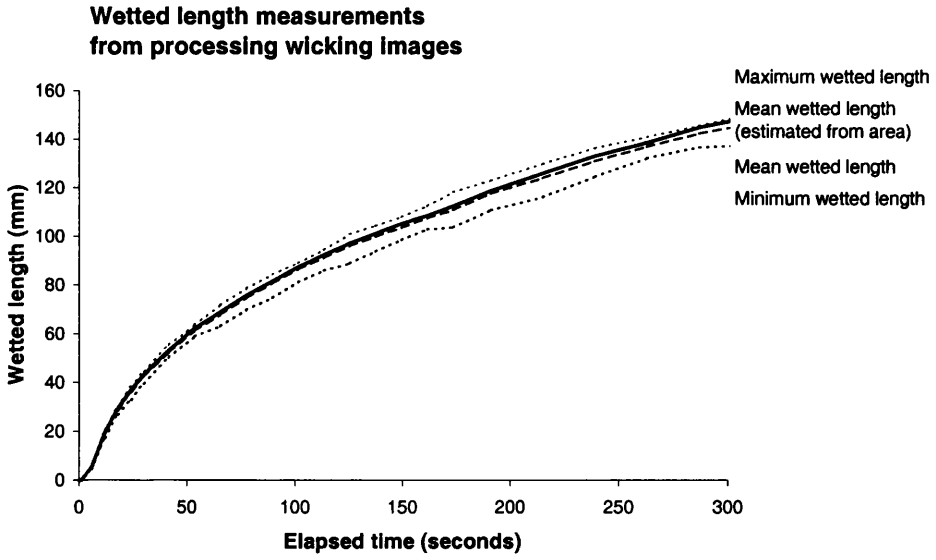

Figure 3.15: Wetted length comparison calculated by different means. The wetted length estimated from the wetted area is compared with the minimum, mean and maximum distances travelled by the wetting front.

From the wetting front image it is possible to find minimum, maximum and mean wetted distances. Figure 3.15 shows the minimum, mean and maximum distances calculated from the wetted front, compared with the mean wetted length estimated from the wet area; using the methods outlined above.

All the image processing was implemented in Matlab, with many of the component operations taken from the image processing toolbox. Specific functions and additional scripting was implemented as necessary to automate the processing of a sequence. The wicking sequence is processed together with the field of view calibrations, and image times to produce text files containing wicked distances at each time specified for the experiment.

3.7 Validating the system for measuring wicking

In order to ensure that area measurements made by the system were accurate a series of test images of known area were constructed. Both regular and irregular shapes were cut out from red card, see figure 3.16. The area of each piece was estimated by careful weighing. Each sample was then placed on the wicking apparatus and a series of images obtained at two magnifications (the first with a field of view of approximately 80 mm length, the second of around 160 mm). The series of images obtained was processed as described in section 3.6. Figure 3.17 shows a plot of the area estimated from weighing the samples, compared with the area obtained from processing the images. This plot shows good agreement between the area measured by weighing the sample cards, and that estimated from the captured images.

In a separate experiment the timing accuracy of image acquisitions was checked. A digital stopwatch was placed in the field of view and a sequence of images acquired. In the captured sequence the stopwatch could be read to a tenth of a second. As far as could be determined the capture times recorded in the results file for each image agreed with the elapsed time shown on the image of the stopwatch.

3.7.1 Wicking measurements

A number of early horizontal wicking experiments were performed using a polyester-viscose needle felt. In these experiments it became apparent that the mass uptake readings regularly showed a discontinuity after about three minutes: the chart in figure 3.18 is a sample of these results. As there is no mechanism to compensate for the loss of liquid from the reservoir, the level of the free liquid surface falls during the experiment. An unexpected consequence of this change in the liquid height was that the liquid meniscus detached from the bottom of the dowel used in the sample support. This was corrected by filling the gap between the bottom of the dowel and the section supporting the sample end with wax.

It became clear when reproducing experiments that wicking measurements using samples of the same material often led to quite different results. This seemed to be particularly

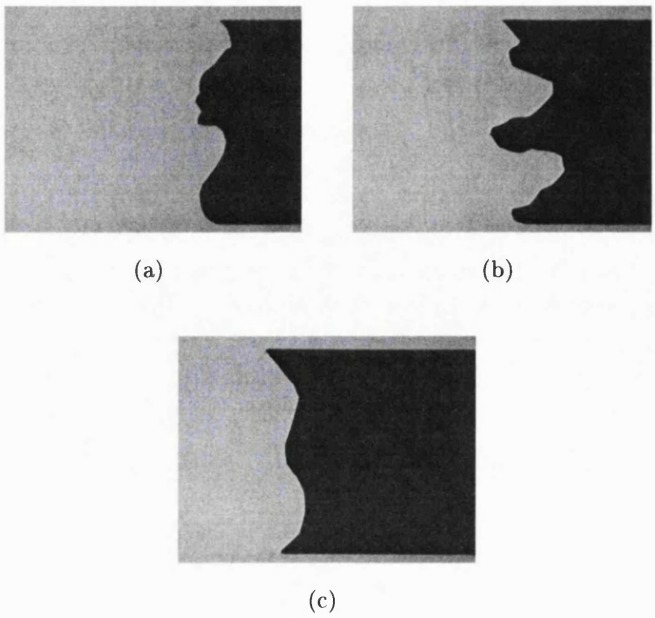

Figure 3.16: Example images using cards of known areas to validate area measurements using image processing.

true for experiments conducted on different days; a similar observation, but to a lesser extent, has been made by Laughlin and Davies when they examined wicking in cotton and felt (see section 2.7.5).

The experiments have each been identified by a short code, for example NPHMA-01. The first two letters designate the fabric used, in this example NP for Ledatec NP450P. The next three the experiment performed, here HMA refers to a Horizontal wicking experiment in the Machine direction of the fabric, in its As received state. Finally the letters following the dash show the number of this experimental repeat in the series. A summary of the experiments performed, and codes used can be found in appendix G.1

Figure 3.19 shows results for mass uptake in samples of the nonwoven fabric supplied by Ledatec (NP450P). This chart, shows the most extreme variations in mass uptake encountered in all the horizontal wicking experiments performed for this fabric. A more typical example of the variations in wicking measurements over a period of a few days is shown in figures 3.20 and 3.21.

A number of factors may lead to the differences observed in results for repeated experiments. Variations in the sample properties, the environment (particularly temperature and humidity), or the experimental setup, can all cause changes in wicking performance.

An unavoidable problem when using fabrics for experimental work is that fabrics are not well controlled materials. Most fabrics have appreciable local variations in their properties, and nominally the same material from different batches can have quite different

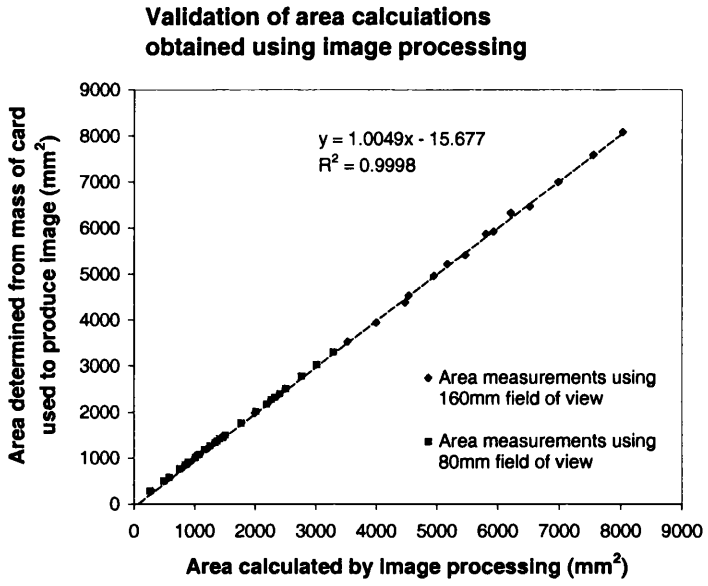

Figure 3.17: Areas calculated by applying image processing to a series of images of cards of various shapes. The areas of the cards were found by weighing, and these areas are compared with results from image processing.

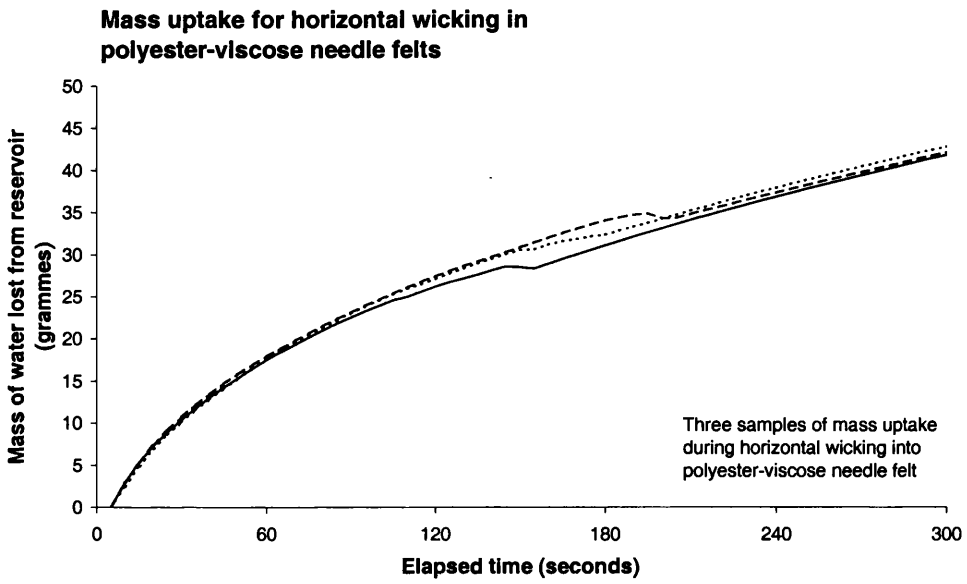

Figure 3.18: Example measurements of mass uptake into polyester-viscose needle-felt during horizontal wicking. The anomalous drop in mass uptake in each case was attributed to meniscus detachment from the apparatus.

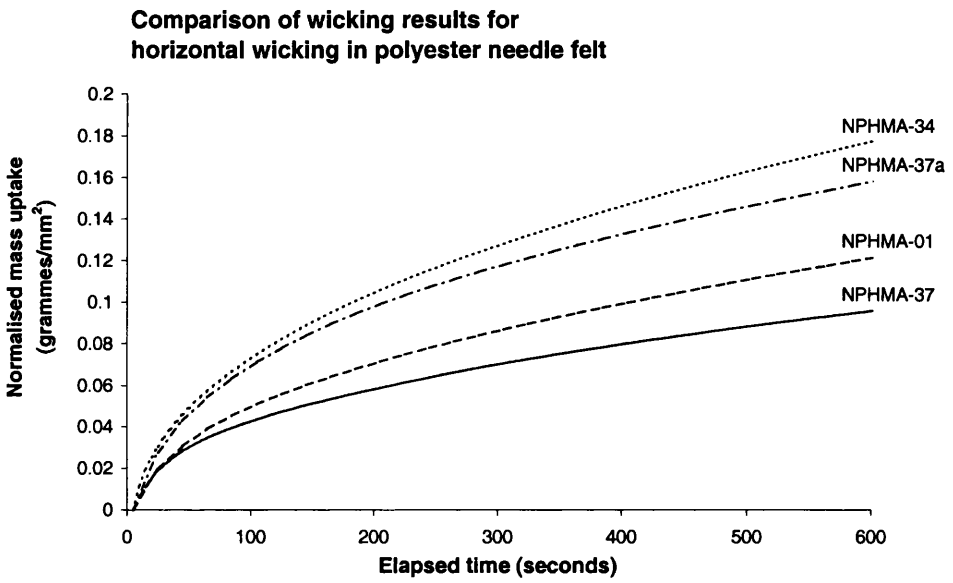

Figure 3.19: Comparison between repeated measurements of wetted length during horizontal wicking into polyester needle-felt. Measurements made over total experimental period of project, to show the large range of results obtained.

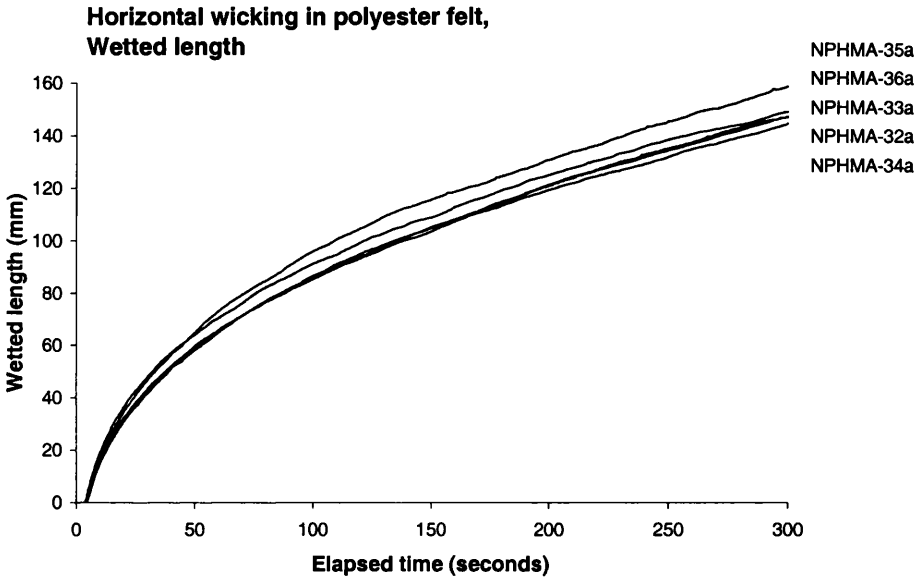

Figure 3.20: Comparison between repeated measurements of wetted length during horizontal wicking into polyester needle-felt. Measurements made over a few days (30-Aug-1999 – 03-Sep-1999).

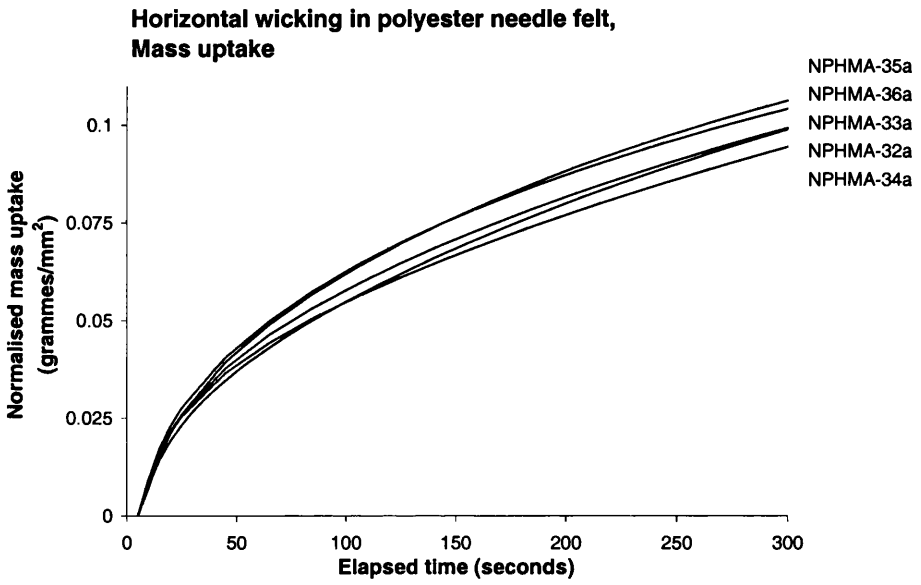

Figure 3.21: Comparison between repeated measurements of mass uptake during horizontal wicking into polyester needle-felt.Measurements made over a few days (30-Aug-1999 – 03-Sep-1999)

properties. Changes in wicking performance for similar fabrics arise from differences in the physical arrangement of the pore space, and also variations in the surface properties of the fibres.

Environmental conditions affect not only the properties of the wicking liquid, but also the surface characteristics of the fibres. It is common practice to precondition textiles under standard conditions of temperature and humidity (20 °C 65% RH for a period of 48 hours), prior to and during experimental use. No facility to precondition samples or control the environment of the experiment was available, but samples were prepared in batches and kept in a sealed container. Similarly the water used in the wicking experiments was stored in sealed bottles and always left overnight, to reach room temperature, before use.

The variation in results for repeated experiments was evident in preliminary experiments using polyester-viscose samples; and considerable care was taken to reproduce the conditions in all subsequent experiments. In addition, an attempt was made to record, where possible, features that may account for the discrepancies in wicking performance.

Changes in the environment were recorded by taking readings of temperature and humidity in the laboratory before each experiment. The mass and thickness of samples were recorded. Thickness was measured using a dial gauge, with the sample subject to a pressure of 2 kPa over a circular area of 50 mm diameter. Measurements for the experiments shown in figures 3.20 and 3.21 are presented in table 3.1. Full details for all experiments are shown in the appendix, section G.1

Experiment	*Sample mass* (g)	*Sample thickness* (mm)	*Temperature* (°C)	*Relative Humidity* (%)
NPHMA-32a	13.73	4.69	27.5	67
NPHMA-33a	13.69	4.44	27	62
NPHMA-34a	12 32	4.04	27.5	63
NPHMA-35a	12.19	4.28	28.5	63
NPHMA-36a	11.16	4.11	28.5	59

Table 3.1: Details of fabric samples

Wicking can be altered by evaporation of liquid, both from the reservoir and the wetted sample. To quantify this the mass loss from both the reservoir, and a saturated fabric sample was monitored for a period of time. Table 3.2 shows the largest rates of evaporation recorded from the sample and reservoir. The combined effect of evaporation from the sample and reservoir is likely to contribute less than 4% of the total loss of liquid during a ten minute experiment. Over the timescales being investigated the loss of liquid by evaporation is relatively small, and was ignored.

One of the compromises in the method for measuring horizontal wicking is that the

Experiment	*Evaporation rate* (g/s)	*Temperature* (°C)	*Relative Humidity* (%)
Reservoir (141 mm × 73.5 mm)	$5.9\times10^{-4} \pm 7.57\times10^{-5}$	28 ± 2.42	58 ± 4.04
Sample (100 mm × 50 mm)	$2.17\times10^{-4} \pm 1.48\times10^{-5}$	28.5 ± 2.12	68 ± 4.24

Table 3.2: Measured evaporation rates from a wet sample and the reservoir (n=5 for evaporation from reservoir, n=2 for sample evaporation, errors are ± one standard deviation).

sample is turned through ninety degrees to submerge the front portion of the sample in the reservoir. This means that liquid must travel a small distance vertically. Increasing this vertical portion will have a detrimental impact on the wicking rate. To investigate this possibility, the distance between the reservoir and the sample holder was deliberately varied using shims. Although the reservoir is raised into position using a labjack, the lifting thread of the jack is stopped using a locknut, fixing the maximum height to which it can be raised. A significant change in the wicking rate was observed when the sample was raised by 4.5 mm, as shown in the chart in figure 3.22. Counteracting the fall in the free liquid level of the reservoir is difficult, and would require a carefully set up mechanism such as that used in the GATS apparatus (see section 2.7.4). Although wicking is clearly affected by the liquid height in the reservoir, it is difficult to correct, and for small volumes of wicked liquid it only causes a small change in wicking performance. In the sample fabric approximately 20 grammes of liquid is wicked after five minutes, leading to a fall in the liquid surface in the reservoir of approximately 2 mm. The wicking measurements shown in figure 3.22, wick from an initial disadvantage which increases, whereas in the sample the 2 mm fall is accrued over five minutes. For wicking over small times in the experimental sample the error in wicking measurements caused by the drop in the reservoir height was ignored.

Figure 3.22 also shows the effect on wicking of errors made in levelling the sample holder. The sample was deliberately angled upwards or downwards at the maximum likely error that would be introduced by misreading the level of the sample support.

The temperature of the wetting liquid has an effect on the rate of wicking. The extent to which changes in liquid temperature were found to affect wicking in this sample can be seen in figure 3.23. Temperatures indicated in figure 3.23 are initial temperatures of water in the reservoir before introduction to the sample. Changing the water temperature by approximately 10 °C has a significant impact on the wicking rate. The increase in wicking rate at higher temperatures is to be expected because the viscosity of water is highly temperature dependent.

The ratio between the wicking numbers for wicking at approximately 30 °C and 40 °C

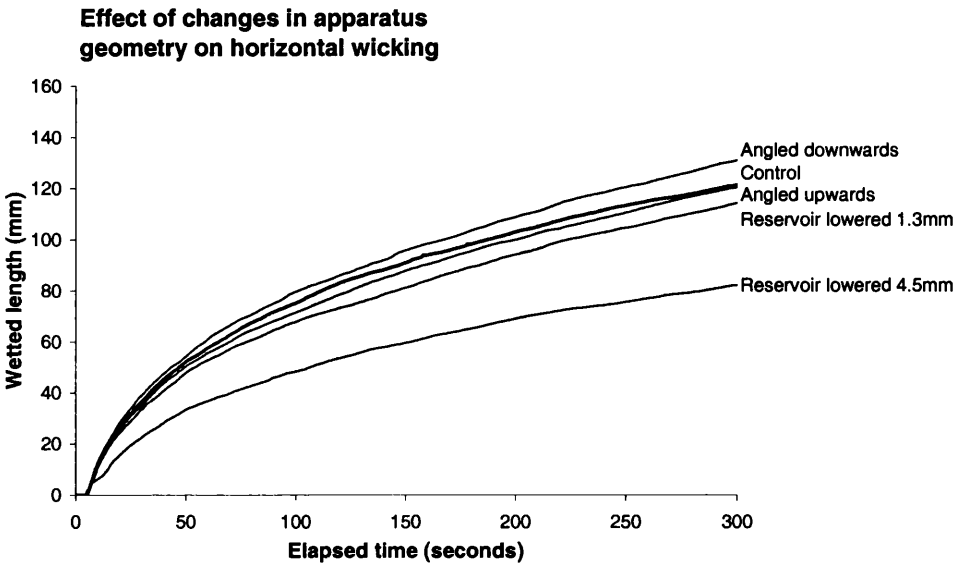

Figure 3.22: Effect on horizontal wicking of incorrectly levelling the sample support or lowering the reservoir. The sample support is angled upwards or downwards at the maximum error that would be introduced by misreading the level of the sample support.

was 0.65 ($\pm$ 0.11, n=3). Assuming the square of the wicking number is inversely proportional to viscosity of the wicking liquid, as indicated by Darcy's equation. The expected ratio of the wicking numbers was calculated from tabulated values of the viscosity of water [129]. In this case approximately 70% of the measured rate at 40 °C is accounted for by the change in viscosity between the two temperatures. The majority of this change results from differences in viscosity rather than surface tension. If the contact angle changes, its values are not known.

Changing the temperature of the wicking liquid, by a relatively small amount has a significant influence on the measured wicking rate in a nonwoven sample. It is therefore important to keep the temperature of the wicking liquid consistent when making wicking measurements.

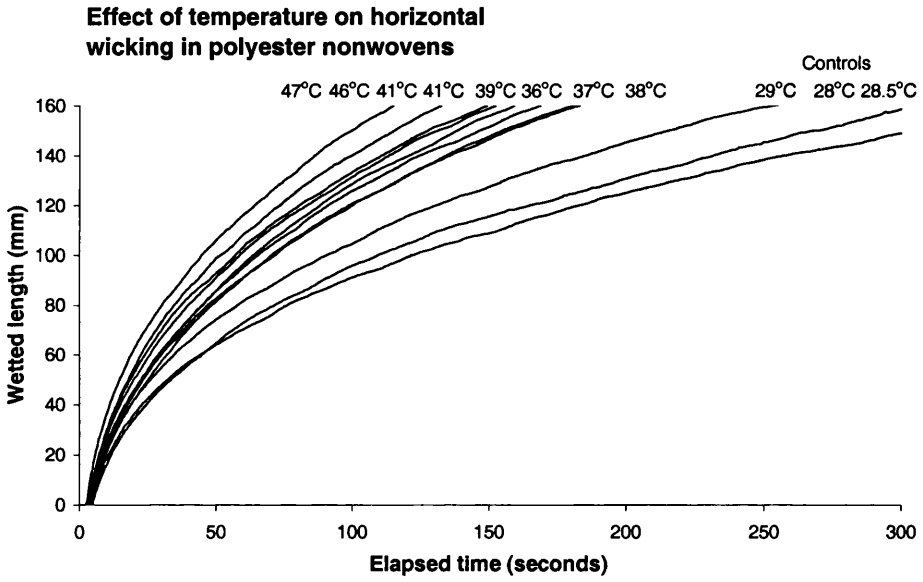

Figure 3.23: Effect temperature of the wicking liquid has on horizontal wicking. Initial temperature of the liquid in reservoir is indicated. Ambient temperature 28 °C, temperature of the liquid in wicking reservoir fell from 41 °C to 34 ° in 17 minutes.

Nonwoven felts are primarily low cost materials, and are produced to specifications where considerable variations in material properties are acceptable[1]. Properties such as the area density of fibres may vary considerably throughout a nonwoven felt. As well as inconsistencies in the distribution of fibres the surface characteristics of the fibres may be

[1]For fabrics 10% tolerance for properties such as area density are common.

variable. Often surfactants are added in the manufacturing process to lubricate the fibres and make mechanical processing easier, resulting in localised changes at the fibre-liquid interface. To explore the effect of any differences between samples, repeated measurements of wicking were made using the same sample, but drying samples thoroughly between experiments. Large differences in wicking were observed between the samples in their received state, compared with repeated experiments. Not only were differences seen following the initial wetting, but further significant changes in the wicking performance were apparent as wicking was measured on subsequent occasions in the same sample. Wicking performance improved as the samples were reused. The same effect can be seen in samples that are rinsed prior to making wicking measurements.

The change in wicking rate, for thoroughly rinsed (five litres clean cold water changed five times) and dried samples, is shown in figure 3.24. Figure 3.24 also shows samples washed using washing powder (five litres, 26.5 ml automatic washing powder 49. °C water, rinsed with five changes of water).

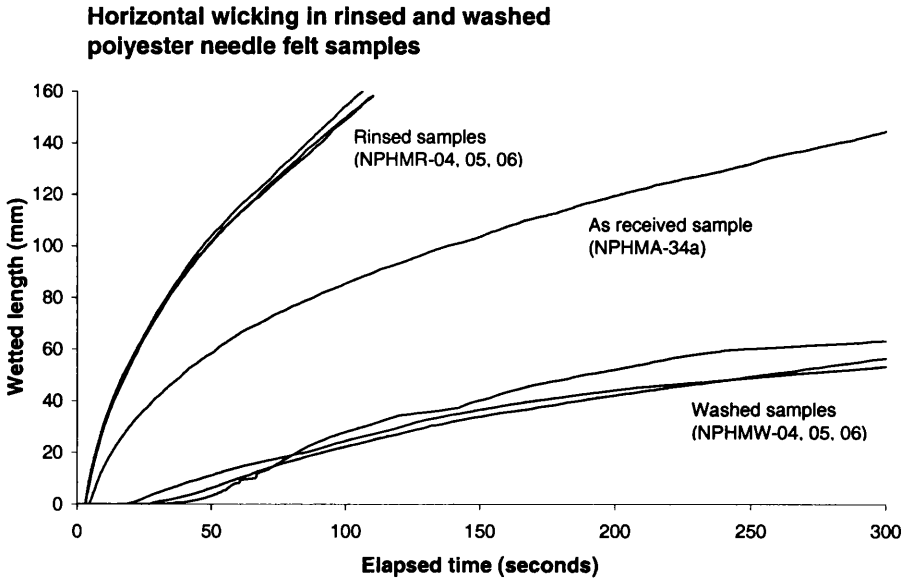

Figure 3.24: Horizontal wicking in samples of polyester needle-felt, where fabric sample has rinsed with clean water or washed in detergent.

Wicking in samples that had been rinsed in clean water was significantly faster than in samples in their as received state. Washing the samples with detergent, however, resulted in much slower wicking performance. Rinsing or washing fabrics can alter their wicking properties either by changing the surface characteristics of the fibres or by altering the

porous structure of the material. For both rinsing and washing the samples were handled similarly. It is likely, then, that the changes in wicking performance are due to changes in the surface properties of the fibres. Rinsing can remove some surfactants from the fibre surface, this can then decrease the fibre-water contact angle. Whereas washing with a detergent might put a surface finish on the fibres, which in turn increases the fibre-water contact angle.

It is important that the dye that is added to the wicking liquid does not affect the rate of wicking. To verify that this was the case the rate of wicking, measured as mass lost from the reservoir, for samples using liquid with and without the addition of dye. Figure 3.25 shows results from these experiments.

The fitted mass uptake for horizontal wicking including a dye was not significantly different from the uptake measured without any dye in the wicking liquid. A wicking number of 0.0042 ($\pm$ 0.0004, n=3) was found for the normalised mass uptake with no dye; a wicking number of 0.0039 ($\pm$ 0.0004, n=3) was found where a dye was added to the liquid.

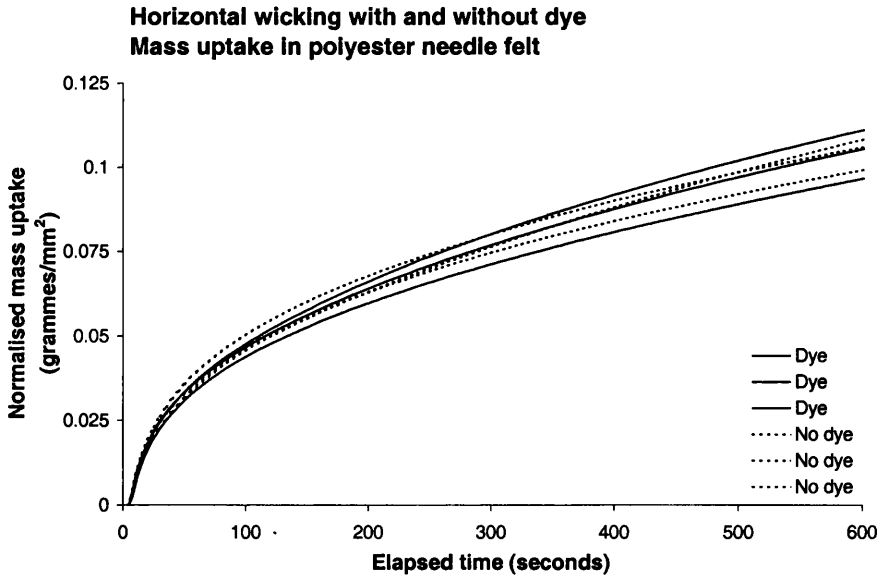

Figure 3.25: Horizontal wicking in samples of polyester needle-felt, with an d without dye added to wicking liquid.

A sample width of 50 mm was used in all experiments. This width was chosen for convenience and because it has been previously used when measuring wicking. It is possible that the width of the sample can influence the rate of wicking, depending on the

homogeneity of the material. For this reason, wicking was measured in samples of different widths, the results of which are shown in figure 3.26. No significant difference in the wicking rates was seen for these samples of different widths.

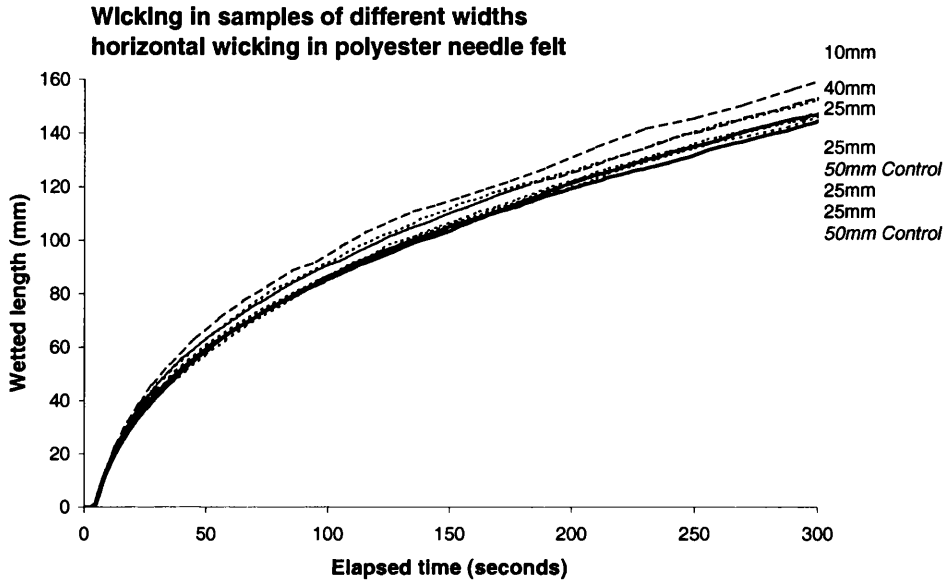

Figure 3.26: Horizontal wicking in samples of polyester needle-felt, using samples of different widths (10 mm, 25 mm, 40 mm, 50 mm).

3.8 Fitting wicking results

As described in section 2.4.1 the horizontal mass uptake or wetted distance is expected to increase with the square root of time. In this experiment, because wicking is started by filling a reservoir, the exact instant at which wicking begins is unknown. In the early part of the experiment wicking takes place while the reservoir is filling. Furthermore, the amount of sample and holder submerged in the reservoir is not known. Meaning that an unknown buoyancy correction needs to be applied to the mass uptake results. A similar consideration needs to be made for the wetted length results, where there is a length of sample outside the field of view.

The unknown offsets in time, and length or mass, can be found by assuming a general form for the wicking equation. Laughlin and Davies [124] found a modified Washburn

equation applied for all the samples they used measure wicking,

$$l = L_0 t^k \tag{3.1}$$

where, l is the measured wetted length, L_0 the length wicking number, t is the measured time, and k is a characteristic exponent The value of the exponent varied from 0.50 down to 0.41. Fitting wicking results from the sample nonwoven to equation 3.1 resulted in a strong correlation between values for L_0 and k indicating over parameterisation in the model. Fitted values for the exponent were close to 0.5.

As noted by Labajos-Broncano *et al.* [122], a new origin for the coordinate system must be used if the distance of penetration and time are not taken from the exact point of contact between the wick and the liquid. In order to find the unknown quantities in the mass and length equations the experimental results were fitted to equations of the form:

$$m = M_0(t - t_0)^{\frac{1}{2}} + m_0 \tag{3.2}$$

where, m the measured mass, M_0 the mass wicking number, t the measured time, m_0 is the mass offset, and t_0 is the time offset. and

$$l = L_0(t - t_0)^{\frac{1}{2}} + l_0 \tag{3.3}$$

where, l is the measured length, L_0 the length wicking number, t is the measured time, l_0 is the length offset, and t_0 is the time offset.

The required parameters in these equations were estimated using a least squares method, implemented in Matlab using Marquardt-Levenberg optimisation [143, 128]. Figures 3.27(b) and 3.27(a) show examples of fitting mass and area results from horizontal wicking using this method.

The mass and length results are recorded simultaneously and, therefore, should share the same time offset. The combined wicking results from mass and wetted length measurements were fitted, requiring the time offset to be the same. Figures 3.28(b) and 3.28(a) show examples for fitting the same results where the value for the time offset is shared. Table 3.3 show the results for fitting an example set of results using these techniques. The measured values for mass and length are extremely closely described by equations increasing as the square root of time. The root mean square residual for the combined fit to wicked length is 3.4, or on average 2.15% of the measured length. There is a tendency for the residuals to be larger at small times, but otherwise no dependence on time was observed. Requiring a shared value for the time offset results in slightly worse fits for the mass and length values. The offsets, however, are more reasonable. The length offset in the example is 12.7 mm compared with 8.7 mm, where the measured value is 15 mm. The time offset is 0.07 seconds for the combined fit, but in the separate fits the time offset for the mass is 18.7 seconds, which is unexpectedly long, and does not compare well with the time offset for the length results in the same experiment, of 2.9 seconds.

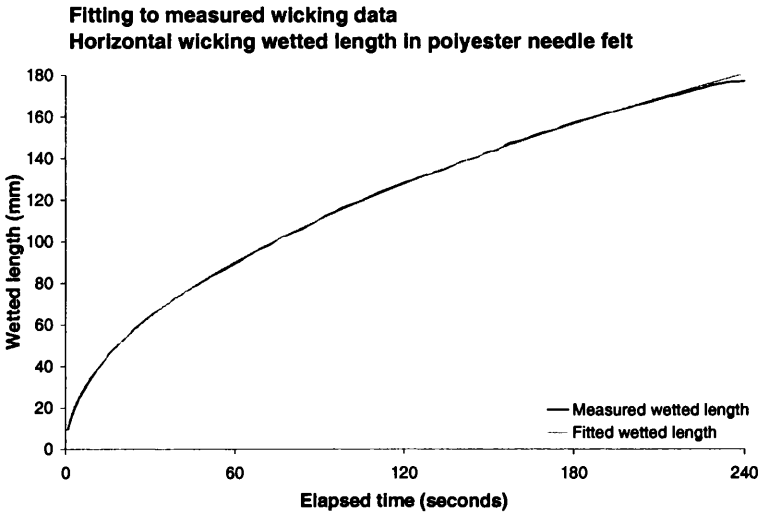

(a)

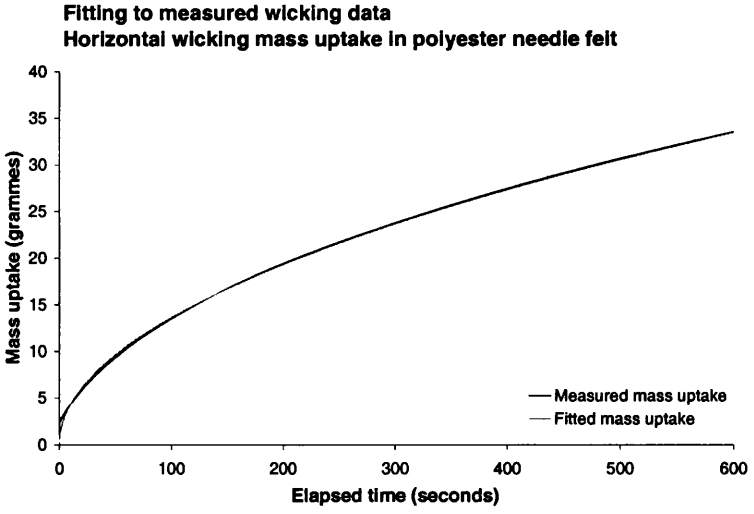

(b)

Figure 3.27: Example fitting of measured mass and length data, assuming wicking advances as $\sqrt{t}$. Wicking number and unknown time and mass offsets are fitted using Marquardt-Levenberg optimisation.

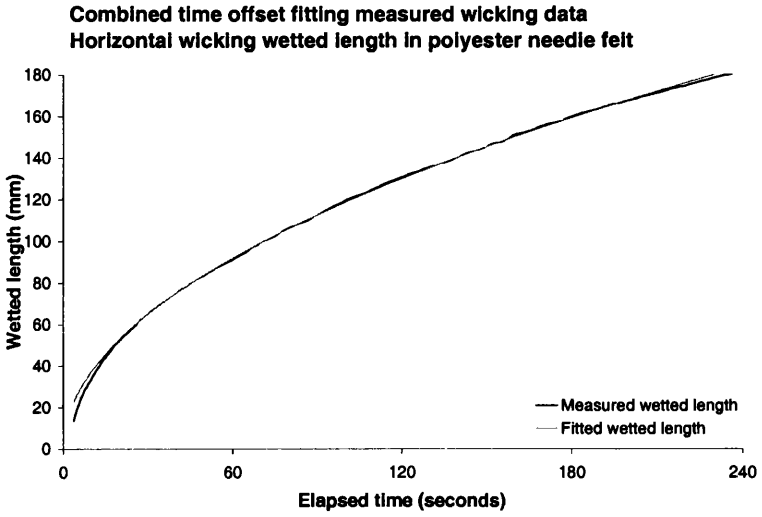

(a)

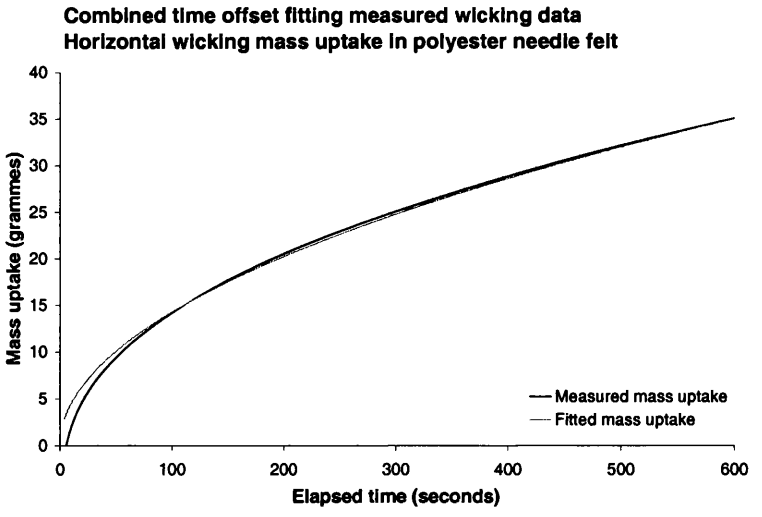

(b)

Figure 3.28: Example fitting of measured mass and length data, assuming wicking advances as $\sqrt{t}$. Wicking number and unknown time and mass offsets are fitted using Marquardt-Levenberg optimisation. Both the mass and length fitting are required to share the same time offset.

	K_l	l_0	t_0
Individual	11.66	-8.69	-2.89
Combined	11.87	-12.68	-0.07

	K_m	m_0	t_0
Individual	1.36	-166.3	-18.7
Combined	1.43	-168.41	-0.07

Table 3.3: Example fitting of measured mass and length data, assuming wicking advances as $\sqrt{t}$ and that the time offset for both mass and length measurements are the same. Wicking number and unknown time and mass offsets are fitted using Marquardt-Levenberg optimisation, across mass and length data sharing the same time offset.

Other researchers have used different methods to find the wicking number for a fabric. The most common procedure is to find a straight line fit to the wetted length plotted against the square root of time, or from a logarithmic plot of wetted length against time [203]. Alternatively, Washburn's equation can be written,

$$dl/dt = K\frac{1}{l} \tag{3.4}$$

where, l is the measured length, K is a constant, t is the measured time, The value of K can be derived from the slope of a plot of dl/dt versus $1/l$ [92]. .

3.9 Nonwoven microstructure

Together with apparatus to measure wicking, the microstructure of the fabric samples was examined. As discussed in section 2.2.1, a variety of direct and indirect techniques exist to characterise the structure of porous materials. Direct evidence of the structure of fabric materials can be obtained by examining prepared sample sections under a microscope. Carefully made microscopic measurements have the advantage of directly reflecting the physical structure of the material. Such measurements are easier to interpret in terms of the raw materials and manufacturing methods used than, for example, measurements of notional pore size.

Both optical and scanning electron microscopy have been used extensively to study textiles, and textile fibres [78]. Scanning electron microscopy offers superb resolution and depth of field. Figures 3.29(a), and 3.29(b) show scanning electron micrographs of the test fabric used in this research (Ledatec NP450P).

Although electron microscopy is ideal for looking at features such as fibre bonding or damage, it is difficult to make measurements of, and study the structure of the fibre

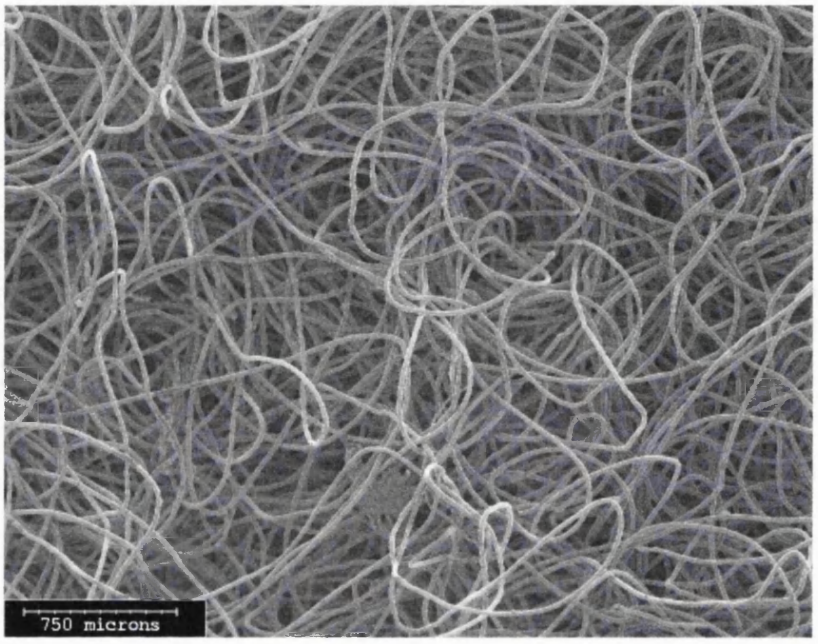

(a)

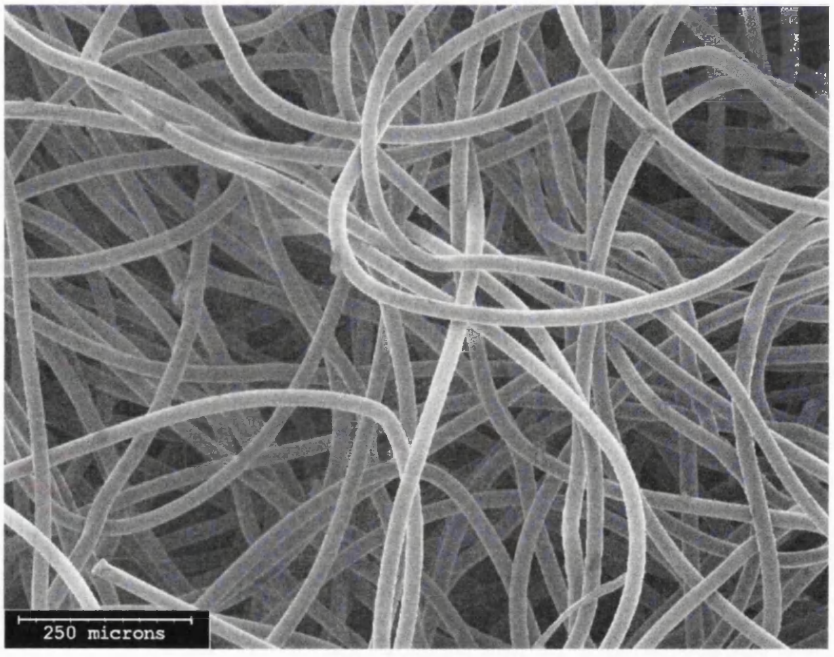

(b)

Figure 3.29: Electron micrographs of Ledatec nonwoven felt (NP450P), courtesy of Acordis

network. Analysis of the three dimensional structure of porous materials is, in most cases, made by looking at cross-sections through the sample (see section 2.2.3). A wide range of approaches are taken to obtain cross-sections through porous materials. Modern techniques allow three-dimensional nondestructive microscopic examination of many materials using micro-tomography [189, 190]; but the necessary equipment is expensive and not yet in common use. A more labour intensive, but well established technique for preparing cross-sections through materials is to grind and polish a section so that it can be examined under an optical microscope. Porous, or more delicate specimens are first encapsulated in a medium to enable them to be polished. Using this technique the spatial location of fibres within a fabric can be preserved, allowing representative cross-sections through the specimen to be examined and characterised.

To prepare a section the fabrics were mounted in a mould and embedded in casting resin. Once hardened the sample was removed and one face ground flat, close to the section of interest. The surface was then be polished until it was ready to be examined.

All cross-sections through the samples were taken perpendicular to the plane of the fabric, because the bulk of the liquid flow of interest occurs through this plane. In order to achieve this the sample had to be embedded upright in the mould, at right angles to its base. The fabric was supported while the resin set, by glueing the fabric samples to the base of the mould. Attaching string to the top of the fabric meant that the sample could be manipulated, and held vertically while the resin hardened, see figure 3.30. The sample itself could not be allowed simply to protrude above the level of the mould, because it wicked resin upwards, which disturbed impregnation and was difficult to remove before polishing the cross-section. The moulds and resin used were supplied by Struers. A two part room temperature fast cure epoxy resin was used (Struers SpeciFix-20).

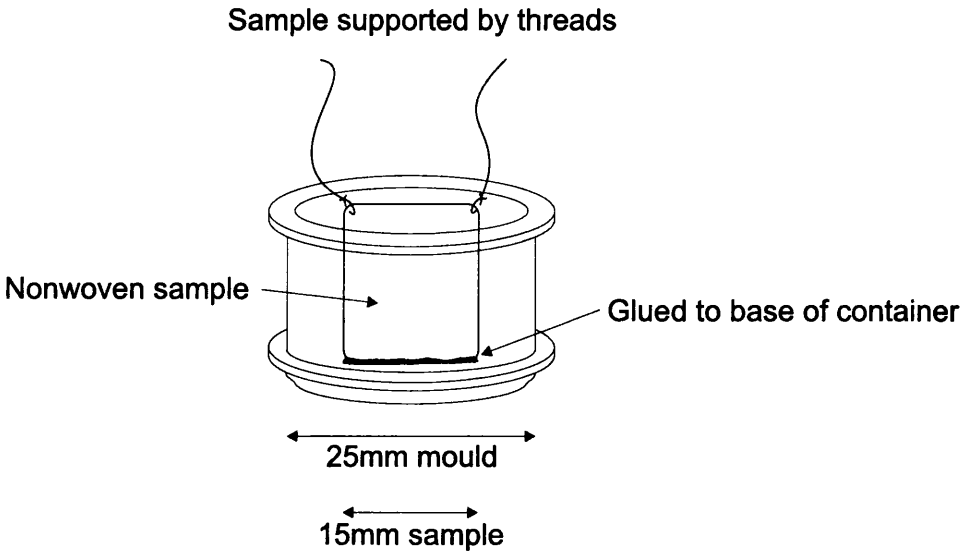

Figure 3.30: Fabric sample supported during encapsulation

Once the resin had hardened, a cross-section suitable for examination under a light microscope was produced. The encapsulated specimens were ground and polished using an automatic polishing machine (Struers Labapol 5 and Labaforce 3). Four grinding steps with SiC paper were followed by two polishing steps with polycrystalline diamond, a final polish was achieved using colloidal silica [208]. Details of the steps used to produce a polished sample are shown in table 3.4.

Abrasive	*Lubricant*	*Applied force*	*Speed*	*Time*
Grinding				
SiC Paper 220	Water	20 N	200 rpm	until plane
SiC Paper 500	Water	20 N	200 rpm	2-3 mins
SiC Paper 800	Water	20 N	200 rpm	2-3 mins
SiC Paper 1200	Water	20 N	200 rpm	2-3 mins
Polishing				
Cloth diamond 1 μm	Green	15 N	150 rpm	3 mins
Cloth diamond 3 μm	Green	15 N	150 rpm	3 mins
Colloidal silica 1-200 nm	Water	20 N	150 rpm	2-3 mins

Table 3.4: Details of polished sample preparation

Polished cross-sections were examined under a reflectance light microscope. An example, section from a polyester needle felt (Texon P6) is shown in figure 3.31. From this image the location of fibres where they intersect the section can be clearly seen. The section shown in figure 3.31 suffers from the inclusion of a number of voids, the larger of which can be clearly seen, caused by entrapped air formed during encapsulation of the sample. In order to prevent air bubbles becoming trapped in the fabric structure samples were encapsulated once the resin had been degassed. Once resin had been introduced the samples were formed under vacuum.

Following this procedure, a number of cross-sectional images of the Ledatec nonwoven (NP450P) were obtained, one such example is shown in figure 3.32. In these micrographs individual fibres can be seen where they intersect the plane of the cross-section. The amount of void space that exists between the fibres is striking. Degassing the resin has vastly reduced the inclusion of trapped air in the sample. The voids that remain mostly result from fibres that are pulled out of the cross-section by the polishing action.

It is also possible to identify some larger structures within the cross-sections, figure 3.33 shows a section through the entire width of the needle-felt, here the region where fibres have been displaced and interlocked as a result of the needling action can be seen. These features, caused in this felt by the penetration of a needle, are often refered to as z-pegs.

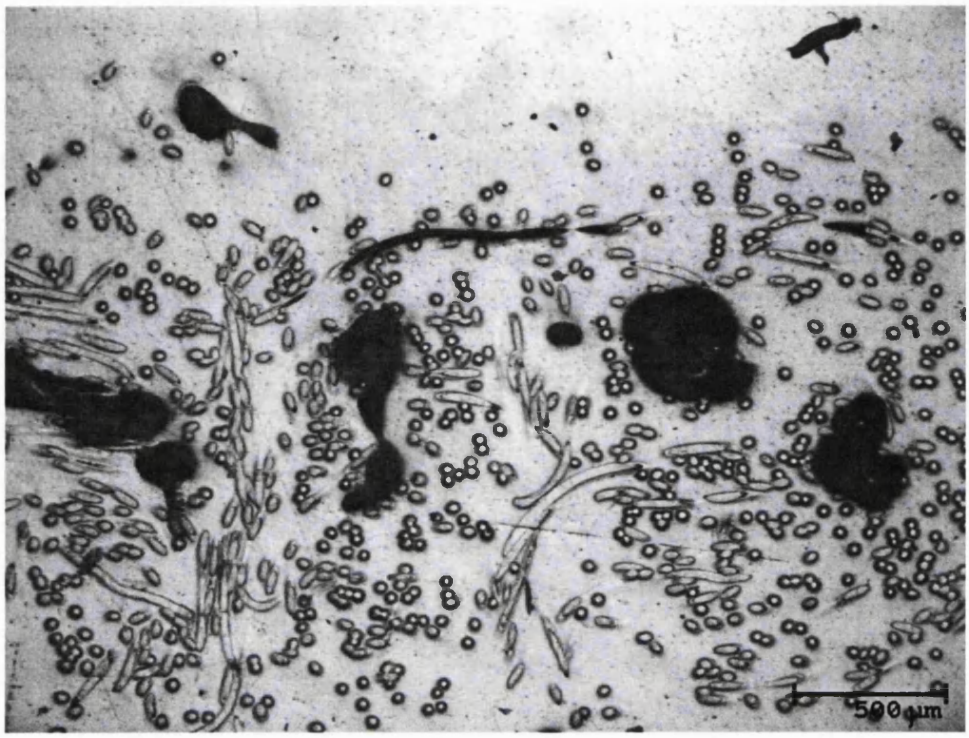

Figure 3.31: cross-section of sample fabric, showing inclusion of air bubbles

In the cross-sections shown so far the fabrics have only been made up of a single fibre size and type. Prepared cross-sections can be particularly revealing for fabrics made from a number of different fibres. For example, figure 3.34 shows a section through a nonwoven used as an industrial spillage fabric (supplied by Ledatec). This nonwoven fabric is made from different fibre types, and contains polypropylene, polyester, and viscose fibres.

3.9.1 Processing cross-sectional images

Characterising the micro-structure of a fabric requires a number of representative sections to be examined. Each section will contain a large number of fibres, and a method to characterise the features of interest must be chosen. Zhou *et al.* [225] looked at prepared sections and identified pores within the resulting images. The cross-section of each pore was considered to be a convex polyhedron and these were delimited between the fibres (see section 2.2.3). There are a number of problems involved in characterising a complicated three dimensional object such as a pore from a two dimensional cross-section (see section 2.5.4). The problems that arise in deriving a representation of the pore space is compounded in these fibrous materials, simply by the fact that the overwhelming majority of the material is void space. For these reasons it was decided instead to concentrate on identifying the fibres themselves; rather than the pore space they form. This has the advantage that the shape of the fibres crossing the cross-section is known. In the case of the

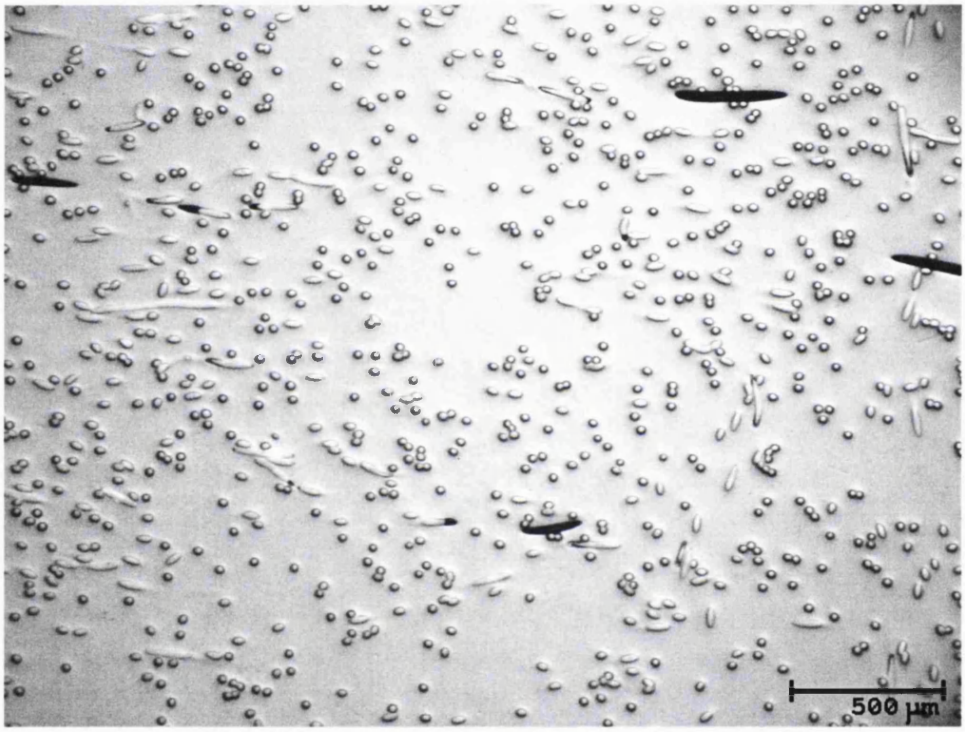

Figure 3.32: Example cross-sectional micrograph obtained through the sample fabric (NP450P)

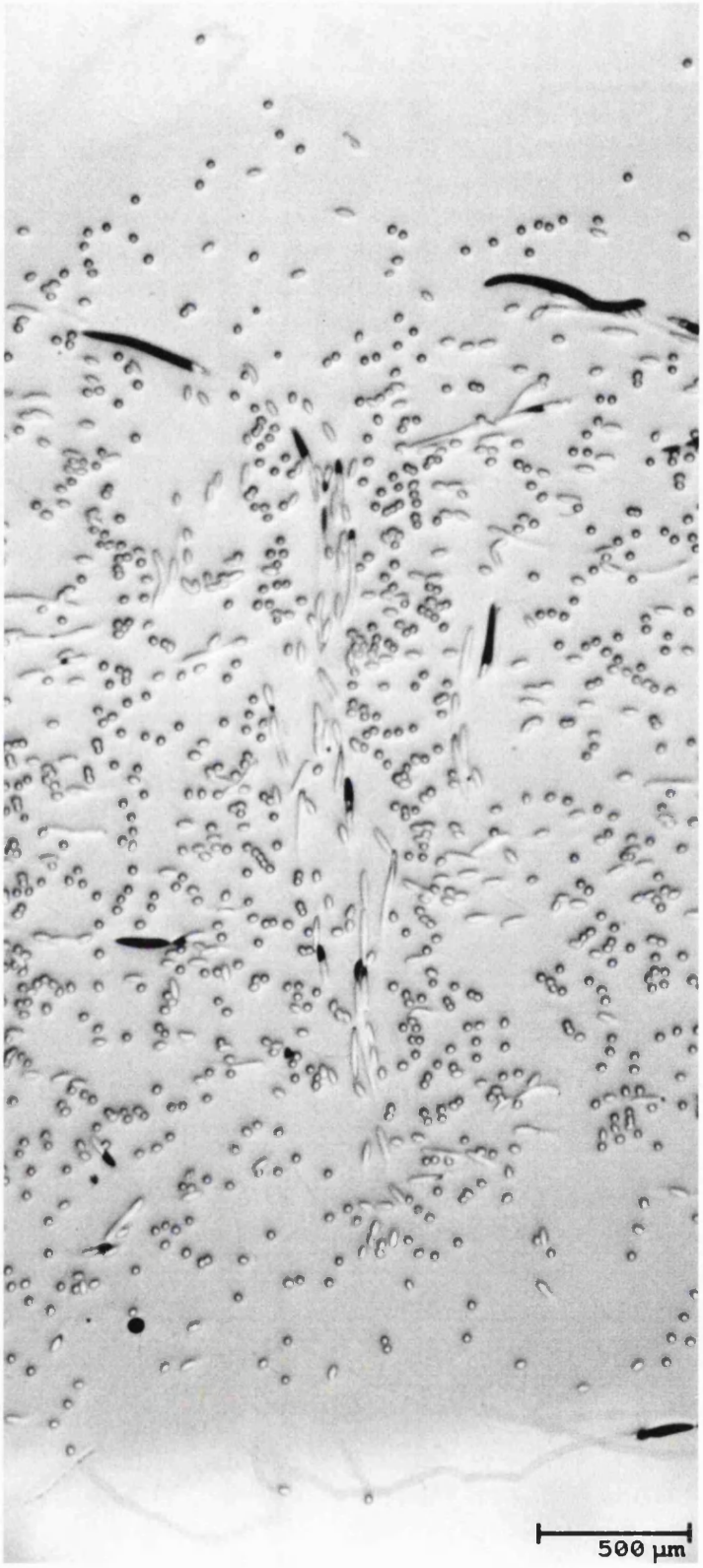

Figure 3.33: cross-section through the full thickness of the sample fabric (NP450P), showing a needle punch, or z-peg

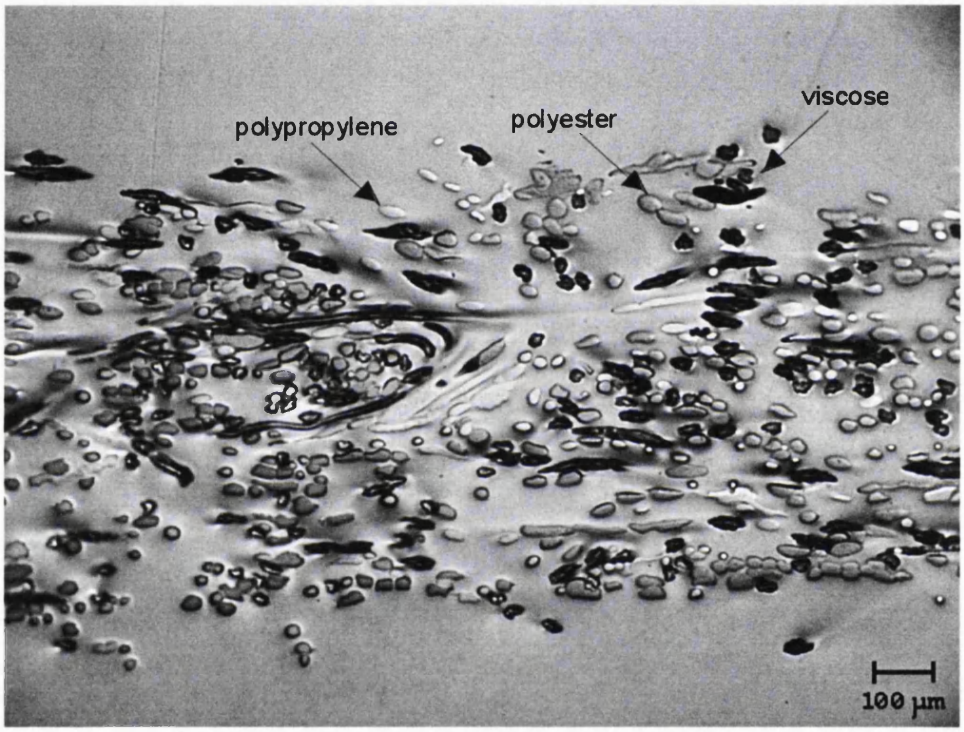

Figure 3.34: cross-section of Ledatec industrial spillage fabric, showing a mixture of fibre types (polypropylene, polyester, viscose)

fibres used in the primary test material (NP450P) the fibres were circular in cross-section and will mostly appear as ellipses where they intersect the cross-section.

The features to be identified in the cross-sectional images are the fibres. Ideally each fibre should be located and its shape specified where it crosses the section. Measurements of size on the images were made in pixel units, but converted into length values by calibrating the image capture using a stage-micrometer.

Given the large number of fibres in each section and the kind of measurements that are to be made it was desirable to find an automatic method for processing the cross-sectional images.

The first stage in processing was to sort pixels in the image belonging to the fibres from those pixels that make up the background. In the case of the images involving polyester fibres, the perimeter of the fibres was distinct from the background. Adequate segmentation could be found by finding minima points in the grey scale values for the images in any of three directions. Before processing the images, illumination correction was needed to compensate for the uneven illumination in the micrographs. A number of images of the polished section that did not have any fibres in were obtained and averaged together to find the necessary illumination correction.

The next step was to find groups of pixels that represent single fibres in the cross-section. Intuitively, this might be tackled by gathering together groups of adjacent pixels. In fact, where fibres are close together, pixels defining the perimeters of individual fibres merge and become shared, see figure 3.35(a). In addition the thresholding process inevitably excludes some pixels that should be selected as belonging to a fibre perimeter, see figure 3.35(b). These two situations alone mean that fibres cannot be recognised by simply finding groups of connected pixels.

Several approaches were taken, to trying to find fibres within the thresholded images. Template matching worked well to pick out a subset of fibres, but a large number of templates would be needed to find more than the most common shapes in the images. Edge following methods were used, combined with gradient information to define a direction around each fibre. Edge following coped well with unusually shaped fibres, and could be made to deal with small breaks in the perimeters; but large gaps in the perimeter and junctions formed where several fibres met proved difficult. The most successful group of methods tried were those based on ellipse specific fitting.

3.9.2 Ellipse specific fitting

A number of procedures have been developed to find ellipses within images, a review of which can be found in Davies [49]. The majority are based on some form of Hough transform, that is mapping between image space and a defined parameter space. The approach used here follows closely that described by McLaughlin [147], and proceeds by first finding candidate ellipses in the image:

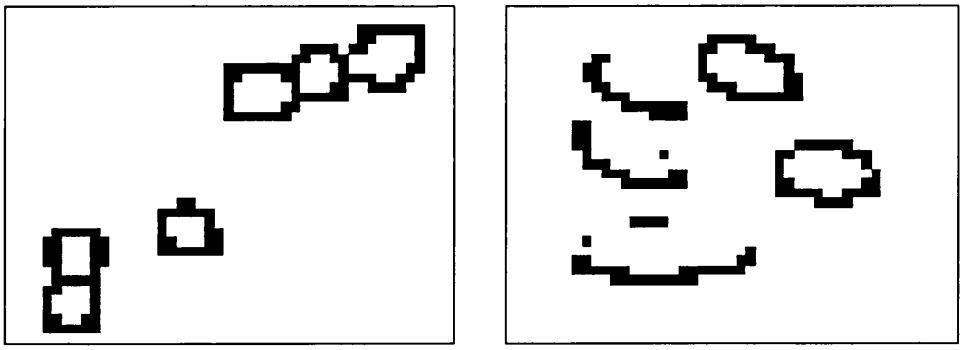

(a) (b)

Figure 3.35: Example of fibre perimeters taken from binary images of the nonwoven cross-section. The fibres in figure (a) are close together and pixels defining the fibre perimeters have become shared. In figure (b) large gaps have opened up in the fibres' outlines where the perimeter has not been detected. The situations shown in (a) and (b), both make automatic identification of the fibres difficult.

- Three pixels, assumed to lie on the perimeter of a single ellipse, are chosen at random from the image.
- Tangents are estimated for the lines local to each of the chosen pixels.
- The centre of the ellipse is then found using a feature of ellipse geometry: taking two points on an ellipse and finding their midpoint, if this midpoint is combined with the point at the intersection of the tangents – a line that passes through the centre of the ellipse can be found. Using two pairs of points from the three chosen points gives two lines that pass through the centre of the ellipse, and so provide an estimate as to the centre of the ellipse.
- The remaining ellipse parameters are estimated by translating the ellipse to the origin of the coordinate system, and solving the simultaneous equations that result from substituting the three chosen points into the general equation of an ellipse.

This method allows a possible ellipse to be generated from any three points chosen from the image (the remaining information comes from the estimates of the tangents).

By repeating the ellipse finding procedure a number of times on a group of pixels a list of possible ellipses are generated. A tolerance is defined in each of the parameters, within which two ellipses are assumed to be the same. A number of iterations of this procedure results in a list of different candidate ellipses. Each ellipse is examined to asses how likely it is that the ellipse represents a fibre in the image. To make a judgement for each fibre a score was generated by counting the number of pixels close enough to be part

of the ellipse, normalised to the length of the ellipse's perimeter. The ellipse scores are subject to minimum value before they are considered valid. The highest scoring ellipse in the list is then assumed to have been found, and its pixels removed from the image. The process is repeated until all pixels are assigned to ellipses, or no more ellipses can be found. Additional criteria are used to increase the liklihood that only ellipses that would result from fibres are identified. For example, the radius of the fibres is approximately known, and so one of the axes of any valid ellipse is required to be close to this value.

Since any valid ellipse will be relatively small, only pixels within a certain area need to be considered at any time. To apply this method to the thresholded images, the image is first divided into groups of pixels each of which is fitted separately.

The fitting procedure was implemented in Matlab, for which core code is included in appendix E.1.

An example of this method of ellipse fitting to a small area from a cross-sectional image is shown in figure 3.36:

- Figure 3.36(a) shows an example area from a micrograph of a cross-section from a sample of NP450P. Approximately 1/30 th of the area of the original cross-sectional image is shown.
- Figure 3.36(b) shows the thresholded image obtained from this area.
- Figure 3.36(c) shows the results of ellipse fitting overlaid on the binary image from which the fits were obtained.
- Figure 3.36(d) is the fitted ellipses, but overlaid onto the original sample from the micrograph of the cross-section.

3.9.3 Improving the ellipse fitting

The ellipse finding mechanism described works well for fitting ellipses to the thresholded images; particularly once judicious choices for valid and high scoring ellipse criteria have been made. There still remain, however, fibres that do not have corresponding ellipses correctly found, see figure 3.36(d). Equally, ellipses are inaccurately placed on the image without corresponding fibres. This means that the list of ellipses must be cleaned up, so an additional processing step is required. A further automatic processing step was considered, but in the short term the most efficient method to improve the fitted ellipses was to manually adjust the ellipse list. A graphical method to show the current list of ellipses, and overlay them on the captured image was developed. Figure 3.37(a) shows an example of the interface to this program. The central portion of the display lists the parameters of the fitted ellipses, which can be loaded or saved. This is attached to an image of the sample cross-section, over which each fitted ellipse is overlaid, figure 3.37(b).

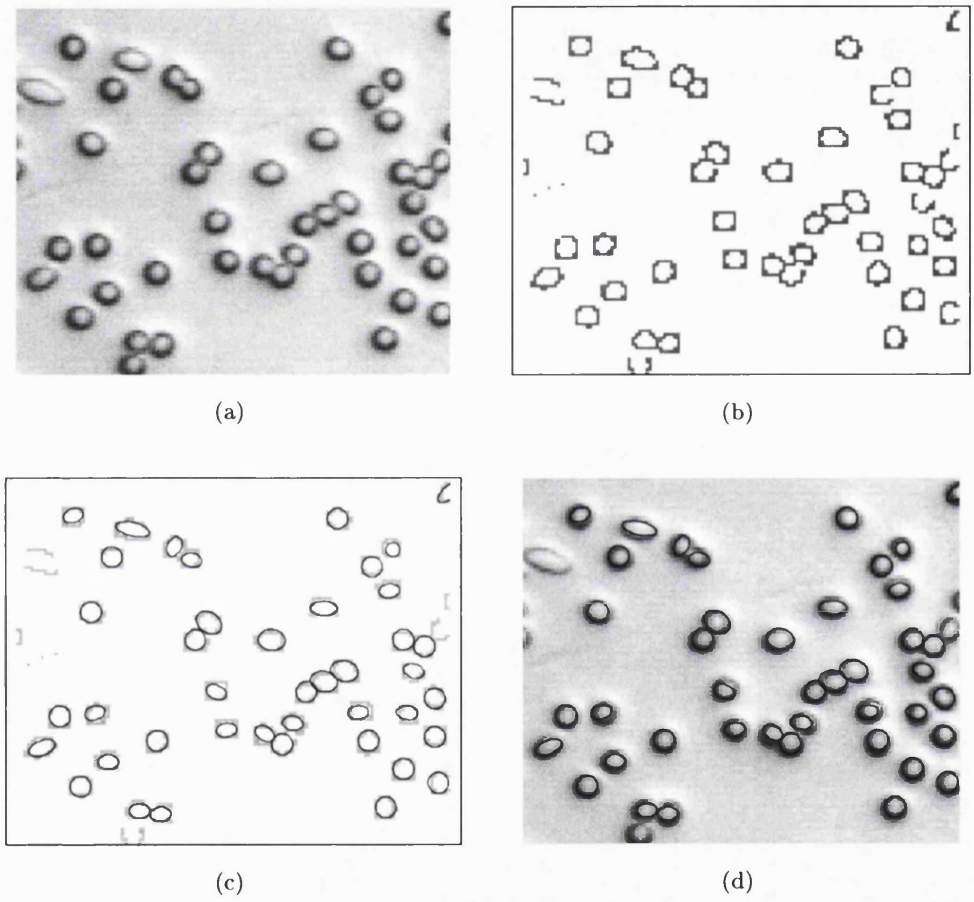

Figure 3.36: Fitting of ellipses to represent fibres crossing the section, using a sample area from a micrograph of NP450P

Ellipses are highlighted in the list directly, or by selecting locations in the image, and then removed. Additional ellipses can be added by selecting the centre of the new ellipse. The surrounding perimeter is then found from the nearest edges moving radially out from this centre point, and an ellipse fitted, figure 3.37(c). The new ellipse can be further refined by adding control points until it is of the desired shape. Alternatively, the ellipse can be fitted solely to selected control points. Finally, this new ellipse can be added to the list of fitted ellipses.

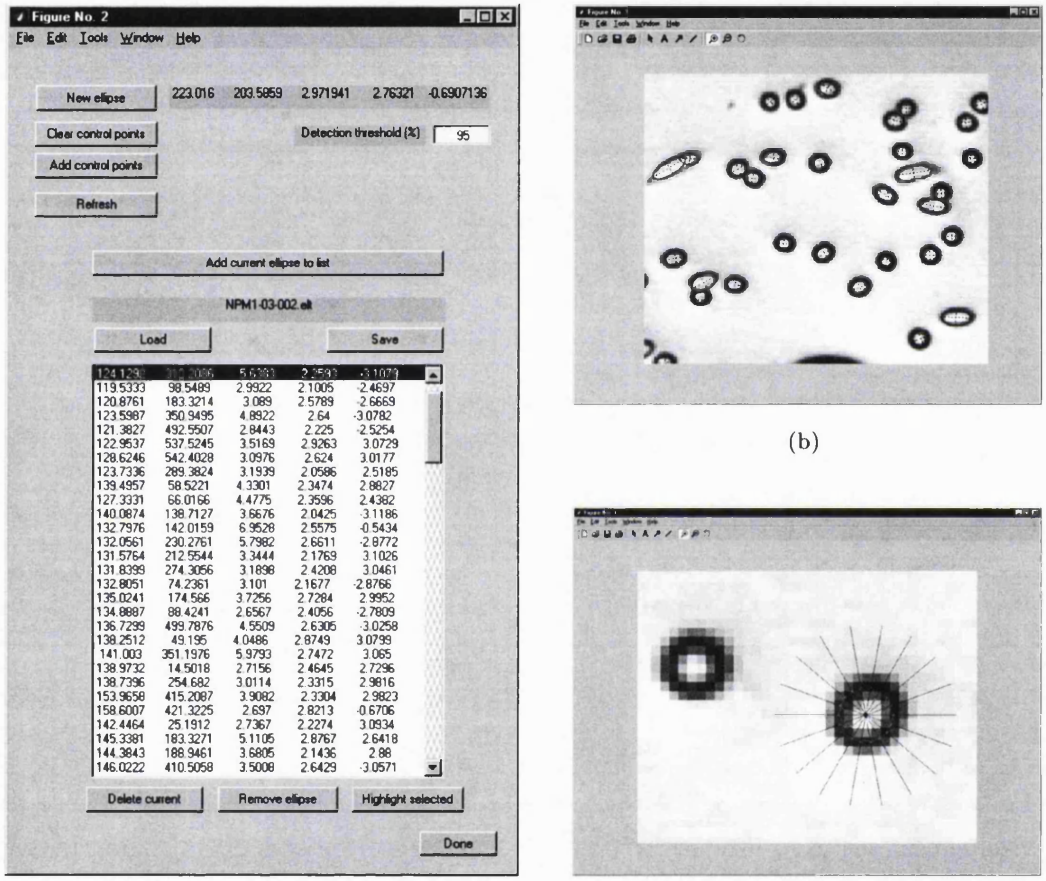

Figure 3.37: Examples of the user interface used to manually correct ellipse fitting to cross-sectional images

3.10 Fabric samples with varied properties

Creating a range of fabric test materials with controlled changes in their physical construction was found to be more difficult than expected. Bespoke nonwoven fabrics can be produced on a small scale using prototyping machines. There are, however, a number

Fibre type	*Fibre size*		
Needling degree	*1.7 dtex*	*3.3 dtex*	*5.0 dtex*
Polyester	**Code**		
Heavily needled	**P1**	**P2**	**P3**
Lightly needled	**P4**	**P5**	**P6**
Viscose			
Heavily needled	**V1**	**V2**	**V3**
Lightly needled	**V4**	**V5**	**V6**

Table 3.5: Overview of custom made needle felt nonwoven fabrics

of disadvantages that arise from small scale production. These difficulties were discussed in section 3.2, but are chiefly concerned with variations in material properties. For the planned experiments fabrics were needed in which, for example, average fibre spacings varied, or fibre decitex was different; but other properties of the fabrics remained the same. The nature of nonwoven felt production means it is difficult to produce materials that conform to these constraints.

It is not always possible to produce a nonwoven material directly from a specification based on physical properties, such as area density. In fact, predicting material properties from the manufacturing methods used to produce them is a topic of nonwovens research [188] with sophisticated techniques such as neural networks [27], and genetic algorithms [51] being investigated. In many instances changing one parameter in the manufacturing process for a needle-felt influences a number of the physical properties of the final material. For example, increasing the needling density leads to a more compact, thinner felt that is likely to have a higher area density, with more closely spaced fibres. Increasing the needling density also introduces more z-pegs into the structure which themselves can effect the wicking properties of the nonwoven. Indeed, manufacturing a felt to have a prescribed area density is often achieved by an iterative process.

Notwithstanding these complications, creating a selection of fabrics with specified features is a powerful way to investigate how changes in the porous structure affect the wicking characteristics of a nonwoven. Changing the construction of the material is the only way to explore the impact microstructure exerts on performance.

A limited range of bespoke needle felts were produced. Only a small number of fabrics could be made, and so small number of materials with sizable changes in their properties were chosen. Two fibre types, polyester and viscose, were used. Each of these fibre types were obtained in three fibre sizes, one of small decitex, one of large decitex, and one of intermediate size. Each of these fibre groups were then carded and needled to produce a nonwoven felt, either using very heavy needling, or very light needling. In all twelve fabrics were produced, as summarised in table 3.5.

These fabrics were produced, under supervision, using prototyping facilities at Texon UK Ltd [201], and fibres for producing the viscose fabrics were supplied by Acordis UK Ltd [2].

Measured quantities of fibres were laid out by hand, onto the feed of a Haigh-Chadwick sample card, as illustrated in figure 3.38 (see section 1.11.1). The carding process passes the fibres over a number of toothed rollers until a web suitable for needling is produced, see figure 3.39(b). After the fibres were formed into a web, the web was turned through a right angle and passed through the carding machine a second time to ensure good randomisation of the fibres. Two such webs were prepared and fed through the carding machine one after another in order to produce a final web with the desired fibre density. Two batches are needed because there is a limit on the weight of fibres the carding machine can process as a single batch.

The webs were then needled using a 0.6 m Dilo needle loom with 40 gauge needles. The web is first lightly tacked using a needle punch density (NPD) of 45 per square centimetre at 9 mm penetration. This needling machine has a down-stroking action, and so needling from both sides of the material was achieved by inverting the sample and passing it through the machine a second time. Figure 3.40, shows a sample as it is removed from the needling machine. The heavily needled fabrics were tacked and then needled again at 100 NPD and 6 mm penetration, passing the fabric through the machine three times, with a final pass at 100 NPD and 12 mm penetration. Fabrics were then trimmed and weighed to calculate their area density. If the area density was too far from the desired value (450 gm^{-2}) the fabric was remade, but with the initial weight of fibres adjusted accordingly.

3.11 Producing controlled nonwoven samples

To supplement the custom made fabrics experiments were also carried out using the standard test nonwoven (NP450P), but compressed to different thicknesses. By physically compressing the sample, the arrangement of fibres could be altered without greatly affecting other properties of the material. Deforming the sample in this way is not a perfect method for achieving the required change in the porous structure. Clearly, the sample thickness is reduced which might introduce some unwanted effects. The needling process tends to lead to samples that have some variation in fibre arrangement in the through thickness direction. A needle punch can have a lower fibre density around its entry point than at the bottom of the z-peg. Such a sample, when compressed might have properties that are dominated by particular regions in the material.

Compression not only provides a good experimental method for producing range of materials with different microstructure, but is also functionally important in many nonwovens. Geotextile materials are used in building and construction work together with earth and aggregates. In these situations the geotextile often acts to prevent mixing be-

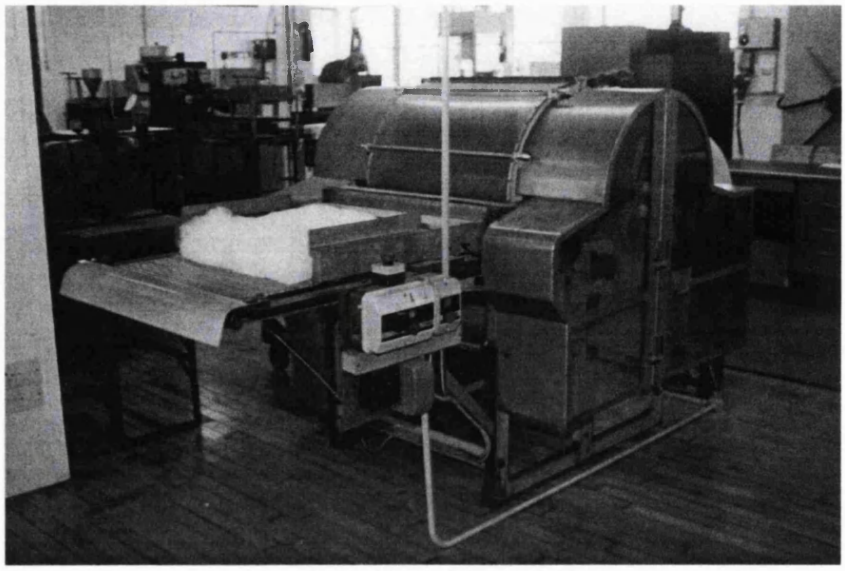

Figure 3.38: Carding machine, showing fibres laid out on the feed roller ready for carding. (Texon UK Ltd, pilot plant). The fibres can be seen stacked on the feeder roller, ready to be carded into a fibre web.

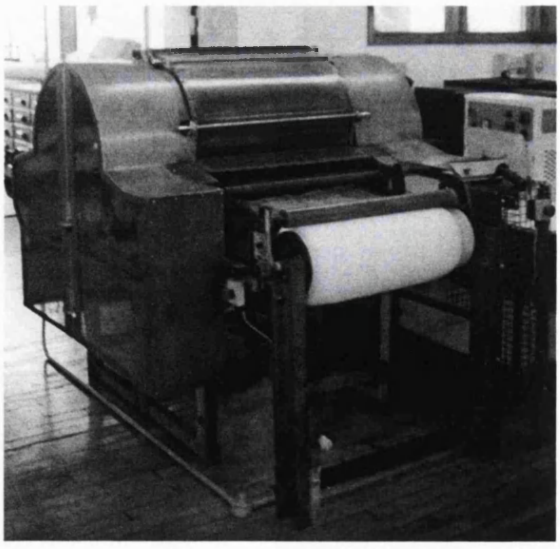

(a) Prepared web is collected on final roller.

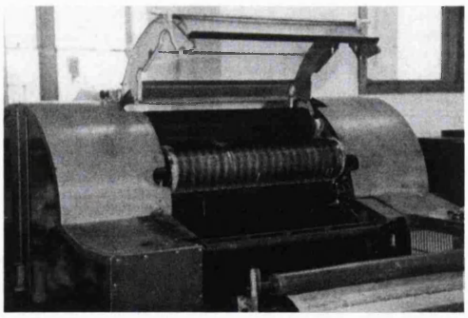

(b) Detail showing the topmost toothed rollers that perform the combing process to lay the fibre web.

Figure 3.39: Carding machine, showing the fibre web as it is removed from the toothed rollers, and collected as a lightly consolidated web. (Texon UK Ltd, pilot plant).

Figure 3.40: Needle loom, showing collection of needled fabric. (Texon UK Ltd pilot plant).

tween layers of soil whilst still allowing drainage. For geotextiles this intended use, as a subsurface layer, will mean the hydraulic properties of interest will often be for the nonwoven in a compressed state. Incontinence products can also be subject to local regions of compression, where the product comes between the user and their bed or chair. Although under normal circumstances these local deformations in the absorbent structure are expected to be small (of the order of 10%).

Possibly the biggest disrupting influence, though, arises from the mechanism used to compress the sample. In order to measure wicking using the image capture process described the fabric samples were compressed using a pair of clear Perspex^{TM} plates. This is similar to the method used by Neederveen [161] to prepare a wedge of fluffed wood pulp, (see section 2.7.5).

Twenty millimetre thick Perspex^{TM} plates were used for this experiment to resist bowing at high compressions. Preliminary experiments had shown that six millimetre plates suffered from considerable distortion when squeezing the sample. Plastic shim material was used to separate the plates to form a sample of known thickness. A compression cell was then formed by bolting the plates and shims together, the bolts were passed through the shims to further reduce bowing of the plates. Evenly distributed compression was achieved by gradually tightening the bolts using a torque wrench, finally applying 15 Nm to each. A feeler gauge was used to ensure the plates were evenly clamped together, leaving no gaps. Figure 3.41 shows the arrangement of a nonwoven sample for wicking within the apparatus. The compression cell held the fabric in exactly the same configuration

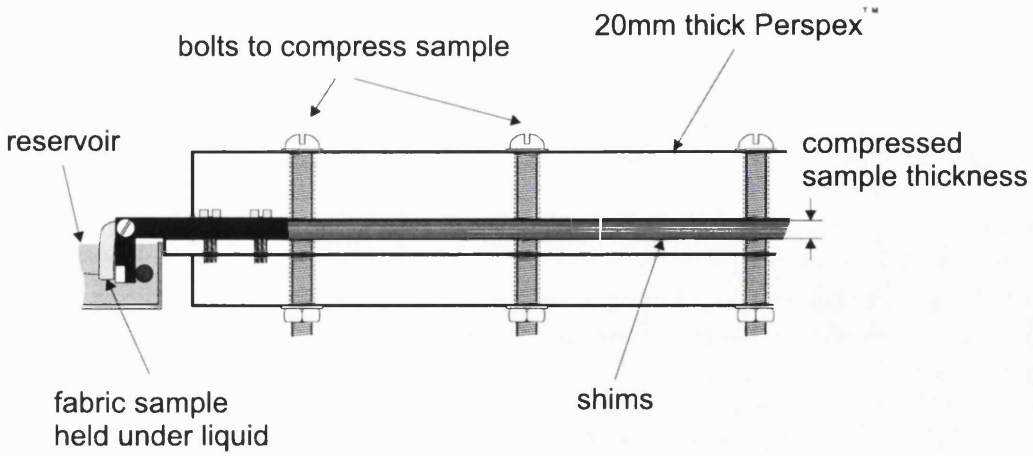

Figure 3.41: Diagram showing compression of a nonwoven sample using Perspex plates separated by shims. Note the reuse of the front portion of the holder to hold the sample in the reservoir.

as did the original support. The cell itself was designed to fit into the same supporting framework, and used the same mechanism as the original wicking apparatus to hold the wetted end of the fabric. Full plans for the compression cell are shown in the appendix D.10. Figure 3.42 shows a sample placed in the compression cell.

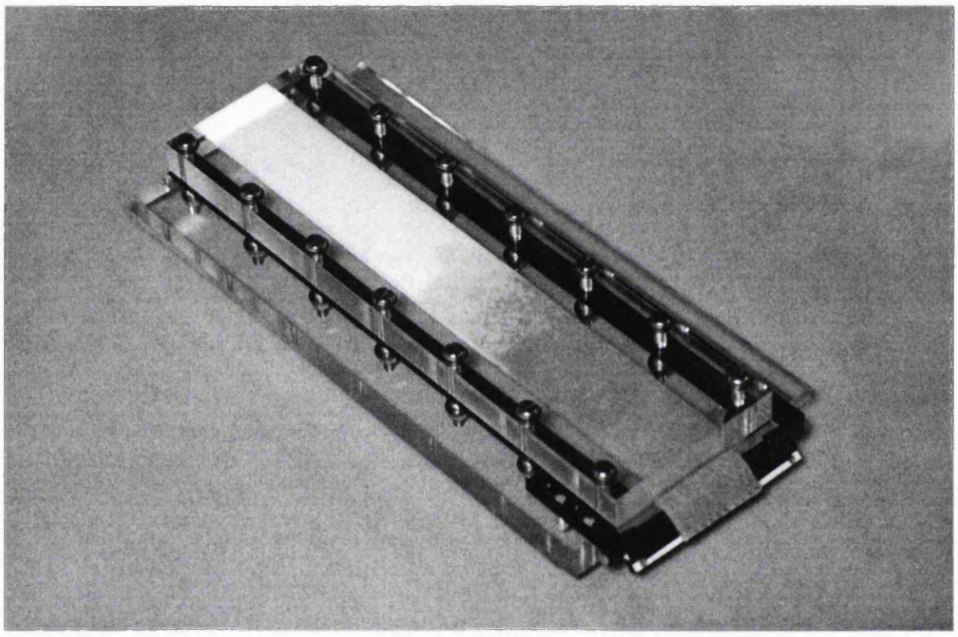

Figure 3.42: Photograph of the compression cell, containing a nonwoven sample.

Chapter 4

Experimental results

A method for measuring wicking under a range of conditions has been devised and its performance characterised. A simple nonwoven felt was obtained and a method was established to examine the structure of fibrous materials. Using these techniques a series of experiments were performed, primarily to evaluate simple wicking models under particular conditions. Where possible the parameters contained in the simple model were measured for the sample materials used.

- A range of bespoke nonwoven felts were prepared to study the effect on wicking of different fibres and manufacturing parameters.
- The effect on the rate of wicking caused by changes in the liquid-solid interfacial energy were examined. When designing a product intended for end use with a particular liquid, the interfacial energy is altered by selecting different fibre types, or by applying surface finishes to the fibres. It is difficult, though, to achieve a uniform distribution of finish over the fibres, as results from instruments such as the scanning wetting balance have shown [105]. For experimental purposes it is more reliable and easier to change the properties of the wicking liquid to investigate changes in interfacial energy.
- Angled wicking experiments, were performed to look at the effect inclining the sample from the horizontal had on wicking performance. Understanding the impact geometry has on wicking performance is important in the design of incontinence products. Absorbent pads have to conform to the user's body shape and it is important that their effective absorbency is not reduced.
- The physical arrangement of the constituent fibres is crucial in determining the wicking characteristics of a fibrous material. The processes used to manufacture nonwoven felts make it difficult to alter a single aspect of fibre arrangement without altering other properties of the final material. For this reason the fibre arrangement

within a single nonwoven sample was altered in a controlled manner by compressing it, allowing the changes this produced in the wicking performance to be explored.

This series of experiments focused on tackling a number of the elements that feature in simple descriptions of wicking such as Washburn's equation (equation 2.11). The results from these experiments were intended to verify whether or not simple wicking descriptions adequately capture the influence factors such as contact angle or capillary radius have on wicking performance in relation to nonwoven felts.

This chapter deals with the results from the above series of experiments, using the methods described in the previous chapter. To investigate the validity of simple capillary models the fundamental parameters such as liquid-fibre contact angle are measured. The microstructural component of the capillary model is obtained from cross-sections through the felt samples.

4.1 Experiments using custom made samples

A number of nonwoven samples were made using prototyping apparatus at Texon UK Ltd (see section 3.10). Samples were produced from two fibre types, in three fibre sizes. Both heavy and light needling processes were used to manufacture needle felts. The fabrics were produced to a specified area density of 450 gm^{-2}. Table 4.1 summarises the fabrics that were made together with the actual area densities achieved.

Initial wicking experiments revealed that none of the polyester samples were able to wick water. A surface finish appeared to have been applied to the fibres that changed the water-fibre contact angle to such an extent that spontaneous wicking did not occur. The wicking experiments were all carried out using only the viscose samples.

Cross-sections through the viscose samples were prepared, example micrographs of which are shown in figure 4.1. These cross-sectional images not only clearly show the different fibre sizes used, but also the reduction in inter-fibre spacing that results when the samples are more heavily needled.

Ellipses were fitted to describe the fibres in each of the cross-sections. Taking the radius of the fibre to be the minor axis of each fitted ellipse, the fibre radius can be estimated from the cross-sectional images. Figure 4.2 shows a comparison between the fibre radius measured using the cross-sections and the fibre radius estimated from the decitex, assuming the fibres to be cylindrical. The fibre radius measured from the cross-sections is in all cases a little larger than would be expected from the linear density of the fibre. This may be attributed to the fact that the viscose fibres are not in fact cylindrical. An over estimation might also be caused by the polishing process which has a tendency to leave the ends of the fibres a little above the surface of the encapsulating material, leading to problems identifying the edge of the fibre.

(a) V1, 1.7 dtex viscose fibres, lightly needled felt

(b) V4, 1.7 dtex viscose fibres, heavily needled felt

(c) V2, 3.3 dtex viscose fibres, lightly needled felt

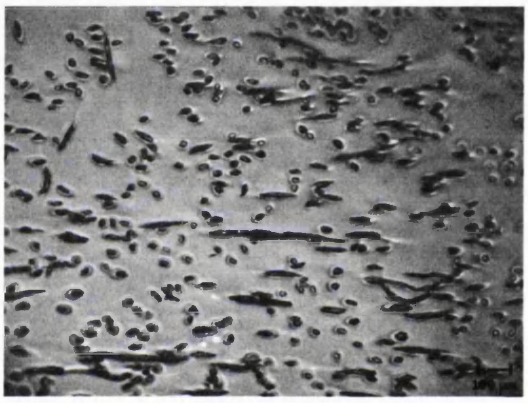

(d) V5, 3.3 dtex viscose fibres, heavily needled felt

(e) V3, 5.0 dtex viscose fibres, lightly needled felt

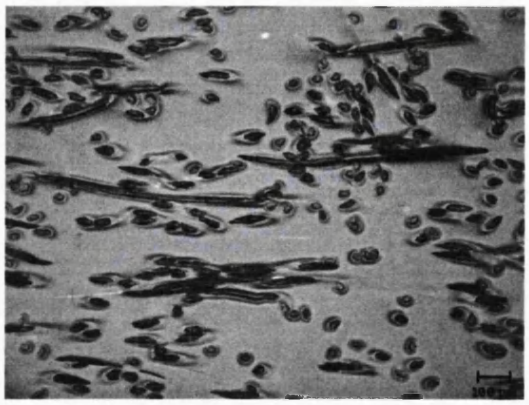

(f) V6, 5.0 dtex viscose fibres, heavily needled felt

Figure 4.1: Epoxy micrographs of polished cross-sections through viscose samples, produced using three fibre types and two needling regimes (V1-V6)

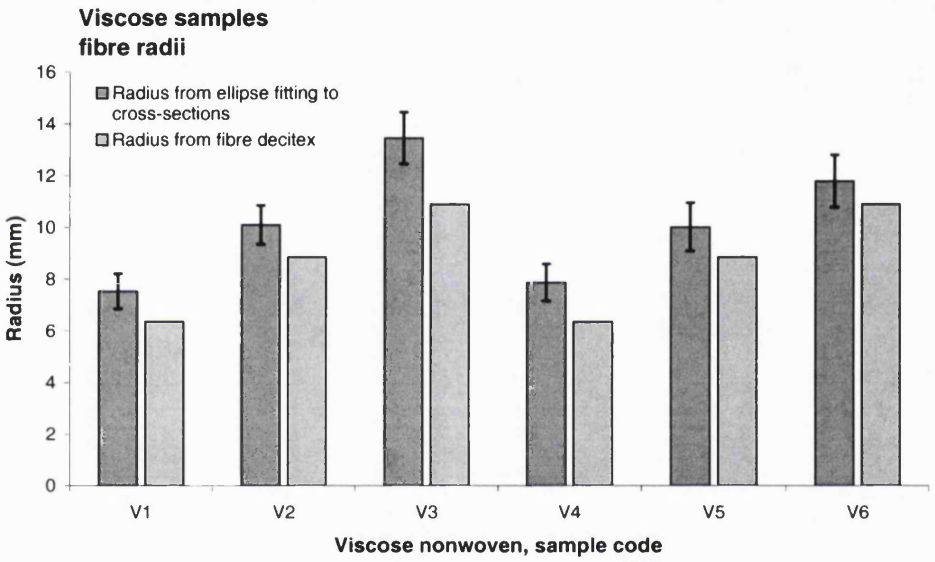

Figure 4.2: Estimates of the fibre radius measured by examining polished cross-sections of custom made fabrics compared with the fibre radius obtained from the linear density of the fibres.

Sample	*Fibre type*	*Fibre dtex (dtex)*	*Needling density (cm^2)*	*Area density (gm^{-2})*	*Thickness (mm)*	*Fibre volume fraction (%)*
P1	Polyester	1.7	45	433	5.5	5.66
P2	Polyester	3.3	45	433	6.2	5.02
P3	Polyester	5.0	45	425	6.5	4.70
P4	Polyester	1.7	100	427	3.3	9.31
P5	Polyester	3.3	100	438	3.0	10.50
P6	Polyester	5.0	100	402	3.0	9.64
V1	Viscose	1.7	45	486	4.9	5.76
V2	Viscose	3.3	45	450	4.9	6.12
V3	Viscose	5.0	45	401	5.4	5.40
V4	Viscose	1.7	100	483	3.5	9.81
V5	Viscose	3.3	100	454	3.6	8.47
V6	Viscose	5.0	100	414	3.0	8.31

Table 4.1: Details of nonwoven samples fabricated to reflect heavy or light needle density production using different fibre sizes and types.

Wicking measurements were made using the viscose fabrics (V1-V6). A chart of horizontal wicking in each of the viscose felts is shown in figure 4.3. Overall the samples produced using a higher needling density wick faster than those produced using a lower needling density. For the higher density fabrics it is difficult to separate the wicking rates considering the size of the expected measurement errors. Of the lower density fabrics the fabric with the small radius fibres appears to wick liquid faster than the other samples.

Measurements of vertical wicking were made for the viscose fabrics, and the relationship between wicked height and time is shown in figure 4.4. The fabrics made from lower decitex fibres wick higher than fabrics made from larger fibres. Fabrics produced using a higher needling density have an equilibrium height advantage over the samples made using lower needling densities. For the samples tested, higher equilibrium wicked heights are seen in the samples with higher fibre fractions.

Using the list of ellipses fitted to a cross-sectional image through each viscose fabric, the wetted perimeter in a cross-section through each of the fabrics was estimated.

The equilibrium height rise of liquid in the fabrics can be treated by looking at energy changes that take place during capillary motion, (see section 2.4.2). The capillary pressure can be estimated by considering the energy changes that take place when a the fibre-air interface in a cross-section is replaced by fibre-liquid interface.

$$P_s \simeq \frac{\gamma \cos \theta p}{A_{flow}} \tag{4.1}$$

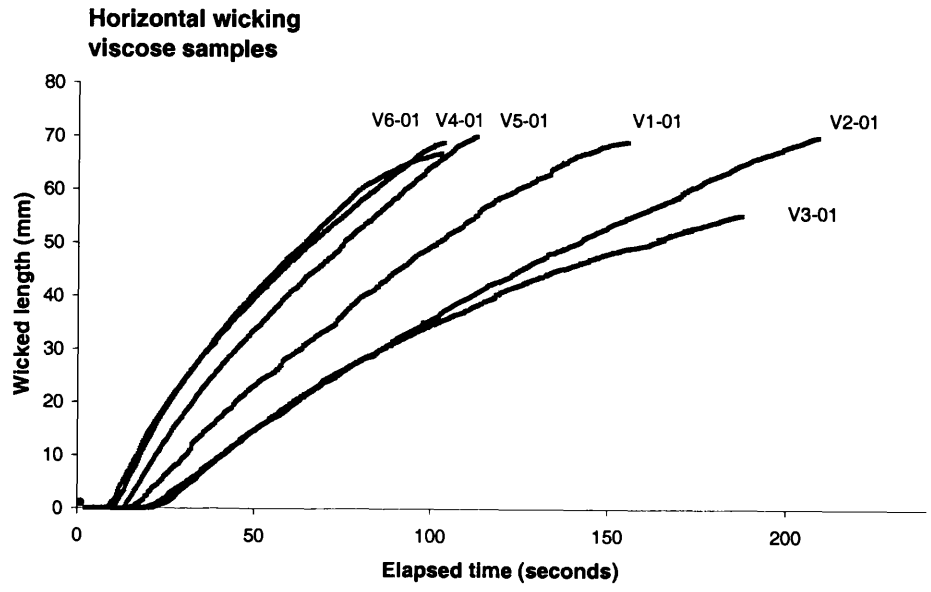

Figure 4.3: Horizontal wicking for custom made viscose felts in free air

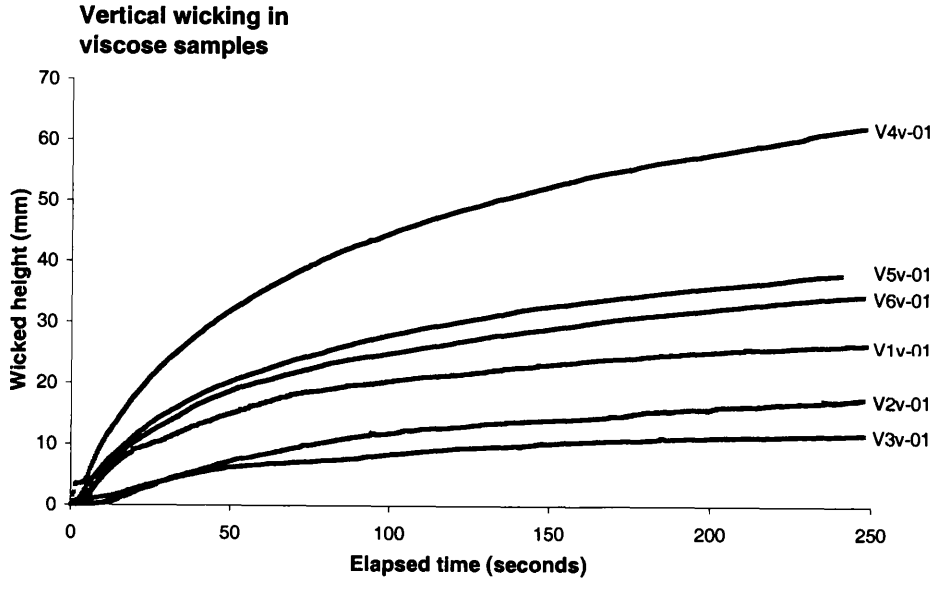

Figure 4.4: Vertical wicking for custom made viscose felts in free air

where, P_s is the capillary pressure, γ is the surface tension of the liquid, θ is the liquid-fibre contact angle, p is the wetted perimeter in the cross-section, and A_{flow} is the area in the cross-section over which flow occurs.

When vertical wicking reaches equilibrium, the net force on the liquid is zero, and the equilibrium height can be expressed as:

$$h_{eq} = \frac{P_s}{\rho g} \tag{4.2}$$

where, h_{eq} is the height of equilibrium capillary rise, P_s is the capillary suction pressure, ρ is the density of the wicking liquid, and g is the rate of acceleration due to gravity.

The water-fibre contact angle was not measured for the viscose fibres, and so had to be estimated by fitting to the experimental values for one of the viscose samples (V1). Using this method, the contact angle was found to be 64°, where a value of between 0° and 60° can be considered reasonable [88]. Although the value found for the contact angle is higher than expected, viscose exhibits a wide range of contact angles and the fitted angle is not far outside this range. Owing to the assumptions made when finding the contact angle it is likely that the influences of, for example fibre swelling, are included in the angle found. Figure 4.5 shows the masses of liquid imbibed by the samples at equilibrium, together with predictions for this mass based on the wetted fibre perimeter at the liquid-air interface and fitted value for the water-fibre contact angle. For these viscose samples, the wicked heights are proportional to the total fibre perimeter found in a cross-section.

4.2 Wicking experiments using a simple nonwoven

The following experiments were conducted using a single nonwoven material, Ledatec NP450P. This material was selected to have a simple fibre type and structure. Before making wicking measurements, the relevant physical properties of the sample, and its liquid interaction, were measured. The solid-liquid interaction is largely determined by measuring the surface tension of the wicking liquid, and the contact angle formed between the liquid and fibre surface. The effect on wicking performance of changes in the liquid-fibre interfacial energy was explored by using a range of liquids. Water and propan-2-ol are mutually miscible over the range of interest and were used to produce a small number of wetting liquids having different liquid-fibre interfacial properties. The primary wicking liquid used was water, and so careful measurements of surface tension and liquid-fibre contact angle were made in water, along with measurements for the chosen range of water-alcohol solutions.

Surface tension was measured using a duNuoy tensiometer (see section 2.3.4). The duNuoy apparatus measures the force required to move a flamed platinum ring through a sample of the liquid. The measured values for surface tension are displayed in the chart shown in figure 4.6. The measured value for the surface tension of water was 73 mN/m

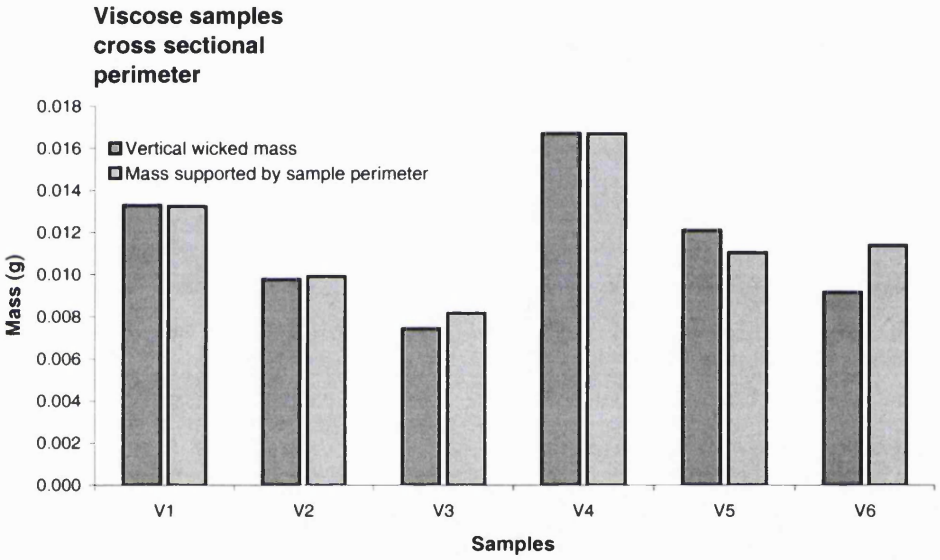

Figure 4.5: Vertically wicked mass for each viscose fabric, compared to predicted wicked mass from wetted fibre perimeters determined using polished cross-sections.

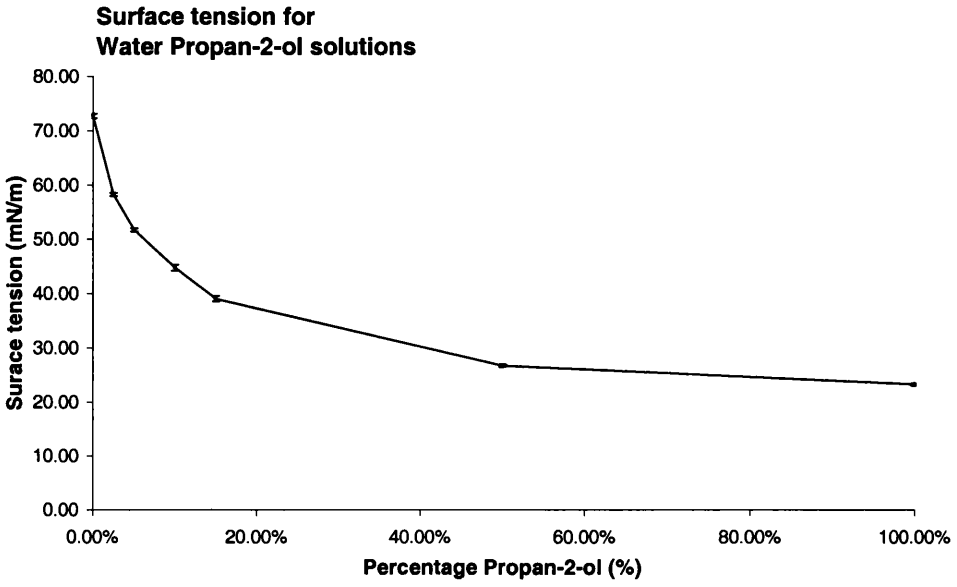

Figure 4.6: Measurements of surface tension for water propan-2-ol solutions (n=10 for each solution, errors indicated are ± one standard deviation, derived from experimental repeats).

(± 0.2 mN/m, n=10), compared with an established value of 71.99 mN/m at 25 °C [129]).

Measurements of contact angle for each of the wicking liquids were made using a dynamic method based on the Wilhelmy wetting force principal (see section 2.3.4). This method is particularly suitable for measuring dynamic contact angles on single fibres. Before calculating the liquid-fibre contact angle from measurements of the wetting force the fibre perimeter must be known. The decitex of the fibres was measured using a vibroscope [160, for example]. Twenty fibres were selected and five measurements of decitex made for each. The mean measured decitex using this method was found to be 6.27 dtex (± 0.528, n=18).

A commercial instrument, the CAHN [35] model 322 dynamic contact angle analyser (DCA) was used to measure liquid-fibre contact angle [58]. An electro-balance records the force on a single fibre held in a fixed position. The wetting liquid is contained in a beaker and placed on a computer controlled stage, which allows the liquid surface to be scanned along the fibre's length at a constant speed. Initial calibration of the balance was performed using a known 500 mg mass. Each measurement used 50 ml of wetting liquid, with the platform set to travel 15 mm at a rate of 151 μm/s. Contact angle measurements were made in two directions, initially advancing the liquid over the fibre surface as the

stage is moved upwards, followed by receding the liquid over the previously wetted surface as the stage descends. The chart shown in figure 4.7 shows an example of the force readings obtained with the DCA, measuring both advancing and receding contact angles. To analyse these results the user is required to identify on the chart regions containing the advancing and receding slopes. Measurements of contact angle were made for both distilled water and five solutions containing water and propan-2-ol. For each solution ten measurements of contact angle were made and the results are shown in figure 4.8. The measured advancing fibre-liquid contact angle for water was found to be 69.2° (±6.85°, n=10). The receding contact angle in these experiments was found to be 54.7° (±6.03°, n=10). The advancing angle for these fibres is comparable with the value of 75° for advancing water contact angle on polyester fibres measured using a Wilhelmy balance apparatus by Miller [153].

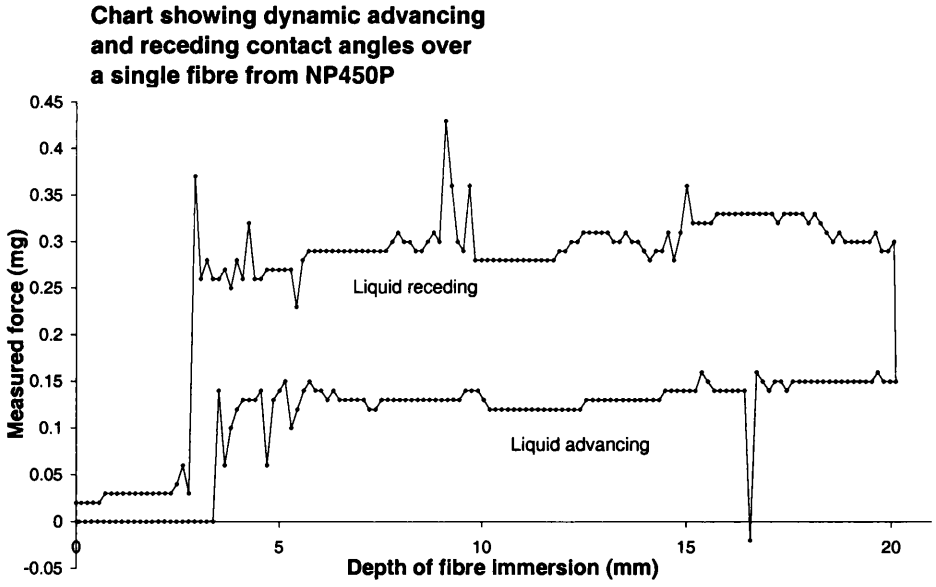

Figure 4.7: Example results of force measurements and fibre immersion depth using Cahn 322 DCA. A single fibre from the Ledatec NP450P nonwoven felt is suspended from the electro-balance, and progressively immersed in a liquid using a computer driven stage.

Fibre staple length was estimated by randomly selecting fibres, removing them from the nonwoven and measuring their length on an oiled board. The staple length measured using this method was 73.7 mm (± 3.90 mm, n=20).

Cross-sections through the NP450P felt were prepared by encapsulating and polishing the sample. Twelve fields of view were analysed in two cross-sections. Ellipses were

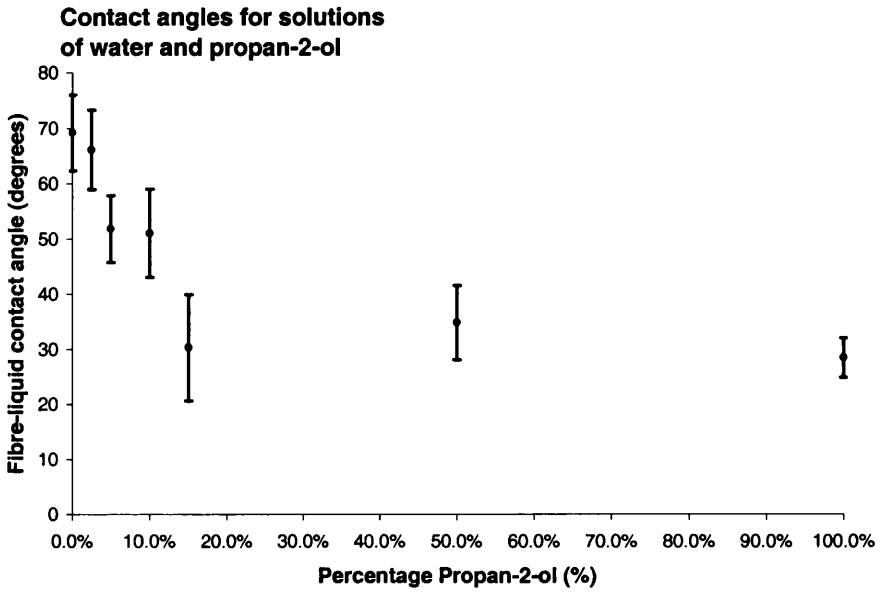

Figure 4.8: Graph of advancing contact angle for single fibres of NP450P measured using the Cahn DCA with propan-2-ol solutions (n=10 for the 0%, 2.5%, 5%, 10%, 15% solutions, and n=5 for the 50% and 100% solutions errors are $\pm$ one standard deviation, derived from experimental repeats.)

fitted to the images using the method previously described (see section 3.9.1). An average of 961(± 130, n=12) ellipses were found in each field of view, where the field of view was 3.20 mm by 2.42 mm. The automatically detected ellipses were manually corrected in each case, an average of 10.4%(± 1.98%) of the detected ellipses were removed and 11.5%(± 2.61%) of the finally placed ellipses were manually added.

The total fibre perimeter in a 50 mm wide sample perpendicular to the wicking direction was found to be 2.46 m (± 0.355 m). The mean minor axis of the fitted ellipses was 10.8 μm (± 0.21 μm), which compares well with the radius calculated from the fibre's decitex. Where the density of polyester is taken as 1.39 g/cm^3 [160] the measured decitex implies a fibre radius of 11.98 μm (± 0.49 μm).

The physical properties for the sample fabric, Ledatec NP450P, are summarised in table 4.2.

Fibre properties			
Material	*decitex*	*Staple length*	*Water contact angle*
Polyester	6.27 dtex (± 0.528)	73.7 mm (± 3.90)	69.2° (± 6.85)
Nonwoven properties			
Thickness	*Area density*	*Fibre vol. fraction*	*Fibre perimeter*
4.2 mm (± 0.91)	535 gm^{-2} (± 89.3)	9.1% (± 0.24)	11.7×10^{3}m m^{-2}

Table 4.2: Physical properties of NP450P sample

4.2.1 Wicking using solutions having different interfacial properties

Horizontal and vertical wicking measurements were made using the wicking apparatus with each of three propan-2-ol and water solutions. The chart in figure 4.9 shows example results for horizontal wicking using each solution. These experiments were intended to investigate changes in contact angle between the fibres in the nonwoven sample and each of the solutions. For this reason wicking was only measured in 5%, 10%, and 15% propan-2-ol solutions, as these cover a range of contact angles from 52° to 30°. Unfortunately the change in the viscosity and surface tension of the solutions was found to be more significant than expected.

The viscosity of each solution was measured using an Ostwald viscometer. This viscometer measures the time taken for each solution to pass through a narrow bore tube. The viscosity of each solution was then calculated from the time taken for the solution to flow through the tube compared with the time taken by a liquid of known viscosity, in this case water. The viscosity in the 15% propan-2-ol solution was 1.44 mPa s (± 0.03, n=10), where the viscosity of water was taken to be 0.890 mPa s at 25 °C [129].

Using the Washburn equation, or from the Darcy equation, the ratio between the

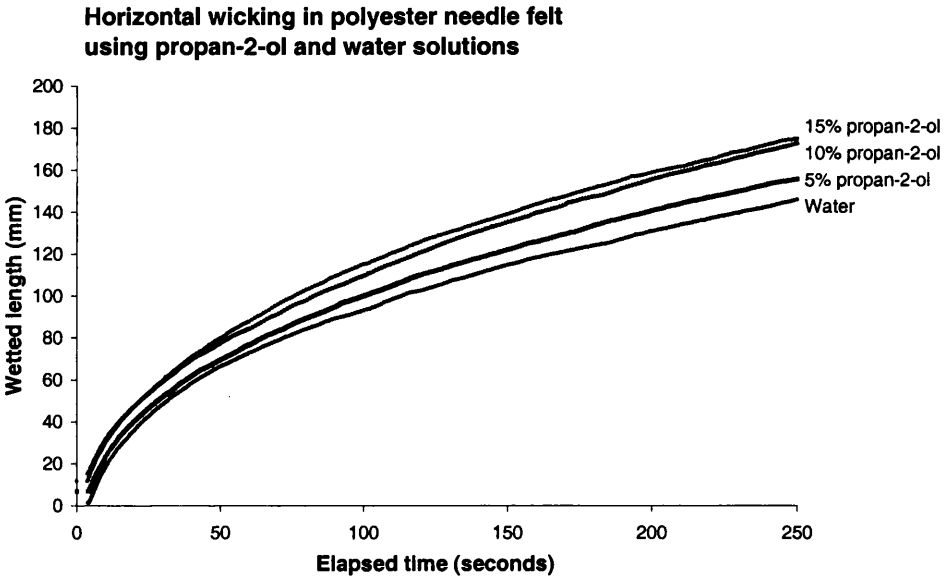

Figure 4.9: Example results showing horizontal wicking with each of three water-propan-2-ol solutions

horizontal wicking numbers in each solution and that in water would be expected to be:

$$\frac{L_{ipa}}{L_0} = \sqrt{\frac{k_\gamma k_{\cos\theta}}{k_\eta}} \tag{4.3}$$

where, k_γ is the ratio of the surface tension of the solution to that of water, $k_{\cos\theta}$ is the ratio of the cosine of the contact angle of the solution to that of water, and k_η is the ratio of the viscosity of the solution to that of water

The calculated values for the change in ratio of the rate constants, together with their fitted experimental values are shown in table 4.3.

The decrease in the contact angle caused by adding propan-2-ol was expected to increase the wicking rate substantially. In practice the change in the contact angle is counteracted by a decrease in the surface tension, and an increase in the viscosity of the solution. The wicking performance in the different solutions was more similar than expected, making it harder to distinguish between the results. The measured wicking numbers show an increase in wicking performance as the proportion of propan-2-ol in the solutions is increased. The predicted wicking numbers indicate that wicking with the 10% and 15% propan-2-ol solutions should be slower than with water. If the measured wicking numbers and properties for the solutions are accurate, it might be that the wicking mechanism is more complicated than allowed in simple capillary models. For example, as the contact angle is reduced the wettability of the fibres is effectively increased and the sample could be more fully wetted out.

% propan-2-ol	*Measured wicking ratio*	*Expected wicking ratio for liquids obeying the Washburn equation*
0%	9.05(± 0.343)	
5%	9.39(± 0.453)	9.51
10%	10.93(± 0.055)	7.91
15%	11.13(± 0.140)	8.12

Table 4.3: Calculated and predicted values for the change in ratio of the wicking number constants for propan-2-ol and water solutions (n=3, errors are ± one standard deviation, derived from experimental repeats.

The equilibrium wicked height in the NP450P sample was measured for each of the propan-2-ol solutions. The equilibrium wicked heights are shown in table 4.4. There were no significant differences between the final wicked heights for the three solutions; there was also no significant difference between the heights attained with the solutions and that for water alone.

The equilibrium wicked height will not be changed by the changing viscosities of the solutions. An estimate of the capillary suction pressure for wicking can be made using

the same method as was used for analysing the viscose samples. The ratio of the equilibrium wicked heights for the solutions to the height for water would be $k_{gamma}k_{\cos\theta}$. The predicted values for the equilibrium wicked heights are, in each case, higher than the actual heights measured using the solutions. Although the size of the predicted heights are not accurate, the measured changes in the heights are as expected. The 5% and 15% propan-2-ol solutions wick to similar heights, both larger than for water alone, and the 10% solution wicks less than either of the other solutions.

% propan-2-ol	*Measured wicked height (mm)*	*Expected wicking height (mm)*
0%	21.3(± 1.74)	
5%	21.6(± 1.75)	26.4
10%	19.2(± 2.54)	23.2
15%	22.8(± 1.95)	27.8

Table 4.4: Calculated and predicted values for the equilibrium wicked heights for propan-2-ol and water solutions (n=3 for the solutions, and n=10 for water, errors are ± one standard deviation, derived from experimental repeats.

4.2.2 Wicking in an inclined sample

Wicking in the sample nonwoven was measured with the sample inclined to the horizontal at known angles. Experiments were carried out at 10°, 30°, 45°, and 60° from the horizontal. The angle of incline was measured in each case using a protractor fixed to the sample's supporting framework, from which the angle was determined with a plumb line.

Wicking measurements for an inclined sample show a marked decrease in the rate of wicking as soon as liquid has to wick against gravity. Wicking was monitored for one hour, after which no further change in the wicked length could be seen. The wetting front was marked on the sample, and each experiment left for a further twelve hours. After this time none of the samples had shown any further discernable movement of the wetting front.

The vertical component of the equilibrium wicked heights is shown for each of the angles investigated in figure 4.10.

The only limiting factor for the vertical component of the wicked height is gravity, and so the height is expected to be the same in each case. At small inclinations, 10° and 30° the sample only wicks to around three quarters of the expected vertical height. It is possible that wicking had not reached equilibrium in these samples. The wicking rates for all the samples had fallen to less than 5×10^{-4} mm/s in the last ten minutes during the hour wicking was recorded. Also the samples inclined by a small amount took noticeably longer

to reach equilibrium. The samples inclined by 45° and 60° both reached 99% of their final measured heights after 40 seconds, but the 30° sample took one minute and the 10° sample took 10 minutes. On the other hand, wicking may actually have been prematurely limited. The wetted length is much longer for the samples inclined by smaller amounts; the sample angled at 10° had more then three times the wetted length of the sample angled at 60°. The increased wetted length might indicate why wicking stops before reaching its maximum height. The increase in wetted area will lead to an increase in evaporation, although this effect is expected to be small. If liquid advances by unsaturated flow it could be difficult for the liquid to move forward against gravity at low saturations, or movement might be pinned by inhomogeneities in the sample.

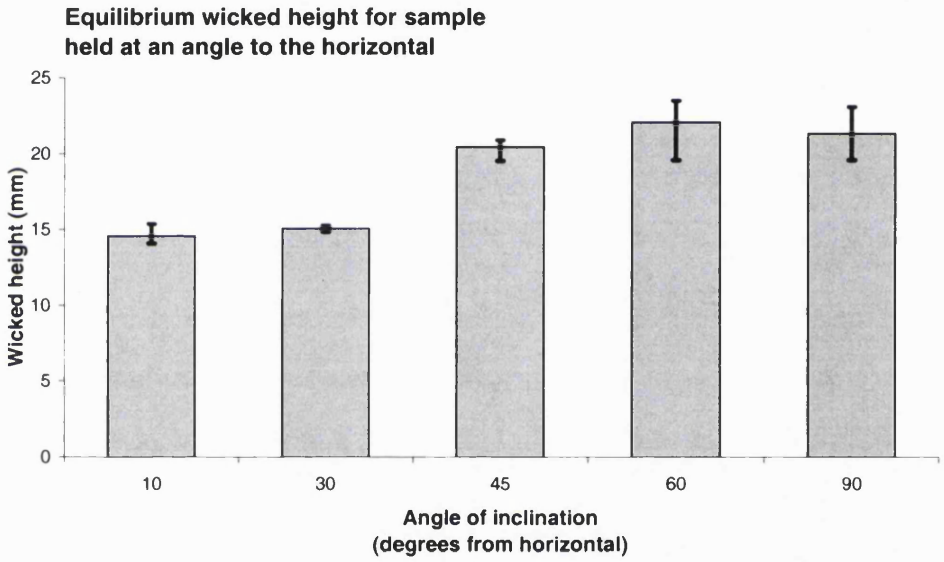

Figure 4.10: Vertical component of the equilibrium wicked height for NP450P sample angle at 10°, 30°, 45°, 60°, and 90° from the horizontal (n=3, errorbars indicate spread of results derived from experimental repeats).

4.2.3 Wicking under vary degrees of sample compression

Horizontal and vertical wicking measurements were made with the sample felt compressed to varying degrees between a pair of Perspex™ sheets, forming a compression cell. The sample was clamped between the plates of the compression cell; with the plates kept apart using a number of shims to produce the desired sample thickness. Experiments were

performed with the compressing plates separated by between 1.0 mm and 4.5 mm using 0.5 mm shims.

The actual thickness of the compressed sample was checked for distortion using a dial gauge mounted a fixed distance above a flat surface, see figure 4.11. Relative changes in the height of the sample above the surface were then measured at sample locations along the surface of the compression cell. Both the upper and lower surfaces of the compression cell were measured in this way. Profiles perpendicular to the wicking direction were measured at 10 mm intervals in three locations across the sample holder. Figure 4.12 shows mean measured profiles for the compression cell. In each case, except for the 1.0 mm sample, the compressed sample thickness is determined by the number of shims used to separate the compressing plates. At the highest compression, though, the sample is not only thicker than expected, but is also curved across its width. This curvature indicates that it is difficult to compress the sample to much less than 1.5 mm, as can be seen in figure 4.13, where 1.0 mm profiles for the compression cell with and without a nonwoven sample are shown.

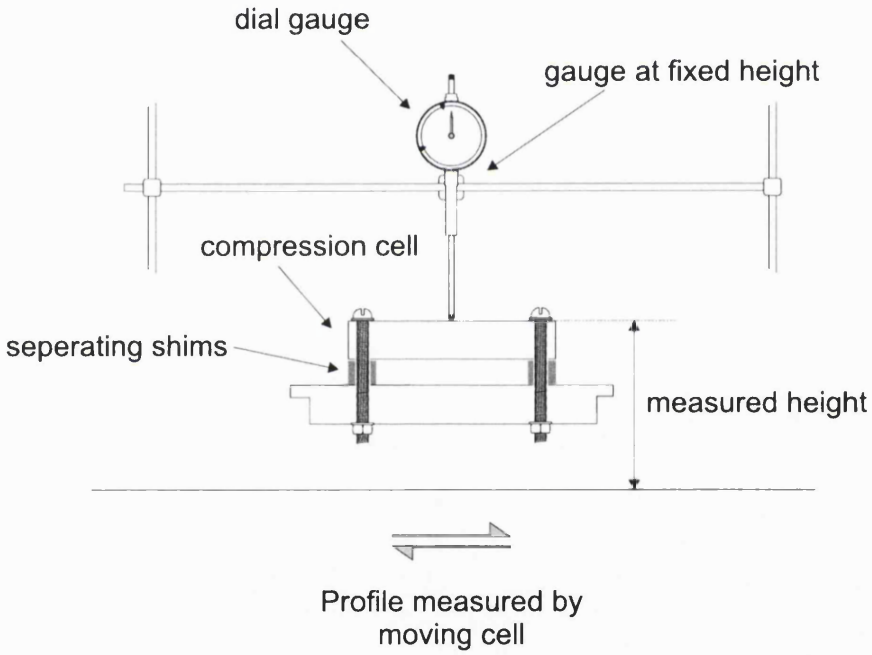

Figure 4.11: Diagram of apparatus used to measure the actual width across the compression cell

Horizontal wicking was measured for eight degrees of sample compression, 1.0 mm to 4.5 mm at 0.5 mm intervals. Figure 4.14 shows an example of how the wicked distance progresses with time for each thickness of sample. The wicking numbers were calculated by fitting the results, using the method described in section 3.8. The wicking number found for horizontal wicking in a sample that is placed on the base of the compression cell,

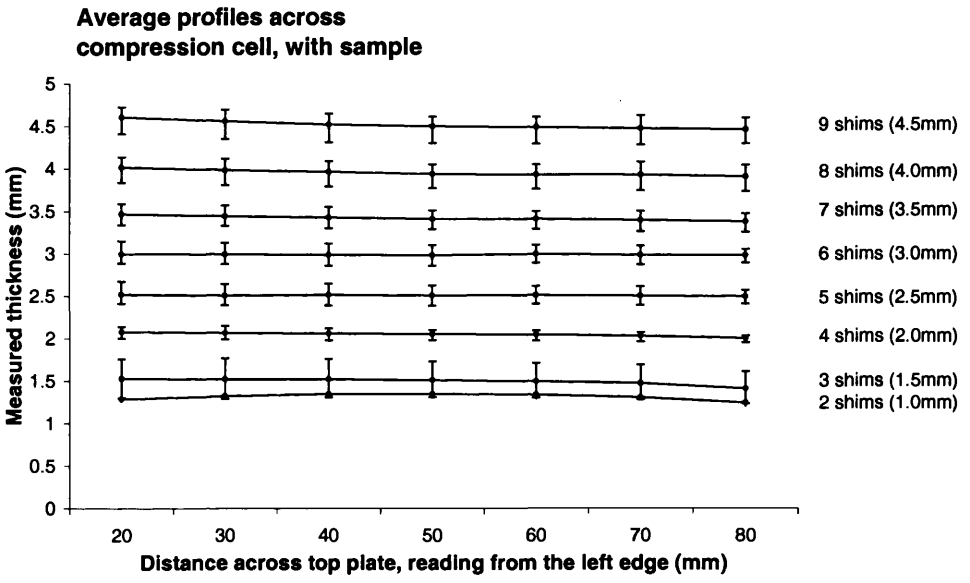

Figure 4.12: Average profile measured across the compression cell (n=3, errorbars indicate spread of results derived from experimental repeats).

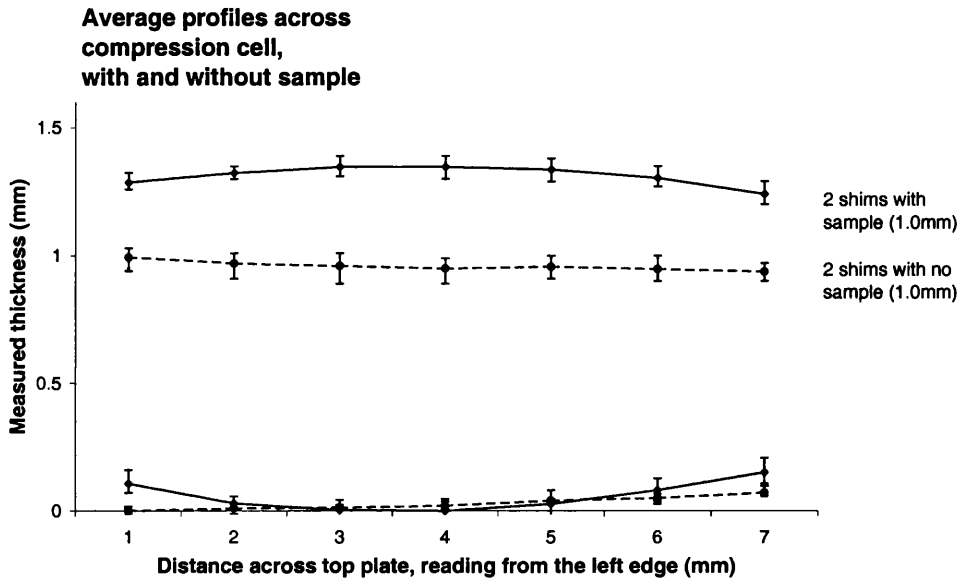

Figure 4.13: Average profile across compression cell. Plates are separated by shims of thickness 1.0 mm in both cases (n=3, errorbars indicate spread of results derived from experimental repeats).

but not compressed with the top plate is also shown on this chart for comparison. The measured wicking numbers for each level of sample compression are shown in figure 4.15.

The horizontal wicking performance shows a clear trend of initially increasing as the sample is compressed; but once the sample is compressed to less than half its thickness wicking performance begins to deteriorate. The mass of liquid wicked in the less compressed samples is greater, because of their larger void volume. It is possible that wicking in the less compressed samples is disrupted by the larger fall of the liquid level in the reservoir. After five minutes the reservoir level has fallen approximately 2 mm in the uncompressed sample, whereas in the most compressed sample it has fallen by 0.6 mm. It is unlikely that this effect can account for the observed differences in the wicking numbers. In a previous experiment where the reservoir was initially lowered by 4.5 mm, the wicked distance after five minutes was 68% of the length covered without altering the reservoir. If the uncompressed sample was affected to this degree, the wicked length would be within 7% of the length measured in the best performing sample. If such a large supposed change in reservoir height does not account for the uncompressed sample performing worse than a more compressed sample it seems unlikely that the change in reservoir height explains the decreasing trend observed for wicking in the lower fibre fraction samples.

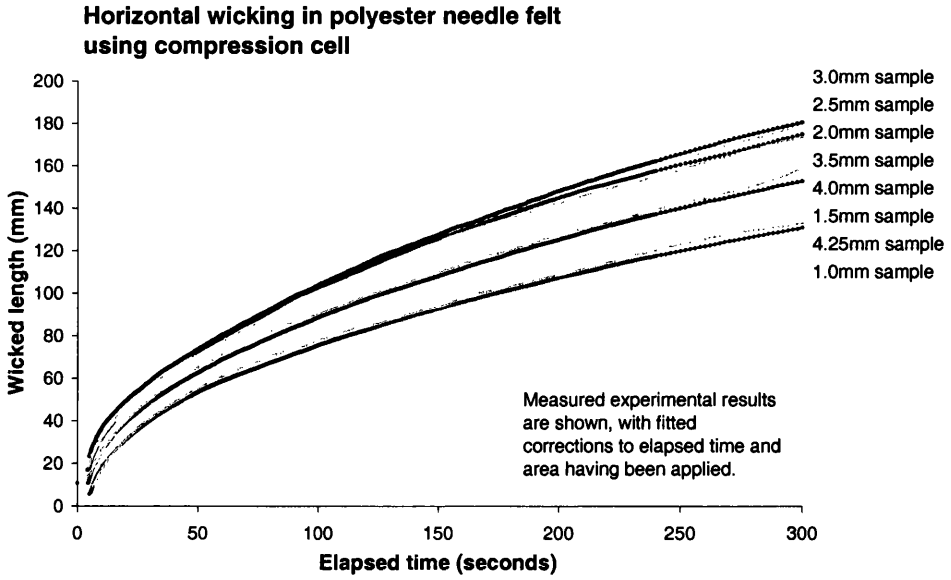

Figure 4.14: Example of wicked distance measurements for horizontal wicking into sample nonwoven felt (NP450P), where felt is compressed to varying degrees.

Vertical wicking was also measured for samples compressed in the cell. An example

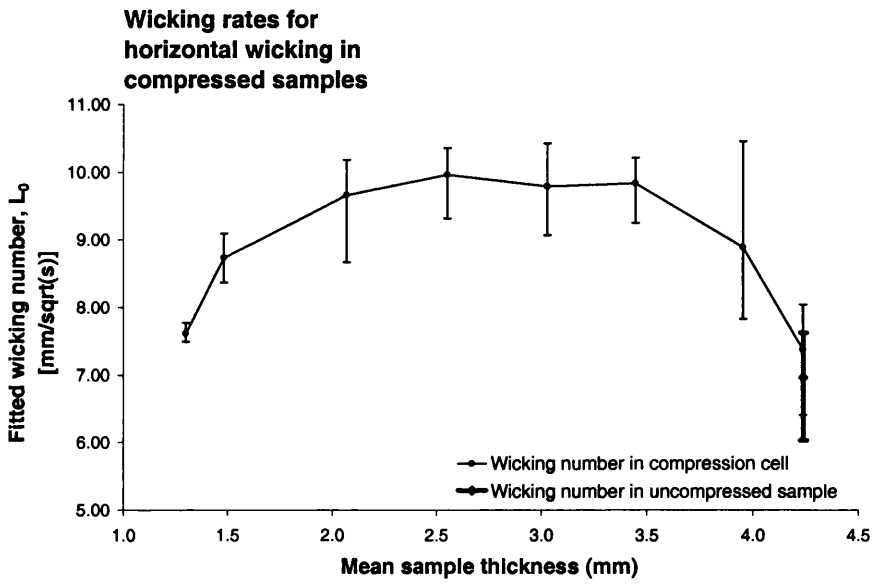

Figure 4.15: Fitted wicking rates for horizontal wicking into compressed sample felt. Rate in an uncompressed sample is shown for comparison (n=4, errorbars indicate spread of results derived from experimental repeats).

showing the development of the wicked height for the series of compressed samples is shown in figure 4.16. The final equilibrium wicked height is shown for each sample in figure 4.17.

Finding the equilibrium wicked mass from the balance readings is more difficult because the vertical mass uptake does not follow a simple square root of time relationship, and so cannot be simply fitted to find the required mass and area offsets. Instead the offsets were found by fitting the mass-area relationships to a straight line. The final wicked mass in the uncompressed samples was estimated to be 8.15 grammes ($\pm$ 2.37, n=7); and the equilibrium wicked masses for the compressed samples were not significantly different. There was, however, some evidence that the wicked mass in the 2.5 mm, and 3 mm samples was a little lower than in the other compressed samples.

The equilibrium wicked mass can be predicted from thermodynamic considerations and the total fibre perimeter in the cross-section. For this sample the expected equilibrium wicked mass was 6.48 grammes, which is lower than the measured equilibrium mass. The final wicked mass is sensitive to changes in the liquid-fibre contact angle, and if the contact angle were reduced from 69° to 63° the modelled wicked mass would agree with the measured value. Assuming complete filling of the void space in the sample, the wicked heights expected for a 63° contact angle are in agreement with the measured values, except for the uncompressed, and 3.5 mm thick sample.

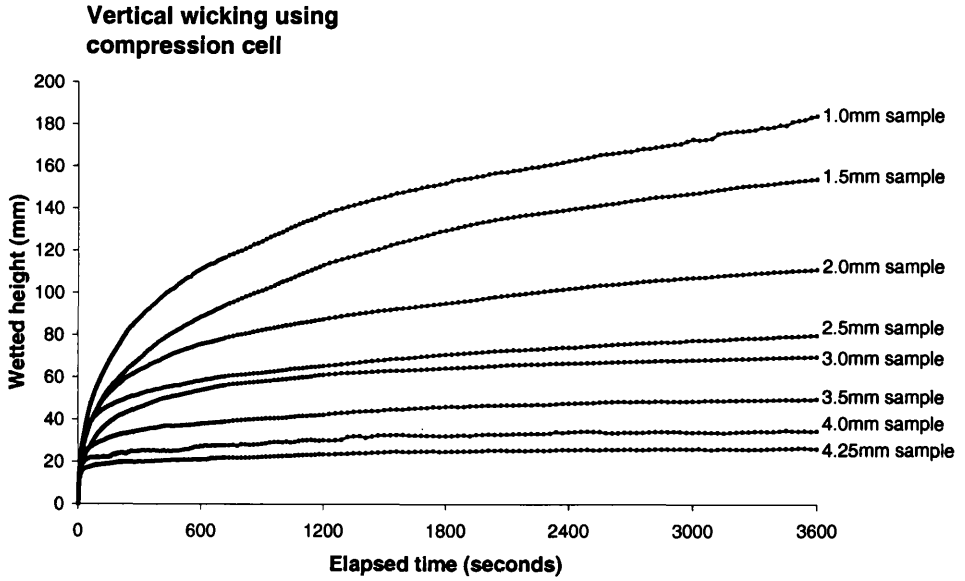

Figure 4.16: Example of wicked height measurements for vertical wicking into sample nonwoven felt (NP450P), where felt is compressed to varying degrees.

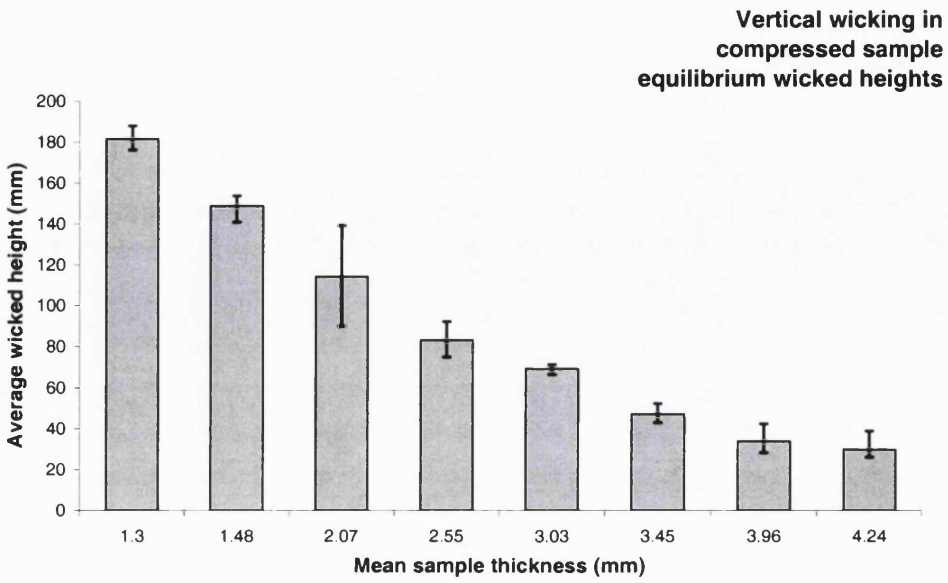

Figure 4.17: Equilibrium wicked height for vertical wicking into compressed nonwoven sample felt (n=4, errorbars indicate spread of results derived from experimental repeats).

4.3 Models for wicking in the sample nonwoven

The rate of liquid wicking in textiles is commonly understood in terms of the Washburn equation (equation 2.11). The Washburn equation is based on analysis of liquid flow in a capillary tube, and as a consequence an effective capillary radius is identified when describing flows in textiles with reference to the Washburn model. In flow through pipes and open channels the hydraulic radius is defined as the ratio between the area of the open cross-section and its wetted perimeter [10]. These values were obtained from the ellipse lists fitted to images of cross-sections through the sample fabric, giving a value for the hydraulic radius in the uncompressed sample felt of $78.45\,\mu$m ($\pm\,27.5\,\mu$m). A correction to distance over which flow occurs is often made by introducing a tortuosity factor (see section 2.2.4). For cylindrical obstacles a tortuosity factor of $(\pi/2)^2$ can be used [171], arising from a straight line path across a cylinder compared with a path taken around its perimeter. Using these values to describe the sample felt, together with the measured values for the liquid and liquid-fibre properties, the wicking number can be predicted using

Washburn's equation and is:

$$L_0 = \sqrt{\frac{r_h \gamma \cos\theta}{2\tau^2 \eta}} \tag{4.4}$$

where, r_h is the hydraulic radius, γ is the surface tension of the wicking liquid, θ is the liquid-fibre contact angle, and η is viscosity of the wicking liquid.

Figure 4.18 shows the values for wicking number predicted by the Washburn equation compared with experimental values for horizontal wicking in the compressed samples. The predicted wicking numbers for the high fibre fraction samples can be fitted to a Washburn type model, particularly if a different choice is made for the tortuosity value. Alternatively, results for the three highest fibre fraction samples can be fitted if the liquid-fibre contact angle is taken to be 63° rather than 69°. The difficulty with Washburn's model for wicking number is that the wicking performance is predicted to rapidly increase for low fibre fraction samples. To account for similar observations in yarns, Hollies *et al.* [90] considered continuity in the inter-fibre capillaries to be important.

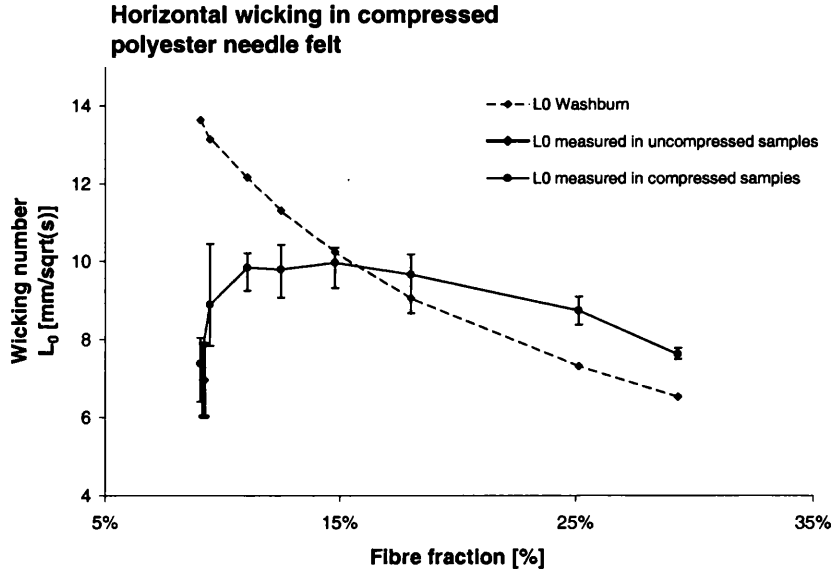

Figure 4.18: Washburn model predictions for the rate of wicking ($L = L_0\sqrt{t}$) compared with experimental values where the fibre fraction is varied by compressing the nonwoven sample (n=4, errorbars indicate spread of results derived from experimental repeats).

The Washburn equation arises from the magnitude of the capillary pressure for an idealised capillary tube, and the Poiseuille law for volumetric flow rate during laminar flow through a pipe. Alternative expressions for wicking can be obtained from Darcy's law

(equation 2.16), following a similar approach to that taken by, for example, Nederveen [161] or Pillai [171].

As for the Washburn equation liquid impregnation is assumed to progress by movement of a well defined air-liquid interface behind which the sample is assumed to be fully saturated. Darcy's law forms a general expression for fluid flow in a porous medium.

Neglecting any pressure changes due to gravity, the pressure gradient will be constant as wicking progresses into a homogeneous medium. The pressure gradient in this case is caused by the interaction between the wicking liquid and the fibres. Inserting the values for capillary suction pressure, and permeability for an idealised capillary into equation 2.16 gives the Washburn relationship. Similarly, other models for capillary suction and permeability can be used.

For cylindrical obstacles with high void volume fractions Davies proposed an experimentally determined relationship for permeability, see section 2.5.3. This equation is easy to apply to a fibrous material where the fibre radius and fibre volume fraction is known. Being empirically determined, this relationship is somewhat unsatisfactory; but at this stage permeability is of interest primarily as a predictor of wicking performance.

The wetting force has been found for a single fibre using the Wilhelmy method. Combining this with the total fibre perimeter measured in the sample cross-section the suction pressure was found from equation 4.1.

Calculated values for the permeability, and capillary suction for the fibre fractions generated in the compressed samples are shown in figure 4.19. Combining equations 2.22 and 4.1 the wicking rate based on the chosen models of permeability and capillary pressure can be found. Figure 4.20 shows the calculated wicking rates compared with values determined experimentally for horizontal wicking in the compressed samples.

As in the case of the Washburn equation, the high fibre fraction samples show good agreement in their wicking numbers compared to the model. The modelled wicking numbers at low fibre fractions are, again, in disagreement with the measured values. As was the case with the Washburn equation, lower fibre fractions are predicted to lead to better wicking performance whereas steadily worse performance was found. In the suction-permeability model either the model used for the permeability, or the capillary suction prediction, or both are incorrect.

4.4 Saturation variation in the samples

One of the key assumptions when applying simple capillary models, of the type described in the preceding section, is that the sample is fully saturated behind the wetting front. Using a gravimetric method the saturation in the sample can be estimated. This method is time consuming because it involves a different experiment to be performed for each time at which a measurement is made.

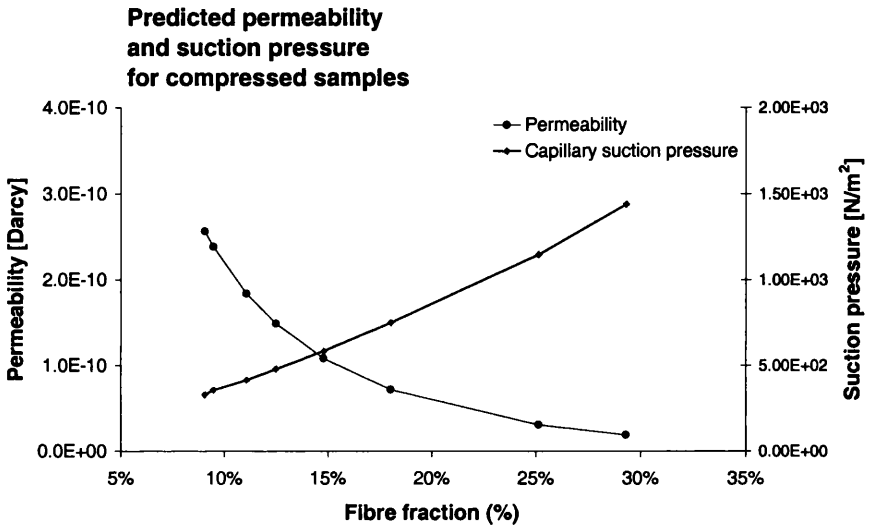

Figure 4.19: Permeability and capillary suction values calculated for nonwoven sample at fibre fractions produced by compression.

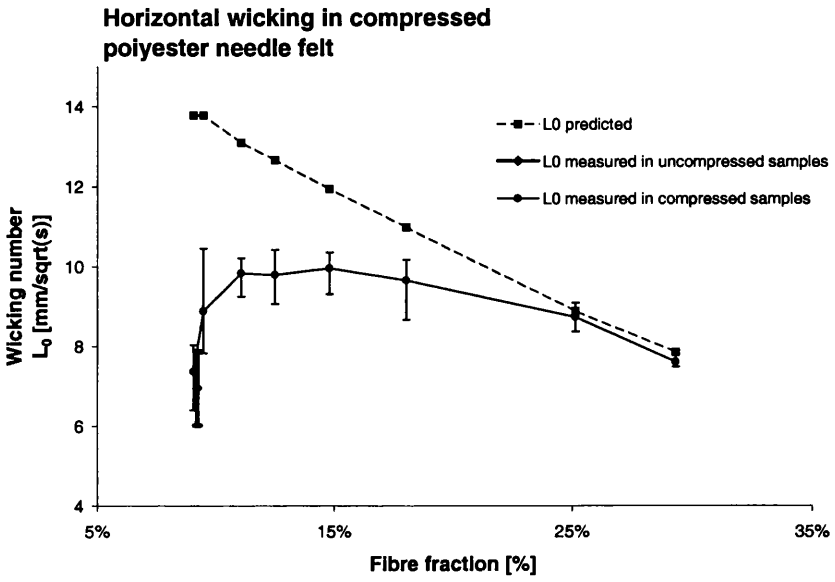

Figure 4.20: Rate of wicking ($L = L_0\sqrt{t}$) predicted using capillary suction and permeability models, compared to experimental values where the fibre fraction is varied by compressing the nonwoven sample (n=4, errorbars indicate spread of results derived from experimental repeats).

Horizontal wicking experiments were carried out as before in the nonwoven sample. After a prescribed time the reservoir of wicking liquid was removed and the sample retrieved from the wicking apparatus. The sample was then immediately cut into 10 mm wide strips perpendicular to the wicking direction, and the strips were weighed. The strips were then dried thoroughly and re-weighed to determine the volume of liquid contained in each. This was repeated for different elapsed times. Figure 4.21 shows the measured saturations for each experiment.

The measured saturation profiles indicate that liquid distribution in the sample is far from fully saturated behind the wetting front. Instead, a wide zone exists over which the sample saturation gradually falls away.

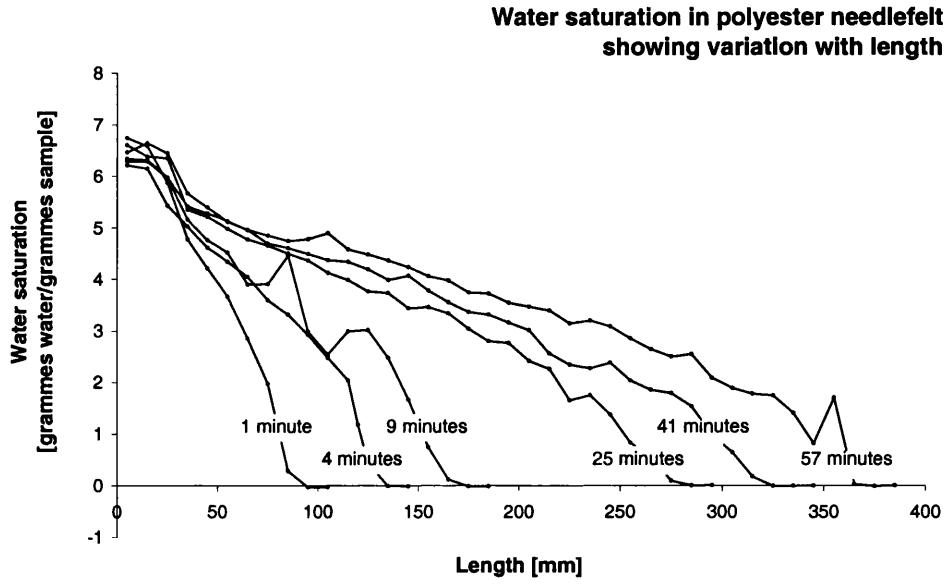

Figure 4.21: Example saturation measurements versus distance from reservoir for horizontal wicking, after fixed elapsed times using a gravimetric method.

Ruoff *et al.* [186] have shown that for one dimensional flow modelled using a diffusion equation the saturation profiles obtained at different times in paper can be reduced to a single curve. Each distance can be reduced to the ratio between the distance and the total distance to the wetting front, a plot of this type using the results in the nonwoven sample is shown in figure 4.22.

Liquid flow in similar situations can be modelled by a saturation dependent diffusion coefficient (see section 2.7.6).

The saturation profile in the equilibrium state for vertical wicking was measured using

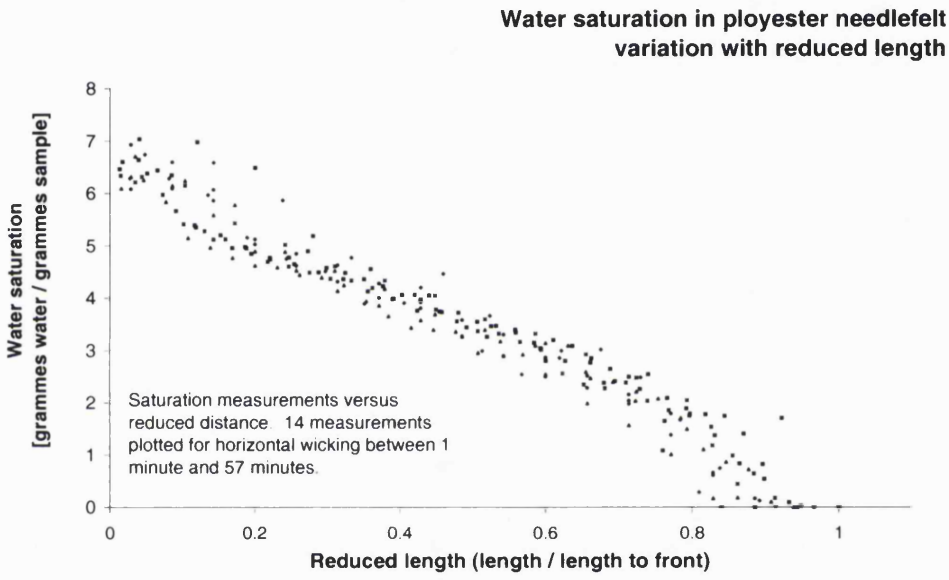

Figure 4.22: Saturation measurements at different time intervals, plotted against reduced length measurements (length) / (total length to front).

a gravimetric method, and is shown in figure 4.23. It is similar to the saturation measured in the horizontal sample.

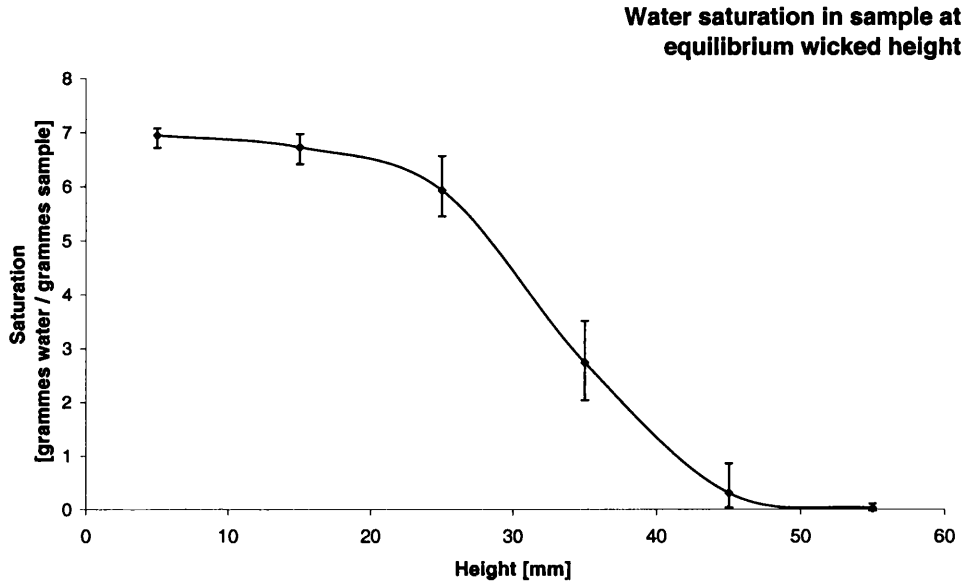

Figure 4.23: Example saturation measurement versus distance from reservoir for vertical wicking to equilibrium (n=3, errorbars indicate spread of results derived from experimental repeats).

Chapter 5

Discussion

In this chapter the success of the apparatus and techniques developed, together with the experimental results obtained will be discussed.

5.1 Apparatus to measure wicking

The need to characterise liquid transport in fabrics has led to the development of many different wicking test methods; reflecting the importance of wicking in a wide variety of situations. The apparatus presented in this research was designed to measure spontaneous wicking, in the plane of a fabric, progressing in one direction, and drawing liquid from a large reservoir. This kind of wicking was chosen because it is simple, yet representative of more complicated absorption processes. Many different methods have been used to measure this type of wicking, but the majority focus on wicking under specific conditions, or are tailored to assessing the suitability of materials for a particular application. The wicking apparatus developed for this work was intended to measure generic wicking as accurately as possible, with the intention of testing models of wicking behaviour in fibrous materials.

The wicking apparatus was able to measure wicking in samples supported horizontally, vertically, and at inclined angles from the horizontal. In each case the same supporting and measuring methods were used and care was taken to keep the geometry and method of liquid introduction as similar as possible. An accurate and objective record of the wetted area was made using video capture equipment, while simultaneously recording mass uptake. The apparatus was largely successful, reliable, and allowed comparable measurements of wicking to be made with the sample supported in different configurations.

A disadvantage of the wicking apparatus was its complexity relative to simple experiments. The equipment used to record mass and image data is expensive; although image capture using personal computers has become common, and cheap hardware is commercially available. A single wicking experiment generates a large amount of image data in relation to the final measurements of wetted length. The image data is stored and pro-

cessed to extract measurements of wicked length and, although the processing is mostly automatic, it takes time and the requirement for the storage of images is high.

The apparatus is not suitable for use with all fabric samples. Measurements of wicking over small areas can be obtained, but measurements for wicked lengths much more than 180 mm would be difficult without altering the current lens arrangement and losing some accuracy. Wicking in coloured fabrics might be expected to present problems, because the wetted area is determined using changes in pixel intensity. In practice a number of coloured fabrics have been successfully used with the wicking apparatus. Wicking has been measured in thin, coloured, woven garment fabrics. These woven fabrics presented a different problem because they altered in size as wicking progressed, making it difficult to obtain difference images. An additional image processing step was needed to counteract this movement. The images had to be aligned by shifting and stretching them prior to taking difference images. This was done automatically using an optimisation process.

Poor reproducibility emerged as a problem when making repeated wicking measurements with the same kind of material. A degree of variation in wicking might well be expected in nonwoven felts because the fibre surface properties and fibre arrangements are not well controlled and can vary considerably within a sample. In addition, wicking measurements appear to be sensitive to changes in environmental temperature and humidity. An improvement in the reproducibility of wicking measurements would be expected if the measurements were conducted under environmentally controlled conditions. Many reported, and standard wicking measurements are performed in an environmentally controlled room. It is also common practice to condition textile samples under standard conditions for a fixed period prior to making wicking measurements. The wicking measurements presented in this research were not performed under environmentally controlled conditions, because no facility to do so was available.

In an ideal experiment, as liquid is wicked out of the reservoir the level of the free liquid surface would remain constant. Changes in the height of liquid in the reservoir modifies the effective driving force for wicking. It is possible to compensate for the loss of liquid, for example by raising the reservoir – although a mechanical solution can be especially difficult to set up. It was felt that the size of the error introduced into the results did not justify making any correction. In other cases it could be appropriate to take steps to eliminate or correct for changes in the height of liquid in the reservoir.

5.2 Cross-sectional examination of fabric samples

The microstructure of the sample nonwoven material was characterised by preparing polished cross-sections of the fabric from samples embedded in resin. The advantage of this technique is that, assuming the impregnation process does not disrupt the fibre arrangement, direct observation and measurement of the fibrous structure can be made. There

seem to have been relatively few experimental investigations that use direct measurements of fabric microstructure to understand liquid movement. Zhou *et al.* [225] have measured the size of the pores in prepared cross-sections of carpet tiles and compared these to measurements of pore size from liquid extrusion. It is, though, difficult to measure pore sizes within nonwoven materials: pore size must be strictly defined and care is needed when inferring three dimensional structures from cross-sectional information. It is particularly unclear what the precise meaning of a 'pore' is in nonwoven materials with low fibre volume fractions.

For these reasons the cross-sectional images were reduced to lists of fitted ellipses, making it easier to apply further processing and make measurements from the cross-sections. There are a number of ways in which the fitting of ellipses to the cross-sectional micrographs could be improved. The separation and identification of fibres within the images could be improved by increasing the contrast between the fibres and void space. The method used to fit the ellipses works reasonably well, but could be improved by introducing additional heuristics into the fitting, for example to prevent fitted ellipses from overlapping.

Some aspects of the information available in the cross-sectional images are not fully exploited. Only relatively simple measurements of total fibre perimeter and free area available for flow have been made. Cross-sectional images could have been used to characterise the geometry of fibre arrangement. In the compressed samples, where wicking performance was known to vary with changes in fibre separation, cross-sectional images were not prepared. A second compression cell suitable for impregnating a compressed sample with resin was designed and made. As in the wicking cell, two Perspex^{TM} sheets are separated using shims, and a central hole was included for the introduction of resin. This was not used for lack of time, and because fibre arrangement was not considered when calculating the capillary suction pressure. Permeability measurements would be interesting to compare with descriptions of fibre arrangement. Measured values for permeability could be described by models of flow around obstacles, but there was some doubt whether the permeability inferred from wicking measurements could be directly related to simple saturated flow situations.

5.3 Wicking in compressed samples

As the nonwoven sample was compressed the void volume in the fabric was reduced, and its porous structure altered. According to Washburn's model, as the sample is compressed, the wicking performance is altered because the hydraulic radius parameter changes. When the porous material is not composed of a bundle of uniform capillary tubes the hydraulic radius must be interpreted in some meaningful way. There are a number of alternative interpretations of the effective capillary radius, for example Gupta [79] has put forward

a structural model for fibrous materials. For the purposes of this research the hydraulic radius was defined by analogy with flow in open channels. Using such a model it is possible to enumerate the hydraulic radius in a fibrous material.

In many practical applications, however, the Washburn equation has required the inclusion of a non-dimensional correction factor. In many instances a tortuosity term is introduced. Although tortuosity is well defined, it is not an easy quantity to measure, and a particular method for finding the tortuosity in a sample can be hard to justify. Once a correction has been applied, its use may be justified if the modelled and calculated values for wicking are similar. In many cases the tortuosity might be expected to change as the pore structure changes, introducing the possibility that the underlying model for calculating tortuosity also changes. The need to introduce a correction factor means it can be difficult to predict wicking performance in a porous material directly from microstructural parameters using a Washburn type equation.

The Washburn equation was used to predict wicking number for the nonwoven sample under different degrees of compression. The hydraulic radius was found using images of polished cross-sections obtained in uncompressed samples. The wetted perimeter was assumed to remain constant under compression. At lower fibre fractions the Washburn equation predicts a rapid increase in wicking number, whereas a decrease in wicking number was experimentally observed.

The Washburn equation is simple and widely accepted to apply to wicking in textiles. This might be largely because wicked length is observed to increase with the square root of time for horizontal and small[1] vertical wicking lengths. In many reported applications of the Washburn equation the meaning ascribed to the hydraulic radius is not clear, and the wicking number is used purely as a figure of merit for wicking in the fabrics being studied.

A weakness of the Washburn equation is that the driving force for capillary flow, and resistance to flow presented by the porous medium are coupled together, through the hydraulic radius [28]. Separating the driving pressure and the resistance of the medium to flow makes it is easier to propose and refine simple models of infiltration. Darcy's equation was used to predict wicking number from different models of capillary suction and permeability, Neederveen [161] and Pillai [171] have described methods using a similar approach.

The capillary suction pressure within the fabric was calculated from interfacial energy considerations. As the sample is compressed the area available for liquid flow decreases, and as a consequence the capillary suction pressure is increased. In the compression cell the presence of the Perspex™ plates will effect the suction pressure. The calculated values for the suction pressure were used to predict the equilibrium wicked height in the compressed samples, taking the mass per unit area from the vertical mass-area plots. Comparison

[1] relative to the equilibrium wicked height

between calculated values and experimental results for equilibrium wicked heights indicate that the capillary suction is larger than expected from the model, but the discrepancy is only significant for the two highest fibre fractions (29.31% and 25.13% fibre).

The resistance to liquid flow was modelled using an empirical equation. This equation was chosen because it is easy to apply and was originally derived from flow experiments in fibrous beds.

Calculations of wicking number using the chosen models for suction pressure and permeability are not significantly different from the experimentally determined wicking numbers at the higher fibre fractions (29.31% and 25.12%). This is not true at the lower fibre fractions, where there are significant differences between the measured and calculated values of wicking number. Indeed, whereas the measured wicking number begins to fall at fibre fractions lower than 12%, the model predicts the opposite trend – an increasing value for the wicking number.

There are a number of possible reasons why the Washburn and suction-permeability models might fail to predict the wicking number correctly at lower permeabilities:

- The suction pressure calculation might be wrong, or the effect of the compressing plates could be significant.

- The permeability model might be incorrect. There are a great many methods available for calculating permeability in various types of porous media, most of which contain some empirically determined element. The Davies equation was chosen to illustrate the calculation of wicking numbers using an assumed model of permeability. The use of the Davies equation to model permeability in the compressed samples could only be properly justified by making separate measurements of permeability in these samples. More recent models for permeability in fibrous beds, such as that described by Kyan *et al.* [121], introduce additional pressure losses to account for the observed permeability in fibrous beds. Unexpectedly high pressure drops have been measured during flow in fibrous beds at high porosities. When flow occurs through a highly porous medium a significant portion of the pore space does not participate in fluid flow, instead it contains stagnant fluid. Some energy is also lost in deflecting the fibres leading to further pressure losses.

A more fundamental problem with all of the models discussed so far is their reliance on an assumption of saturated flow. Saturated flow assumes that there exists a well defined liquid-vapour interface behind which the entire void volume of the sample is filled with liquid at all times. Infiltration into nonwoven samples does not appear to occur by a saturated flow mechanism. In the acquired images patches of sample that appear to remain dry for some time after the wetting front has passed have been observed. The intensity of a pixel as it becomes wet takes some time to reach a level after which no further significant

changes can be seen. Finally, gravimetric determination of liquid content in the sample, during wicking, shows a gradual transition in saturation near the wetting front, from fully saturated to dry. These changes in saturation are not taken into consideration in any of the simple capillary models used in this investigation. If a sample is not fully saturated it is unlikely that the entire available fibre surface area has been wetted, and as a result the suction pressure will be lower than expected. By definition an unsaturated sample does not have all of its available void space filled with liquid, consequently only a fraction of free space is available for flow, considerably reducing the permeability of the sample.

The failure of simple capillary models to predict the experimentally observed wicking performance at low fibre fractions can be attributed to the occurrence of unsaturated flow. A loss of continuity in the capillary channels caused by localised regions of large inter fibre spaces is more likely to occur in more porous structures. A similar experimental observation was made by Hollies *et al.* [90] when examining wicking from drops in yarns (see section 2.7.5). Unexpectedly low water transport rates were observed in low twist yarns and this was attributed to a loss of continuity in the inter-fibre capillaries. In the low fibre fraction felts, it is suggested that the low wicking rates observed here are, similarly, due to the existence of capillary spaces that are not filled by the wicking front, as it advances, leading to unsaturated flow.

The failure of the Washburn and suction-permeability models for low fibre fractions is a particular problem for wicking in nonwovens. The fibre fractions at which these models appear to perform badly are near to the fibre fractions found in the majority of manufactured nonwovens.

Unsaturated flow has been extensively studied in soil physics, where liquid movement is modelled by analogy to a diffusion process. A difficulty arises, though, because diffusivity for unsaturated flows are highly dependent on the degree of saturation. In general the relationship between the diffusivity and saturation will be nonlinear and complicated; and in most practical applications is best determined experimentally.

5.4 Implications for absorbent products

In terms of the design of absorbent products the results obtained in this work suggest some areas that might be explored further. The best wicking performance is not achieved by the most open structures. Instead, there appears to be an optimum value for the volume fraction of fibre needed in a material if wicking speed is important.

The extent to which wicking properties can be changed by compressing felts suggests a mechanism for tailoring wicking properties using local variations in void fraction. Clearly there is a trade off between the volume of liquid that can be stored in a location and the ability of a region to imbibe liquid spontaneously from adjacent locations. This is particularly true when products need to transport liquid against gravity. In addition, a

loss of continuity can greatly reduce the ability of a product to reach its full potential for absorbing liquid. There is no gain, from the point of view of spontaneous transport, in having absorbent material in a product if the adjoining regions do not become sufficiently wet. As a result there might be some benefit in varying the capillary suction in a material locally, by changing the volume fraction of fibres, or the wettability of the fibres. For example, for efficient vertical wicking a material would be, as far as possible, saturated at every step. This might be achieved by increasing the volume fraction of fibre as the vertical height increases. A compression cell could be used to explore this design, for example by introducing shims into the cell to locally compress the sample.

Chapter 6

Conclusions and further work

Incontinence is a serious problem, affecting 4% of men and 7% of women in the United Kingdom. The managment of incontinence is also expensive, and about two-thirds of expenditure on incontinence products is spent on absorbent pads. Absorbent incontinence products continue to become increasingly sophisticated, but still the best products for heavy incontinence leak about a third of the time. The use of superabsorbent polymers has dramatically increased the absorption capacity and retention of absorbent products. Nevertheless, the speed and extent of liquid distribution remain important factors in determining the performance of a product. The liquid distribution properties of absorbent products might be improved if the details of liquid transport in these fibrous materials were better understood. The work presented here has looked at the ability of fibrous absorbent structures to imbibe liquid, in relation to their microstructural and fibre surface properties.

An apparatus was built to make routine, accurate measurements of wicking from a reservoir. Liquid uptake was measured using both mass and wetted area. Measurements of horizontal wicking were found to be well described by a square root of time relationship. Reproducibility between experiments, however, was much worse than expected. Nonwoven felts are not well controlled materials, and there is inevitably some variation between samples. However, the bulk of the differences between wicking measurements were attributed to changes in the environmental conditions. Altering the liquid temperature had a significant impact on wicking, some of which was accounted for by changes in the viscosity of the liquid. Care was needed to keep the distance between the surface of the liquid in the reservoir and the plane of horizontal wicking as small as possible; as wicking progresses this distance increases, and this increase too needs to be kept to a minimum. Rinsing the samples substantially improved the wicking performance, whereas washing using detergent decreased the wicking. The alterations in wicking due to rinsing and washing were thought to be caused by changes in the surface properties of the fibres, as surface agents were either removed or deposited.

The microstructure of the nonwoven felts were characterised by analysing prepared cross-sections. Optical micrographs were obtained in which individual fibres intersecting the plane of a cross-section could be clearly identified. Measurements of the microstructure were made by first fitting ellipses to these micrographs. An automatic process of ellipse identification, although needing some manual correction, was used to gather the required list of fitted ellipses efficiently.

A range of six custom made nonwoven felt samples using viscose were prepared. Wicking and cross-sectional measurements were made for these viscose samples. As expected from thermodynamic considerations, the equilibrium wicked masses in the viscose samples were proportional to the total fibre perimeter in the examined cross-sections. The rates of horizontal wicking were found to be faster in the more heavily needled samples.

A number of experiments were carried out to explore wicking using a single sample nonwoven. A simple nonwoven felt was selected, having circular cross-section polyester fibres that did not swell significantly on contact with water. The fibre-water contact angle for the constituent fibres of the felt was measured using water and solutions of propan-2-ol. Cross-sections of this felt were prepared and analysed.

Using a number of solutions with differing proportions of water and propan-2-ol horizontal and vertical wicking measurements were made. The equilibrium wicked heights varied as might be expected from the fibre-liquid interactions for the solutions, though the horizontal wicking rates did not.

Wicking against gravity was measured not only vertically, but also by inclining the samples to the horizontal. At larger inclinations, 45° and 60°, the equilibrium wicked heights were found to have the same vertical component as for vertical wicking. At smaller inclinations, however, 10° and 30°, the vertical component was less than expected. Wicking at smaller inclinations appeared to come to a premature stop.

The sample nonwoven was compressed to varying degrees to explore the effect that changes in the microstructure of the sample have on wicking performance. In the compressed samples, at high fibre fractions wicking performance was close to that predicted by Washburn or Darcy type models. As the fibre fraction was reduced in the sample, by compressing it to a lesser degree, wicking performance improved. At much lower fibre fractions, the wicking performance began to fall off again. Wicking performance was observed to pass through an optimum as the volume fraction of fibres was decreased. The Washburn relationship gave an acceptable indication of wicking performance at approximately 15% or greater volume fibre fraction. At lower fibre fractions the Washburn relationship indicated increased wicking performance, where much reduced performance was observed. Using a Darcy type relationship with assumed values for the permeability, a similar failure in the predictions for wicking number was seen.

The measurements of wicking number obtained for a nonwoven sample subject to varying degrees of compression show that there is a fibre fraction at which the highest

value for the wicking number will be obtained. By comparison between calculated values for the wicking number using simple capillary models, and experimentally measured values, the models failed to predict the wicking number adequately at low fibre fractions. What is more, simple wicking models suggest much better than observed wicking performance in the range of fibre fractions commonly found in manufactured nonwovens.

It is suggested that the observed failure of simple capillary models to predict wicking in low fibre fraction felts is due to the development of unsaturated flow. The Washburn and Darcy type models explored here are both based on assumptions of saturated flow. Liquid distribution in the felt sample was measured gravimetrically at various stages during wicking. Considerable changes in saturation were found, saturation fell within the first tenth of the wetted length, and continued to fall steadily as the wetting front was approached. The transition zone extended across majority of the wetted length.

In order to better model liquid uptake by the nonwoven felt examined the existence of unsaturated flow needs to be taken into consideration. Absorbent nonwovens are particularly susceptible to the shortcomings of simple capillary models, often having high void fractions to improve absorbent capacity. Washburn type equations continue to be useful in as much as they offer an explanation for wicking that advances with the square root of time. Wicking number is a common measurement and is valuable for grading the performance of different materials.

Considering the use of nonwovens in reusable absorbent products, the results obtained suggest that the best wicking performance is not necessarily obtained by using the most open structures. There appears to be an optimum value for the volume fraction of fibre in a material if wicking speed is important. The different wicking performances observed as the nonwoven was compressed suggests that variations in fibre volume fraction might be used to tailor local transport properties within an absorbent.

The importance of unsaturated conditions in determining the nature of the flow within an absorbent material has been highlighted. Tackling the problem requires both models that incorporate considerations of unsaturated flow, together with measurements of local liquid saturation within materials. As has been shown, it is possible to make an estimate of liquid saturation using a gravimetric method, and indeed this was used to support the conclusion that the deviation from saturated conditions in a nonwoven material can be significant. Measurement of saturation using a gravimetric method has a number of drawbacks, though; particularly the problem of liquid redistribution during handling to obtain the samples. It would be preferable to be able make nondestructive measurements of the distribution of liquid within an absorbent material in terms of saturation. To this end a separate piece of work investigating the use of magnetic resonance imaging of absorbent pads was undertaken. The work involving magnetic resonance imaging is described in appendix A.

6.1 Further work

Accurate measurement of saturated permeability in the samples used would be an important step towards better modelling the underlying flow. In-plane saturated flow measurements could be made using the sample material. Indeed permeability measurements could be made in the sample when it is compressed to the different degrees used in the wicking experiments. Permeability measurements would serve two purposes: the empirical relationship used could be compared to measured values of permeability, and saturated permeability provides an upper limit to the rate of transport that can occur from unsaturated flow.

By analysing cross-sections of the felts for which permeability measurements have been made, permeability could also be compared to microstructural parameters. Many advanced computational flow models have been developed, that could be used together with microstructural parameters to get a much better understanding of the nature of flow within fibrous materials. Making accurate permeability measurements and relating these to the structure of the material would be a substantial project in its own right.

Unsaturated flow could then be explored by making measurements of wicking as before, but quantifying the degree of saturation using magnetic resonance, X-ray or gravimetric methods. These results may be combined with models that incorporate the existence of unsaturated flow. It remains important to explore models that predict flow based on considerations of the fibrous microstructure. Such a relationship might be achieved through measurements of pore volume distributions applied to models of capillary flow, or by indirectly linking microstructural measurements to measured rates of flow at different degrees of saturation.

The work presented here has only scratched the surface of the complexity present in any fibrous structure intended for use as an absorbent. Although many complications have been deliberately avoided, some are crucial to the performance of real absorbents. Future work could benefit by building on the simple material explored here to include absorbents that contain, for example, swelling fibres, a mixture of fibre types, interfaces between layers or regions of different fibre types, or fibres with more complex cross-sections.

Further extension to wicking in two dimensional geometries and from finite volumes of liquid also remains to be explored.

Appendix A

Magnetic resonance imaging

One of the keys to understanding the movement of liquid within a porous material is the ability to measure the liquid distribution as it changes inside the medium. An exciting technique being used to examine liquid inside porous structures is magnetic resonance imaging (MRI) [167, 140].

The potential for using MRI to look at liquid inside disposable incontinence products was explored in the preliminary experiments described in this chapter. In the first instance, liquid was introduced into sections of products while acquiring a sequence of MRI images. In addition to measuring the location of water MRI can be used to make measurements as to the environment of the water. The nature of absorbed water in an incontinence pad is of particular interest in products that make use of superabsorbent polymers, where the water is held in a gel. Experiments were carried out to look in detail at the nature of water in individual constituents of a disposable product.

The use of MRI will be described, together with experiments to take images, and make spectroscopic measurements of liquid introduced into disposable incontinence products.

A.1 Introduction to magnetic resonance imaging

Magnetic resonance imaging (MRI) is a non-invasive, diagnostic imaging technique that can be found in routine use in most major hospitals. MRI makes it possible to obtain high resolution images of soft tissues within the human body.

Nuclear magnetic resonance (NMR), upon which MRI is based, is a well established technique used by chemists to investigate the structure of solids and liquids. In clinical use it is the NMR signal from hydrogen nuclei that are of primary importance. A thorough introduction to the principles and application of MRI can be found in Webb [214].

An isolated proton consists of an electrical charge having angular momentum; resulting in a magnetic field and dipole moment. If an external magnetic field is applied, the proton will align itself either parallel or anti-parallel to the field. The proton has two possible orientations of angular momentum: spin up, or spin down. Spin is a fundamental property,

like charge or mass.

For systems of two spin states, the energy separation between the states is ΔE,

$$\Delta E = \gamma h B_0 \tag{A.1}$$

where, ΔE is the energy separation between the two states, γ is the gyromagnetic ratio, h is Planck's constant divided by 2π, and B_0 is the flux density of the external magnetic field.

The proton may then move from its lower energy state into the upper energy state by absorption of a photon with energy $\gamma h|B_0|$. The energy possessed by a photon is related to its frequency and in NMR experiments photons in the radio frequency (RF) range are used.

$$h\omega_0 = \gamma h B_0 \tag{A.2}$$

In order to move the proton from one energy state to another, energy must be supplied at the Larmor, ω_0, angular frequency.

When referring to a single nucleus a quantum mechanical description should be used. It is easier, however, to consider a large assembly of independent nuclei, using a classical description in order to explain the important processes.

To make NMR measurements the net magnetic moment of a sample is tilted away from its equilibrium orientation, by application of a magnetic field. As the excited nuclei decay back to their equilibrium state a signal is generated, and this signal can be observed using a receiving coil.

A.1.1 T_1 processes

The relaxation of the net magnetisation occurs through the loss of energy. The time constant that describes the transfer of energy to or from the spin system, causing spin state changes, is called T_1 or the spin-lattice relaxation. T_1 information provides an indication of the ability of neighbouring spins to tumble or rotate.

A.1.2 T_2 processes

T_2 or spin-spin relaxation, occurs when spins are able to exchange energy without losing any energy to the surrounding lattice. T_2 relaxation results both from a loss of phase coherence, and as a result of longitudinal relaxation.

A.1.3 Imaging techniques

In order to form an image of NMR signal within an object, the source and strength of each signal region must be determined. By imposing a gradient on the main magnetic

field, different regions of the sample can be made to experience different magnetic field strengths.

The nuclei in a particular slice can then be excited using a short radio frequency pulse at the correct frequency. The position of regions within the slice may then be determined by a combination of frequency and phase encoding.

A.1.4 Scanning sequences

Spin-echo

Spin echo forms the basis of many commonly used pulse sequences. By altering the pulse timing, proton density, T_1, or T_2 weighted images can be obtained.

The spin echo sequence gets its name from a pulse that is applied to refocus the magnetisation, producing an echo.

Magnetisation transfer contrast

Magnetisation transfer contrast (MTC) is used to investigate the bound water pools in a sample. Water bound to macromolecules is not normally visible to NMR because the line width of the component is too great. In an MTC sequence a pulse is applied away from the resonant frequency for free water. Water bound to other components in the sample will be saturated, instead of the free water. As the bound component cross-relaxes with the mobile water pool it becomes possible to detect using MRI.

Echo planar imaging

Magnetic resonance images often take some time to acquire, and benefit from the use of a number of averages. In situations where the object under investigation is moving, image quality can be severely limited. Echo planar imaging (EPI) is a technique that allows the rapid acquisition of images. An EPI image can be obtained in less than 1/10th of a second, and EPI is often used to observe rapidly changing processes.

A.1.5 Magnetic resonance spectroscopy

Magnetic resonance spectroscopy (MRS) does not use phase or slice selection while signal is received from the object being examined. No positional information is collected from a spectroscopic scan.

MRS may be used with a variety of pulse sequences. Many of the same sequences used in MRI are also used in MR spectroscopy, with any slice selection steps omitted.

A.2 MRI experimentation

The advantage of MRI is that it offers a window into certain aspects of the interaction between water and an absorbing material that cannot be obtained by other means. The use of MRI opens up the possibility of imaging the distribution of water inside an absorbent product without disturbing the structure. MRI is also able make some measurement as to the state of water within a material, that is how 'free' or 'bound' it is within the structure.

MRI is a complex technique, and there are inevitably compromises to be made between time and spatial resolution. Considerable effort will need to be invested in investigating a range of different measurements and scanning schemes, before the full potential of any particular experimental technique can be realised.

A.2.1 The use of disposable incontinence pads

Modern disposable incontinence pads are often surprisingly complex, with the use of layers of different absorbent materials becoming increasingly popular. The introduction of laminated structures is straightforward from a manufacturing point of view, but assessing how the layered product performs can be difficult. MRI stands out as a suitable technique for exploring the processes that occur within a composite absorbent product.

The pads to be studied in these experiments are from Paul Hartmann[86], and besides the usual coverstock and waterproof backing, consist of a three layered absorbent core. The structure of the pad is shown in figure A.1 and the layers are as follows:

Top layer This layer is predominantly made up of short curly fluffed wood pulp fibres, and lies directly under a thin spunbonded coverstock material, closest t o the user. This component is intended to allow the rapid transmission of urine into the pad, and is confined to the crotch region. The stiffer curly fibres a re intended to maintain an open structure, when wet as well as dry, so as not to impede the inflow of liquid. By resisting wet collapse, this top layer also helps to keep absorbed liquid away from the user's skin.

Middle layer This is the densest layer, and consists of fluffed wood pulp and p articles of SAP, covering most of the pad area, targeting the central region. This layer performs the majority of the absorbent function of the pad, in terms of liquid storage.

Bottom layer This is a relatively thin layer extending over the entire pad area , containing only fluffed wood pulp. It sits above the waterproof backing of the pad. The bottom layer is designed to act as a temporary reservoir, holding any liquid that is not absorbed by the middle layer, as a result of the time taken for the SAP to swell. The majority of the pad area is covered with this layer.

For the purposes of this experimental work the manufacturer has supplied separate samples of each layer and superabsorber, alongside entire pads.

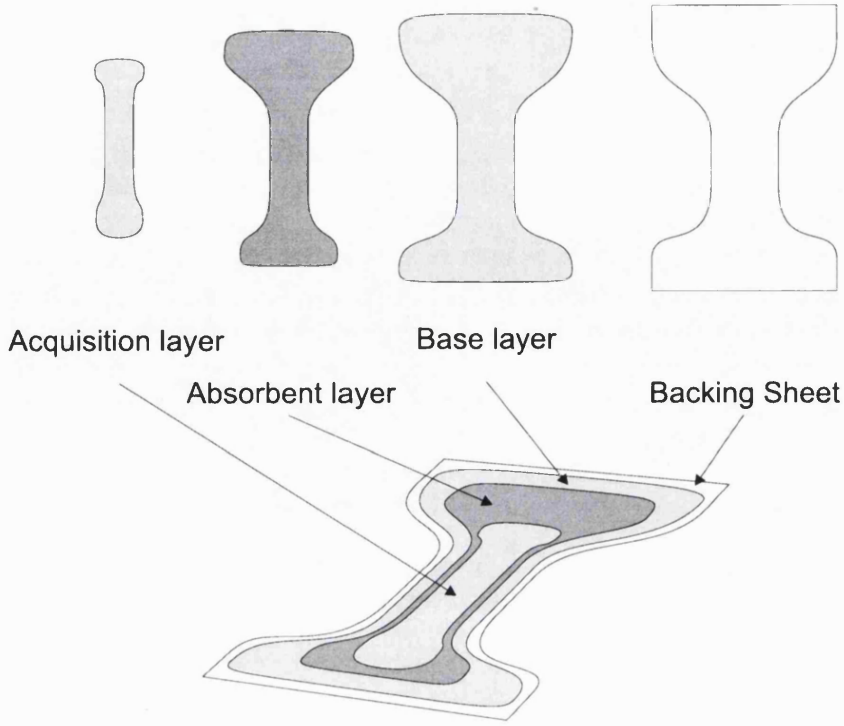

Figure A.1: Layered structure of Hartmann incontinence pad, coverstock not shown

A.3 Materials and Methods

All experiments were carried out on a 2.35 T horizontal bore magnet (Oxford Instruments, Oxford, UK) interfaced to a SMIS console (Guilford, UK). The radio-frequency (RF) pulses were transmitted with a birdcage, volume coil of length 6.5 cm. The SAP used in this study was a mixture of crosslinked polyacrylic acid and sodium polyacrylate having a principal particle size of 300 μm (FAVOR T5271 (EK-X 3), Stockhausen [199]). Figure A.2 shows the images, obtained using optical microscopy, of a single SAP grain before and after the addition of water.

The liquids used in these experiments were varying concentrations of sodium chloride (NaCl) solution. A 0.9wt% of NaCl solution is often used as a urine analogue.

A.3.1 Imaging experiments

In order to find out how a liquid distributes itself after entering an absorbent product MRI was used to look at water in 'slices' through the sample. This is especially valuable in the case of laminate structures, where it might become possible to evaluate whether the fluid behaves as the designer has intended.

In the Hartmann pads liquid is expected to wet quickly through the top, acquisition, layer without being absorbed to any great extent. Instead the liquid is supposed to be

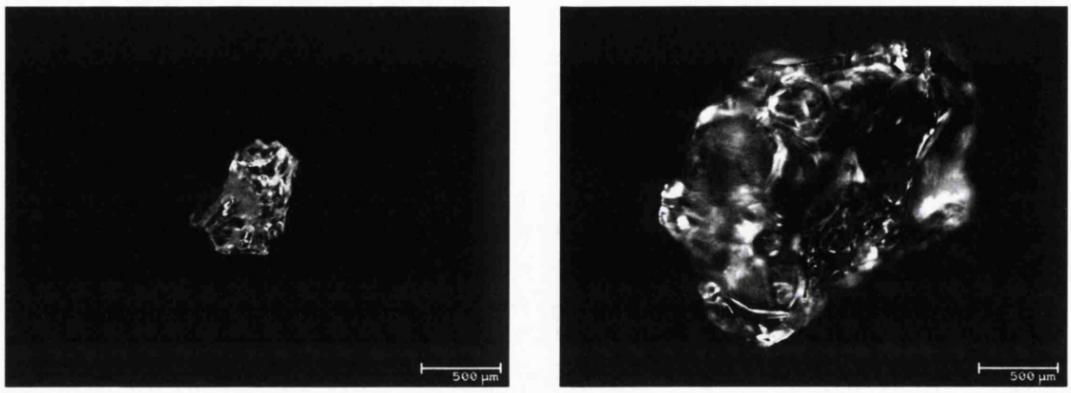

(a) (b)

Figure A.2: Example optical image of a single SAP grain used in the experiments (a) SAP grain prior to addition of water. (b) SAP grain following addition of water.

stored, temporarily, in the second and third layers until it is drawn into the superabsorbent particles.

Whole pad images

A 4 cm × 4 cm sample of whole pad was placed into centre of the bore of the MRI machine. 10 ml of tap water was then introduced from above into the middle of the pad sample. A syringe was used so that liquid can be introduced during a scanning sequence. The initial movement of liquid into the pad structure occurs extremely quickly. In order to gather images of the redistribution of fluid an EPI sequence was used.

Figure A.3 shows examples of the images acquired from the EPI sequence. In these images the image represents a slice of thickness 2.3 mm from the centre of the centre of the sample. The image is 55 cm along each edge, and contains 128 × 128 pixels.

The speed of the EPI sequence means that the images can be quite indistinct. Though it is possible to see the location of the liquid and in these images, the swelling of the pad and the time taken for the liquid to stop moving can be seen. The later images appear to show the liquid as much less intense, as if the signal is fading as the scan progresses. EPI is very sensitive to changes in the susceptibility gradient, and it is expected be that as the liquid forms adjacent localised wet and dry regions this causes the loss of image clarity.

The EPI scanning continued until it was believed that the liquid had settled into a final configuration, which occurs after around 100 seconds. At this stage a proton density weighted image was obtained to record the final distribution of liquid within the pad. As there is no further liquid movement much longer can be spent acquiring the images, obtaining more detail, and taking a number of averages. Both transverse and coronal slices are gathered, the slice thickness was 1.1 mm and the images contain 256 × 256 pixels.

(a) 0 seconds (b) +2 seconds (c) +5 seconds

(d) +10 seconds (e) +60 seconds (f) +100 seconds

Figure A.3: EPI images from whole pad samples

Fifteen slices in all were imaged, with the slice number indicating increasing location in x and y.

Figure A.4 shows a selection of three transverse images and A.5 shows coronal images. From these images it is apparent that the absorbed water is largely held in clumps, presumably in swelled superabsorbent particles.

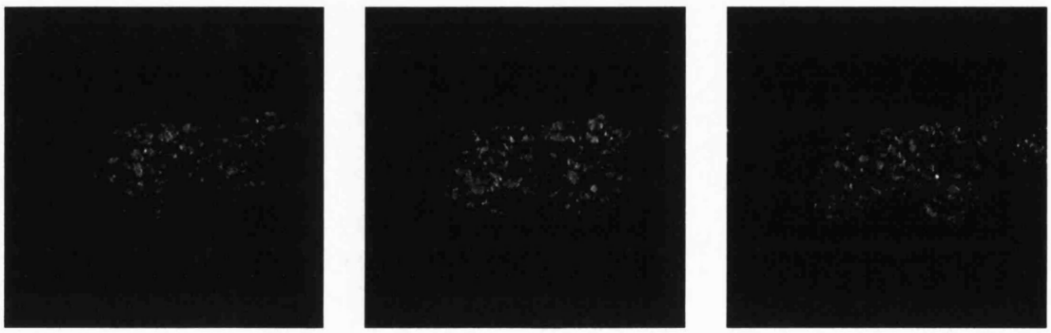

(a) slice 1 (b) slice 5 (c) slice 9

Figure A.4: Proton density images from whole pad samples, transverse slices

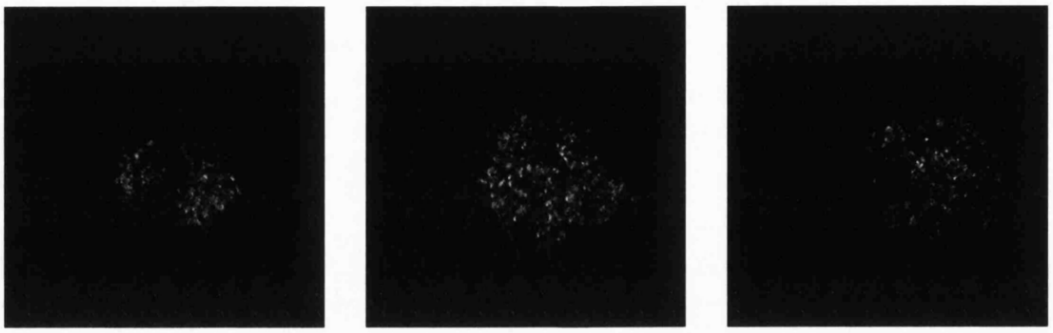

(a) slice 2 (b) slice 8 (c) slice 15

Figure A.5: Proton density images from whole pad samples, coronal slices

Comparing a slice from the EPI sequence after the water has ceased changing position, to a proton density weighted image, it can be seen that the EPI image provides a reasonable reflection of the distribution of liquid. Figure A.6 shows an EPI image next to a proton density weighted image.

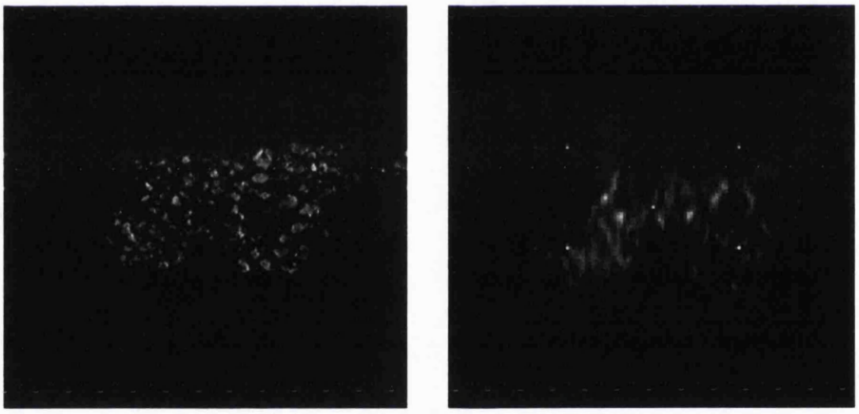

(a) Proton weighted

(b) EPI image 2 $\frac{1}{2}$ minutes after addition of water

Figure A.6: Comparison EPI and proton density images from whole pad samples. EPI image scaled twice normal size.

A.4 Spectroscopic experiments

In modern incontinence pads the retention of liquid is principally achieved using superabsorbent polymer (SAP) powder scattered through a fluffed wood-pulp material. Figure A.7 shows a MRI image of a composite pad in which water-filled capillary tubes have

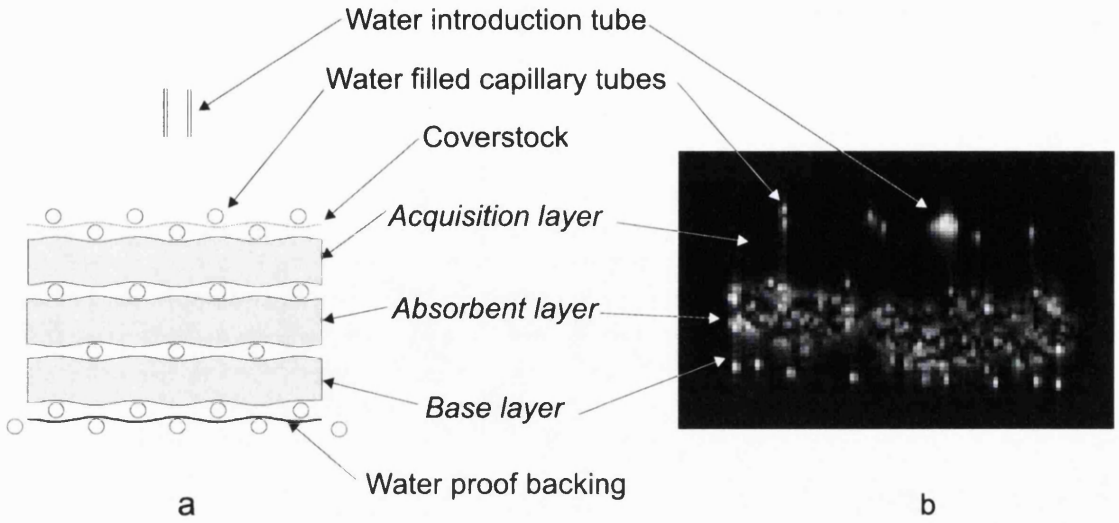

Figure A.7: Arrangement (a) and MRI image (b) of a composite pad in which water-filled capillary tubes have been used to delineate boundaries between the constituent layers.

been employed to delineate boundaries between the constituent layers. The majority of the water is held in the middle layer, containing SAP and fluffed wood-pulp.

A.5 Investigating the state of absorbed water

The T_2-weighted NMR profiles provide information as to the state of water in its free state. With the relatively short echo time (echo time, $T_E = 30\,\text{ms}$) used, the signal provides information that can be related to the proton density of the sample. Bound water is not visible with this technique since the linewidth of this component is too great to be detected by the spin-echo sequence. The technique of magnetisation transfer contrast (MTC) provides an indication of the relative proportion of the free and bound water pools in the absorbed liquid [219]. The bound compartment will cross-relax with the mobile water pool and reduce the magnetisation of the latter compartment. The apparent diffusion coefficient (ADC) reflects the random, translational motion of water within the material which will be affected by viscosity changes and compartmental restriction [125, for example]. Relaxometry supplies further information regarding the translational and also rotational mobility of water via the interplay of inter- and intra-molecular magnetic dipole forces between the water protons. The two principal mechanisms of magnetisation relaxation involve spin-lattice and spin-spin interactions and are described by the parameters T_1 and T_2 respectively.

A.5.1 T_1, T_2 and ADC measurements (n=4 experiments)

After a period of control imaging, 1 g of (a) SAP and (b) fluffed wood-pulp, were each added to 10 ml of (i) distilled water and (ii) 10wt% NaCl solution. Transverse, 1-D profiles of the entire volume were acquired with a standard spin-echo sequence, with phase and slice gradients turned off. For measurements of the spin-lattice relaxation time, T_1, the TR was varied in eight steps from 0.5 to 5 sec (500, 100, 1500, 2000, 2500, 3000, 3500 and 5000 ms) and the data fitted to a saturation recovery curve. For measurements of the spin-spin relaxation time, T_2, the T_E was varied in eight steps from 30-900 ms (30, 60, 100, 200, 400, 500, 700 and 900 ms). For ADC measurements, a spin-echo sequence with bipolar diffusion gradients alternatively applied along read (x) and phase (y) gradient directions, was employed (T_E = 90 ms; diffusion-gradient parameters, (Δ = 44 ms and δ = 22 ms; diffusion-weighting factor (b-value) = 700 sec/mm^2. The two diffusion coefficients (ADC_x and ADC_y) were averaged together since the mixtures are proved to have isotropic diffusion characteristics along these axes. Profiles were analysed by integration to obtain the area.

A.5.2 T_2-weighted and MTC measurements, (n=3 experiments)

One gramme of (a) SAP, (b) fluffed wood-pulp and (c) a mixture of 50% SAP and 50% fluffed wood-pulp, were added to 10 ml of each of (i) distilled water, (ii) 0.5wt% sodium chloride/water solution [0.086M], (iii) 1wt% NaCl solution; (iv) 10% NaCl solution. After a period of control imaging with liquid and substrate separate, they were mixed together. A similar sequence as described previously was implemented (repetition time, T_R = 15 sec; echo time. T_E = 30 ms; 6 or 30 repeated acquisitions before and after the addition of liquid) with an RF top-hat pre-pulse for MTC (RF amplitude, B1 = 60 mG (255 Hz); pulse length, T_p = 5 sec). Acquisition of proton-density (frequency offset, (f = 100 kHz) and MTC spectra ((f = 2 kHz) were interleaved throughout the experiment. It was necessary to apply the MTC pulse at a large frequency offset during the T_2-weighted acquisition because the 5 sec pre-pulse affected the subsequent RF amplifier characteristics. Profiles were analysed by integrating for the area.

A.5.3 Time course investigation

In order to further evaluate the absorption time course, T_2-weighted 1-D profiles were acquired with a 10 s time resolution during this phase (SAP and fluffed wood-pulp samples; T_R = 10 s, T_E = 30 ms). After a period of control imaging with both fluid and substrate separate, they were mixed together and profile acquisition continued for one hour.

A.6 Results

A.6.1 T_1, T_2 and ADC measurements

T_1, T_2, and ADC results are shown in figure A.8 which also shows the percentage ratio of parameter changes. For example, in the case of T_1 and the fluffed wood-pulp/water combination, this ratio becomes

$$\Delta T_1(\%) = \left[\frac{T_1(\text{water}) - T_1(\text{fluff} + \text{water})}{T_1(\text{water})}\right] \times 100 \tag{A.3}$$

where T_1 (fluffed wood-pulp + water) is the relaxation time of the mixture. A decline in all the parameters was observed on mixing the material and liquids together.

T_1 : The T_1 decline of water in the presence of fluffed wood-pulp was of a significantly greater magnitude than for SAP (P=0.02, paired t-test). In the case of NaCl solution, the difference between the relaxation time of the solution in the two materials did not achieve statistical significance. The data suggested that the 10% NaCl solution possesses a lower T_1 than water (control data) but this did not achieve statistical significance.

T_2 : The T_2 change for water added to fluffed wood-pulp substantially exceeds the T_2 change for water added to SAP (P<0.001). It can be seen in Figure A.8 that the relative T_2 changes between the two materials (ΔT_2 (%)[fluffed wood pulp]/ΔT_2 (%)[SAP]) is greater than the corresponding T_1 change (P=0.01, paired t-test onSAP:fluffed wood pulp ratios).

ADC : The ADC of the NaCl solution was significantly lower than water (control data) (P<0.0001). On mixing the liquid and material substrates, a decline in the diffusion coefficient was observed but there was no significant variation betweenSAP and fluffed wood-pulp with either water or NaCl.

The diffusion coefficient of sodium chloride is approximately 15% less than the ADC of pure water. This perhaps indicates the increased viscosity of 10% NaCl solution due to the accumulation of hydrated sodium ions [69]. The Stokes-Einstein diffusion coefficient relates viscosity to diffusion according to

$$D = \frac{kT}{6\pi\eta R_{HD}} \tag{A.4}$$

where, D is the diffusion coefficient, η the viscosity, and R_{HD} the hydrodynamic radius of the spherical particle.

A.6.2 T_2-weighted and MTC measurements

A representative data series from one of the experiments is shown in Figure A.9, and the overall results are shown in Figure A.10; with the T_2-weighted and the MTC ratio (MTR) normalised to the control level (water and substrate separate). The MTR is defined as

$$\text{MTR} = \frac{M_S(\Delta f = 2\text{kHz})}{M_0(\Delta f = 100\text{kHz})} \tag{A.5}$$

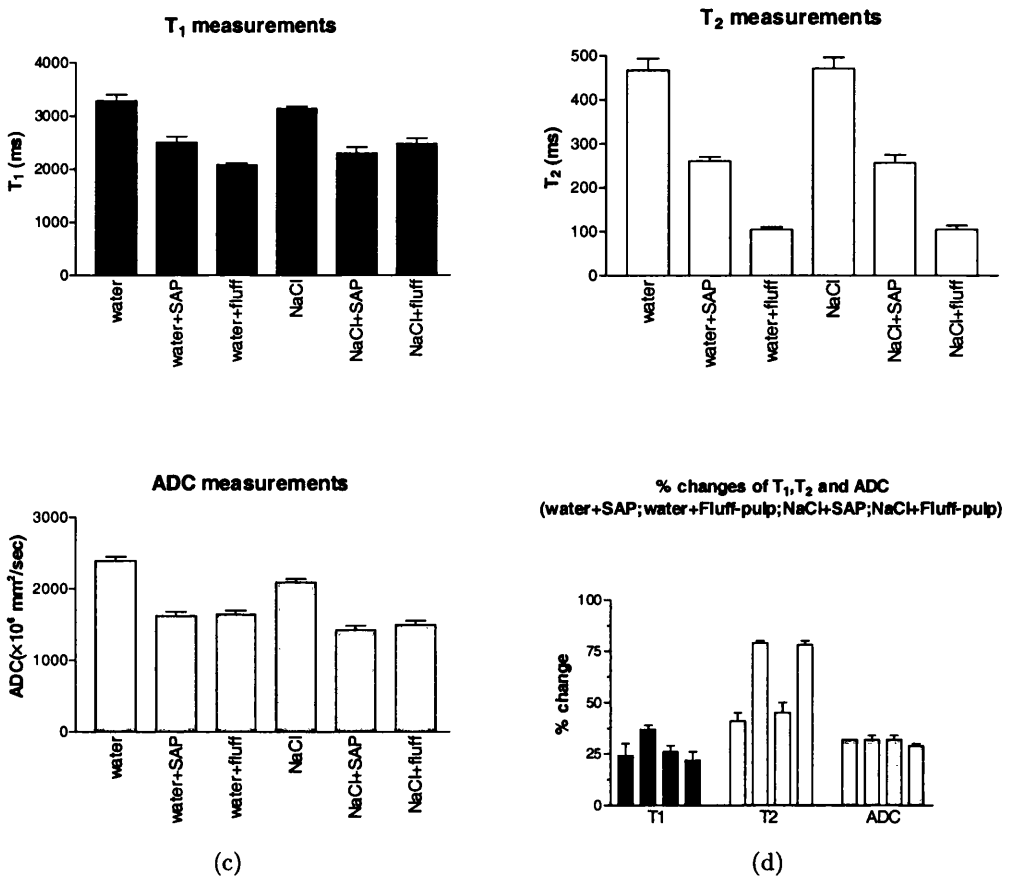

Figure A.8: Summary of T_1, T_2 and ADC data Measurements of (a) T_1, (b) T_2 and (c) the ADC, in SAP and fluffed wood-pulp with water and 10wt% NaCl solution; (d) Percentage change (before addition / after addition). For each parameter, ratios are displayed for, in order, water+SAP, water+fluffed wood-pulp; 10%NaCl+SAP; 10%NaCl+fluffed wood-pulp. In (d), a positive percentage change indicates a decrease of the parameter. Error bars are $\pm$ SEM, derived from experimental repeats.

where M_0 and M_S are the interleaved T_2-weighted and MTC-weighted profiles respectively.

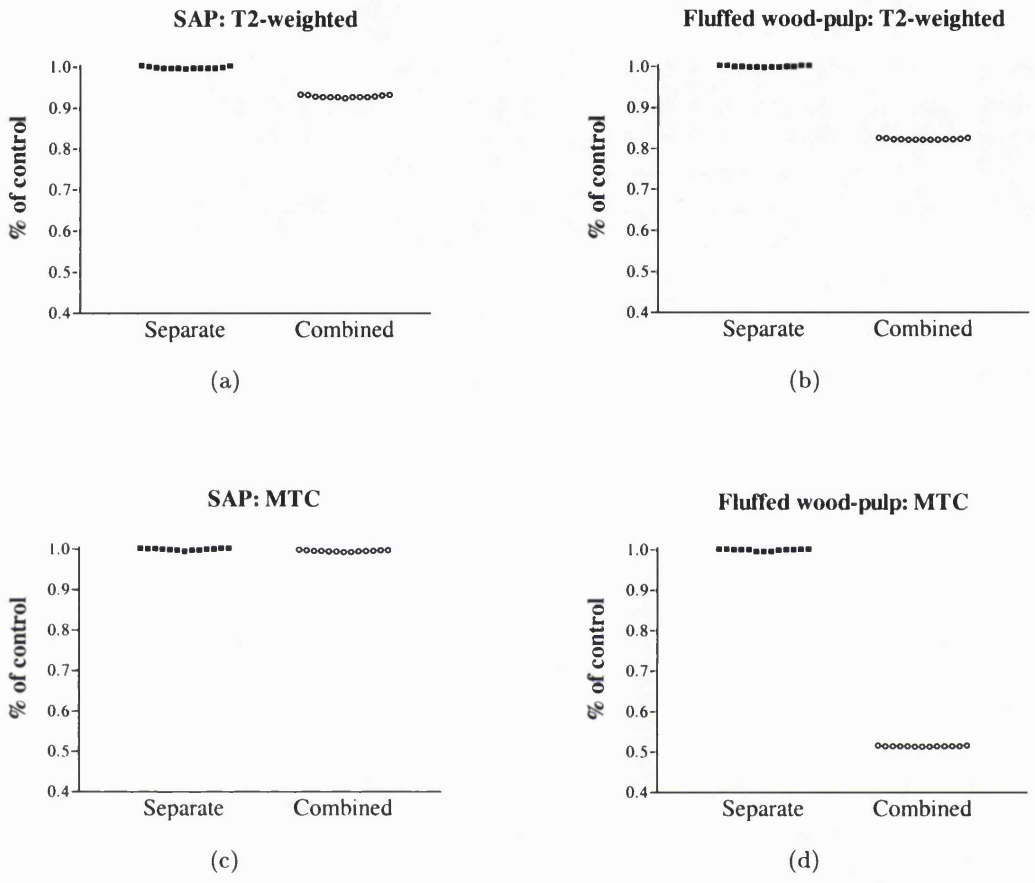

Figure A.9: Representative experimental data series from T_2-weighted and MTC experiments in SAP and fluffed wood-pulp. The data shown are normalised to the control level before and after the liquid and substrate are mixed together. After combining the materials, a period of approximately three minutes was waited before collecting spectra spectra, to avoid the initial period of time-dependent changes in signal intensity.

T_2-weighted profiles: The T_2-weighted signal always declined on mixing together the fluid and material sample but to varying degrees in each case. This indicates different degrees of water binding in these samples. Between the materials, the magnitude of the T_2-weighted change was smallest in SAP, followed by the 50%:50% mixture of SAP and fluffed wood-pulp. Between the different solution concentrations, the magnitude of the T_2-weighted change decreased with increasing concentration of the NaCl solution (10% NaCl). For the fluffed wood pulp, this was not a statistically significant difference.

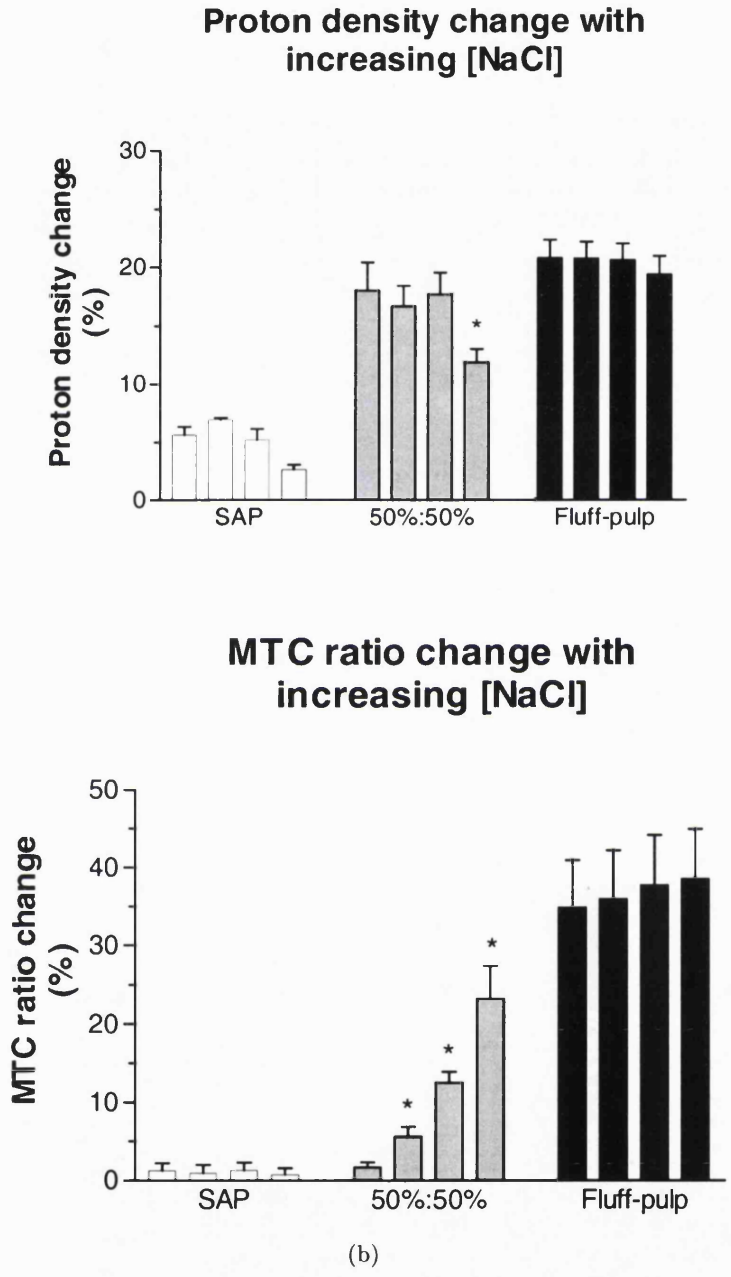

(b)

Figure A.10: T_2 and MTC ratio changes with increasing concentration of NaCl (0%, 0.5%, 1% and 10% by weight). * indicates a significant difference with respect to the values obtained with water ($P < 0.05$). A positive percentage change indicates a decrease in the parameter after mixing the liquid and material. Error bars are $\pm$ SEM, derived from experimental repeats.

	A(0)	c	k [sec-1]
SAP	25.2 (±2.7)	506.4 (±3.3)	78.9 (±12.3)
Fluffed wood-pulp	86.9 (±5.0)	463.7 (±5.4)	7.9 (±0.1)

Table A.1: Fitted exponential time constants obtained from 1-D profile (see figure A.11) data with data fitted to $A(t) = A_0 e^{-t/k} + c$

A.7 Time course investigation

The 1-D profile experiment provided T_2-weighted spectra every 10 s. The integrated area under the spectra is proportional to the T_2. Figure A.11 shows a time course of these areas which were fitted with an exponential curve ($A(t) = A_0 e^{-t/k} + c$) where k is the time constant and A(t) is the area under the profile at time t, and c is the baseline level). The data were fitted up to 200 s (post mixing) after which no significant subsequent change was visible.The values for the fitted rate constant were 78.9 ±12.3 s^{-1} for SAP and 7.9 ±0.1 s^{-1} for fluffed wood pulp. Table A.7 shows the results of this fitting procedure.

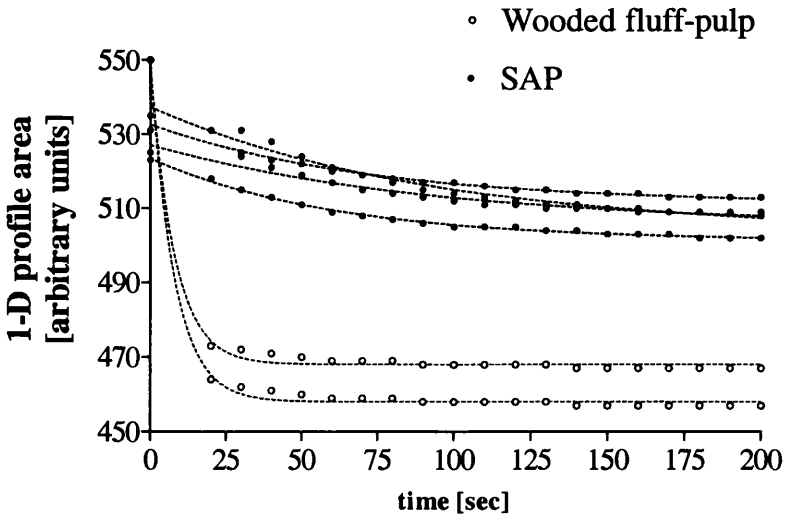

Figure A.11: Graph showing 1-D profile data from individual experiments with corresponding exponential fits ($A(t) = A(0)exp^{-t/k} + c$ where t is the time and k is the time constant, and c is the baseline constant) for SAP (n=4) and fluffed wood-pulp (n=2).

MTC profiles: The change in the MTR was minimal and insignificant when mixing the superabsorber with the liquids. In the other material combinations, a decrease in the

MTR was observed. Between materials, the magnitude of the MTR change increased in the order, SAP- mixture - fluffed wood-pulp. The magnitude of the MTC change tended to rise with increasing NaCl concentration in both fluffed wood pulp and the 50%/50% mixture.

A.8 Discussion

A.8.1 T_1 and T_2 measurements

Mono-exponential recovery curves were fitted to all the T_2 data. This treatment assumes a mono-phasic character of water in these materials within the exchange time defined by the measurement time of our experiments ($\approx$ 30 ms). Biexponential behaviour is expected especially in fluffed wood-pulp in which a substantial bound water component has been predicted. The limited SNR of our study and the number of data points (minimum T_E = 30 ms) were insufficient to confirm this hypothesis. The division of water into free and bound compartments is a simplification and intermediate components, for example, hydration water may need to be considered.

The relaxation times both declined on mixing the water and the samples of SAP and fluffed wood-pulp (ΔT_1 = -23% and -36% and ΔT_2 = -40% and -78%, in SAP and fluffed wood-pulp respectively). The reduction in the spin-spin relaxation time was apparent in the T_2-weighted data (see section A.8.3). The decreasing relaxation times, reflects the porous nature of the two materials. Previous studies have employed relaxometry to investigate porosity and permeability in different porous materials [89, 114, for example]. An NMR study of the porosity of hydrogels has analysed the volume-to-surface-area ratios of the pores (in the order of nm) using a fibre-cell model of fast diffusion [30].

On changing the fluid from water to NaCl solution, the pattern in the relaxation time data does not appear to differ significantly and the same relative signal changes are observed in the SAP and fluffed wood-pulp as with water, see figure A.8. The mechanism of absorption in the presence of a salt solution presumably reflects an osmotic response, and therefore would not be expected to result in a noticeable NaCl dependent response.

A.8.2 ADC measurements

A decline in the ADC was measured on mixing the liquid and material together, indicating a further restriction in translational water mobility. No significant difference was found in these changes when using different liquid or material combinations.

A.8.3 T_2-weighted and MTC measurements

The absolute T_2 changes measured are sufficient to account for the T_2-weighted signal changes (for T_E = 30 ms) found in this study. For example the change in the measured

T_2 on adding water to fluffed wood-pulp from approximately 450 ms (water) to 100 ms (water+pulp) corresponds to the T_2-weighted signal change of approximately 20% found in this study ($M(t) = M_0 e^{T_E/T_2}$, where M(t) is the time dependent signal).

The relatively small T_2-weighted signal decline on mixing water withSAP indicates important information regarding the state of water in these superabsorbent materials. In SAP it is apparent that water is not principally being tightly bound by the polymer, because only a relatively small T_2-weighted signal decline is observed. The principal mode of water transport through the SAP is believed to be a diffusive mechanism [19]. The fibre-like polymer chains are cross-linked so that the polymer gains rigidity and remains insoluble through the ingress of water. The water molecules are free to diffuse through the pores that exist between these complex chains driven by osmotic and electrostatic mechanisms. The minimal change of the MTR in SAP is a further indication of the absence of a *tight* water binding mechanism. The principal binding site of water to SAP appears to be that of hydration of the sodium ions and a significant T_2-weighted change is, therefore, not expected. The resulting hydrogen bond is apparently of insufficient strength or present in insufficient numbers, to affect its NMR relaxation properties greatly. Water will bind to the fixed charge (Na^+) via its OH^- group. The water molecule's remaining proton is electropositive and attracts surrounding water molecules. The resulting electric dipole bonds are not as strong as the hydrogen bond (and therefore will not cause a significant T_2-weighted decrease) but may participate in the water-mediated linking of the polymer chains.

With an increasing concentration of NaCl solution, the T_2-weighted and MTC change decreased to a small extent. This reflects the reduced ability of hydrogels to absorb fluid in the presence of salt solutions. The mobile Na^+ from the simple electrolyte will act to reduce the absorptive capacity of the polymer by diminishing the osmotic pressure that drives the process of water absorption.

The 1-D profile data provides an NMR-based measurement that can be related to the activation time of SAP. The fitted time constant (approximately 80 s, see A.7) reflects the time taken for the mobility of the water protons to decrease as the water is enclosed by the polymer chains. Other values for this measurement using the vortex technique indicate it is around 100 s (Stockhausen, personal communication).

In the fluffed wood-pulp, the change in T_2-weighted and MTC ratios were of greater magnitude. The fluffed wood-pulp is principally composed of cellulose fibres. Cellulose fibres are ribbon like and hollow presenting a large surface area that offers many suitable binding sites to water (OH^- H^+). The resultant hydrogen bonds are strong enough to cause a large T_2-weighted signal change in the fluffed wood-pulp material, and the large interfacial area results in a significantly larger MTC effect for fluffed wood-pulp than in the case of SAP.

In the fluffed wood-pulp, with an increasing sodium chloride concentration, the T_2-

weighted change at the higher concentration was only slightly reduced. The resulting Na^+–H_2O (via the hydroxyl group in water rather than a hydrogen-bond, and the Na^+ ion from NaCl) is apparently of insufficient strength and in insufficient numbers to be observed as a change in the T_2-weighted signal intensity. The MTC change displayed a more clear tendency to rise with increasing concentration although this was not to a statistically significant level. A suggested mechanism for this MTC response is that the increased size of the structure formed with the sodium ions, may result in a larger MTC effect either (i) by increasing the size of the macromolecular structure that can cross-relax with the mobile, bulk water, or (ii) by providing a greater opportunity for the relatively free protons in the hydration shells themselves to cross-relax with the bound compartment within the cellulose structure.

The 50%:50% mixture of SAP and fluffed wood-pulp would be expected to display an intermediate response. On addition of water, to the combined materials, the MTC data implies a significant component absorbed in the SAP whereas the T_2-weighted decline implies a greater than expected proportion of water within the fluffed wood-pulp component (approximately 75% using the absolute T_2 values obtained previously), see figure A.8. These observations require further investigation. The water is expected to be principally confined to the SAP component for water and lower concentrations on NaCl solution. On addition of the water to the mixture, the fluffed wood-pulp would be expected to retain a small proportion of the water with which it comes into initial contact. This water compartment would be diffuse within the wood-pulp and would, therefore, not be expected to result in a significant degree of cross-relaxation and subsequent MTC change. However, this would not account for the magnitude of the T_2-weighted signal change that was observed. The corresponding observation in the T_2-weighted response of a larger signal change than expected may be due to the proximity of the absorbed water to the fluffed wood-pulp in the mixture in which the SAP grains are embedded. The influence of the surrounding material on the state of the water within the SAP may be caused by the relatively free nature of this water compartment. The inherent sensitivity of T_2 relaxation to the environment of the water proton as described by the relationship of the parameter to the correlation time, τ_c [14] may be reflected by the sensitivity of the T_2 and not the MTC measurement to this effect. The increasing MTR with greater NaCL concentration may signify a further increase in water within the fluffed wood-pulp component as the SAP becomes gradually less effective in absorbing water. This may also be reflected in the reduction in T_2 change that was observed at high NaCl concentration.

A.9 Conclusion

This study has demonstrated the utility of NMR to investigate the state of water in the different components that constitute the absorbent layer in an incontinence pad. Quan-

titative measurements of relaxation times, T_2-weighted, and MTC measurements have provided information related to the state of the absorbed water. Relaxation times are controlled by a number of processes operating in parallel, such as bulk relaxation, compartmental relaxation rates, and relaxation by diffusion through field gradients. Nevertheless, by examining the relative changes in these times on varying the liquid and material combinations, it has been possible to infer properties of water mobility and environment.

It has been shown that the unique absorbent properties of SAP are not characterised by *tight* water bonding. Instead, the water molecules are more likely to be absorbed and transported by diffusive and osmotic forces into the interior of the polymer structure where they remain relatively mobile. In contrast, in the fluffed wood-pulp, the MTC data indicates that a considerable proportion of the water becomes cross-relaxed by contact with the cellulose molecules.

The relatively mobile nature of water in the hydrogel has been implicated by a low-temperature NMR study that reported a substantial free water signal obtained at sub-zero temperatures [221]. An NMR study using ^{17}O-labelled water reached similar conclusions to those described in this investigation [183]. The use of labelled oxygen rather than hydrogen within the water molecule allowed closer investigation of the shorter time-scale, intra-molecular state of the molecule (the relaxation rate of the oxygen is on the order of ms). In this study, no evidence of a bound component was obtained and the mobile state of the water was demonstrated.

By substituting water with sodium chloride solution, it has been possible to demonstrate the effect of simple electrolytes on the absorptive abilities of the material substrates. A chemical rather than a structural change has been implicated. In the aforementioned ^{17}O NMR study, the results were similarly unchanged by the substitution of water with sodium chlorate ($NaClO_4$) solution [183]. The absorptive changes with salt concentration are of practical importance since human urine contains a high salt concentration (0.75%wt NaCl equivalent [81]), and the altered properties of the incontinence pad, and in particular, the reduced ability of SAP to absorb salt solution, have a direct bearing on the effectiveness of the material for absorption of urine.

While NMR has a great deal of potential for examining wicking and liquid distribution it is most useful for obtaining information not available by other means, such as nature of absorbed water.

Appendix B

Calculations

B.1 Total wetted fibre perimeter in sample cross-section

A number of the parameters needed to predict wicking were measured from polished cross-sections through the sample nonwoven (NP450P).

The fibre radius was estimated from the minor axis of the fitted ellipses:

$$r = a \tag{B.1}$$

where, r is the fibre radius, and a is the semi-minor axis of the ellipse.

The wetted fibre perimeter in the cross-section was calculated from the fitted ellipses using an approximation for the ellipse perimeter due to Ramanujan [176]:

$$C_p \simeq \sum_{i=1}^{n} \pi[(3a_i + 3b_i) - \sqrt{(a_i + 3b_i)(3a_i + b_i)}] \tag{B.2}$$

where, C_p is the wetted fibre perimeter in the cross-section, a_i is the semi-minor axis of the ith ellipse, and b_i is the semi-major axis of the ith ellipse.

The free area in the cross-section, over which flow can occur, was found from the area of the fitted ellipses,

$$C_f = C_a - \sum_{i=1}^{n} (\pi a_i b_i) \tag{B.3}$$

where, C_f is the free area in the cross-section, C_a is the total area in the cross-section, a_i is the semi-minor axis of the ith ellipse, and b_i is the semi-major axis of the ith ellipse.

B.1.1 Results for experimental sample

Sample width, S_w	$= 5.0\times10^{-2}$ m
Sample thickness, S_t	$= 4.24\times10^{-3}$ m
Pixel to length conversion factor	$= 4.22\times10^{-6}$ m pixel^{-1}
FOV dimensions	= 759 pixels × 574 pixels

Fibre radius, r $= 10.80\times10^{-6}$ m ($\pm0.21\times10^{-6}$, n=12)
Wetted fibre perimeter, C_p $= 2.46$ m ($\pm3.55\times10^{-1}$, n=12)
Free area for flow, C_f $= 1.93\times10^{-4}$ m ^{2} ($\pm3.11\times10^{-5}$, n=12)

B.2 Fibre fractions in compressed samples

The total volume of fibre contained in the experimental samples was

$$V_f = \frac{m_s}{\rho_p} \tag{B.4}$$

where, V_f is the volume of fibre in the sample, m_s, is the mass of the sample, and ρ_p is the density of polyester.

The fibre fraction was found as the ratio of the volume of fibre to total volume of the fabric sample

$$f_f = \frac{V_f}{S_w S_t S_l} \tag{B.5}$$

where, f_f is the volume fraction of fibre in the sample, V_f is the volume of fibre in the sample, S_w, is the width of the sample, S_t, is the thickness of the sample, and S_l, is the length of the sample.

B.2.1 Results for experimental sample

Density of polyester, ρ_p $= 1390\,\mathrm{kg\,m^3}$
Sample width, S_w $= 5.0\times10^{-2}$ m
Sample length, S_l $= 4.5\times10^{-1}$ m

The fibre fractions in the compressed samples is,

	NPHS2	*NPHS3*	*NPHS4*	*NPHS5*
Sample mass	1.15×10^{-2} kg	1.16×10^{-2} kg	1.17×10^{-2} kg	1.18×10^{-2} kg
Sample thickness	1.25×10^{-3} m	1.48×10^{-3} m	2.07×10^{-3} m	2.55×10^{-3} m
Fibre volume, V_f	8.24×10^{-6}	8.37×10^{-6}	8.40×10^{-6}	8.49×10^{-6}
Fibre fraction, f_f	29.31%	25.13%	18.03%	14.79%
	NPHS6	*NPHS7*	*NPHS8*	*NPHS9*
Sample mass	1.18×10^{-2} kg	1.19×10^{-2} kg	1.17×10^{-2} kg	1.20×10^{-2} kg
Sample thickness	3.03×10^{-3} m	3.45×10^{-3} m	3.96×10^{-3} m	4.24×10^{-3} m
Fibre volume, V_f	8.52×10^{-6}	8.59×10^{-6}	8.44×10^{-6}	8.65×10^{-6}
Fibre fraction, f_f	12.49%	11.06%	9.48%	9.07%

B.3 Capillary suction pressure

The movement of liquid into the porous material destroys an amount of fibre-air interface, and replaces it with fibre-liquid interface. The change in free energy is given by:

$$E = \gamma_{LV} A_{LV} + (\gamma_{SL} - \gamma_{SV}) A_{SL} + K \tag{B.6}$$

where, E is the change in free energy; A_{LV}, and A_{SL} are the liquid-vapour, solid-liquid, and solid vapour areas; and γ_{LV}, γ_{SL},and γ_{SV} are the liquid-vapour, solid-liquid, and solid vapour surface tensions.

Equation B.6 can be differentiated with respect to length to give:

$$\frac{dE}{dl} = \gamma_{LV} \frac{d(A_{LV})}{dl} + (\gamma_{SL} - \gamma_{SV}) \frac{d(A_{SL})}{dl} \tag{B.7}$$

where, l is the wetted length.

For vertical wicking from a reservoir into a fabric,

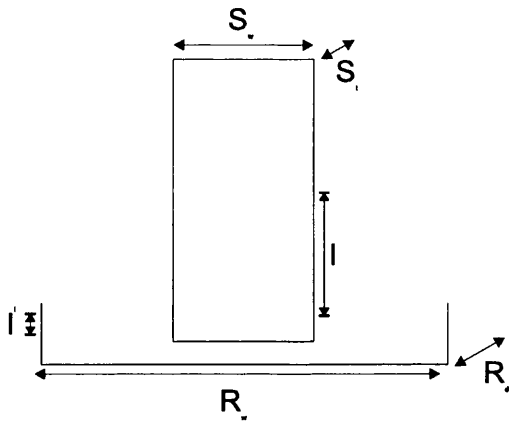

The change in the area A_{SL} is

$$\Delta A_{SL} = \Delta l C_p - l' 2(R_w + R_d) \tag{B.8}$$

where, ΔL is the length by which the liquid in the sample rises. C_p is the wetted fibre perimeter in the cross-section, l' is the length by which the liquid level in the reservoir falls, R_w is the width of the reservoir, and R_d is the depth of the reservoir.

The increase in the solid area at the reservoir edge and is considered small and ignored. Similarly for the increase in liquid-vapour area surrounding the sample.

The resulting force is distributed over the cross-sectional area available for flow, from which the capillary suction pressure can be found.

B.3.1 Results for experimental sample

Reservoir width, R_w	$= 1.41\times10^{-1}$ m
Reservoir depth, R_d	$= 7.35\times10^{-2}$ m
Sample width, S_w	$= 5.0\times10^{-2}$ m
Sample thickness, S_t	$= 4.24\times10^{-3}$ m
Wetted fibre perimeter, C_p	$= 2.46$ m
Free area available for flow, C_f	$= 1.93\times10^{-4}$ m^2
Surface tension, γ	$= 7.27\times10^{-2}$ Nm
Contact angle, θ	$= 69.2^\circ$

The force due to the liquid-fibre interface, calculated in the uncompressed sample is

$$\text{Force} = 63.5\times10^{-3}\,\text{N}$$

The capillary pressure in the compressed samples is

	NPHS2	*NPHS3*	*NPHS4*	*NPHS5*
Fibre fraction	29.31%	25.13%	18.03%	14.79%
Sample thickness	1.25×10^{-3}	1.48×10^{-3}	2.07×10^{-3}	2.55×10^{-3}
Free area, C_a	4.42×10^{-5}	5.54×10^{-5}	8.48×10^{-5}	1.09×10^{-4}
Suction pressure	1.44×10^{3}	1.15×10^{2}	7.5×10^{2}	5.85×10^{2}
	NPHS6	*NPHS7*	*NPHS8*	*NPHS9*
Fibre fraction	12.49%	11.06%	9.48%	9.07%
Sample thickness	3.03×10^{-3}	3.45×10^{-3}	3.96×10^{-3}	4.24×10^{-3}
Free area, C_a	1.33×10^{-4}	1.53×10^{-4}	1.79×10^{-4}	1.93×10^{-4}
Suction pressure	4.80×10^{2}	4.15×10^{2}	3.55×10^{2}	3.30×10^{2}

B.4 Equilibrium wicked height

The equilibrium wicked height can be predicted from the change in free energy due to the wetted fibres. At equilibrium the wicked mass is supported by the liquid-air interface,

$$F = mg \tag{B.9}$$

where, F is the force, m is the equilibrium wicked mass, and g is the acceleration due to gravity.

Mass of liquid wicked into fabric sample, at wicked height h,

$$m = hS_wS_t(1 - f_f)\rho_w \tag{B.10}$$

where, m is the equilibrium wicked mass, h is the equilibrium wicked height, S_w is the sample width, S_t is the sample thickness, f_f is the fibre fraction, and ρ_w is the density of water.

B.4.1 Results for experimental sample

Sample width, $S_w = 5.0\times10^{-2}$ m
Sample thickness, $S_t = 4.24\times10^{-3}$ m
Density of water, $\rho_w = 997.048$ kg/m^3

The equilibrium wicked heights expected in the compressed samples are,

	NPHS2	*NPHS3*	*NPHS4*	*NPHS5*
Fibre fraction, f_f	29.31%	25.13%	18.03%	14.79%
Sample thickness	1.25×10^{-3}	1.48×10^{-3}	2.07×10^{-3}	2.55×10^{-3}
Eqm mass, m (kg)	6.48×10^{-3}	6.48×10^{-3}	6.48×10^{-3}	6.48×10^{-3}
Eqm height, h (m)	147×10^{-3}	117×10^{-3}	77×10^{-3}	60×10^{-3}
Measured height (m)	1.82×10^{-1}	1.49×10^{-1}	1.14×10^{-1}	8.33×10^{-2}

	NPHS6	*NPHS7*	*NPHS8*	*NPHS9*
Fibre fraction	12.49%	11.06%	9.48%	9.07%
Sample thickness	3.03×10^{-3}	3.45×10^{-3}	3.96×10^{-3}	4.24×10^{-3}
Eqm mass, m (kg)	6.48×10^{-3}	6.48×10^{-3}	6.48×10^{-3}	6.48×10^{-3}
Eqm height, h (m)	49×10^{-3}	42×10^{-3}	36×10^{-3}	33×10^{-3}
Measured height (m)	6.94×10^{-2}	4.72×10^{-2}	3.40×10^{-2}	2.99×10^{-2}

B.5 Washburn equation

The Washburn equation predicts the wetted distance to increase with the square root of time,

$$l(t) = \sqrt{\frac{r_h \gamma \cos\theta}{2\tau^2 \eta}}\sqrt{t} \tag{B.11}$$

where, l is the wetted length, r_h is the hydraulic radius, γ is the surface tension, θ is the liquid-fibre contact angle, τ is the tortuosity, η is the liquid viscosity, and t is the elapsed time.

The characteristic number for wicking is,

$$l_{W0} = \sqrt{\frac{r_h \gamma \cos\theta}{2\tau^2 \eta}} \tag{B.12}$$

The hydraulic radius can be estimated, with reference to conduit flow,

$$r_h = \frac{C_f}{C_p} \tag{B.13}$$

where, C_f is the cross-sectional area available for flow, and C_p is the total wetted fibre perimeter in the sample cross-section.

B.5.1 Results for experimental sample

Sample width, S_w $= 5.0\times10^{-2}$ m
Tortuosity, τ $= 2.47$
Surface tension, γ $= 7.27\times10^{-2}$ Nm
Contact angle, θ $= 69.2^{\circ}$
Liquid viscosity, η $= 8.9\times10^{-4}$ Nm^2
Wetted perimeter, C_p $= 2.46$ m

Washburn's equation predicts the wicking numbers in the compressed samples to be,

	NPHS2	*NPHS3*	*NPHS4*	*NPHS5*
Sample thickness (m)	1.25×10^{-3}	1.48×10^{-3}	2.07×10^{-3}	2.55×10^{-3}
Fibre volume, V_f (m^3)	8.24×10^{-6}	8.37×10^{-6}	8.40×10^{-6}	8.49×10^{-6}
Fibre fraction, v_f (%)	29.31	25.13	18.03	14.79
Free c/s area, C_f (m^2)	4.42×10^{-5}	5.54×10^{-5}	8.48×10^{-5}	1.09×10^{-4}
Hydraulic radius, r_h (m)	1.79×10^{-5}	2.25×10^{-5}	3.44×10^{-5}	4.41×10^{-5}
Wicking, l_{W0} ($\sqrt{\text{ms}^{-1}}$)	6.53×10^{-3}	7.31×10^{-3}	9.05×10^{-3}	1.02×10^{-2}
	NPHS6	*NPHS7*	*NPHS8*	*NPHS9*
Sample thickness (m)	3.03×10^{-3}	3.45×10^{-3}	3.96×10^{-3}	4.24×10^{-3}
Fibre volume, V_f (m^3)	8.24×10^{-6}	8.37×10^{-6}	8.40×10^{-6}	8.49×10^{-6}
Fibre fraction, v_f (%)	12.49	11.06	9.48	9.07
Free c/s area, C_f (m^2)	1.33×10^{-4}	1.53×10^{-4}	1.79×10^{-4}	1.93×10^{-4}
Hydraulic radius, r_h (m)	5.38×10^{-5}	6.23×10^{-5}	7.28×10^{-5}	7.82×10^{-5}
Wicking, l_{W0} ($\sqrt{\text{ms}^{-1}}$)	1.13×10^{-2}	1.22×10^{-2}	1.32×10^{-2}	1.36×10^{-2}

B.6 Darcy type model for wicking

The Darcy equation is

$$V = \frac{K}{\eta}\frac{dP_s}{dl} \tag{B.14}$$

where, V is the Darcy velocity of the wicking liquid (dl/dt), K is the permeability of the porous medium, η is viscosity of the flowing liquid. P_s is the capillary suction pressure, and l is the coordinate length along the macroscopic direction of flow.

The Darcy equation gives a wicking number of

$$l_{D0} = \sqrt{\frac{2KP_s}{\eta}} \tag{B.15}$$

where, l_{D0} is the Darcy wicking number,

The permeability can be calculated using a number of formulae, the empirical equation proposed by Davies is used here [48]:

$$K = \frac{2r^2}{64(f_f)^{\frac{3}{2}}[1 + 56(f_f)^3]} \tag{B.16}$$

where, K is the permeability, r is the fibre radius, and f_f is the fibre fraction.

The capillary suction has been previously described

B.6.1 Results for experimental sample

Fibre radius, $r = 10.80\times10^{-6}$ m

	NPHS2	*NPHS3*	*NPHS4*	*NPHS5*
Fibre fraction, v_f (%)	29.31	25.13	18.03	14.79
Permeability, K (Darcy)	1.91×10^{-11}	3.06×10^{-11}	7.17×10^{-11}	1.08×10^{-10}
Suction p., P_s (Nm^2)	1.44×10^{3}	1.15×10^{3}	7.50×10^{2}	5.85×10^{2}
Wicking, l_{D0} ($\sqrt{ms^{-1}}$)	7.85×10^{-3}	8.89×10^{-3}	1.10×10^{-2}	1.19×10^{-2}
	NPHS6	*NPHS7*	*NPHS8*	*NPHS9*
Fibre fraction, v_f (%)	12.49	11.06	9.48	9.07
Permeability, K (Darcy)	1.49×10^{-10}	1.84×10^{-10}	2.38×10^{-10}	2.56×10^{-10}
Suction p., P_s (Nm^2)	4.80×10^{2}	4.15×10^{2}	3.55×10^{2}	3.30×10^{2}
Wicking, l_{D0} ($\sqrt{ms^{-1}}$)	1.27×10^{-2}	1.31×10^{-2}	1.38×10^{-2}	1.38×10^{-2}

B.7 Saturation fitting

Expected mass per unit area in the saturated sample can be found by assuming the available void volume is filled with water.

$$V_v = S_t(1 - f_f) \tag{B.17}$$

where, S_t is the sample thickness, and f_f is the fibre fraction.

Giving the mass of water per unit area as

$$M_A = V_v\rho_w \tag{B.18}$$

where, M_A is the mass per unit area, and ρ_w is the density of water.

This mass per unit area, based on full filling of the sample void space, van be compared to the measured mass per unit area found by plotting and fitting the wicked mass against the wicked area.

B.7.1 Results for experimental sample

Density of water, $\rho_w = 997.048\,\mathrm{kg/m^3}$
Sample width, $S_w \quad = 5.0\times10^{-2}\,\mathrm{mm}$

Measured saturations in the compressed samples,

	NPHS2	*NPHS3*	*NPHS4*	*NPHS5*
Sample thickness (m)	1.25×10^{-3}	1.48×10^{-3}	2.07×10^{-3}	2.55×10^{-3}
Fibre fraction, f_f (%)	29.31	25.13	18.03	14.79
Maximum M_A (kg $\mathrm{m^{-1}}$)	8.81×10^{-1}	1.10	1.69	2.17
Fitted M_A (kg $\mathrm{m^{-1}}$)	8.70×10^{-1}	1.13	1.45	1.83
Saturation, (%)	98.7	101.9	86	84.5
	NPHS6	*NPHS7*	*NPHS8*	*NPHS9*
Sample thickness (m)	3.03×10^{-3}	3.45×10^{-3}	3.96×10^{-3}	4.24×10^{-3}
Fibre fraction, f_f (%)	12.49	11.06	9.48	9.07
Maximum M_A (kg $\mathrm{m^{-1}}$)	2.64	3.06	3.57	3.84
Fitted M_A (kg $\mathrm{m^{-1}}$)	2.12	2.46	2.78	2.70
Saturation, (%)	80.36	80.42	77.69	70.37

Appendix C

Experimental equipment specifications

C.1 Apparatus specification

Camera

Hitachi Denshi CCD array camera model KP-M1E/K

including

(TA-M1) mount

(PSU - 130/12PP) power supply

Optics

Close up manual zoom lens (LMZ45C5)

18-108mm (6:1)

HOYA Green filter

Lighting

1 pair 24W PLL lamps (Ballast: Quicktronic QT 1x24/230-240 40kHz))

Frame grabber

Matrox Meteor PPB Standard analogue colour/monochrome

IMG-7W2-TO-1BNC input cable

Image capture computer (hardware)

Dell Optiplex GXa6266 266Mhz 64MB 4.3GB

4GB SCSI System

+ 17" Ultrascan monitor

+ 12/24x CD-ROM

+ 4GB SCSI-3

Additional storage
- EIDE CD-RW
  - Hewlett Packard 71000i (EIDE-ATAPI) CD Re-writer (internal)
  - Iomega 100MB Zip drive (SCSI internal)

Image capture computer (software)
- Microsoft Windows NT Version 4.00.1381
- Microsoft Visual C++ Version 5.0
- Microsoft Office '97
- MIL-Lite libraries ver 5.1
- Mathworks Matlab Version 5.3.0.10183 R11
  - Optimisation toolbox Version 2.0 (09-Oct-1998)
  - Image processing toolbox Version 2.2 (05-Aug-1998)

Balance
- Sartorius BP310s
  - Readability 0.001 g
  - Capacity 310 g
  - Reproducibility ±0.001g

Balance capture computer (hardware)
- 486 Personal Computer

Balance capture computer (software)
- Microsoft Quickbasic routines

Polishing Machine
- Struers Labapol 5 (grinding and polishing machine)
  - 50-500 rpm
- Struers Labaforce 3 (semi-automatic specimen mover)
  - mover plate for three specimens
  - force 5 N to 40 N

Microscope
- Leica DM LM metallagraphic microscopic
  - Reflectance and transmission illuminators
  - N PLAN 5×
  - N PLAN 10×
  - Eye piece HC PLAN 10×

Grey filter

Cahn dynamic contact angle analyser model 322

500mg calibration weight

300mg counter balance, using balance loop 'B' for measurements

Stage travel 15 mm at 151 microns per second.

Appendix D

Apparatus plans

D.1 Apparatus plans

Apparatus plan	*figure*
Fabric support	D.1
Wicking rig support	D.2
Wicking rig (top)	D.3
Base	D.4
Rail support	D.5
Rail plate clamp	D.6
Camera support	D.7
Camera support	D.8
Transmission illumination lampholder	D.9
Compression cell	D.10

Table D.1: Plans in appendix

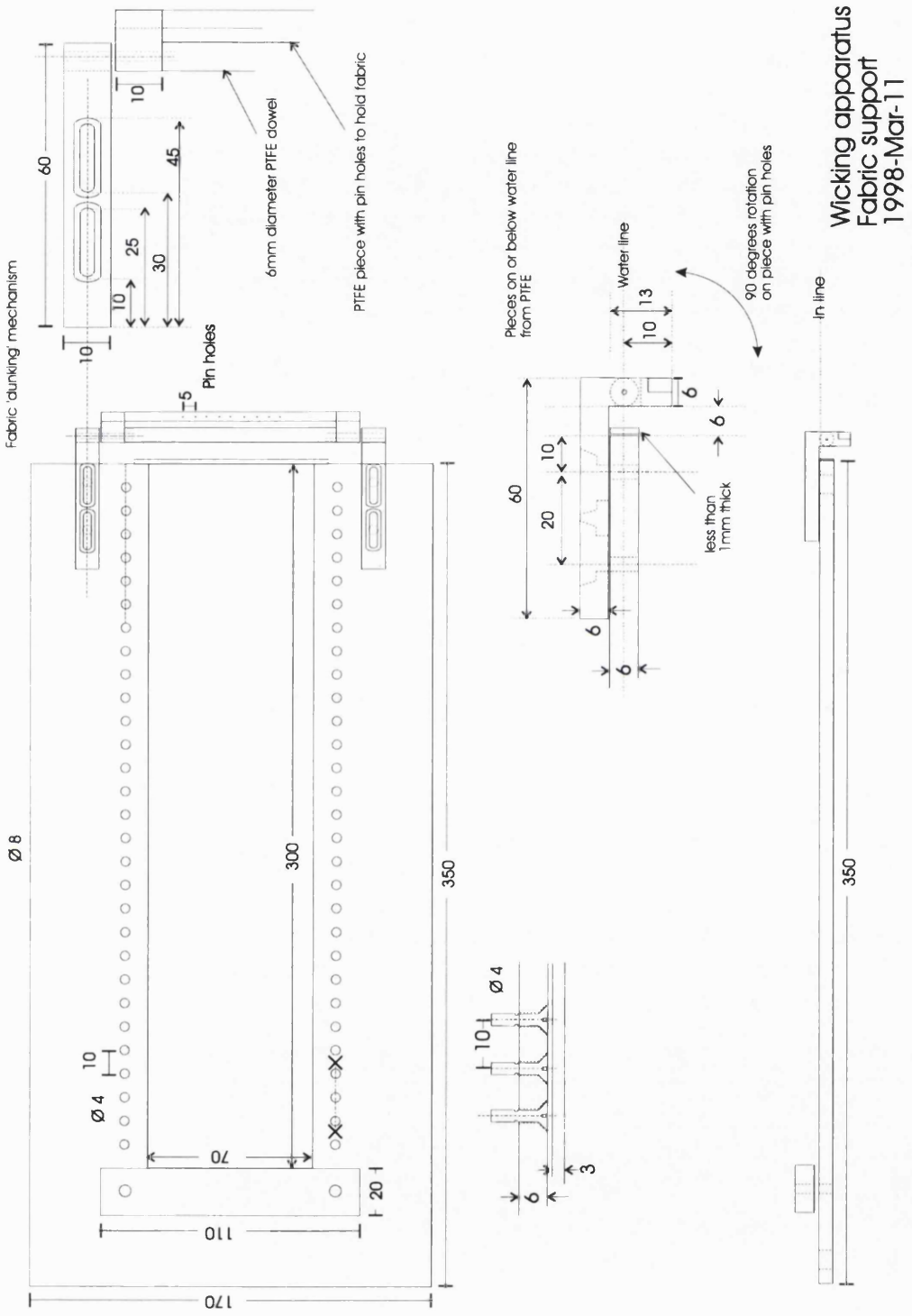

Figure D.1: Fabric support

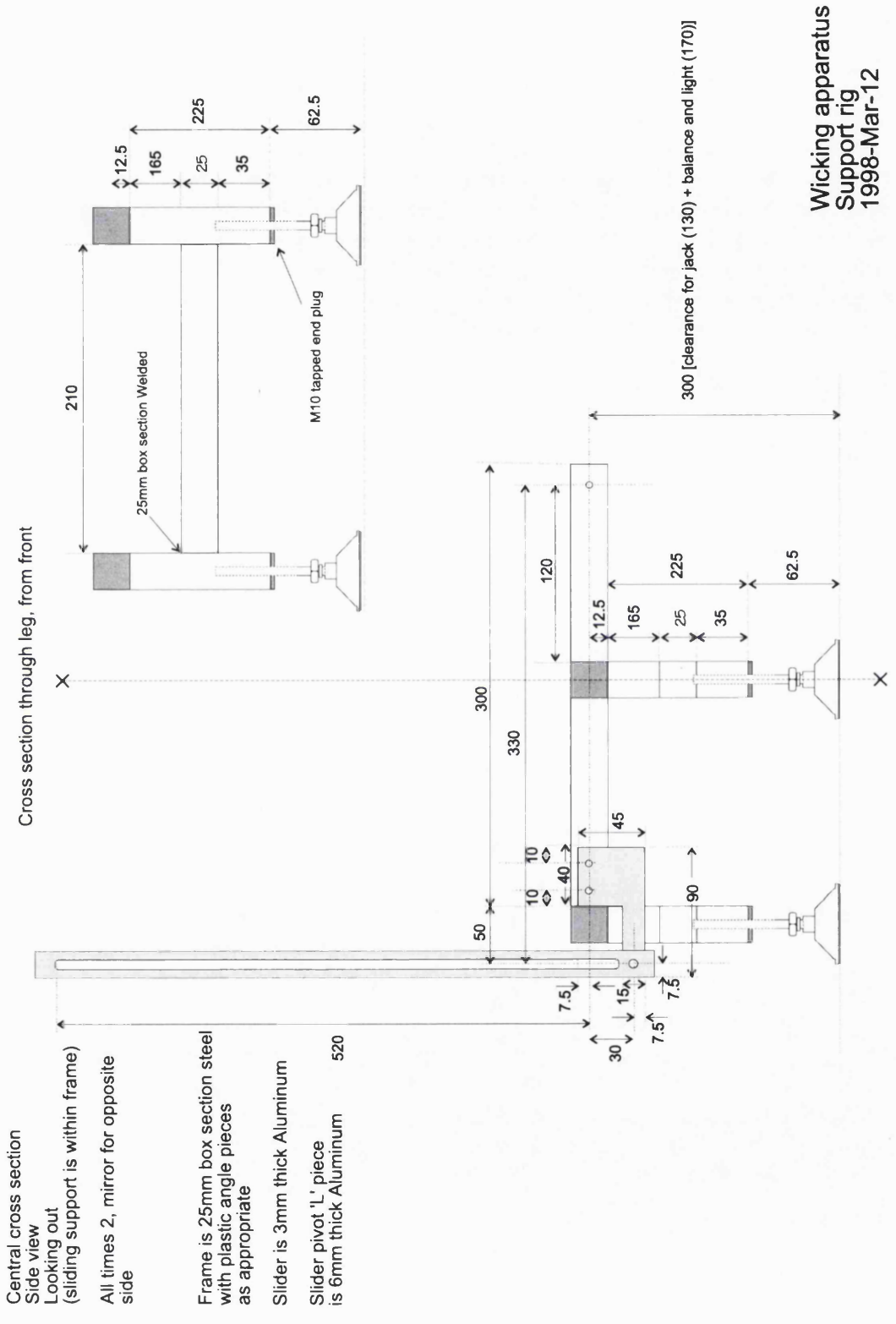

Figure D.2: Wicking rig support *elevation*

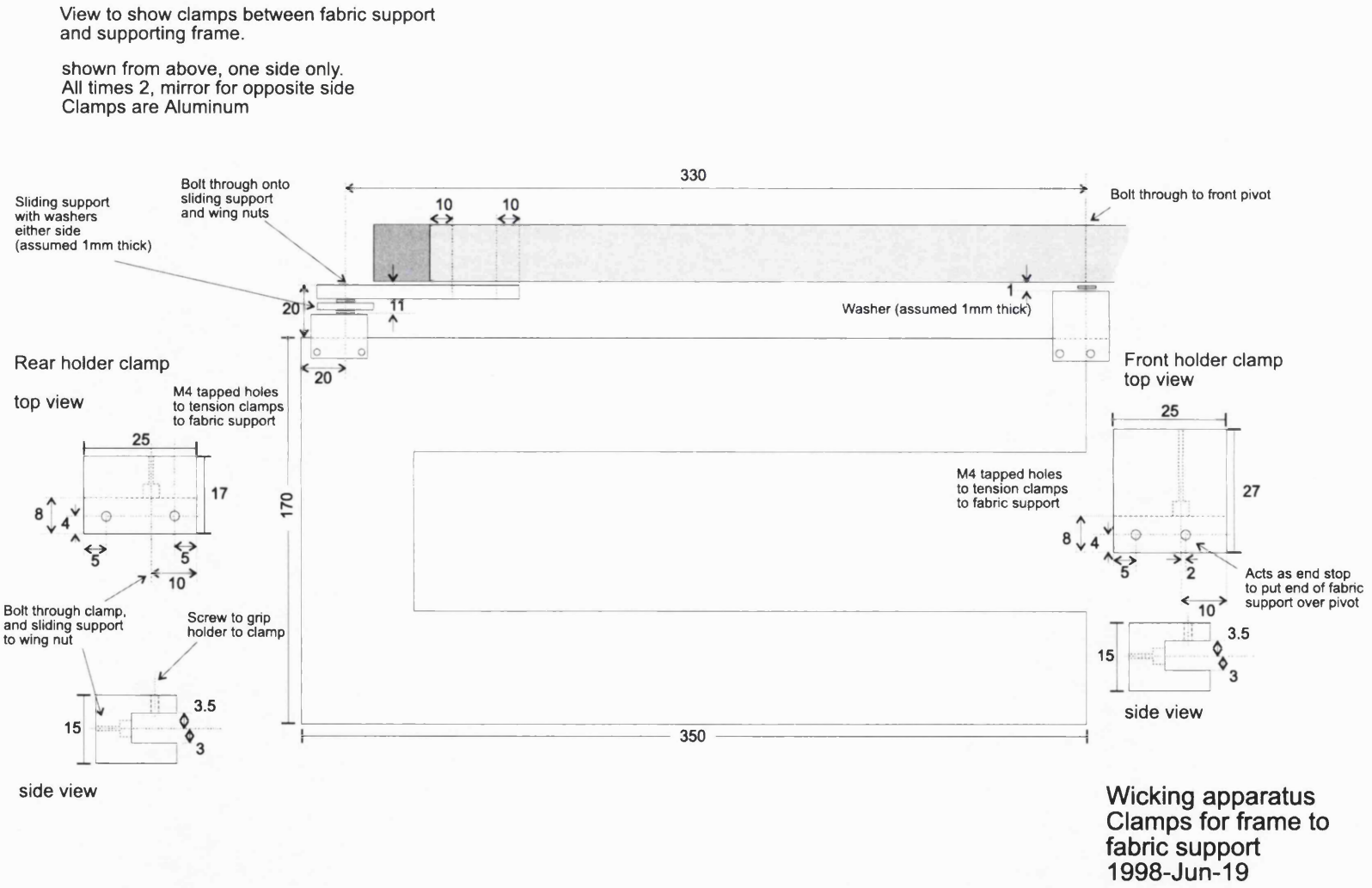

Figure D.3: Wicking rig support *top view*

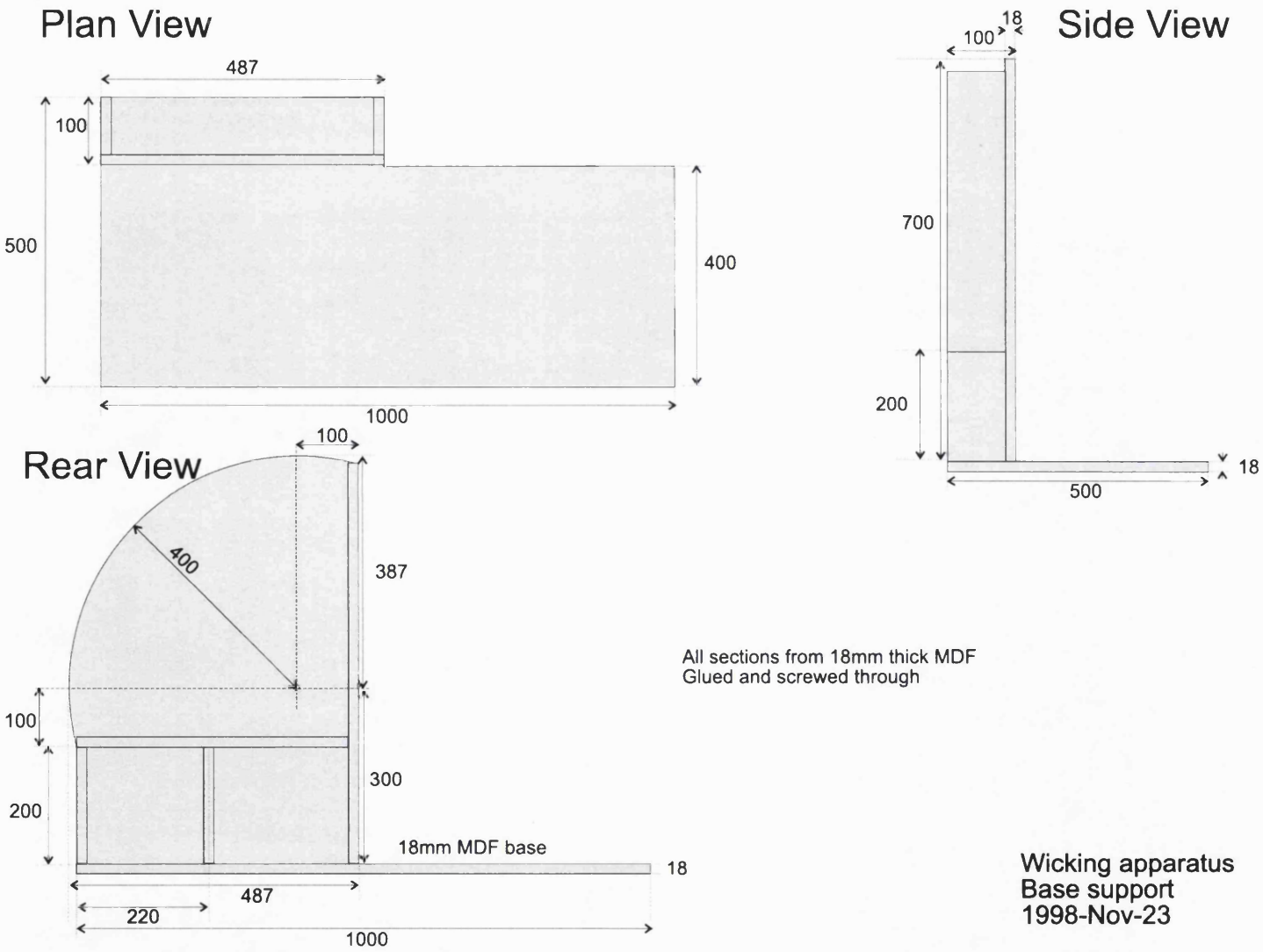

Figure D.4: Base

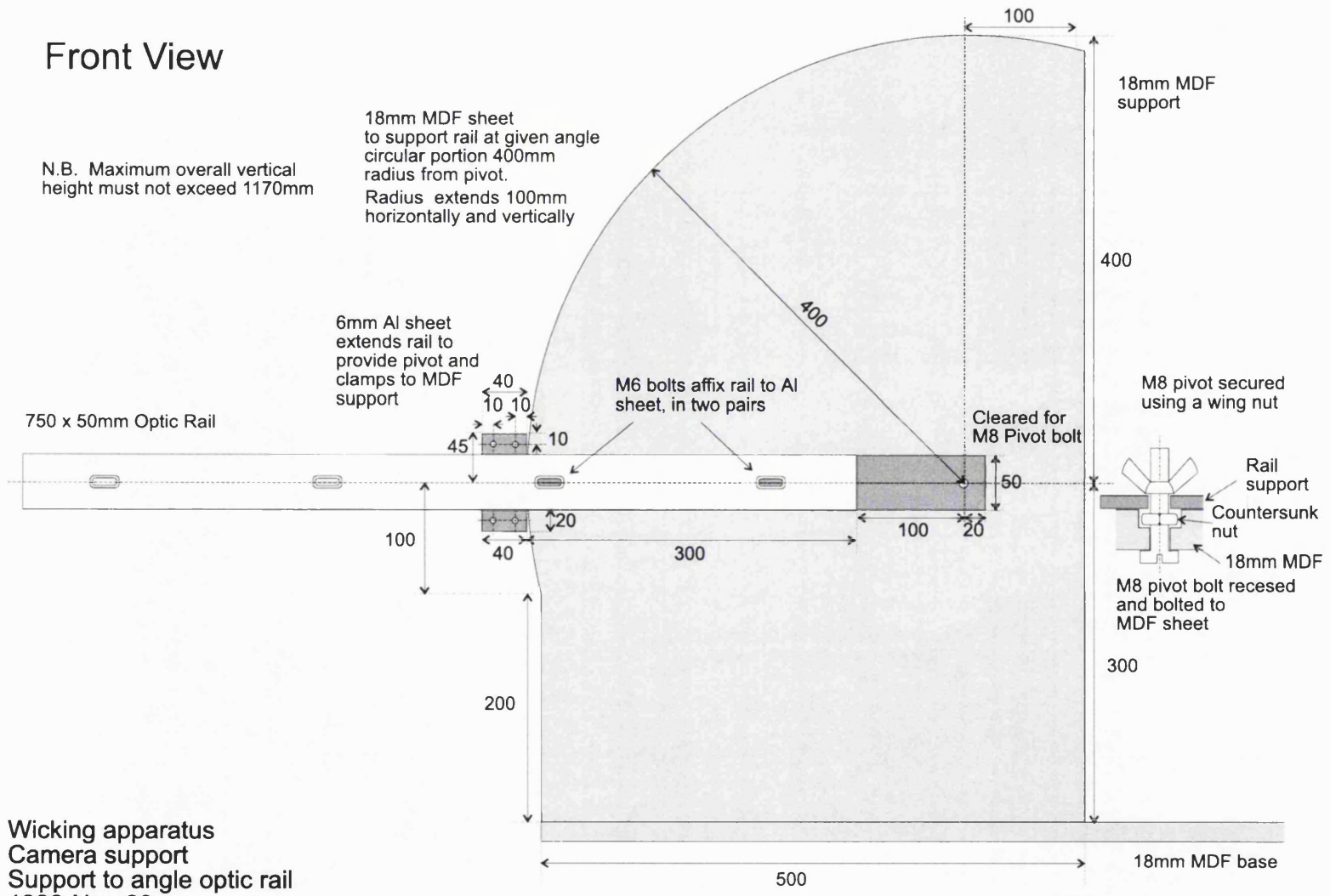

Figure D.5: Rail support, to support pivoted rail

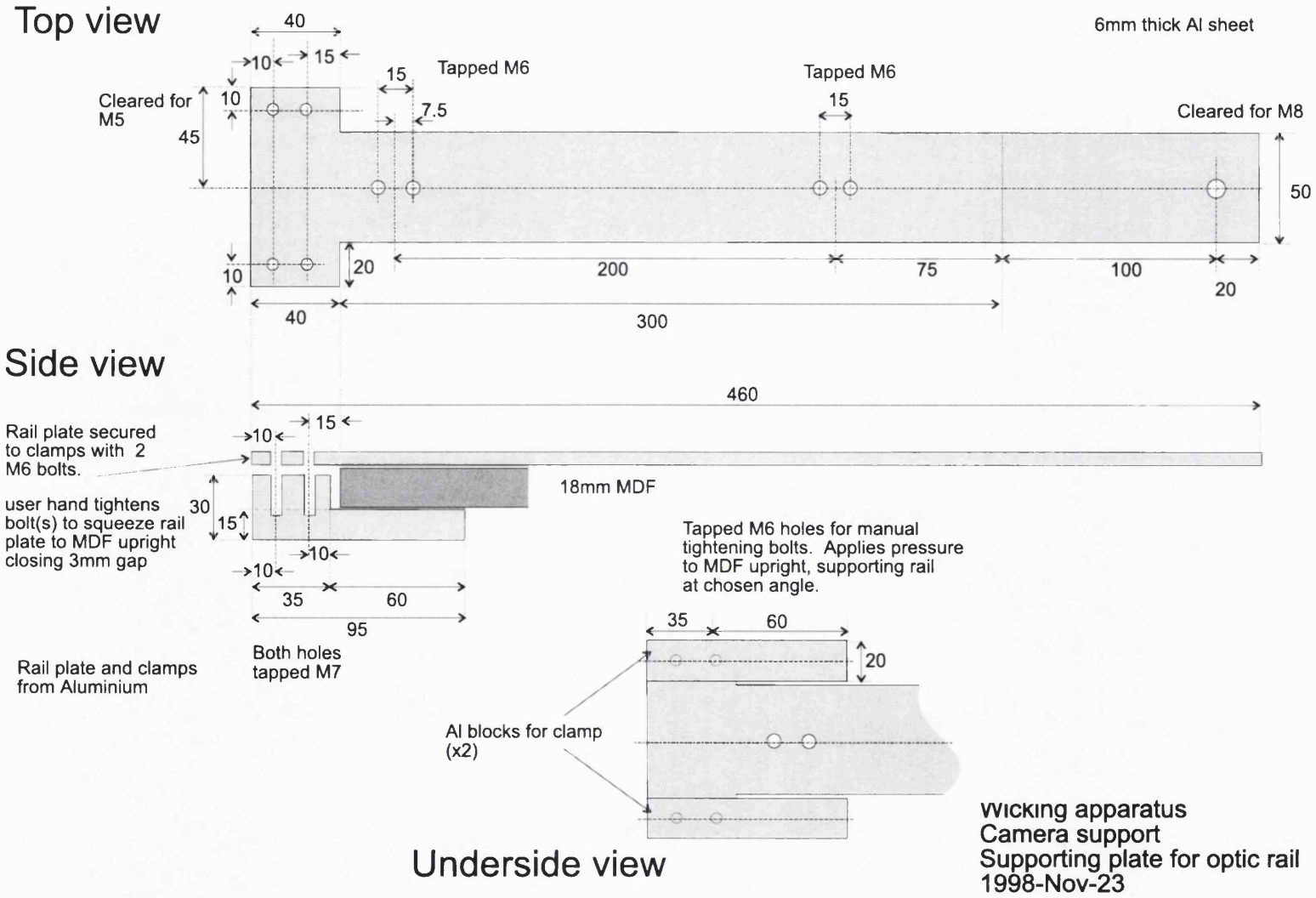

Figure D.6: Rail plate, to support rail on backplate

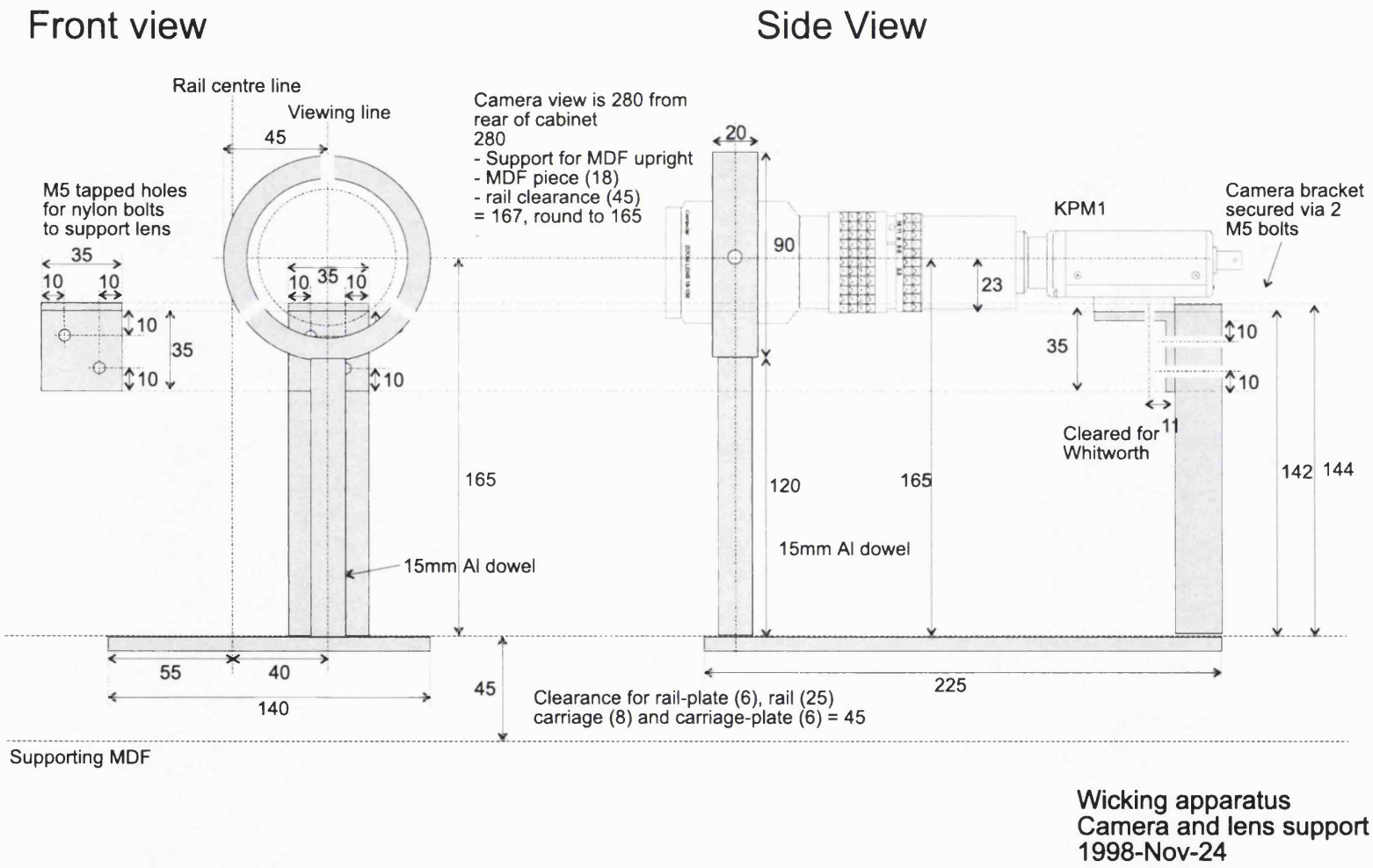

Figure D.7: Rail mounted camera support *elevation*

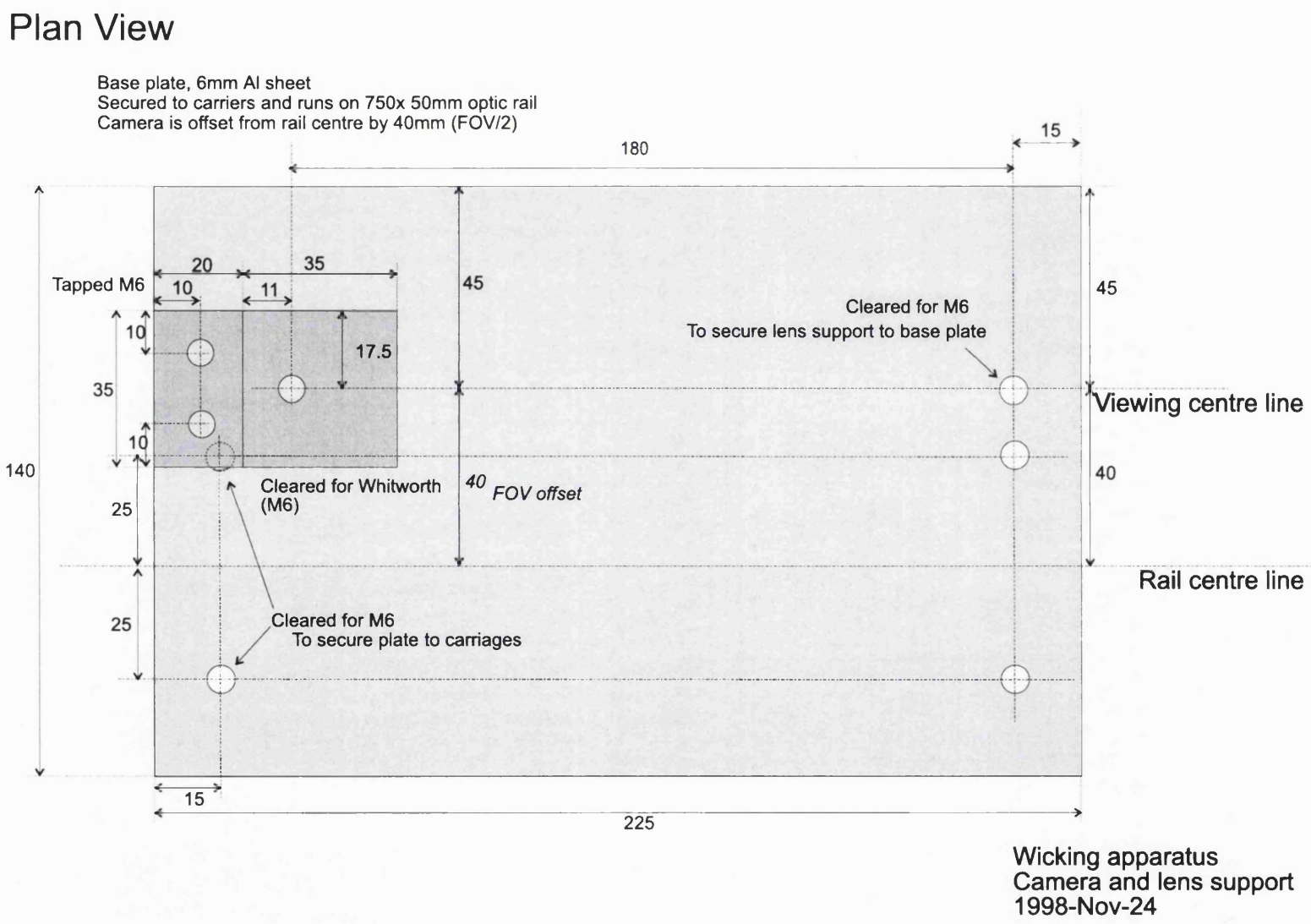

Figure D.8: Rail mounted camera support *top view*

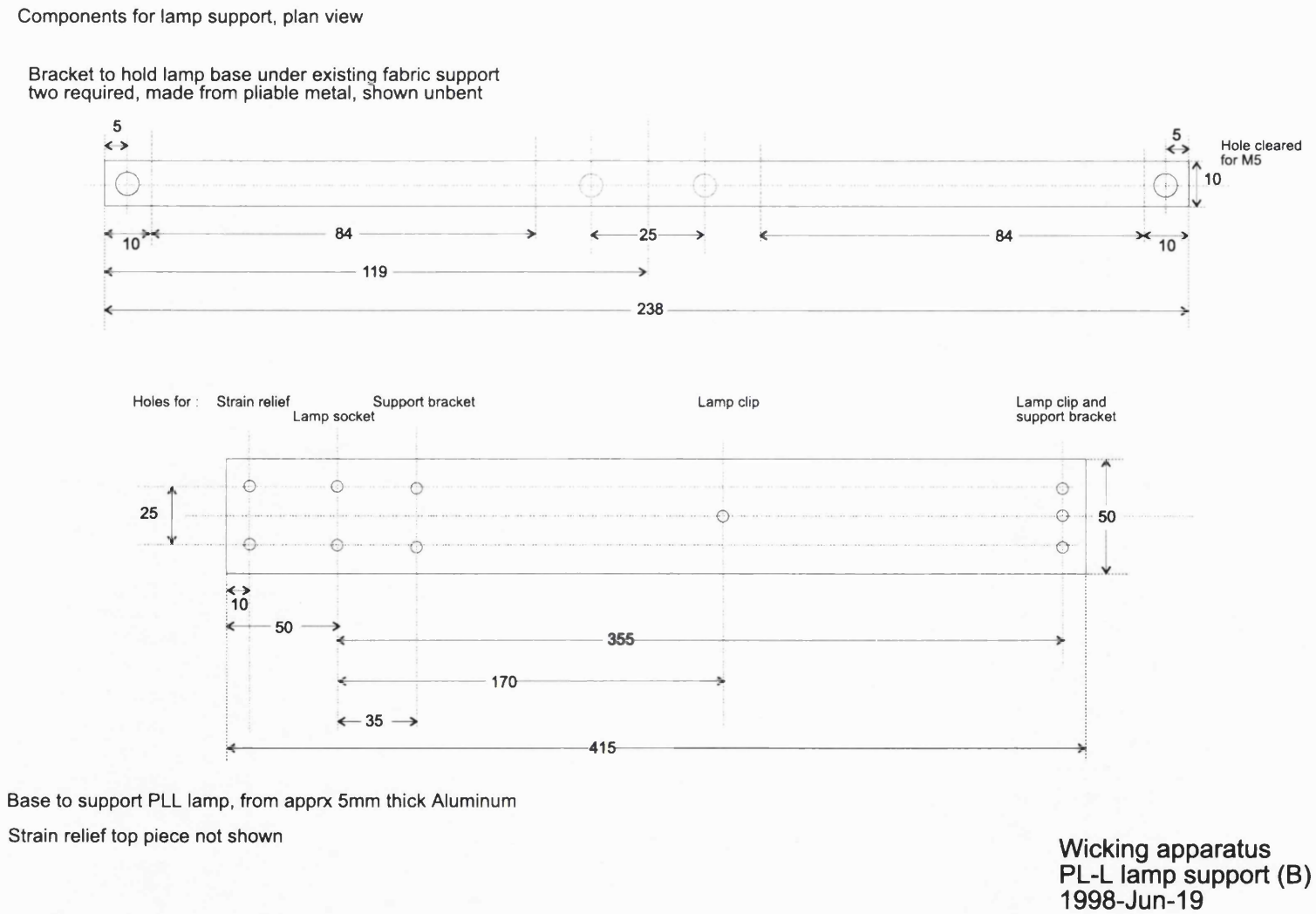

Figure D.9: Lampholder parts for transmission illumination of sample

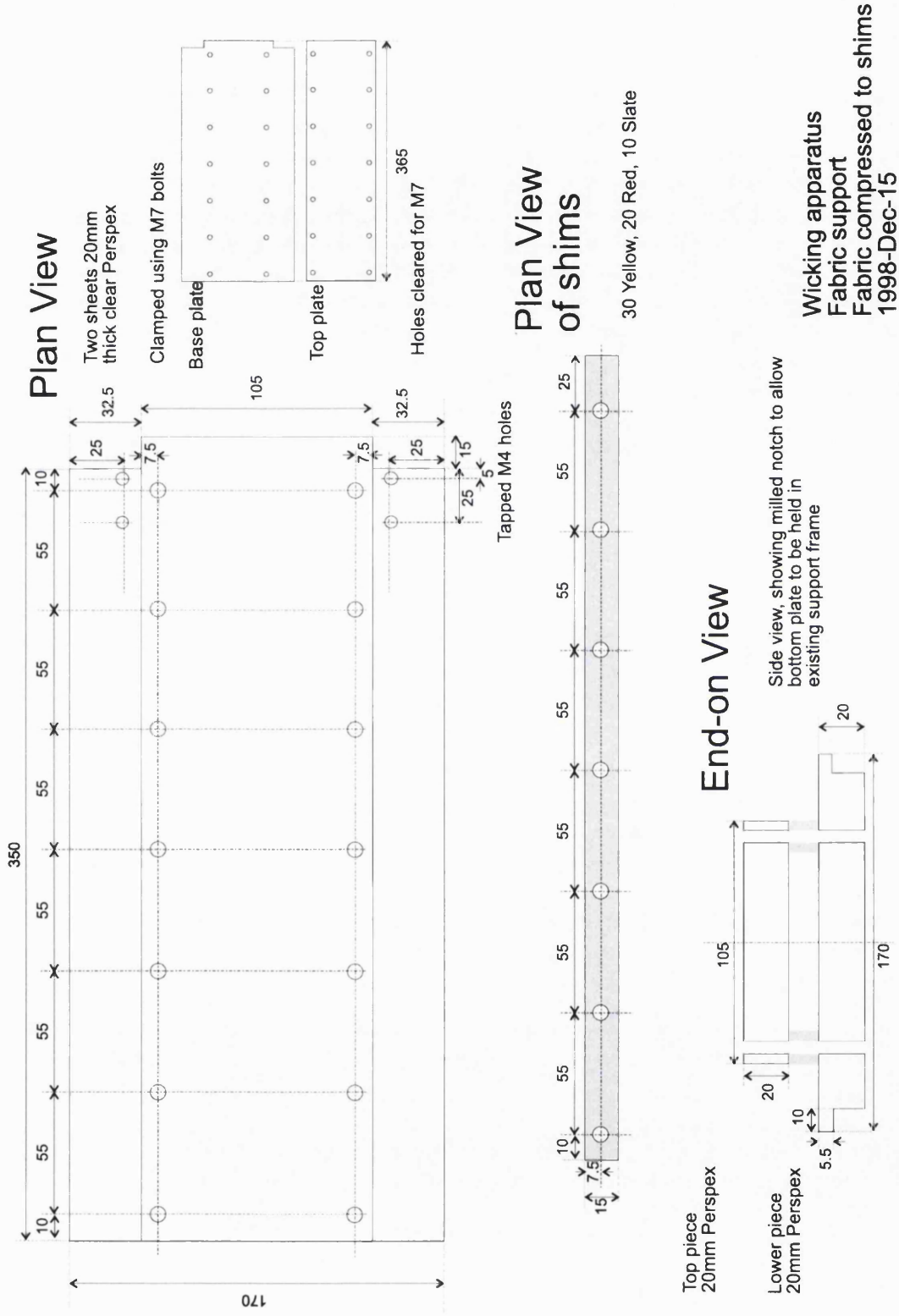

Figure D.10: Compression cell

Appendix E

Code

E.1 Matlab code

Listings for the core Matlab code are presented in this appendix. Graphical user interface code used in the ellipse fitting has been omitted for brevity.

Image processing for area calculation from wicking images

`area_calc.m` Matlab function to calculate the wet areas for each image in a sequence of wetting images. Wetted pixels are determined as those that exceed a threshold difference between the image under consideration and a reference image.

Ellipse identification for cross sectional analysis

`find_ellipses.m` Matlab function to find ellipses within a binary, labelled object image. This function mainly acts to wrap calling the ellipse fitting function repeatedly for the image

`rht_fit_ellipses.m` Repeatedly calls the ellipse fit on an image, until all ellipses are believed to have been found.

`rht_epochs.m` Applies an ellipse specific randomised Hough transform, to propose ellipse fits from the the supplied points. This is an implementation of the method described by McLaughlin [147].

`count_pts_near_ellipse.m` A function used to score the goodness of a proposed ellipse fit for a range of points. The score is found from the number of points close enough to be considered part of the ellipse described by the supplied parameters; and normalised to the perimeter of the ellipse, estimated using Ramanujan's method [176].

area_calc.m Page 1/13

```
function [wet_area_details, wet_sums] = ...
   area_calc(input_directory, image_prefix, image_type, ...
   reference_image_number, start_image_number, end_image_number, image_step, ...
   output_directory)

%% Matlab function to calculate the wet areas for each image in a sequence
%% Uses image differences from a reference image
%% Each pixel is designated as wet when it's intensity exceeds
%% max_threshold * (max intensity in sequence)
%% Where max intensity is precalculated and loaded from a file
%% To exclude noise a pixel must also exceed a 'noise_threshold' to be
%% considered wet
%%
%% options are currently set in the first few lines of the script
%% e.g,
%%
%% filter = 'median'/'none'
%% cleanup = 'true'/'false'
%% difference_type = 'reference'/'adjacent'
%% staywet = 'true'/'false'
%% wetting_cleanup = 'true'/'false'
%%
%% noise_threshold = value
%% max_threshold = value
%%
%% extract_row = value
%% sample_pixel_col = value
%% sample_pixel_row = value
%%
%% MAL (1998-May-28)

%% User set values
iptsetpref('ImshowBorder', 'tight'); %% use whole figure window for images
warning off; %% stop moaning about divide by zeros(!)

chatty_mode = 'off' %% chatty-ness
filter = 'median'
majority_cleanup = 'false'
region_fill = 'true'
difference_type = 'reference'
staywet = 'false'
wetting_cleanup = 'false'
illumination_correction = 'true'
area_to_length = 'true'
lighting_mode = 'reflectance'

wet_threshold = 25 %% 15 or 7; %% Threshold to determine wet pixels
liquid_entry_col = [];
entry_ignore = 50;

extract_row = 150; %% Sample row to extract from sequence
sample_pixel_col = 150; %% Sample pixel to extract from sequence
sample_pixel_row = 150; %% Sample pixel to extract from sequence
fabric_extraction = 'mask' % window or use mask
fabric_window_start = 80
fabric_window_end = 500

calc_front_results = 'yes'
save_extracted_rows = 'yes'
save_wet_rows = 'yes'
save_difference_image = 'no'
save_front_image = 'no'
save_wet_image = 'no'
save_front_overlay = 'no'
save_wet_overlay = 'no'
```

area_calc.m Page 2/13

```
overlay_intensity = 0; %% pixel intensity in overlay
jpeg_quality = 100; %% quality of images saved by processing
file_num_format = '%04i'; %% ie 0xxx

%%%% Filenames to use
%% Input
processing_filename = ('area_processing.txt');
bg_mask_filename = 'bg_mask';
bg_mask_file = [output_directory bg_mask_filename '.tif'];
edge_mask_filename = 'edge_mask';
edge_mask_file = [output_directory edge_mask_filename '.tif'];
expt_param_filename = ('experiment_details.txt');
%% file written by the expt dialog

%% Ouput
area_filename = ('wet_area.txt');
front_filename = ('wet_front.txt');
wet_rows_filename = ('row_extract_wet.tif');
extracted_rows_filename = ('row_extract.tif');
difference_file_prefix = ('diff');
front_file_prefix = ('front');
wet_file_prefix = ('wet_pixels');
fronto_file_prefix = ('front_image') %% overlays
weto_file_prefix = ('wet_image') %% overlays

%% Initialise the following variables from the parameter file
FOV_width = str2num( get_parameter('FOV width', ...
   [input_directory expt_param_filename], ':') );

FOV_height = str2num( get_parameter('FOV height', ...
   [input_directory expt_param_filename], ':') );

expt_ref = get_parameter('Experiment reference', ...
   [input_directory expt_param_filename], ':');
disp(['Experiment reference : ' expt_ref]);

sample = get_parameter('Sample reference', ...
   [input_directory expt_param_filename], ':');
disp(['Sample reference : ' sample]);

%%%%% Initialisation of data used by this script
reference_image = [];

extracted_rows = [];
wetting_rows = [];

wet_image = [];
wet_area_details = [];
wet_front_details = [];
wet_sums = [];
wet_length_details = [];
saturation_sequence = [];
wetting_sequence = [];
sample_pixel_intensities = [];
sample_pixel_wetting = [];

%%%%% Set up for processing sequence
start_time = clock;

disp('Set-up for sequence processing')
%% Load in the reference image
if(strcmp(difference_type, 'reference'))
   %% load in the reference image
   disp(' Loading the reference image');
   image_filename ...
      = local_imname(image_prefix, image_type, reference_image_number);
```

area_calc.m Page 3/13

```
   image_file = [input_directory image_filename];
   reference_image = imread(image_file);
else
   disp(' Loading the reference image (should be the start image)');
   image_filename ...
       = local_imname(image_prefix, image_type, reference_image_number);
   image_file = [input_directory image_filename];
   reference_image = imread(image_file);
end

[num_image_rows num_image_cols] = size(reference_image);
pixel_height_mm = FOV_height / num_image_rows;
pixel_width_mm = FOV_width / num_image_cols;
pixel_area_mm = (FOV_height * FOV_width) / (num_image_rows * num_image_cols);

%% Having loaded the reference_image the following variables can be initialised
liquid_entry_col = num_image_cols;
%% initialise wet_image
wet_image = zeros(size(reference_image));
%% initialise wetting_sequence
wetting_sequence = zeros(size(reference_image));

if(strcmp(calc_front_results, 'yes'))
   disp([' Loading pre-calculated Edge pixels  ' edge_mask_file]);
   edge_mask = imread(edge_mask_file);
   edge_mask = logical(edge_mask); %%want logical rather than uint8

   %% Find the background pixels, used to extract the fabric edges in wetting
   %% front image
   if(strcmp(chatty_mode, 'on'))
      disp('-> Edge mask');
      imshow(edge_mask);
      title('Edge mask');
      pause;
   end
end

if(strcmp(area_to_length, 'true'))
   disp([' Loading pre-calculated background pixels  ' bg_mask_file]);
   bg_mask = imread(bg_mask_file);
   bg_mask = logical(bg_mask); %%want logical rather than uint8

   %% Find the background pixels, used to find the mean width
   %% front image
   mean_width_pixels = mean(sum(~bg_mask(:, 1:(end - entry_ignore)) ));
   mean_width_mm = mean_width_pixels .* pixel_height_mm;

   disp([' Mean sample width= ' num2str(mean_width_pixels) ' pixels, ' ...
         num2str(mean_width_mm) 'mm' ]);

   if(strcmp(chatty_mode, 'on'))
      disp('-> Background mask');
      imshow(bg_mask);
      title('Background mask');
      pause;
   end

   bg_mask = [];
end

%% use the reference image to calculate the illumination correction
if(strcmp(illumination_correction, 'true'))
      disp('-> Calculating background illumination');

      %% correct left right only
      mean_lr_illum ...
```

area_calc.m Page 4/13

```
          = double( mean(reference_image(:, 1:(end - entry_ignore)) ));

      %% find the polynomial that describes the variance
      [P, S] = polyfit([1:num_image_cols - entry_ignore], mean_lr_illum, 3);
      illum_variation = polyval(P, [1:num_image_cols]);

      illum_correction = repmat(mean(illum_variation) ./ illum_variation, ...
                                num_image_rows, 1);
      disp('-> Done');

      reference_image ...
          = uint8(double(reference_image) .* illum_correction);

     if(strcmp(chatty_mode, 'on'))
       plot(mean_lr_illum, 'b');
       hold on
       plot(illum_variation, 'r');
       title('Illumination variance');
       pause;

       imshow(mat2gray(illum_correction));
       title('Illumination correction image');
       disp('-> Illumination correction');
       pause

       imshow(reference_image);
       title('Illumination corrected image');
       disp('-> Illumination corrected image');
       pause
     end

     %% free these, as we don't need them anymore
     P = [];
     S = [];
     illum_variation = [];
     mean_lr_variaion = [];
end

%% Can now calculate the wetting thresholds
if(strcmp(lighting_mode, 'transmission'))
   wetting_thresholds = wet_threshold;
elseif (strcmp(lighting_mode, 'reflectance'))
   %% remember in reflectance pixels are wet once below the threshold
   wetting_thresholds =  wet_threshold;
end

%%%%%%%%%%%%%%%%%%%% Processing images %%%%%%%%%%%%%%%%%%%%%%%%%%%%%%
disp('Processing images');
for current_image_num = start_image_number:image_step:end_image_number,

   %% Work out the current file name
   image_filename = local_imname(image_prefix, image_type, current_image_num);
   image_file = [input_directory image_filename];

   %% Tell user the current image file and load it
   disp(image_file);
   this_image = imread(image_file);

   if(strcmp(chatty_mode, 'on'))
      disp('-> Loaded the current image');
      imshow(this_image);
      title('this image');
      pause;
   end

   if(strcmp(illumination_correction, 'true'))
```

area_calc.m Page 5/13

```
    this_image = uint8(double(this_image) .* illum_correction);

    if(strcmp(chatty_mode, 'on'))
      disp('-> Illumination correcting image');
      imshow(this_image);
      title('Illumination corrected image');
            disp('-> Illumination corrected image');
      pause;
    end
  end

  %% Calculate the difference image
  if (strcmp(lighting_mode, 'transmission'))
    difference_image = double(this_image) - double(reference_image);
  elseif (strcmp(lighting_mode, 'reflectance'))
    difference_image = double(reference_image) - double(this_image);
  end

  if(strcmp(chatty_mode, 'on'))
    disp('-> Calculating difference image');
    imshow(mat2gray(difference_image));
    title('difference image');
    pause;
  end

  %% filter if needed
  if(strcmp(filter, 'median'))
     % Clean image using a median filter
     difference_image = medfilt2(difference_image);
     if(strcmp(chatty_mode, 'on'))
        disp('-> Median filtering difference image');
        imshow(mat2gray(difference_image));
        title('difference image');
        pause;
     end
  end

  if(strcmp(save_difference_image, 'yes'))
    image_num_str = sprintf(file_num_format, current_image_num);
    difference_image_file = ...
                            [output_directory difference_file_prefix ...
                             image_num_str '.jpg'];
    disp([' Saving difference image file, ' difference_image_file]);
    imwrite(mat2gray(difference_image), difference_image_file, ...
            'jpg', 'Quality', jpeg_quality);
  end

  %%%%%%% Find 'wet' pixels
  % wet pixels are those that have changed in intensity
  % by more than the threshold amount
  wet_image = logical(difference_image > wetting_thresholds);

  if(strcmp(chatty_mode, 'on'))
     disp('-> Calculating wet pixels as those that meet the wetting_threshold')
;
     imshow(wet_image);
     title('wet image');
     pause;
  end

  if(strcmp(majority_cleanup, 'true'))
     % clean up by removing unconnected pixels
     wet_image = logical(bwmorph(uint8(wet_image), 'majority'));
     if(strcmp(chatty_mode, 'on'))
        disp('-> Cleaning wet image by using a majority filter');
        imshow(wet_image);
```

area_calc.m Page 6/13

```
        title('wet image (post majority filter)');
        pause;
     end
  end

  if(strcmp(region_fill, 'true'))
     % only take pixels that are connected to the liquid_entry_col of the image
     [first_wet_rows, first_wet_cols] = ...
        find(wet_image(:, liquid_entry_col) == 1);
     %% In the above find the relevant col has been extracted,
     %% so will only contain ones, need the col in the image
     first_wet_cols = liquid_entry_col .* first_wet_cols;

     wet_image = ...
        bwselect(wet_image, ...
        first_wet_cols, first_wet_rows, 4);

     if(strcmp(chatty_mode, 'on'))
        disp('-> Calculating connected pixels');
        imshow(wet_image);
        title('connected wet image');
        pause;
     end
  end

  %%%%% Save wet images if needed
  if(strcmp(save_wet_image, 'yes'))
    image_num_str = sprintf(file_num_format, current_image_num);
     wet_image_file = ...
        [output_directory wet_file_prefix ...
         image_num_str '.jpg'];
     disp([' Saving wet image file, ' wet_image_file]);
     imwrite(wet_image, wet_image_file, 'jpg', 'Quality', jpeg_quality);
  end

  if(strcmp(save_wet_overlay, 'yes'))
    image_num_str = sprintf(file_num_format, current_image_num);
    wet_overlay_file = ...
        [output_directory weto_file_prefix ...
           image_num_str '.jpg'];
     wet_overlay = this_image;
     wet_overlay(find(bwperim(wet_image, 8))) = overlay_intensity;
     disp([' Saving wet image overlay file, ' wet_overlay_file]);
     imwrite(wet_overlay, wet_overlay_file, 'jpg', 'Quality', jpeg_quality);
  end

  %%%%% Front extraction
  if(strcmp(calc_front_results, 'yes'))
     %% This is new method (hopefully faster)
     dry_image = (wet_image == 0);

     if(strcmp(chatty_mode, 'on'))
       %% Show the dry image
       imshow(dry_image);
       disp('-> Dry image');
       pause;
     end

     %% find dry areas linked to lhs, ie exclude dry 'patches'
     [lhs_dry_rows, lhs_dry_cols] = ...
        find(dry_image(:, 1) == 1);
     dry_image = ...
        bwselect(dry_image, ...
                 lhs_dry_cols, lhs_dry_rows, 4);

     if(strcmp(chatty_mode, 'on'))
```

area_calc.m Page 7/13

```
  %% Show the dry image
  imshow(dry_image);
  disp('-> Dry image removing dry patches');
  pause;
end

%% NB in 'find' there is only one col hence returns [ 1 1 1 ...]'
%% image of front without dry patches behind
wet_front_image = (dry_image == 0);

wet_front_image = bwperim(wet_front_image);
%% perimeter of front, includes fabric edges

if(strcmp(chatty_mode, 'on'))
  %% Show the wet front image
  imshow(wet_front_image);
  disp('-> Wetting front including fabric sides');
  pause;
end

%%%%% Remove the fabric sides from the wetting front image
if(strcmp(fabric_extraction,'mask'))
  wet_front_image(find(edge_mask)) = 0;
else
  wet_front_image(1:fabric_window_start, :) = 0;
  wet_front_image(1:fabric_window_end, :) = 0;
end

if(strcmp(chatty_mode, 'on'))
   %% Show the wet front image after applying mask/window
   imshow(wet_front_image);
   disp('-> Wetting front having applied mask/window');
   pause;
end

%%%%% clean up wet front, once fabric sides are removed
[front_rows, front_cols] = ...
   find(wet_front_image == 1);

%% find the furthest point

[front_of_front, front_index] = min(front_cols);

%% max from front section

%% extract the front as those points connected to the furthest point
wet_front_image ...
    = bwselect(wet_front_image, ...
               front_of_front, front_rows(front_index), 8);

if(strcmp(chatty_mode, 'on'))
   %% Show the wet front image after fabric sides have been removed
   imshow(wet_front_image);
   disp('-> Wetting front having removed fabric sides');
   pause;
end

%%%%% Save front image files if needed
if(strcmp(save_front_image, 'yes'))
  image_num_str = sprintf(file_num_format, current_image_num);
  front_image_file = ...
                    [output_directory front_file_prefix ...
                     image_num_str '.jpg'];
  disp([' Saving wet front image file, ' front_image_file]);
  imwrite(wet_front_image, front_image_file, ...
          'jpg', 'Quality', jpeg_quality);
```

area_calc.m Page 8/13

```
  end

  if(strcmp(save_front_overlay, 'yes'))
    image_num_str = sprintf(file_num_format, current_image_num);
    front_overlay_file = ...
                         [output_directory fronto_file_prefix ...
                          image_num_str '.jpg'];
    wet_front_overlay = this_image;
    wet_front_overlay(find(wet_front_image)) = overlay_intensity;
    disp([' Saving wet front overlay file, ' front_overlay_file]);
    imwrite(wet_front_overlay, front_overlay_file, ...
            'jpg', 'Quality', jpeg_quality);
  end

  %%%%% Find data from the wetting front
  [front_row, front_col] = find(wet_front_image == 1);
  wet_length_max = liquid_entry_col - min(front_col);
  wet_length_min = liquid_entry_col - max(front_col);
  wet_length_mean = liquid_entry_col - mean(front_col);
  front_length = sum(wet_front_image(:));

  %% If something goes wrong with the calculation note this
  if(isempty(wet_length_max) | isnan(wet_length_max))
    wet_length_max = 0;
  end
  if(isempty(wet_length_min) | isnan(wet_length_min))
    wet_length_min = 0;
  end
  if(isempty(wet_length_mean) | isnan(wet_length_mean))
    wet_length_mean = 0;
  end
end

%%%%%% Store data from the current image
%% store the 'saturation_sequence', by summing cols in the wet image
saturation_sequence = [saturation_sequence; sum(wet_image)];

%% Store the wetting sequence
wetting_sequence = wetting_sequence + double(wet_image);

%% Extract a wetting sequence for the extract row
wetting_row = double(wet_image(extract_row, 1:num_image_cols)) ...
              .* 150; %% 150 to give mid_gray in images
wetting_rows = [wetting_rows; wetting_row];

%% Save the wet area
wet_area = bwarea(wet_image);
if(strcmp(area_to_length, 'true'))
  wet_area_details = ...
                     [wet_area_details; ...
                      [...
                       current_image_num, ...
                       wet_area, ...
                       (wet_area * pixel_area_mm) ...
                       (wet_area./ mean_width_pixels).* pixel_width_mm ...
                       ] ...
                      ];
else
  wet_area_details = ...
                     [wet_area_details; ...
                      [...
                       current_image_num, ...
                       wet_area, ...
                       (wet_area * pixel_area_mm)] ...
                      ];
end
```

area_calc.m Page 9/13

```
  if(strcmp(chatty_mode, 'on'))
    disp(['-> Calculated the wet area as ' num2str(wet_area)]);
    pause;
  end

  wet_sum = sum(sum(double(wet_image)));
  wet_sums = ...
             [wet_sums; ...
              [current_image_num, wet_sum, (wet_sum * pixel_area_mm)] ...
              ];
  if(strcmp(chatty_mode, 'on'))
    disp(['-> Calculated the wet sum as ' num2str(wet_sum)]);
    pause;
  end

  if(strcmp(calc_front_results, 'yes'))
    if(strcmp(chatty_mode, 'on'))
      disp(['-> Calculated the wet min as ' num2str(wet_length_min)]);
      disp(['-> Calculated the wet max as ' num2str(wet_length_max)]);
      disp(['-> Calculated the wet mean as ' num2str(wet_length_mean)]);
      disp(['-> Calculated the front length as ' num2str(front_length)]);
      pause;
    end

    wet_front_details = [wet_front_details; ...
                         current_image_num, ...
                         wet_length_mean, ...
                         wet_length_max, ...
                         wet_length_min, ...
                         front_length, ...
                         wet_length_mean .* pixel_width_mm, ...
                         wet_length_max .* pixel_width_mm, ...
                         wet_length_min .* pixel_width_mm, ...
                         front_length .* pixel_height_mm ...
                         ];
  end

  sample_pixel_intensities ...
      = [sample_pixel_intensities ; ...
         current_image_num, ...
         double(this_image(sample_pixel_row, sample_pixel_col))];
  %% If the sample pixel is wet, then record this time
  if(isempty(sample_pixel_wetting))
    if( wet_image(sample_pixel_row, sample_pixel_col) ~=0)
      sample_pixel_wetting = current_image_num;
    end
  end

  %% Also get the extract row from the raw image data
  extracted_row = this_image(extract_row, 1:num_image_cols);
  extracted_rows = [extracted_rows; extracted_row];

  %%%%% Ready to repeat for next image
  %% Get the new reference is needed and repeat for next image
  if(strcmp(difference_type, 'adjacent'))
    % taking reference image or adjacent differences
    reference_image = this_image;
    if(strcmp(chatty_mode, 'on'))
      disp('-> Calculating adjacent differences, so this image becomes referenc
e');
      imshow(reference_image);
      title('reference image');
      pause;
    end
  end
```

area_calc.m Page 10/13

```
  %%%%% Repeat for next image
  if(strcmp(chatty_mode, 'on'))
    disp('-> Repeating for next image ...');
    end
end

  end_time = clock;
  %%%%% End of processing, Plot data and show images
  experiment_info = [' - ' sample ', ' expt_ref];
  sequence_info = ['images ' num2str(start_image_number) ...
                   '-' num2str(end_image_number) ...
                   ', image_step =' num2str(image_step) ...
                   ', ref =' num2str(reference_image_number) ...
                   ];

  %% Plot the wet areas
  figure, plot(wet_area_details(:, 1), wet_area_details(:, 2), 'c');
  hold on;
  plot(wet_area_details(:, 1), wet_sums(:, 2), 'r:');
  title(['Wet areas' experiment_info]);
  xlabel(sequence_info);
  ylabel('Area of ''wet'' pixels');
  hold off;

  if(strcmp(calc_front_results, 'yes'))
    %% Plot the wet lengths
    figure, plot(wet_area_details(:, 1), wet_front_details(:,2), 'k-');
    hold on;
     plot(wet_area_details(:, 1), wet_front_details(:,3), 'c:');
     plot(wet_area_details(:, 1), wet_front_details(:,4), 'r:');
     title(['Wet lengths (mean, max, min)' experiment_info]);
     xlabel(sequence_info);
     ylabel('Length of ''wet'' pixels');
     hold off;
  end

  %% Show extracted wetting sequence from images
  figure, subplot(2,1,1), imshow(extracted_rows);
  title(['Sequence of rows, row ' num2str(extract_row) experiment_info]);
  xlabel(sequence_info);
  subplot(2,1,2), imshow(uint8(wetting_rows));
  title(['Wetting rows, row ' num2str(extract_row) experiment_info]);
  xlabel(sequence_info);

  if strcmp(save_extracted_rows, 'yes');
    imwrite(extracted_rows, ...
            [output_directory extracted_rows_filename]);
  end

  if strcmp(save_wet_rows, 'yes');
    imwrite( uint8(wetting_rows), ...
             [output_directory wet_rows_filename]);
  end

  %% Show wetting image
  figure, imshow( mat2gray(wetting_sequence) );
  title(['Wetting sequence' experiment_info]);
  xlabel(sequence_info);

  %% Show saturation_sequence image
  figure, imshow( mat2gray(saturation_sequence) );
  title(['Saturation sequence' experiment_info]);
  xlabel(sequence_info);

  %% Show sample pixel intensity variation
```

```
figure, plot(sample_pixel_intensities(:,1), sample_pixel_intensities(:,2));
title(['Sample pixel ' ...
       num2str(sample_pixel_row) ', ' num2str(sample_pixel_col) ...
       ' intensity, ' experiment_info]);
ylabel('pixel intensity');
xlabel(sequence_info);
%% Show point at which sample pixel became wet (if at all)
if(~isempty(sample_pixel_wetting))
  hold on;
  plot([sample_pixel_wetting; sample_pixel_wetting], ...
       [ min(sample_pixel_intensities(:,2)); ...
         max(sample_pixel_intensities(:,2)) ], ...
       'r:x');
  hold off;
end

%% Calculate time strings
start_time_str = [num2str(start_time(4)) ':' ...
                  num2str(start_time(5)) ':' num2str(start_time(6))];

end_time_str = [num2str(end_time(4)) ':' ...
      num2str(end_time(5)) ':' num2str(end_time(6))];
disp(['Processing started at ' start_time_str ...
      ' and finished at ' end_time_str]);

%%%%% Save data to output directory
%% Save the area data
disp(['Writing areas to file ' area_filename]);
area_file = [output_directory area_filename];
fid = fopen(area_file, 'w'); %% open for write

if fid ~= -1,
   fprintf(fid,['%% Processed on ' date '\n']);
   fprintf(fid,['%% Processing started at ' start_time_str ' ']);
   fprintf(fid,['and finished at ' end_time_str '\n']);
   fprintf(fid,['%% Experiment ' experiment_info '\n']);
   fprintf(fid,['%% Pixel area (mm^2) ' num2str(pixel_area_mm) '\n']);
   fprintf(fid,['%% Pixel height (mm) ' num2str(pixel_height_mm) '\n']);
   fprintf(fid,['%% Mean sample width ' ...
                num2str(mean_width_pixels) ' pixels, ' ...
                num2str(mean_width_mm) 'mm \n']);
   fprintf(fid,['%% ' sequence_info '\n']);
   fprintf(fid,['%%\n' ...
                '%% image_number, calculated area(pixels), ' ...
                'calculated area(mm^2), '...
                'calculated front length(mm)\n']);
   if(strcmp(area_to_length, 'true'))
     fprintf(fid, '%6i %6.3f %6.3f %6.3f\n', wet_area_details');
   else
     fprintf(fid, '%6i %6.3f %6.3f\n', wet_area_details');
   end

   fclose(fid);
else
  error('could not save area data')
end

if(strcmp(calc_front_results, 'yes'))
  %% Save the wet front data
  disp(['Writing front details to file ' front_filename]);
  front_file = [output_directory front_filename];
  fid = fopen(front_file, 'w'); %% open for write

  if fid ~= -1,
    fprintf(fid, ['%% Processed ' date '\n']);
    fprintf(fid, ['%% Processing started at ' start_time_str ' ']);
```



```
    fprintf(fid, ['and finished at ' end_time_str '\n']);
    fprintf(fid, ['%% Experiment 'experiment_info '\n']);
    fprintf(fid, ['%% Pixel width (mm) ' num2str(pixel_width_mm) '\n']);
    fprintf(fid, ['%% ' sequence_info '\n']);
    fprintf(fid, ['%%\n' ...
                  '%% image_number, ' ...
                  'wet_front_mean(pixels), ' ...
                  'wet_front_max(pixels), ' ...
                  'wet_front_min(pixels), ' ...
                  'wet_front_length(pixels) \n']);
    fprintf(fid, ...
            ['%%  wet_front_mean(mm), ' ...
             'wet_front_max(mm), ' ...
             'wet_front_min(mm), ' ...
             'wet_front_length(mm), ' ...
             '\n']);
    fprintf(fid,'%6i %6.3f %6.3f %6.3f %6.3f %6.3f %6.3f %6.3f %6.3f\n', ...
            wet_front_details');
    fclose(fid);
  else
    error('could not save area data')
  end
end

%% Save the processing details
disp(['Writing processing details to file ' processing_filename]);
processing_file = [output_directory processing_filename];
fid = fopen(processing_file, 'w'); %% open for write

if fid ~= -1,
   fprintf(fid,['%% Processed ' date '\n']);
   fprintf(fid,['%% Processing started at ' start_time_str ' ']);
   fprintf(fid,['and finished at ' end_time_str '\n']);
   %% use unix style directory
   %% so as not to confuse fprintf by including control
   %% characters in the output
   fprintf(fid,['%% Input directory ' ...
                strrep(input_directory, '\', '/') '\n']);
   fprintf(fid,['%% Output directory ' ...
                strrep(output_directory, '\', '/') '\n']);
   fprintf(fid,['%% Experiment ' expt_ref '\n']);
   fprintf(fid,['%% Sample ' sample '\n']);
   fprintf(fid,['%% Sequence ' sequence_info '\n']);
   fprintf(fid,['chatty_mode = ' chatty_mode '\n']);
   fprintf(fid,['filter = ' filter '\n']);
   fprintf(fid,['majority_cleanup = ' majority_cleanup '\n']);
   fprintf(fid,['region_fill = ' region_fill '\n']);
   fprintf(fid,['difference_type = ' difference_type '\n']);
   fprintf(fid,['staywet = ' staywet '\n']);
   fprintf(fid,['wetting_cleanup = ' wetting_cleanup '\n']);
   fprintf(fid,['lighting_mode = 'lighting_mode '\n']);
   fprintf(fid,['FOV_width = ' num2str(FOV_width) '\n']);
   fprintf(fid,['FOV_height = ' num2str(FOV_height) '\n']);
   fprintf(fid,['liquid_entry_col = ' num2str(liquid_entry_col) '\n']);
   fprintf(fid,['entry_ignore = ' num2str(entry_ignore) '\n']);
   fprintf(fid,['wet_threshold = ' num2str(wet_threshold) '\n']);
   fprintf(fid,['pixel_height_mm = ' num2str(pixel_height_mm) '\n']);
   fprintf(fid,['pixel_width_mm = ' num2str(pixel_width_mm) '\n']);
   fprintf(fid,['pixel_area_mm = ' num2str(pixel_area_mm) '\n']);
   fprintf(fid,['extract_row = ' num2str(extract_row) '\n']);
   fprintf(fid,['sample_pixel_col = ' num2str(sample_pixel_col) '\n']);
   fprintf(fid,['sample_pixel_row = ' num2str(sample_pixel_row) '\n']);
   fprintf(fid,['fabric_extraction = ' fabric_extraction '\n']);
   fprintf(fid,['fabric_window_start = 'num2str(fabric_window_start) '\n']);
   fprintf(fid,['fabric_window_end = ' num2str(fabric_window_end) '\n']);
   fprintf(fid,['save_extracted_rows = ' save_extracted_rows '\n']);
```

area_calc.m Page 13/13

```
      fprintf(fid,['save_wet_rows = ' save_wet_rows '\n']);
      fprintf(fid,['save_difference_image = ' save_difference_image '\n']);
      fprintf(fid,['save_front_image = ' save_front_image '\n']);
      fprintf(fid,['save_wet_image = ' save_wet_image '\n']);
      fprintf(fid,['save_front_overlay = ' save_front_overlay '\n']);
      fprintf(fid,['save_wet_overlay = ' save_wet_overlay '\n']);
      fprintf(fid,['bg_mask_file = ' ...
                   strrep(bg_mask_file, '\', '/') '\n']);
      fprintf(fid,['edge_mask_file = ' ...
                   strrep(edge_mask_file, '\', '/') '\n']);
      fprintf(fid,['calc_front_results = ' calc_front_results '\n']);
      fprintf(fid,['illumination correction = ' illumination_correction '\n']);
      fprintf(fid,['wet area converted to length = ' area_to_length '\n']);
      fclose(fid);
    else
      error('could not save area data')
    end

%%%%%%%%%%%%%%%%%%%%%%%%%%%%%% local functions %%%%%%%%%%%%%%%%%%%%%%%%%%%%%%%%
%%
function [image_filename] = local_imname(image_prefix, image_type, image_number)
,

  padded_zero = '0';
  padding_size = 4;

  for i =1:(padding_size - 1)
    padded_zero = strcat(padded_zero, '0');
  end

  %% Work out the current file name
  num_start = padding_size - length(num2str(image_number));
  image_index = [padded_zero(1:num_start) num2str(image_number)];
  image_filename = [image_prefix num2str(image_index) '.' image_type];

  return

  %%
```

area_calc.m

find_ellipses.m Page 1/2

```
function [fitted_ellipse_list] ...
    = find_ellipses(labelled_object_image, filename),
%% [fitted_ellipses] = find_ellipses(labelled_object_image)
%%
%% Time-stamp: <2002/02/10 11:33:50 Mark Landeryou>
%%
%% find ellipses from a labelled obect image
%%
%%  MAL (1999-Mar-05)
display = 'off';

tic

%% make sure the ellipse 'plotting' routines are available
addpath('d:\users\mark\matlab\ellipse_plotting')
close all; %% don't accumulate figures

  %% initialise the list for all propsed ellipses
  fitted_ellipse_list = [];

%% show the bitmap image of the ellipses
if(strcmp(display, 'on')),
   imshow(1 - (labelled_object_image > 0).*0.5);
   hold on;
end

  last_object = max(unique(labelled_object_image(labelled_object_image ...
                                                 ~= 0)) );
  for current_object ...
        = unique(labelled_object_image(labelled_object_image ~= 0))',

%% tell the user how many objects have been dealt with
disp('----------------------------------------');
    disp(['Current object: ' num2str(current_object) ...
          ' of ' num2str(last_object)]);

    %% call the rht to find ellipses in the current object
    fitted_ellipse_list = [fitted_ellipse_list; ...
                           rht_fit_ellipses(labelled_object_image == ...
                                            current_object)];
  end

  toc

  %% plot the ellipses found over the bitmap
  if(strcmp(display, 'on') & ~isempty(fitted_ellipse_list))
     for i = 1:length(fitted_ellipse_list(:,1))

        cx = fitted_ellipse_list(i, 1);
        cy = fitted_ellipse_list(i, 2);
        r1 = fitted_ellipse_list(i, 3);
        r2 = fitted_ellipse_list(i, 4);
        theta = fitted_ellipse_list(i, 5);

        [fex, fey] = ellipse(cx, cy, r1, r2, theta, 20);

        plot(fex, fey, 'r:');
        zoom on
         hold off;
     end
  else
     if(isempty(fitted_ellipse_list))
        warning('No ellipses found');
     end
  end
```

find_ellipses.m Page 2/2

```
  if( exist('filename', 'var') & ~isempty(fitted_ellipse_list) )
     save_ellipse_list(fitted_ellipse_list, filename);
  end
```

rht_fit_ellipses.m Page 1/1

```
function [fitted_ellipse_list] = rht_fit_ellipses(ellipse_image),
%%
%% Time-stamp: <1999/03/23 17:27:42 >
%%
%% [fitted_ellipse_list] = rht_fit_ellipses(ellipse_image)
%%
%% Passed a bitmap that is thought to contain ellipses
%% Randomized Hough Transform is then called until the number
%% of points that remain not fitted falls below a fixed number;
%% or the RHT is called unsuccesfully a fixed number of times
%%
%%  MAL (1999-Mar-05)

  %% Note max attempts t fit defines the maximum number of ellipses
  %% that will be fitted to an 'object'
  max_attempts_to_fit = 15;
  min_points_to_fit = 8;

  fitted_ellipse_list = [];

  %% Generate points in the bitmap
  [y_pts_to_fit, x_pts_to_fit] = find(ellipse_image);
  number_pts_to_fit = length(x_pts_to_fit);
  disp([' Object has 'num2str(number_pts_to_fit) ' pixels.']);

  attempts_to_fit = 0;

  while(number_pts_to_fit >= min_points_to_fit ...
        & attempts_to_fit < max_attempts_to_fit)

    attempts_to_fit = attempts_to_fit + 1;

    %% fit using rht
    [cx, cy, r1, r2, theta, ...
     x_pts_to_fit, y_pts_to_fit] ...
        = rht_epochs(x_pts_to_fit, y_pts_to_fit);

    number_pts_to_fit = length(x_pts_to_fit);

    %% if an ellipse was found add this to tbe list
    if( ~isempty(cx) )
      fitted_ellipse_list(end + 1, :) ...
         = [cx, cy, r1, r2, theta];
   else
      disp('  No ellipse was found.');
end
  end
```

rht_epochs.m Page 1/4

```
function [mp_cx, mp_cy, ....
      mp_r1, mp_r2, mp_theta, ...
      not_fitted_x, not_fitted_y] = rht_epochs(x_pts, y_pts),
%%
%% Time-stamp: <2002/02/10 11:37:30 Mark Landeryou>
%%
%% [mp_cx, mp_cy, ....
%%  mp_r1, mp_r2, mp_theta, ...
%%  not_fitted_x, not_fitted_y] = rht_epochs(x_pts, y_pts),
%%
%% Use a randomized Hough method to find an ellipse among the points
%% x_pts and y_pts
%%
%% following method of
%%  McLaughlin, R. A.
%%   Technical Report - Randomized Hough transform:
%%   Improved ellipse detection with comparison
%%   Centre for Intelligent Information Processing
%%   Systems ,1999
%%  The University of Western Australian, Nedlands, W.A. 6907
%%
%%  MAL (1999-Mar-05)

warning off;
chatty_mode = 'on';

count_distance = 1;
remove_distance = 1;

min_axis = 2;
max_axis = 30;

min_score = 0.5;

fibre_radius_min = 2;
fibre_radius_max = 7;

min_area = (fibre_radius_min) * (fibre_radius_min);
max_area = (max_axis) * (fibre_radius_max);

rejected_unreal = 0;
rejected_axes_small = 0;
rejected_axes_large = 0;
rejected_fibre_radius = 0;
rejected_small = 0;
duplicate_ellipses = 0;
rejected_score = 0;

%% now start an epoch
ellipses_in_epoch = length(x_pts) .* 3;
ellipses_found = 0;
valid_ellipses_found = 0;
ellipse_list = [];

max_epochs = 3000;
epoch = 0;

tolerance = [1, 1, 1, 1, pi/10];
while(valid_ellipses_found < ellipses_in_epoch & ...
      epoch < max_epochs),
   epoch = epoch + 1;

   %% find an ellipse
   [cx, cy, major_axis, minor_axis, theta] ...
      = rht_possible_ellipse(x_pts, y_pts);
   ellipses_found = ellipses_found + 1;
```

rht_epochs.m Page 2/4

```
   valid_ellipse = 1;
   if(isnan(cx) & isnan(cy) ...
         & isnan(minor_axis) & isnan(major_axis) & isnan(theta)),
      valid_ellipse = 0;
      rejected_unreal = rejected_unreal + 1;
   end

   if(valid_ellipse & (isinf(cx) | isinf(cy) | ...
         isinf(minor_axis) | isinf(major_axis) | ...
         isinf(theta)) ),
      valid_ellipse = 0;
      rejected_unreal = rejected_unreal + 1;
   end

   if(valid_ellipse & (~isreal(cx) | ~isreal(cy) | ...
         ~isreal(minor_axis) | ~isreal(major_axis) | ...
         ~isreal(theta)) ),
      valid_ellipse = 0;
      rejected_unreal = rejected_unreal + 1;
   end

   %% don't allow ellipses with axes less than set value
   if(valid_ellipse & ((minor_axis < min_axis) | (major_axis < min_axis)) ),
      valid_ellipse = 0;
      rejected_axes_small = rejected_axes_small + 1;
   end

   %% don't allow ellipses with axes greater than set value
   if(valid_ellipse & ((minor_axis > max_axis) | (major_axis > max_axis)) ),
      valid_ellipse = 0;
      rejected_axes_large = rejected_axes_large + 1;
   end

   %% don't allow ellipses unless one of the axes is within the fibre
   %% radius range
   if(valid_ellipse & ((minor_axis < fibre_radius_min ...
         | minor_axis > fibre_radius_max) | ...
         (major_axis < fibre_radius_min ...
         | major_axis > fibre_radius_max)) ),
      valid_ellipse = 0;
      rejected_fibre_radius = rejected_fibre_radius + 1;
   end

   %% don't allow ellipses unless their area is greater than a min
   ellipse_area = (minor_axis * major_axis);
   if(valid_ellipse & ((ellipse_area < min_area) | ...
         (ellipse_area > max_area)) );
      valid_ellipse = 0;
      rejected_small = rejected_small + 1;
   end

   %% record this ellipse in the ellipse_list
   if(valid_ellipse == 1)
      valid_ellipses_found = valid_ellipses_found + 1;

      score = count_pts_nr_ellipse(x_pts, y_pts, ...
         cx, cy, major_axis, minor_axis, theta, ...
         count_distance);

      if(isempty(ellipse_list) & score >= min_score),
         ellipse_list(1, :) = [cx, cy, major_axis, minor_axis, theta, 0];
      end

      if( ~isempty(ellipse_list) ),
         in_tolerance = [];
```

rht_epochs.m Page 3/4

```
        in_tolerance(:, 1) ...
           = abs(cx - ellipse_list(:,1) ) <= tolerance(1);
        in_tolerance(:, 2) ...
           = abs(cy - ellipse_list(:,2) ) <= tolerance(2);
        in_tolerance(:, 3) ...
           = abs(major_axis - ellipse_list(:,3) ) <= tolerance(3);
        in_tolerance(:, 4) ...
           = abs(minor_axis - ellipse_list(:,4) ) <= tolerance(4);
        in_tolerance(:, 5) ...
           = abs(theta - ellipse_list(:,5) ) <= tolerance(5);

        similar_ellipse = find(sum(in_tolerance, 2) == 5);

        if(~isempty(similar_ellipse)),
           duplicate_ellipses = duplicate_ellipses + 1;
        end
     end

     %    [ex,ey]=ellipse(cx, cy, major_axis, minor_axis, theta, 30);
     %    plot(ey,ex);

     %score =fast_score_ellipse(x_pts, y_pts, ...
     %                          cx, cy, major_axis, minor_axis, theta);
     %
     %% store this ellipse if it scores more than minimum score
     if(score < min_score & isempty(similar_ellipse))
        rejected_score = rejected_score + 1;
     end

     if(score >= min_score)
        if( isempty(similar_ellipse) )
           %% add to the list
           ellipse_list(end + 1, :) ...
              = [cx, cy, major_axis, minor_axis, theta, score];
        elseif(score > ellipse_list(similar_ellipse, 6))
           %% if this ellipse is higher scoring than the existing ellipse
           %% then replace it in the list

           ellipse_list(similar_ellipse, 1) = cx;
           ellipse_list(similar_ellipse, 2) = cy;
           ellipse_list(similar_ellipse, 3) = major_axis;
           ellipse_list(similar_ellipse, 4) = minor_axis;
           ellipse_list(similar_ellipse, 5) = theta;
           ellipse_list(similar_ellipse, 6) = score;

        end
     end

  end
end

%% find the most popular ellipse
%ellipse_list
if(~isempty(ellipse_list))

   %% Now choose the best ellipse
   best_ellipse_score = max(ellipse_list(:,6));
   best_ellipse_indx ...
   = find(ellipse_list(:,6) == best_ellipse_score);
   if(strcmp(chatty_mode, 'on')),
      [ellipses_in_list, degfree] = size(ellipse_list);
      disp([' ' num2str(ellipses_found) ' ellipses were considered, ' ...
            num2str(valid_ellipses_found) ' ellipses were valid, and ' ...
            num2str(ellipses_in_list) ' unique ellipses were listed.']);
      disp([' Of the rejected ellipses:']);
      disp(['  ' num2str(rejected_unreal) ' were not real,']);
```

rht_epochs.m Page 4/4

```
      disp(['  ' num2str(rejected_axes_small) ' axes were too small,']);
      disp(['  ' num2str(rejected_axes_large) ' axes were too large,']);
      disp(['  ' num2str(rejected_fibre_radius) ' did not correspond to the fibr
e radius ,']);
      disp(['  ' num2str(rejected_small) ' were too small.']);
      disp([' Of the valid ellipses some were not listed because:']);
      disp(['  ' num2str(duplicate_ellipses) ' were similar to already listed el
lipses,']);
      disp(['  ' num2str(rejected_score) ' scored below the threshold.']);
      disp([' Best ellipse found scores ' num2str(best_ellipse_score) ...
            ' and was found in ' num2str(epoch) ' epochs.']);
   end

   if(length(best_ellipse_indx) > 1)
      %% if there is more than one best ellipse, choose the largest
      best_ellipse_indx ...
      = best_ellipse_indx(find(max...
         (ellipse_list(best_ellipse_indx, 3) .* ...
         ellipse_list(best_ellipse_indx, 4) )) );
   end

   mp_cx = ellipse_list(best_ellipse_indx, 1);
   mp_cy = ellipse_list(best_ellipse_indx, 2);
   mp_r1 = ellipse_list(best_ellipse_indx, 3);
   mp_r2 = ellipse_list(best_ellipse_indx, 4);
   mp_theta = ellipse_list(best_ellipse_indx, 5);
   mp_score = ellipse_list(best_ellipse_indx, 6);

   [pts_near_ellipse, pts_in_ellipse] ...
      = get_pts_near_ellipse(x_pts, y_pts, ...
      mp_cx, mp_cy, mp_r1, mp_r2, mp_theta, ...
      remove_distance);

   %% plot the best ellipse and the not_fitted points
   % [epx, epy] = ellipse(mp_cx, mp_cy, mp_r1, mp_r2, mp_theta, 40);
   % plot(epy, epx, 'rx');

   not_fitted_x = x_pts(~pts_near_ellipse);
   not_fitted_y = y_pts(~pts_near_ellipse);
   % plot(not_fitted_y ,not_fitted_x, 'bo');

   if(strcmp(chatty_mode, 'on')),
      disp([ '  ' num2str(length(not_fitted_x)) ' pixels remain in this object.'
]);
   end
else
   if(strcmp(chatty_mode, 'on')),
      [ellipses_in_list, degfree] = size(ellipse_list);
      disp([' Ellipse list is empty ' num2str(ellipses_found) ' ellipses were co
nsidered, ' ...
            num2str(valid_ellipses_found) ' ellipses were valid, and ' ...
            num2str(ellipses_in_list) ' unique ellipses were listed.']);
      disp([' Of the rejected ellipses:']);
      disp(['  ' num2str(rejected_unreal) ' were not real,']);
      disp(['  ' num2str(rejected_axes_small) ' axes were too small,']);
      disp(['  ' num2str(rejected_axes_large) ' axes were too large,']);
      disp(['  ' num2str(rejected_fibre_radius) ' did not correspond to the fibr
e radius ,']);
      disp(['  ' num2str(rejected_small) ' were too small.']);
   end
end
```

count_pts_nr_ellipse.m Page 1/2

```
function [normalised_num_pts] ...
    = count_pts_nr_ellipse(x_pts, y_pts, ...
                           centre_x, centre_y, a, b, theta, ...
                           min_distance),
%%
%% Time-stamp: <1999/03/25 10:51:03 >
%%
%% Find those points in x,y points that are near the ellipse
%%
%%  MAL (1999-Mar-05)
plot_on = 0;

%% Find ellipse perimeter
%% Use the approximation formula by Ramanujan
perimeter ...
    = pi * (3*(abs(a) + abs(b)) - ...
    sqrt((abs(a)+3*abs(b))*(3*abs(a)+abs(b)) ) );

  number_x_pts = length(x_pts);

  if(perimeter > 200)
    normalised_num_pts = 0;
    return
  end

  % Loop around segments of the ellipse counting points
  % that fall within distance 'min_distance' of the ellipse
  % points

  %% scale the number of points by the perimeter
  step = 2*pi/perimeter;
  min_distance = min_distance .* min_distance; %% save sqrt for large matrices

  t = [step:step:2*pi + step];
  ellipse_x = a*cos(theta)*cos(t)' - b*sin(theta)*sin(t)' + centre_x;
  ellipse_y = a*sin(theta)*cos(t)' + b*cos(theta)*sin(t)' + centre_y;
  number_ellipse_pts = length(ellipse_x);

  x_distances = repmat(x_pts', number_ellipse_pts, 1) ...
                - repmat(ellipse_x, 1, number_x_pts);

  y_distances = repmat(y_pts', number_ellipse_pts, 1) ...
                - repmat(ellipse_y, 1, number_x_pts);

  distances = ( ((x_distances) .* (x_distances)) + ...
                ((y_distances) .* (y_distances)) );
  %% all points within min_distance of the ellipse

  near_pts = sum(distances < min_distance);
  num_near_pts = sum(near_pts > 0);

  y_distances = [];
  x_distances = [];
  distances = [];

  if(plot_on)
    %%  plot_pts_near
    plot(y_pts(near_pts > 0), x_pts(near_pts > 0), 'bo');
  end

  %% remove the near points from the list
   y_pts(near_pts > 0) = [];
   x_pts(near_pts > 0) = [];
  %%
  %% find points that are within the ellipse
  %% that is within the polgon that defines the ellipse
```

count_pts_nr_ellipse.m Page 2/2

```
   num_pts_in_ellipse ...
      = sum(inpolygon(x_pts, y_pts, ellipse_x, ellipse_y));
  if(num_pts_in_ellipse == 0)
    normalised_num_pts = (num_near_pts) ./ perimeter;
  else
    normalised_num_pts = 0;
  end

  if(plot_on)
    %% plot the ellipse
    plot(ellipse_y, ellipse_x, 'rx');

    %% in_ellipse = inpolygon(x_pts, y_pts, ellipse_x, ellipse_y);
    %%    plot(y_pts(in_ellipse), x_pts(in_ellipse), 'g+');
    keyboard
  end
```

Appendix F

Example output files

F.1 Experimental details

The details for each experiment are captured from the user, and stored as a text file with the captured images. This text file is read when processing the captured sequence, for example the field of view dimensions are used to convert pixel values to distance measurements.

F.1.1 Example experiment details file

```
   Experimental details
21:51 Monday August 02, 1999

Experiment reference : 1999-Aug-02
Experiment description : NP450P Horizontal wicking
 machine direction as received
 -- NPHMA-34
Sample reference : NPHMA-34
Sample length : 450
Sample width : 50
Sample thickness : 4.35
Sample mass : 13.06
Fibre type : PES
Needling : 0
Staple length (mm) : 60
Area density (gsm) : 450
Sample orientaton : MD
Fibre dTex : 0
FOV width : 162.5
FOV height : 67
FOV location : 15
```

```
Balance filename : NPHMA-34.BAL
Angle from horizontal : 0
Humidity : 54.5
Temperature : 29
Lighting : Reflected
Balance calibrated : 1
Camera focused : 1
Apparatus level : 1
```

F.2 Processing details

The parameters used to process captured images are recorded as a text file with the processed results. This allows the processing to be reproduced from the captured images.

F.2.1 Example area processing file

```
   % Processed 03-Aug-1999
% Processing started at 23:48:53.015 and finished at 0:10:1.859
% Input directory d:/users/mark/1999-Aug-02/NPHMA-34/
% Output directory d:/users/mark/1999-Aug-02/processing/NPHMA-34/
% Experiment 1999-Aug-02
% Sample NPHMA-34
% Sequence images 0-399, ref =0
chatty_mode = off
filter = median
majority_cleanup = false
region_fill = true
difference_type = reference
staywet = false
wetting_cleanup = false
lighting_mode = reflectance
FOV_width = 162.5
FOV_height = 67
wet_threshold = 10
pixel_height_mm = 0.22333
pixel_width_mm = 0.21495
pixel_area_mm = 0.048005
extract_row = 288
sample_pixel_col = 150
sample_pixel_row = 288
fabric_extraction = mask
fabric_window_start = 80
fabric_window_end = 500
```

```
save_extracted_rows = yes
save_wet_rows = yes
calc_front_results = yes
illumination correction = true
Wet area converted to length = true
```

Appendix G

Experiment summary

G.1 Experiment summary

Each experiment has been identified with a five letter code. This consists of: two letters to identify the fabric used (NP for Ledatec NP450P), and three letters to identify the experiment performed. Table G.1 summarises the experimental codes used. Numbers following the dash, indicate the experimental repeat with a series; for example the third horizontal wicking experiment is labelled NPHMA-03.

Experiment code	*Experimental conditions*
NPHMA	Horizontal wicking in the machine direction of the fabric as received
NPVMA	Vertical wicking in the machine direction of the fabric as received
NPHXA	wicking in the cross machine direction
NPHMI	wicking using IPA
NPHMR	the sample has been rinsed prior to wicking
NPHMW	the sample has been washed prior to wicking
NPHMH	wicking using water heated to above room temperature
NPHMT	experiment used to test the wicking sensitivity to changes in the apparatus
NPHSn	wicking using the compression apparatus, with plates seperated by n 0.5 mm shims
NPAnn	wicking using the sample angled nn degress from the horizontal

Table G.1: Codes used for experiments

Table G.2: Experiment summary

Experiment ref.	Wicking angle	Experiment	mass	thickness
1999-Jul-20 (27.5 °C, 70% RH)				
NPHMA-01	Horizontal	Control	12.48	4.58
NPHMA-02	Horizontal	Control	12.33	4.64
NPHMA-03	Horizontal	Control	12.32	4.22
NPHMA-04	Horizontal	Control	11.67	
NPHMA-05	Horizontal	Control*	11.7	4.22
NPHMA-06	Horizontal	Control*	12.01	4.19
NPHMA-05a	Horizontal	Control	11.5	4.21
NPHMA-06a	Horizontal	Control	12.09	4.2
1999-Jul-21 (25 °C. 55% RH)				
NPHMA-07	Horizontal	No dye	11.99	4.29
NPHMA-08	Horizontal	dye	11.95	
NPHMA-09	Horizontal	dye		
NPHMA-10	Horizontal	Control		
NPHMA-11	Horizontal	Control	12.17	
raise front of sample support into line				
NPHMA-12	Horizontal	Control	11.9	
NPHMA-13	Horizontal	40 °C dye		
NPHMA-14	Horizontal	RT no dye	12.18	
NPHMA-15	Horizontal	40 °C dye	11.57	
1999-Jul-22 (24 °C, 60% RH)				
NPHMA-16	Horizontal	no dye	12.82	
NPHMA-17	Horizontal	Control	12.19	
1999-Jul-26 (28 °C 53% RH)				
NPHMA-18	Horizontal	no dye	12.17	4.31
NPHMA-19	Horizontal	no dye	12.2	
NPHMA-20	Horizontal	35 °C no dye	12.26	4.45
NPHMA-21	Horizontal	35 °C no dye	12.87	4.42
NPHMA-22	Horizontal	40 °C no dye*	12.23	4.35
1999-Jul-27 (27 °C, 55% RH)				
NPHMA-23	Horizontal	dye	13.41	4.25
new reservoir				
NPHMA-24	Horizontal	37 °C no dye	13.34	4.48
NPHMA-25	Horizontal	dye	14.14	4.79
NPHMA-26	Horizontal	dye	13.6	4.68
NPHMA-27	Horizontal	dye	13.41	4.51
EVAPR-02		Evaporation from reservoir		
NPHXA-01	Horizontal	Cross direction	14.51	4.1

Experiment ref.	Wicking angle	Experiment	mass	thickness
NPHXA-02	Horizontal	Cross direction	14.95	4.35
NPHXA-03	Horizontal	Cross direction	15.16	4.09
1999-Jul-28 (27 °C, 60% RH)				
NPHMA-28	Horizontal	Control	11.85	4.28
NPHXA-04	Horizontal	Cross direction	15.25	4.18
NPHXA-05	Horizontal	Cross direction	14.77	4.37
NPHXA-06	Horizontal	Cross direction	13.26	4.15
NPHXA- sections 515mm				
long not 450mm				
1999-Jul-29 (28 °C, 60% RH)				
NPHMA-29	Horizontal	Control	11.82	4.14
EVAPR-03				
NPHMW-01	Horizontal	Hand washed samples	13.01	4.95
NPHMW-02	Horizontal	Hand washed samples	12.44	4.97
NPHMW-03	Horizontal	Hand washed samples	12.35	4.98
NPHMA-30	Horizontal	Control		
EVAPR-04		Evaporation from reservoir		
1999-Jul-30 (30.5 °C 54% RH)				
NPHMR-01	Horizontal	Rinsed sample	11.89	4.81
NPHMA-31	Horizontal	Control	12.11	4.42
EVAPR-05		Evaporation from reservoir		
NPHMR-02	Horizontal	Rinsed sample	11.97	4.74
NPHMR-03	Horizontal	Rinsed sample	11.9	4.72
1999-Aug-01				
NPHMI-01	Horizontal	10% IPA	12.53	4.5
NPHMI-02	Horizontal	10% IPA	12.21	4.45
NPHMI-03	Horizontal	10% IPA	12.03	4.45
1999-Aug-02 (29 °C, 50% RH)				
New section from roll				
NPHMA-32	Horizontal	Control	13.79	4.72
NPHMA-33	Horizontal	Control	13.65	4.81
NPHMA-34	Horizontal	29 °C water	13.06	4.35
NPHMI-04	Horizontal	10% IPA	12.24	4.54
1999-Aug-03 (30 °C. RH=65%)				
NPHMI-05	Horizontal	10% IPA	11.82	4.15
NPHMI-06	Horizontal	10% IPA	11.58	4.4
NPHMA-35	Horizontal	Control		
SEVAP-01	Horizontal	Evaporation, sample		
NPHMI-07	Horizontal	10% IPA	11.65	4.12
1999-Aug-04 (28 °C, 64% RH)				

Experiment ref.	Wicking angle	Experiment	mass	thickness
NPHMR-04	Horizontal	Rinsed sample	12.01	4.75
NPHMR-05	Horizontal	Rinsed sample	12.1	4.19
NPHMA-36	Horizontal	Control	11.96	4.27
NPHMR-06	Horizontal	Rinsed sample	12.31	4.25
NPHMI-08	Horizontal	15% IPA	12	4.35
NPHMI-09	Horizontal	15% IPA	12.17	4.27
NPHMI-10	Horizontal	15% IPA	11.8	4.33
NPHMI-11	Horizontal	5% IPA	12.24	4.39
NPHMI-12	Horizontal	5% IPA	12.16	4.43
NPHMI-13	Horizontal	5% IPA	12.18	4.19
1999-Aug-05 (29.5 °C, 58% RH)				
NPHMW-04	Horizontal	Washed sample	12.35	4.76
NPHMW-05	Horizontal	Washed sample	12.45	4.83
1999-Aug-06 (28 °C, 63% RH)				
NPHMW-06	Horizontal	Washed sample	12.11	4.57
1999-Aug-09 (27 °C, 71% RH)				
NPHSN-01	Horizontal	Squashing rig, no cover	12.18	4.27
NPHSN-02	Horizontal	Squashing rig, no cover	12.34	4.14
NPHSN-03	Horizontal	Squashing rig, no cover	12.2	4.14
SEVAP-02		Sample evaporation		
1999-Aug-10 (25.5 °C, 69% RH)				
NPHSN-04	Horizontal	Squashing rig, no cover	12.15	4.41
NPHMA-37	Horizontal	Control	12.14	4.31
NPHMA-38	Horizontal	Control	12.53	4.32
EVAP-06				
NPHS1-00	Horizontal	Test	12.16	4.42
1999-Aug-11 (25.5 °C, 60%RH)				
NPHS1-01	Horizontal	Squashed 2.25mm	12.69	4.5
NPHS0-01	Horizontal	Squashed 2.5mm	12.52	4.23
NPHS2-01	Horizontal	Squashed 2.0mm	13.16	4.42
NPHS3-01	Horizontal	Squashed 1.5mm	13.21	4.48
NPHS4-01	Horizontal	Squashed 1.0mm	13.53	4.56
NPHS5-01	Horizontal	Squashed 3.0mm	13.5	4.48
1999-Aug-12 (26 °C, 62% RH)				
new Section				
NPHS6-01	Horizontal	Squashed 3.5mm	12.82	4.64
NPHS7-01	Horizontal	Squashed 4.0mm	13.03	4.42
NPHS8-01	Horizontal	Squashed 4.5mm	12.04	4.31
1999-Aug-14 (24 °C, 67% RH)				
NPHS9-02	Horizontal	Squashed 4.5mm	11.68	4.52

Experiment ref.	Wicking angle	Experiment	mass	thickness
1999-Aug-15 (24.5 °C 67%)				
NPHS8-02	Horizontal	Squashed 4.0mm	11.31	4.46
NPHS7-02	Horizontal	Squashed 3.5mm	11.68	4.24
NPHS6-02	Horizontal	Squashed 3.0mm	11.98	4.09
NPHS5-02	Horizontal	Squashed 2.5mm	11.59	3.92
NPHS4-02	Horizontal	Squashed 2.0mm	11.54	4.07
NPHS3-02	Horizontal	Squashed 1.5mm	11.3	4.01
1999-Aug-16 (24 °C 68% RH)				
NPHS2-02	Horizontal	Squashed 1.0mm	11.35	4.14
NPHS2-03	Horizontal	Squashed 1.0mm	11.56	4.17
NPHS3-03	Horizontal	Squashed 1.5mm	11.63	4.32
1999-Aug-17 (23.5 °C 69% RH)				
NPHS4-03	Horizontal	Squashed 2.0mm	11.73	4.29
NPHS5-03	Horizontal	Squashed 2.5mm	11.85	4.26
NPHS6-03	Horizontal	Squashed 3.0mm	11.73	4.232
NPHS7-03	Horizontal	Squashed 3.5mm	12.05	4.46
NPHS8-03	Horizontal	Squashed 4.0mm	11.55	4.48
NPHS9-03	Horizontal	Squashed 4.5mm	11.92	4.39
NPHS2-04	Horizontal	Squashed 1.0mm	11.46	4.2
1999-Aug-18 (23 °C 72.5% RH)				
NPHS3-04	Horizontal	Squashed 1.5mm	11.97	4.12
NPHS4-04	Horizontal	Squashed 2.0mm	11.74	4.03
NPHS5-04	Horizontal	Squashed 2.5mm	11.95	4.19
NPHS6-04	Horizontal	Squashed 3.0mm	11.8	4.22
NPHS7-04	Horizontal	Squashed 3.5mm	12.07	4.29
NPHS8-04	Horizontal	Squashed 4.0mm	12.35	4.08
NPHS9-04	Horizontal	Squashed 4.5mm	12.45	4.06
1999-Aug-25 (25.5 °C, 72%RH)				
NPHMT-01	Horizontal	Control	12.57	4.19
NPHMT-02	Horizontal	Angled down	12.68	4.65
NPHMT-03	Horizontal	Angled up	12.99	4.47
NPHMT-04	Horizontal	Raised (4.5mm)	13.49	4.38
NPHMT-05	Horizontal	Raised (1.3mm)	14.09	4.59
1999-Aug-30 (27 °C, 67% RH)				
NPHMA-32a	Horizontal	Control	13.731	4.69
NPHMH-01	Horizontal	Water 42.5 °C	13.55	4.49
NPHMH-02	Horizontal	Water 47.5 °C	12.969	4.32
NPHMH-03	Horizontal	Water 38.5 °C	12.762	4.25
NPHMH-04	Horizontal	Water 35 °C	12.498	4.39
NPHMH-05	Horizontal	Water 31 °C	12.173	4.17

Experiment ref.	Wicking angle	Experiment	mass	thickness
1999-Aug-31 (27.5 °C, 63% RH)				
NPHMA-33a	Horizontal	Control	13.69	4.44
NPHMS-01	Horizontal	25mm sample	6.44	4.22
NPHMS-02	Horizontal	10mm sample		4.31
NPHMS-03	Horizontal	40mm sample	10.251	4.31
NPHMS-04	Horizontal	25mm sample	6.627	4.22
NPHMS-05	Horizontal	25mm sample	6.471	4.19
NPHMS-06	Horizontal	25mm sample	6	4.19
NPHMA-34a	Horizontal	Control	12.32	4.04
1999-Sep-02 (30 °C 63% RH)				
NPHMA-35a	Horizontal	Control	12.188	4.28
NPHMH-06	Horizontal	35 °C	12.12	4.12
NPHMH-07	Horizontal	39 °C	11.837	3.92
NPHMH-08	Horizontal	47 °C	11.97	4.08
1999-Sep-03 (30 °C 59% RH)				
NPHMA-36a	Horizontal	Control	11.6	4.11
NPHMH-09	Horizontal	37 °C	11.56	4.42
NPHMH-10	Horizontal	41 °C *	11.93	4.27
NPHMH-11	Horizontal	46 °C	11.27	4.31
NPHMH-12	Horizontal	41 °C	11.6	4.23
NPHMH-13	Horizontal	36.5 °C	11.51	4.39
NPHMH-14	Horizontal	44 °C *	11.84	4.28
NPHMA-37a	Horizontal	Control	11.86	4.42
1999-Sep-05 (30 °C, 62% RH)				
NPVMA-01	Vertical	Control	11.66	4.23
1999-Sep-06 (28.5 °C. 65% RH)				
NPVMA-02	Vertical	Control	11.69	4.21
NPVMA-03	Vertical	Control	11.56	4.32
NPVMA-04	Vertical	Control	11.75	4.14
NPVMA-05	Vertical	Control	12.14	4.11
NPVMA-06	Vertical	Control	11.96	4.22
NPVMA-07	Vertical	Control	12.05	4.17
1999-Sep-07				
NPVSM2-01	Vertical	Squashed 1.0mm	12.5	4.38
NPVMS2-02	Vertical	Squashed 1.0mm	11.72	4.19
NPVMS9-01	Vertical	Squashed 4.5mm	12	4.2
NPVMS3-01	Vertical	Squashed 1.5mm	11.15	4.15
NPVMS8-01	Vertical	Squashed 4.0mm	11.48	3.9
NPVMS4-01	Vertical	Squashed 2.0mm	11.38	4.09

Repeat experiments with :

Experiment ref.	Wicking angle	Experiment	mass	thickness
image and mass data for 1 hour,				
prevent spillage from reservoir,				
reduce FOV to 170mm				
1999-Sep-09				
NPVMS2-01	Vertical	Squashed 1.0mm	11.71	4.06
NPVMS9-01	Vertical	Squashed 4.5mm	11.03	3.92
NPVMS8-01	Vertical	Squashed 4.0mm	11.39	4.07
Washer to reduce flow rate from solenoid	Vertical			
1999-Sep-10				
NPVMS3-01	Vertical	Squashed 1.5mm	11.72	4.04
NPVMS7-01	Vertical	Squashed 3.5mm	11.16	4.26
NPVS4-01	Vertical	Squashed 2.0mm	11.62	4.12
NPVS4a01	Vertical	Squashed 2.0mm	11.63	4.18
Suspect wicking into holder				
NPVS4b01	Vertical	Squashed 2.0mm*	11.75	4.35
Start experiments again				
NPVS4-01	Vertical	Squashed 2.0mm	13.59	4.72
NPVS9-01	Vertical	Squashed 4.5mm	12.5	4.23
1999-Sep-13 (26 °C 63% RH)				
NPVS2-01	Vertical	Squashed 1.0mm	12.37	4.33
NPVS3-01	Vertical	Squashed 1.5mm	13.12	4.67
NPVS8-01	Vertical	Squashed 4.0mm	13.35	4.74
NPVS5-01	Vertical	Squashed 2.5mm	12.89	4.53
1999-Sep-14 (25 °C 63% RH)				
NPVS6-01	Vertical	Squashed 3.0mm	12.53	4.47
1999-Sep-15 (23.5 °C 70% RH)				
NPVS7-01	Vertical	Squashed 3.5mm	12.25	4.23
NPVS5-02	Vertical	Squashed 2.5mm	12.24	4.4
NPVS3-02	Vertical	Squashed 1.5mm	12.14	4.25
1999-Sep-16 (22.5 °C 72% RH)				
NPVS9-02	Vertical	Squashed 4.5mm*	11.76	4.12
NPVS9a02	Vertical	Squashed 4.5mm	11.8	4.45
NPVS8-02	Vertical	Squashed 4.0mm	11.72	4.09
NPVS6-02	Vertical	Squashed 3.0mm	12.07	4.04
NPVS4-02	Vertical	Squashed 2.0mm	11.87	4.2
1999-Sep-18 (23.5 °C 18% RH)				
NPVS7-02	Vertical	Squashed 3.5mm	12.14	4.3
NPVS2-02	Vertical	Squashed 1.0mm	11.95	4.2
New sample sections cut from roll				
NPVS2-03	Vertical	Squashed 1.0mm	13.37	4.52

Experiment ref.	Wicking angle	Experiment	mass	thickness
1999-Sep-20 (23 °C 76% RH)				
NPVS9-03	Vertical	Squashed 4.5mm	13.12	4.5
NPVS8-03	Vertical	Squashed 4.0mm	12.82	4.29
NPVS7-03	Vertical	Squashed 3.5mm	12.29	4.37
NPVS6-03	Vertical	Squashed 3.0mm	11.78	4.14
1999-Sep-21 (23 °C 78% RH)				
NPVS5-03	Vertical	Squashed 2.5mm	11.64	4.33
NPVS3-03	Vertical	Squashed 1.5mm	11.94	4.26
NPVS4-03	Vertical	Squashed 2.0mm	12.13	4.25
NPVS2-03	Vertical	Squashed 1.0mm	12.45	4.46
1999-Sep-22 (23.5 °C 78% RH)				
NPVS3-04	Vertical	Squashed 1.5mm	11.91	3.78
NPVS5-04	Vertical	Squashed 2.5mm	12.13	4.33
NPVS4-04	Vertical	Squashed 2.0mm	12.22	4.18
NPVS2-04	Vertical	Squashed 1.0mm	12.07	4.1
1999-Sep-23 (24 °C 79% RH)				
NPVS6-04	Vertical	Squashed 3.0mm	12.24	4.19
NPVS7-04	Vertical	Squashed 3.5mm	11.96	4.22
1999-Sep-24 (23 °C 80% RH)				
NPVS8-04	Vertical	Squashed 4.0mm	11.98	4.07
NPVS9-04	Vertical	Squashed 4.5mm	11.54	4.2
1999-Oct-31 (25.5 °C 60% RH)				
NPVMA-08		Control	12.25	4.13
NPVMI-01		10% IPA	11.98	4.1
1999-Nov-01 (25.5 °C 65% RH)				
NPVMA-09	Vertical	Control	12.47	3.81
NPVMI-02	Vertical	10% IPA	11.62	4.19
NPVMI-03	Vertical	10% IPA	12.21	4.17
NPVMI-04	Vertical	15% IPA	11.74	4.41
1999-Nov-02 (26 °C 55% RH)				
NPVMI-05	Vertical	15% IPA	12.1	4.21
NPVMI-06	Vertical	15% IPA	12.22	4.32
NPVMA-10	Vertical	Control	12.74	4.1
1999-Nov-04 (26.5 °C 59% RH)				
NPVMI-07	Vertical	5% IPA	13.27	4.52
NPVMI-08	Vertical	5% IPA	12	4.2
NPVMA-11	Vertical	Control	12.31	4.34
NPVMI-09	Vertical	5% IPA	13.49	4.53
1999-Nov-06 (26.5 °C 55% RH)				
NPVMI-10	Vertical	15% IPA	13.24	4.46

Experiment ref.	Wicking angle	Experiment	mass	thickness
1999-Nov-07 (23.5 °C 57% RH)				
NPVMA-12	Vertical	Control	11.8	4.28
1999-Nov-09 (25.5 °C 56% RH)				
NPA30-01	Angled	30 ° Angle	11.5	4.25
NPA30-02	Angled	30 ° Angle	11.58	4.12
NPA30-03	Angled	30 ° Angle		
1999-Nov-10 (25 °C 57% RH)				
NPA30-04	Angled	30 ° Angle	12.7	4.43
NPA10-01	Angled	10 ° Angle	12.07	4.01
NPA10-02	Angled	10 ° Angle	11.75	4.14
1999-Nov-11 (24.5 °C 56% RH)				
NPA10-03	Angled	10 ° Angle	11.86	4.19
NPSCP-01	Angled	Step compressions	12.39	4.07
NPA45-01	Angled	45 ° Angle	11.66	4.1
left overnight				
1999-Nov-12 (24.5 54% RH)				
NPA45-02	Angled	45 ° Angle	11.76	4.08
NPA45-03	Angled	45 ° Angle	12.2	4.32
NPA60-01	Angled	60 ° Angle	12.14	4.34
NPA60-02	Angled	60 ° Angle	11.9	4.36
NPA60-03	Angled	60 ° Angle	11.61	4.29
left overnight				

Bibliography

[1] P. Abrams, S. Khoury, and A. Wein (editors). *Incontinence* (Health Publications Ltd, Plymbridge Distributors Ltd, Plymouth UK, 1999).

[2] Acordis. *Acordis UK Ltd (formerly Courtaulds).* 101 Lockhurst Lane, Coventry, CV6 5RS.

[3] K. L. Adams and L. Rebenfeld. *In-plane flow of fluids in fabrics:Structure/Flow characterization.* Textile Research Journal **57**(11), 647–654 (1987).

[4] A. W. Adamson. *Physical chemistry of surfaces* (Wiley (Interscience), 1967).

[5] E. Aharonov and D. Rothman. *Non-Newtonian flow (through porous media): a lattice Boltzmann method..* Geophysical research letters **20**, 679–682 (1993).

[6] J. Anderson, P. Abrams, J.G Blaivas, and S.L. Stanton. *The standardisation of terminology of lower urinary tract function..* Scandinavian Journal of Urology and Nephology, Supplement **114**, 5–19 (1988).

[7] G. Ashcroft, D. D. Marsh, D. D Evans, and L. Boersma. *Numerical method for solving the diffusion equation: I Horizontal flow in semi-infinte media.* Soil Science society proceedings 522–525 (1962).

[8] *Standard test method for biological clogging of geotextile or soil/geotextile filters.* ASTM D 1987 - 91.

[9] *Standard test method for constant head hydraulic transmissivity (in-plane flow) of geotextiles and geotextile related products.* ASTM D 4716 - 87.

[10] Jacob Bear. *Dynamics of flow in porous media* (Elsevier, New York, 1972).

[11] J. G. Berryman and S. C. Blair. *Use of digital image analysis to estimate fluid permeability of porous materials: Application of two-point correlation functions..* Journal of Applied Physics **60**(6), 1930–1938 (1986).

[12] S.K. Bhatia, J. L. Smith, and B. R. Christopher. *Geotextile characterization and pore size distribution:Part IIII. Comparison of methods and application to design.* Geosynthetics International **3**(3), 301–329 (1996).

[13] W. C. Bliesner. *A study of the porous structure of fibrous sheets using permeability techniques.* Tappi Journal **47**(7), 392–400 (1964).

[14] N. Bloembergen, E. M. Purcell, and Pound R.V. *Relaxation effects in nuclear magnetic resonance absorption.* Phys. Review **73**, 679–712 (1948).

[15] E. A. Boucher and Evans M. J. B. *Determination of interfacial tensions using rods.* Journal of Physics E:Scientific instruments **10**, 306 (1977).

[16] R. R. Bruce and A. Klute. *The measurement of soil moisture diffusivity.* Soil Science Society Proceedings **20**, 498–462 (1956).

[17] *Determination of the resistance to wicking.* BS 3424, Method 21 (1973).

[18] *Determination of wettability of textile fabrics.* BS 3554 (1970).

[19] F. L. Buchholz and A. T. Graham. *Modern superabsorbent polymer technology* (John Wiley and Sons, New York, 1998).

[20] S. V. Buldyrev, Barabasi A. L., Havlin S., Kertesz J., Stanley H.E., and xenias H. S. *Anomalous interface roughening in 3D porous media: experiment and model.* Physica A **191**, 220–226 (1992).

[21] B. J. Carroll. *The accurate measurement of contact angle, phase contact areas, drop volume, and Laplace excess pressure in drop-on-fibre systems.* Journal of Colloid and Interface Science **57**, 488–495 (1976).

[22] R. T. Cary and G. B. Sproles. *Absorbency of Terry Towels: A comparative evaluation of test methods.* Textile Research Journal **49**(12), 691–698 (1979).

[23] C. M. Case. *Rate of rise of liquid in a capillary tube-revisited..* Am. J. Physics **58**, 888–889 (1990).

[24] R. Chandler, J. Koplik, K. Lerman, and Willemsen J. G. *Capillary displacement and percolation in porous media.* J. Fluid Mech. **119**, 249–267 (1982).

[25] K. S. Chang and F. A. L. Dullien. *Section diameter method for non-spherical objects.* J. Microscopy **108**, 61–68 (1976).

[26] R. Chapas, K. Chinai, E. Tan, and D. Young. *New truly thin absorbent product designs.* Nonwovens world (Summer edition) 41–45 (1998).

[27] R. A. Chapman. *Liquid absorption of needlefelts - product modelling and optimisation using neural networks.* In *Medical Textiles International conference, Bolton UK*, 76–81 (1996).

[28] P. K. Chaterjee. *Absorbency*, volume 7 of *Textile Science and Technology* (Elsevier, New York, 1985).

[29] E. C. Childs and N. Collis-George. *The permeability of porous materials..* Proceedings of the Royal Society **201A**, 392–405 (1950).

[30] M. M. Chui, R. J. Philipps, and M. J. McCarthy. *Measurement of the porous microstructure of hydrogels by nuclear magnetic resonance.* Journal of Colloid and Interface Science **174**, 336–344 (1995).

[31] S. J. Chwastiak. *A wicking method for measuring wetting properties of carbon yarns.* Journal of Colloid and Interface Science **42**(2), 298–309 (1973).

[32] A. L. Clarke. *Surface tension balance.* Journal of Physics E:Scientific instruments **9**, 592–594 (1976).

[33] Royal college of physicians working party on incontinence. *Incontinence: Causes, management and provision of services.* Journal of the Royal College of Physicians, London **29**(4), 272–273 (July/August 1995).

[34] G. E. Collins. *A surface tension method for measuring the perimeters of fibres and the contact angles of liquids against fibres.* J. Textile Institute **38**, 73–77 (1947).

[35] CAHN Dynamic contact angle analyser. *CAHN ATI (Analytical technology inc.).* 1001 Fourier drive, Madison, WI 53717 USA, (UK supplier SM Scientific and medical products ltd., Shirley institute, 856 Wilmslow Road, Didsbury, Manchester, M20 2SA.

[36] T. F. Cooke. *Current concepts on superabsorbent fibres.* INDA Journal of Nonwovens Research **4**(1), 41–51 (1992).

[37] Kimberly-Clarke Corporation. *2 287 041 A.* UK Patent Application (1995).

[38] A. M. Cottenden. *Incontinence pads: clinical performance, design, and technical properties.* Journal Biomedical Engineering **10**, 506–514 (November 1988).

[39] A. M. Cottenden. *Clinical Nursing Practice: The promotion and management of continence (Brenda Roe ,editor)*, chapter Aids and appliances for incontinence (Prentice Hall, New York, 1992).

[40] A. M. Cottenden, G. E. Dean, and R. J.. Brooks. *Predicting the leakage performance of small disposable bodyworn incontinence pads using laboratory tests.* Medical Engineering and Physics **19**(6), 556–571 (September 1997).

[41] A. M. Cottenden, M. J. Fader, Barnes K. E., T. M. Jones, and Malone-Lee J. G. *The clinical performance of incontinence pads in relation to technical testing.* In *Proceedings INSIGHT '87*, volume 11 of *Adult Incontinence Products Conference*, 1–30 (Toronto, Canada, 1987).

[42] A. M. Cottenden and Ledger D. J. *Predicting the leakage performance of bodyworn disposable pads and pants for heavy incontinence using laboratory tests.* Journal Biomedical Engineering **15**, 212–220 (May 1993).

[43] Franck Courtray. *Courtray Consulting Labservice.* Centre Tertia, Z.I. Douai Dorignies, 710 Rue Jean Perrin F 59500 Douai.

[44] G. E. Cusick and T. Hopkins. *Absorbent Incontinence Products.* Technical report, The Textile Institute (1990).

[45] Wilkinson D. and Willemsen J. F. *Invasion percolation: a new form of percolation theory.* J. Phys A:Math. Gen. **16**, 3365–3376 (1983).

[46] H. Darcy. *Les Fontaines Publiques de la Ville de Dijon.* (Dalmont, Paris, 1856).

[47] B. K. Das, C. R. Debnath, and P. K. Ray. *Scanning electron microscope observations of nonwoven fabrics from jute and other textiles.* Textile Research Journal **87**, 528–531 (1987).

[48] C. N. Davies. *The separation of airbourne dust and particles.* Proc. Inst. Mech. Eng. **1B**, 185–198 (1952).

[49] E. R. Davies. *Machine Vision: Theory, Algorithms, Practicalities* (Academic Press Ltd, 24-28 Oval Road London, UK, 1990).

[50] J. De Coninck, N. Fraysse, M. P. Valignat, and A. M. Cazabat. *A microscopic simulation of the spreading of layered droplets.* Langmuir **9**, 1906–1909 (1993).

[51] T. de Weijer. *Prediction of PET spunbond properties using natural computation.* In *Index '99 Nonwovens Congress, R and D 2* (EDANA, 1999).

[52] M. Defever, K. Kesteloot, K. Coucke, E. Steeman, and T. Gruwez. *Socio-economic evaluation of incontinence in adults.* Technical report, Faculty of Medicine, Catholic University of Leuven, Belgium, Faculty of Medicine, School of public health, Centre for Health Services and Nursing Research, Kapucijnenvoer 35, 4, B-3000 LEUVEN,Belgium (1997).

[53] Allen Denver. *Serial communications in Win32.* Technical report, Microsoft Windows developer support (1995). Http://www.microsoft.com/win32dev/base/serial.htm.

[54] *Determination of the rate of absorption of water by textile materials (height of rise method).* DIN (1978).

[55] European Disposables and Nonwovens Association. *Nonwoven coverstock liquid strike through time.* Paper (1984).

[56] J. S. Dixon. *Advances in pore size measurement techniques for nonwoven fabrics.* In *Proceedings, INDA-TEC* (1996).

[57] M. Dolman. *The cost of incontinence.* Nursing Times **84**(31), 67–69 (1988).

[58] J. Domingue. *Probing the chemistry of the solid/liquid interface.* American Laboratory (1990).

[59] M. Dong and I. Chatzis. *The imbibition and flow of a wetting liquid along the corners of a square capillary tube.* Journal of Colloid and Interface Science **172**, 278–288 (1995).

[60] F. A. L. Dullien. *Rate of capillary rise in porous media with nonuniform pores.* AIChE J. **21**, 299 (1975).

[61] F. A. L Dullien. *Porous media fluid transport and pore structure* (Academic press, London, 1992).

[62] F. A. L. Dullien and G. K. Dhawan. *Bivariate pore-size distributions of some sandstones.* Journal of Colloid and Interface Science **52**(1), 129–135 (1975).

[63] F. A. L. Dullien, M. S. El-Sayed, and V. K. Batra. *Rate of capillary rise in porous media with nonuniform pores.* Journal of Colloid and Interface Science **60**, 497–506 (1977).

[64] F. A. L. Dullien and P.N. Mehta. *Particle size and pore (void) size determination by photomicrographic methods.* Powder Technology **5**, 179 (1971-1972).

[65] K. Dyrmose-Jensen. *Smart materials for liquid control the marriage of acquisition and re-wet with distribution.* In *International Nonwovens Symposium* (EDANA, 1998).

[66] M. J. Fader, L. Pettersson, L. Clinton, G. E. Dean, R. D. Brooks, and A. M. Cottenden. *Disposable, shaped, bodyworn pads with pants for heavy incontinence: an evaluation.* Disability Equipment Assessment Report IN.1, Medical Devices Agency, London, England (1998).

[67] L. R. Fisher and P. D. Lark. *An experimental study of the Washburn equation for liquid flow in very fine capillaries.* Journal of Colloid and Interface Science **69**(3), 486–492 (1979).

[68] J. L. Fowler and K. L. Hertel. *Flow of a gas through porous media.* J. Appl. Phys **11**, 496–502 (1940).

[69] F. Franks. *Aqueous solutions of simple electrolytes*, volume 3 of *Water: A comprehensive treatise* (Plenum Press, New York;London, 1973).

[70] B. B. Freud and H. Z. Freud. *A theory for the ring method for the determination of surface tension.* Am. Chem. Soc. J. **52**, 1772 (1930).

[71] U. Frisch, B. Hasslacher, and Y. Pomeau. *Lattice gas automata for the Navier-Stokes equation.* Phys. Rev. Lett **56**, 1505–1507 (1986).

[72] H. Fujita. *On the distribution of liquid ascending in a filter paper.* J. Phys. Chem. **56**, 625–629 (1952).

[73] D.N. Gans. *The rarity of zero contact angles.* J. Phys. Chem **49**, 165–166 (1945).

[74] W. R. Gardner and M. S. Mayhugh. *Solutions and tests of the diffusion equation for the movement of water in soil..* Proceedings of the Soil Science Society of America **22**, 197–201 (1958).

[75] W. R. Gardner and J. A. Widtsoe. *The movement of soil moisture.* Soil Sci. **11**, 215–233 (1921).

[76] T. Gillespie. *The spreading of low vapour pressure liquids in paper.* Journal of Colloid and Interface Science **13**, 32–50 (1958).

[77] T. Gillespie. *The capillary rise of a liquid in a vertical strip of filter paper.* Journal of Colloid and Interface Science **14**, 123–130 (1959).

[78] P. H. Greaves and B. P. Saville. *Microscopy of textile fibres.* Royal Microscopy Society Microscopy Handbooks (Bios Scientific Publishers, 9 Newtec Place, Magdalen Road, Oxford, OX4 1RE, 1995).

[79] B. S. Gupta. *The effect of structural factors on the absorbent characteristics of nonwovens.* Tappi Journal 147–152 (August 1988).

[80] B. S. Gupta and H. S. Whang. *Capillary absorption behaviours of hydro-entangled and needlepunched webs of cellulosic fibres.* In *INDA Tec* (1996).

[81] A. C. Guyton. *Textbook of medical physiology* (W.B. Saunders Company, Philadelphia, 1991), 8 edition.

[82] S. Haeker. *What's best reusable or disposable incontinece products?.* Textile rental 86–90 (1986).

[83] J. Happel. *Viscous flow relative to arrays of cylinders.* A.I.Ch.E. Journal **5**(2), 174–177 (1959).

[84] W. D. Harkins and F. J. Hubert. *A method for the determination of surface and interfacial tension from the maximum pull on a ring.* Am. Chem. Soc. J. **52**, 1751 (1930).

[85] P. R. Harnett and P. N. Mehta. *A survey and comparison of laboratory test methods for measuring wicking.* Textile Research Journal **54**, 471–478 (1984).

[86] Paul Hartmann. *Paul Hartmann AG.* Heidenheim, Germany.

[87] D. J. Henderson and W. F Rogers. *Hospital trials of incontinence underpads*. Nursing Times 141–142 (4 February 1972).

[88] K. T. Hodgson and Berg J. C. *Single fibre wettability properties of fluff pulps and their relationships to absorbency*. In *2nd International Nonwovens conference proceedings, Absorbency '89 2nd International Pira Conference*, volume 1 (Aarhus, Denmark, 1989).

[89] M. P. Hollewand and L. F. Gladden. *Probing the structure of porous pellets: An NMR study of drying*. Magn. Reson. Imag. **12**, 291–294 (1994).

[90] N. R. S. Hollies, M. M. Kaessinger, and H. Bogaty. *Water transport mechanisms in textile materials, Part I:The role of yarn roughness on Capillary-type penetration*. Textile Research Journal **27**, 829–835 (1956).

[91] N. R. S. Hollies, M. M. Kaessinger, B. S. Watson, and H. Bogaty. *Water transport mechanisms in textile materials, Part II:Capillary-type penetration in yarns and fabrics*. Textile Research Journal **27**, 8–13 (1957).

[92] Y Hsieh. *Liquid transport in fabric structures*. Textile Research Journal **65**(5), 299–307 (1995).

[93] Y Hsieh and B. Yu. *Liquid wetting, transport and retention properties of fibrous assemblies, Part I:Water wetting properties of woven fabrics and their constituent single fibres*. Textile Research Journal **62**(11), 677–685 (1992).

[94] X. Huang and R. R. Bresee. *Characterizing nonwoven web structures using image analysis techniques Part I:Pore analysis in thin webs*. INDA Journal of Nonwovens Research **5**(1), 13–21 (1993).

[95] G. S. Hwang, C. K. Lu, and M. F. Lin. *Transmissivity behaviour of layered needlepunched nonwoven geotextiles*. Textile Research Journal **69**(8), 565–569 (1999).

[96] G. J. I. Igwe. *Needle felts in gas and dust filtration* (Ellis Horwood limited, 1987).

[97] Porous Materials Inc. *Porous Materials Inc.*. Cornell Business and Technology Park, 83 Brown Rd, Ithaca, NY 14850, USA.

[98] W. L. Ingmanson, B. D. Andrews, and R. C. Johnson. *Internal Pressure distributions in compressible mats under fluid stress*. Tappi Journal **42**(10), 840–849 (1959).

[99] E Ising. *A contribution to the theory of of ferromagnetism*. Z. Physik **31**, 253 (1925).

[100] ISO. *Urine absorbing aids - Part 1: Whole Product Testing (ISO 11948-1)* (1996).

[101] ISO. *Urine absorbing aids - Part 2: Determination of short time liquid release (leakage) performance under conditions of light incontinence and low pressure (ISO 11948-2)* (1997).

[102] G. W. Jackson and D. F. James. *The permeability of fibrous porous media*. The Canadian Journal of Chemical Engineering **64**, 364–374 (1986).

[103] A. A. Jeje. *Rates of spontaneous movement of water in capillary tubes*. Journal of Colloid and Interface Science **69**(3), 420–429 (1979).

[104] P. Joos, P. van Remoorter, and Bracke M. *The kinetics of wetting in a capillary*. Journal of Colloid and Interface Science **136**(1), 189–197 (1990).

[105] Y. K. Kamath, C. J. Dansizer, S. Hornby, and H. Weigmann. *Surface wettability scanning of long filaments by a liquid membrane method.* Textile Research Journal **57**, 205–212 (1987).

[106] T. Kawanishi, T. Seimiya, and T. Sasaki. *Corrections for surface tension measured by Wilhelmy method.* Journal of Colloid and Interface Science **32**(4), 622–627 (1970).

[107] T. Kawase, Y. Morimoto, T. Fujii, and M. Minagawa. *Spreading of liquids in textile assemblies, Part III:Application of an image analyser system to capillary spreading of liquids.* Textile Research Journal **58**, 306–308 (1988).

[108] T. Kawase, S. Sekoguchi, T. Fujii, and M. Minagawa. *Spreading of liquids in textile assemblies, Part I:Capillary spreading of liquids.* Textile Research Journal **56**, 409–414 (1986).

[109] T. Kawase, S. Sekoguchi, T. Fujii, and M. Minagawa. *Spreading of liquids in textile assemblies, Part I:Effects of softening on capillary spreading.* Textile Research Journal **56**, 617–621 (1986).

[110] D. Kirkham and C. L. Feng. *Some tests of the diffusion theory, and laws of capillary flow, in soils.* Soil science **67**, 29–40 (1949).

[111] D. Kirkham and W. Powers. *Advanced soil physics.* (Wiley-Interscience, New York;London, 1972).

[112] E. Kissa. *Capillary sorption in fibrous assemblies.* Journal of Colloid and Interface Science **83**, 265–272 (1981).

[113] E. Kissa. *Wetting and wicking.* Textile Research Journal **66**(10), 660–668 (1996).

[114] R. L. Kleinberg. *Pore size distributions, pore coupling, and transverse relaxation spectra of porous rocks.* Magn. Reson. Imag. **12**, 271–274 (1994).

[115] R. M. Koerner, J. L. Guglielmetti, and J. L. Rosenfarb. *On the permeability testing of fabrics and fabric/soil systems.* In *Eighth technical symposium: Nonwovens – Innovative fabrics for the future*, 143–154 (INDA, 1980).

[116] J. Koplik. *Creeping flow in two-dimensional networks.* J. Fluid Mech. **119**, 219–247 (1982).

[117] J. Koplik, C. Lin, and M. Vermette. *Conductivity and permeability from microgeometry.* J. Appl. Phys.. **56**(11), 3127–3131 (1984).

[118] H. J. Koslowski. *Dictionary of man-made fibres, terms, figures, trademarks* (International business press publishers, Frankfurt, 1998).

[119] J. Kozney. *Über kapillare Leitung des Wassers im boden.* Royal Academy of Science, Vienna, Proc. Class I **136**, 271–306 (1927).

[120] R. Krčma. *Manual of nonwovens* (Textile trade press, Manchester England, 1971).

[121] C. P. Kyan, D. T. Wasan, and R. C. Kintner. *Flow of single phase fluids through fibrous beds.* Ind Eng. Chem. Fundam. **9**(4), 596–603 (1970).

[122] L. Labajos-Broncano, M. L. González-Martín, B. Jańczuk, J. M. Bruque, and C. M. González-García. *Distance-Time measurements in capillary penetration: Choice of coordinate system.* Journal of Colloid and Interface Science **211**, 175–177 (1999).

[123] R. P. Labrecque. *The effects of fibre cross-sectional shape on the resistance to the flow of fluids through fibre mats.* Tappi Journal **51**(1), 8–15 (1968).

[124] R. D. Laughlin and J. E. Davies. *Some aspects of capillary absorption in fibrous textiles.* Textile Research Journal **31**, 904–910 (1961).

[125] D. LeBihan. *Molecular diffusion nuclear magnetic resonance imaging.* Magn. Reson. Quart **7**, 1–30 (1991).

[126] Ledatec. *Ledatec.* Longshaw Industrial Park, Highfield Road, Blackburn, Lancashire, BB2 3AS.

[127] R. Lenormand, C. Zarcone, and A. Sarr. *Mechanisms of the displacement of one fluid by another in a network of capillary ducts.* J. Fluid Mech. **135**, 337–353 (1983).

[128] K. Levenberg. *A method for the solution of certain problems in least squares.* Quart Applied Mathematics **2**, 164–168 (1944).

[129] D. R. Lide and Frederikse H.P.R. *CRC Handbook of chemistry and physics* (CRC Press Inc, Boca Raton, New York, 1997-1998), 78 edition.

[130] C. Lin and M. Cohen. *Quantitative methods for micro-geometric modelling.* J. Appl. Phys. **53**(6), 4152–4165 (1982).

[131] J. D. Lindsay and P. H. Brady. *Studies of anisotropic permeability with applications to water removal in fibrous webs.* Tappi Journal **76**(9), 119–127 (1993).

[132] D. Lukáš. *Computer simulation of liquid wetting dynamics in fibre structures using the Ising model.* The Journal of the Textile Institute **88**(2), 149–161 (1997).

[133] D. Lukáš. *Ising model simulation of liquid mixtures spreading on fibres.* In *2nd International Workshop on Wetting and self-organisation in thin liquid films*, volume 3, 43–48 (Ludwig-Maxmilians Universität, Munich Germany, 1998).

[134] D. Lukáš. *Recent studies of fibrous materials wetting dynamics.* In *Index 99 Nonwovens conference*, volume RD2 (European disposables and nonwovens association, Avenue Eugene Plasky 157-1030, Brussels, Belgium, 1999).

[135] J. Lunenschlosss and W. Albrecht (editors). *Non-woven and bonded fabrics* (Elliss Horwood Limited, Halsted Press: a dvision of John Wiley and sons, New York;Chichester;Toronto;Brisbane, 1985).

[136] I. F. Macdonald, P. Kaufmann, and Dullien F. A. L. *Quantitative image analysis of finite porous media:Development of genus and pore map software.* J. Microscopy **144**, 277–296 (1986).

[137] I. F. Macdonald, P. Kaufmann, and Dullien F. A. L. *Quantitative image analysis of finite porous media:Specific genus of cubic lattice models and Berea sandstone.* J. Microscopy **144**, 297–316 (1986).

[138] I. F. Macdonald, H. Q. Zhao, and M. J. Kwiecien. *Analysis of the approaches to 3-D reconstruction of porous media.* Journal of Colloid and Interface Science **173**, 245–248 (1995).

[139] M. Maejima. *Applying capillarity to estimation of space structure of fabrics.* Textile Research Journal 427–434 (1983).

[140] Magnetic Resonance Imaging. *Recent advances in magnetic resonance applications to porous media*, volume 12(2). Special edition.

[141] A. D. Mahale, R. K. Prud'homme, and L. Rebenfeld. *Characterisation of voids formed during liquid impregnation of non-woven multifilament glass networks as related to composite processing.* Composites Manufacturing **4**(4), 199–207 (1993).

[142] S.S. Manna, H. J. Herrmann, and D. P. Landau. *A stochastic method to determine the shape of a drop on a wall.* Journal of Statistical Physics **66**(3/4), 1155–1163 (1992).

[143] D. Marquardt. *An algorithm for least-squares estimation of nonlinear parameters.* SIAM Journal Applied Mathematics **11**, 431–441 (1963).

[144] T. J. Marshall, J. W. Holmes, and C. W. Rose. *Soil physics.* (Cambridge University Press, United Kingdom, 1996), 3rd edition.

[145] G. Mason and R. Morrow. *Capillary behaviour of a perfectly wetting liquid in irregular triangular tubes.* Journal of Colloid and Interface Science **141**(1), 262–274 (1991).

[146] J. Masounave, R. Denis, and A. L. Rollin. *Prediction of hydraulic properties of synthetic nonwoven fabrics used in geotechnical work.* Canadian Geotexh. Journal **17**, 517–525 (1980).

[147] R. A. McLaughlin. *Technical Report - Randomized Hough transform: Improved ellipse detection with comparison.* Technical report, Centre for Intelligent Information Processing Systems, The University of Western Australian, Nedlands W.A. 6907 (1999).

[148] B. Miller and D. B. Clark. *Liquid transport through fabrics:wetting and steady state flow, Part 1: a new experimental approach.* Textile Research Journal 150–155 (March 1978).

[149] B. Miller, H. L. Friedman, R. A. Johnson, and C. E. Holmes. *Pro and anti-gravity wicking compared.* In *Proceedings, Indatec '96*, 13.1–13.15 (1996).

[150] B. Miller and S. H. Jansen. *Wicking of liquids in nonwoven fibre assemblies.* In *Proceedings of the 10th Technical Symposium on Advances in Nonwovens Technology*, 216–226 (November 17-19, 1982).

[151] B. Miller and I. Tyomkin. *Liquid porosimetry:New methodology and applications.* Journal of Colloid and Interface Science **162**, 163–170 (1994).

[152] B. Miller and I. Tyomkin. *Methods for determining pore size distributions in nonwoven materials.* In *Proceedings of the TAPPI Nonwovens Conference*, 169–174 (April 20-23, 1986).

[153] B. Miller and R. A. Young. *Methodology for studying the wettability of filaments.* Textile Research Journal **45**, 359–365 (1975).

[154] F. W. Minor, Schwartz A. M., Wulkow E. A., and Buckles C. B. *The migration of liquids in textile assemblies Part III: The behaviour of liquids on single textile fibres.* Textile Research Journal **29**(12), 940–949 (1959).

[155] F. W. Minor, A. M. Schwartz, E. A. Wulkow, and C. B. Buckles. *The migration of liquids in textile assemblies Part I.* Textile Research Journal **29**(12) (1959).

[156] F. W. Minor, A. M. Schwartz, E. A. Wulkow, and C. B. Buckles. *The migration of liquids in textile assemblies Part II: The wicking of liquids in yarns.* Textile Research Journal **29**(12), 931–939 (1959).

[157] S. Montgomery, B. Miller, and L. Rebenfeld. *Spatial distribution of local permeabilities in fibrous networks.* Textile Research Journal **62**(3), 151–161 (1992).

[158] M. Morra, E. Occhiello, and F. Garbassi. *Surface studies on untreated and plasma treated carbon fibres.* Composites Science and Technology **42**, 361–372 (1991).

[159] N. R. Morrow. *Physics and thermodynamics of capillary action in porous media.* Industrial and engineering chemistry. **62**, 32–57 (1970).

[160] W.E. Morton and Hearle J.W.S. *Physical properties of textile fibres* (Textile institute, 1993).

[161] C. J. Nederveen. *Absorption of liquid in highly porous nonwovens.* Tappi Journal 174–180 (December 1994).

[162] L. Nilsson and S. Stenström. *A study of the permeability of pulp and paper.* In.t J. Multiphase flow **23**(1), 131–153 (1997).

[163] C. Norris, A. Cottenden, and D. Ledger. *A multi-comparative trial of six reusable bedpads.* Technical report, Final project report to the Department of Health (1993).

[164] C. Norris, A. Cottenden, and D. Ledger. *Underpad Overview.* Nursing Times **89**(21), 68–74 (May 1993).

[165] Du Nouy. J. Gen. Physiol. **1**, 521 (1918).

[166] Y. Okamura, K. Gotoh, M. Kosaka, and M. Tagawa. *Capillary wetting rates in nylon fibrous assemblies.* J. Adhesion Sci. Technol. **12**(6), 639–654 (1998).

[167] McDonald P. and Strange J. *Magnetic resonance and porous materials.* Physics world 29–34 (July 1998).

[168] D. Payne. Nature **172**, 261 (1953).

[169] M. G. C. Peiris and K. Tennakone. *Rate of rise of liquid in a capillary tube.* Am. J. Physics **48**, 415 (1980).

[170] E. J. Phillip, Cottenden A. M., and Ledger D. J. *The reuser's guide.* Nursing Times **88**(4), 66–72 (1992).

[171] K. M. Pillai and S. G. Advani. *Wicking across a fiber-bank.* Journal of Colloid and Interface Science **183**, 100–110 (1996).

[172] W. K. Pratt. *Digital image processing* (New York:John Wiley and Sons Inc, 1991).

[173] H. M. Princen. *Capillary phenomena in assemblies of parallel cylinders: Capillary rise between two cylinders.* Journal of Colloid and Interface Science **30**(1), 69–75 (1969).

[174] H. M. Princen. *Capillary phenomena in assemblies of parallel cylinders: Capillary rise in systems with more than two cylinders.* Journal of Colloid and Interface Science **30**(3), 359–371 (1969).

[175] J. A. Quiblier. *A new three dimensional modelling technique for studying porous media.* Journal of Colloid and Interface Science **98**(1), 84–102 (1984).

[176] S. Ramanujan. *Modular equations and approximations to* π. Quart. J. Pure Applied Math **45**, 350–372 (1913-1914).

[177] M. A. Rebollo, Hogert E. N., J. Albano, C.A. Raffo, and N.G. Gaggioli. *Correlation between roughness and porosity in rocks*. Optics and laser technology **28**, 21–23 (1996).

[178] J. S. Reed. *Liquid permeability of packed particles: why perpetuate the Carmen-Kozney equation*. J. Amer. Ceram Soc. **76**(2), 547 (1993).

[179] M. Reed and V. Howard. *Unbiased Stereology: Three-Dimensional Measurements in Microscopy*. Royal Microscopy Society Microscopy Handbooks (Bios Scientific Publishers, 9 Newtec Place, Magdalen Road, Oxford, OX4 1RE, 1998). ISBN 1859960715.

[180] P. A. Rice, D. J. Fontugne, R. G. Latini, and A. J. Barduhn. *Anisotropic permeability in porous media*. Industrial Engineering and Chemistry **62**(6), 22–31 (1970).

[181] L.A. Richards. *Capillary conduction of liquids in porous mediums*. Physics **1**, 318–333 (1931).

[182] H. L. Ritter and L.C. Drake. Ind. Eng. Chem. Anal. Ed. **17**, 782 (1945).

[183] W. Roorda. *Review: Do hydrogels contain different classes of water?*. Journal Biomaterials Science Polymer Edition **5**, 383–395 (1994).

[184] D. H. Rothman. *Cellular-automaton fluids: A model for flow in porous media*. Geophysics **53**, 509–518 (1988).

[185] D.F. Rudd. *On the paper adsorption chromatographic phenomena*. Journal of Physical Chemistry **64**, 1254–1256 (1960).

[186] A. L. Ruoff, Prince L. Denver, J. Calvin Giddings, and G. H. Stewart. *The diffusion analogy for solvent flow in paper*. Kolloid-Zeitschrift **266**, 144–151 (1959).

[187] S.J. Russel, I. Ahmed, and M. J. Tipper. *Structural modification of natural cellulose fibres by water jet impact*. In *Seminar proceedings: Dry laid nonwovens, United Kingdom*, 12–23 (Nonwovens network, 1999).

[188] R. L. Salvada, M. J. Pereira, Silvy J., and M. Nunes. *Identification of nonwovens structural parameters: Correlation with their properties and Manufacturing process*. In *Index '99 Nonwovens Congress, R and D 2* (EDANA, 1999).

[189] A.Y. Sasov. *Microtomography. Part 1:Methods and Equipment*. Journal of Microscopy **147**, 169–178 (1987).

[190] A.Y. Sasov. *Microtomography. Part 2:Examples of Applications*. Journal of Microscopy **147**, 179–192 (1987).

[191] Scandanavian Pulp, Paper and Board Comitee. *Fluff specific volume and absorption properties*. Paper, SCAN-C 33:80 (1980).

[192] A. E. Scheidegger. *The physics of flow through porous media* (University of Toronto press, Toronto, Buffalo (NY), 1974).

[193] A. M. Schwartz. *Capillarity: Theory and practice*. Ind. Eng. Chem. **61**(1), 10–21 (1969).

[194] A. M. Schwartz and F. W. Minor. *A simplified thermodynamic approach to capillarity I: Application to flow in capillary channels*. Journal of Colloid and Interface Science **14**, 572–583 (1959).

[195] A. M. Schwartz and F. W. Minor. *A simplified thermodynamic approach to capillarity II: Applications to contact angle and spreading phenomena.* Journal of Colloid and Interface Science **14**, 584–597 (1959).

[196] G. J. Scoffin. *Conditions improved in test bed hospital.* Laundry and Cleaning News (22nd February 1980).

[197] W. Shen, I. H. Parker, and Y. J. Sheng. *The effects of surface extractives and lignin on the surface energy of eucalypt kraft pulp fibres.* J. Adhesion Sci. Technol. **12**(2), 161–174 (1998).

[198] R. Steele. *Capillary size distribution.* Textile Research Journal **28**, 144–147 (1958).

[199] Stockhausen. *Stockhausen GmBH.* Krefeld, Germany.

[200] J. Szekely, A. W. Neumann, and Y. K. Chuang. *The rate of capillary penetration and the applicability of the Washburn equation.* Journal of Colloid and Interface Science **35**, 273–278 (1971).

[201] Texon. *Texon UK Ltd.* Ross Walk, Belgrave, Leicester, LE4 5BX, United Kingdom.

[202] P. H. Thornburn, A. M Cottendden, and D. J. Ledger. *Undercover trials.* Nursing Times **88**(13), 72–78 (1992).

[203] A. F. Turbak. *Nonwovens: Theory, Process, Performance, and Testing* (TAPPI Press, 1993).

[204] J. Van Brakel and P. M. Heertjes. *Capillary rise in porous media. Part I: A Problem.* Powder Tech. **16**, 75–81 (1977).

[205] J. Van Brakel and P. M. Heertjes. *Capillary rise in porous media. Part III: The role of contact angle.* Powder Tech. **16**, 92–96 (1977).

[206] L. D. M. van der Brekel and E. J. de Jong. *Hydrodynamics in packed textile beds.* Textile Research Journal **59**, 433–440 (1989).

[207] J. VanBrakel and P. M. Heertjes. *Capillary rise in porous media.* Nature **254**, 585–586 (1975).

[208] G. F. Vander Voort. *Metallography:Principles and practice* (McGraw Hill Book Co., NY, 1984).

[209] O. Vizika and A. C. Payatakes. *Parametric experimental study of forced imbition in porous media.* Physico Chem. Hydrodynamics **11**, 187–204 (1989).

[210] C.I. Voss. *SUTRA (SAturated Unsaturated TRAnsport).* Technical report, US Geological Survey, Water resources division, 437 National centre, 12201 Sunrise Valley Drive, Reston, VA 22092 (1984).

[211] F.C. Wang and V. Lakshminarayana. *Mathematical simulation of water movement through unsaturated nonhomogeneous soils.* Proceedings of the Soil Science Society of America **32**, 329–334 (1968).

[212] S. B. Warner. *Fiber Science* (Prentice Hall, Englewood Cliffs, New Jersey 07632, 1995).

[213] E. W Washburn. *The dynamics of capillary flow.* Physics Review **17**, 273–283 (1921).

[214] S Webb. *The physics of medical imaging* (IOP Publishing Ltd, London, 1988).

[215] K. Y. Wei, T. L. Vigo, B. C. Goswami, and K. E. Duckett. *Permeability of soil-geotextile systems.* Textile Research Journal **55**, 620–626 (1985).

[216] S. P. Wesson, Kamath Y. K., and A. D. Mahale. *A computer model for wetting hysteresis. A virtual wettability scanning balance.* Colloids and surfaces A **89**, 133–143 (1994).

[217] A. G. Wilkes. *A new viscose rayon fibre for nonwovens.* In *Book of papers, International nonwoven fabrics conference, INDATEC 89*, 499–516 (Association of the nonwoven fabrics industry, Philladelphia, 1989).

[218] J. Willhelmy. *Ueber die abhängigkeit der capillaritäts constanten des alkohols von substanz und gestalt des benetzten festen körpers.* Ann. Physik Leipzig **119**, 177–217 (1863).

[219] S. D. Wolff and R. S. Balaban. *Magnetic transfer contrast (MTC) and tissue water relaxation in vivo.* Magn. Reson. Med. **10**, 135–144 (1989).

[220] S. Wolfram. *Cellular automaton fluids 1: Basic theory.* J. Stat. Phys. **45**, 471–526 (1986).

[221] H. Yasuda, H. G Olf, B. Crist, C. E. Lamaze, and A. Peterlin. *Water structure at the water-polymer interface*, volume 10, chapter Movement of water in homogeneous water-swollen polymers, 39–55 (Plenum Press, 1972). Jellinek, H.H.G. (ed).

[222] R. Yerworth. Ph.D. thesis, University College London (2000).

[223] T. Young. Philosophical transactions of the Royal Society **95**, 65 (1805).

[224] C. P. Yu and T. T. Soong. *A random cell model for pressure drop prediction in fibrous filters.* Journal of Applied Mech., Trans **65**(5), 299–307 (1995).

[225] W. Zhou and S. Warner. *Pore sizes in carpet.* Textile Research Journal **69**(6), 423–430 (1999).